Designing Boron Nitride Nanotubes and their Macroscopic Assemblies via Sacrificial Templating



Ruth Sang Jones

St Catherine's College

University of Oxford

A thesis submitted for the degree of

Doctor of Philosophy

Hilary 2021

This thesis is dedicated to
My Mother and Grandmother
for being the women who made me

"Man never made any material as resilient as the human spirit."

— Bernard Williams

Acknowledgements

I have imagined reaching this moment many times, yet I am somewhat in disbelief that it is here. What a journey it has been. I could fill so many pages about my personal experience, with all its peaks and troughs, as a research student at Oxford over the last 4 years. But within the constraints of this little snippet that exposes my humanness, I'd like to highlight one emotion, which is one of gratitude towards those who have helped me along this journey.

I would first like to thank my supervisor, Professor Nicole Grobert, for giving me the opportunity to join the Nanomaterials by Design research group and for fostering my intellectual independence and confidence. I would like to extend my gratitude to Professor Derek Raine at the University of Leicester for inspiring me during my undergraduate years with his passion for learning and for supporting my decision to pursue a doctorate degree. I am also indebted to Dr Barbara Maciejewska for her knowledgeable advice and her unwavering encouragement over the last two years and throughout the duration of my thesis writing.

Many thanks to the entire NbD group for the many entertaining lunch time chats and mug-pong battles, and the overall friendly research environment out there in Begbroke. I'd also like to express my appreciation for Dr Babenko, who influenced my interest in boron nitride, as well as Santamon, Koen, Albert and Toppy, all of whom offered their valuable time to assist me in the lab or at the materials facilities in town. Shout out also to Jesus and Pierre for being great teammates on our side group project, and to Eoin, Dillon, John and Kai Ling for their valuable questions during group meetings. Thanks also to Pablo for being a very understanding colleague and friend with whom I could share my frustrations and their comedic value. I also wish to thank Yifeng Gao, who was especially helpful as a visiting student in the summer of 2018.

Within the Materials Department, I'd like to gratefully acknowledge the people at the David Cockayne Centre for Electron Microscopy, particularly Dr Ian Griffiths, who patiently spent many hours with me on the ARM, and Dr Neil Young, and Jennifer Holter for training me to use the microscopes. I'd also like to recognise the valuable advice on EELS that I received from Dr Rebecca Nicholls. Many thanks should also go to Dr Philip Holdway, who offered me a great amount of assistance with XPS and XRD measurements, as well as Nicola Flanagan and Dr

Colin Johnston, who were instrumental in helping me access other Oxford Materials Characterisation Services facilities. Thanks also to Professor Andrew Watt and his student Wing Chung for allowing me to access their lab facilities and showing me how to use the four-point probe. And a special thanks to Greg Cook and Richard Turner, whose help with any and everything in the Hirsch building cannot be overestimated.

I also had the great pleasure of interning at the NASA Ames Research Center in my 3rd year, and would like to extend my sincere thanks to Dr Beomseok Kim for the opportunity to work with him and for his confidence in my abilities.

I must also give a big shout-out to all the new friends I made at Oxford. I appreciate them all for some of the best memories of my 20s. Thanks to Sue, my very first friend at Oxford, for motivating me to work harder. I must also say a special thanks to Matthew, whose puns always made me laugh. And in the final writing up stages, Anka's kind words and supply of memes were truly appreciated. Many thanks should also go to some of my oldest but dearest of friends- Danielle, Alix and Petal- who were so supportive all these years even though we are oceans apart.

To my kind and caring Aleksandr, the treasure that I discovered at Oxford, thank you for always bringing out the best in me. Your love and encouragement were the best daily fuel to keep me going.

Finally, I cannot begin to express my love and deepest appreciation for my parents, Xiao Ping and Allan. Thank you for your nurturing, your sacrifices and your profound belief in me. Thank you for giving me a reason to succeed.

Abstract

Hexagonal boron nitride nanotubes (BNNTs) have properties advantageous for the development of next generation materials and advanced composites that exhibit improved mechanical strength, high temperature resistance and thermal conductivity.

The future exploitation of BNNTs depends on the development of economically accessible and safe production methods. These should also present a scope for BNNT structural tunability, and output a high purity of BNNTs versus other possible hexagonal boron nitride (h-BN) structures. In this thesis, a novel synthesis technique is validated that is primarily motivated by a demand to address these issues.

Here, atmospheric pressure chemical vapour deposition (APCVD) is employed in conjunction with a safe and easy-to-handle compound, ammonia borane ($H_3N{-}BH_3$), to deposit h-BN coaxially onto the surface of multi-wall carbon nanotubes (MWCNTs). Subsequently, thermal oxidation is demonstrated to remove/sacrifice the MWCNTs, thereby leaving BNNTs as shells that exhibit diameter dependence on their MWCNT templates. By this method, BNNTs with walls 2-3 nm thick are synthesised, and nanotube outer diameters 16±2 nm and 40±16 nm are obtained using separate grades of MWCNT templates. The achieved BNNT diameter control exemplifies the versatility of MWCNT as a template material, which is justified by its structural compatibility to BNNTs, commercial scale availability and established morphological diversity. It is also argued here that use of $H_3N{-}BH_3$ precursor favours the van der Waals isolation of the deposited h-BN from the MWCNT template, which is advantageous for the h-BN purity of the BNNT shell.

The work presented here also establishes that the proposed APCVD and sacrificial templating method, when implemented in combination with vacuum filtration, is a novel and adaptable means of fabricating macroscopic assemblies of BNNTs. This is achieved at the cm-scale for BNNTs randomly entangled within a low density, self-supporting and sheet-like architecture with thicknesses $<100\mu$m. Furthermore, platelet crystals discovered on the surface of these BNNT assemblies, revealed to be boric acid, provide evidence in support of a new theory on the oxidation behaviour and moisture sensitivity of BNNTs.

Throughout this work, newly synthesised nanomaterials (non-assembled and assembled) are characterised by multiple techniques including electron microscopy, spectroscopy and thermogravimetry, in order to determine their qualities such as dimensionality, crystallinity, chemical composition and thermal stability.

Publications/Conferences

Peer-Reviewed Publications

- **Ruth Sang Jones**, Barbara Maciejewska, Nicole Grobert, *Synthesis, characterisation and applications of core-shell carbon-hexagonal boron nitride nanotubes*, Nanoscale Advances, 2 (11), 4996-5014, (2020)
  The content of this publication is partly reproduced in **Chapter 2.**

- Albert W. Xiao, Koen Evers, Marzena Tkaczyk, **Ruth Sang Jones**, Claire Saxby, Kalin Dragnevski, and Nicole Grobert , *Electrophoretic Fabrication of Robust Carbon Nanotube "Buckyfilms" for Flexible Electronics*, ACS Applied Nano Materials, 2 (8), 5190-5199 (2019)

- Panagiotis Dallas, Elena Tomšík, **Ruth Sang Jones**, Albert Xiao, Eleanor Milnes-Smith, Nicole Grobert, Kyriakos Porfyrakis, *Electrochemically active water repelling perfluorinated polyaniline films*, Chemical Physics, 528,110540 (2020)

- Beomseok Kim, Thaddeus J. Norman, **Ruth Sang Jones**, Dong-il Moon, Jinwoo Han, and M. Meyyappan, *Carboxylated Single-Walled Carbon Nanotube Sensors with Varying pH for the Detection of Ammonia and Carbon Dioxide Using an Artificial Neural Network*, ACS Applied Nano Materials, 2 (10), 6445-6451 (2019)

- **Ruth Sang Jones**, Beomseok Kim, Jin-Woo Han, M. Meyyappan, *pH Modeling to Predict SWCNT-COOH Gas Sensor Response to Multiple Target Gases*, J. Phys. Chem C, 125, 17, 9356-9363 (2021)

In Preparation

- **Ruth Sang Jones *et al.*,** *Atmopsheric Pressure Chemical Vapour Deposition with Ammonia Borane as a route to carbon/h-BN heteronanotubes and boron nitride nanotubes*

- **Ruth Sang Jones *et al.*,** *The Oxidation Behaviour of Boron Nitride Nanotube Buckypapers: A Case of Boric Acid Pox*

- Seyyed Shayan Meysami, **Ruth Sang Jones**, Megan Carter, Xiewen Liu, Koen Evers, Vitaly Babenko, Brooke Lear, Jesus A. I Acapulco Jr., Santamon Luanwuthi, Albert Xiao, Philip Holdway, Ian Griffiths, Neil Young, Farzaneh Shayeganfar, Rouzbeh Shahsavari, Nicole Grobert, *Foliating Carbon nanotubes with Boron Nitride-rich flakes*

Conferences

International Conference on Crystal Growth and Epitaxy

Keystone, Colorado, USA, 2019

- Invited Speaker: *Hexagonal Boron Nitride Synthesis with Ammonia Borane*

Royal Society of Chemistry, Materials Chemistry Division Symposium

London, UK, 2018

- Poster Presentation & Summary Talk: *Boron Carbon Nitride and Boron Nitride Nanotubes*

Statement of Ownership

The work presented herein was performed by me, and any use of the first personal plural is stylistic. If the work was carried out by other researchers, their contribution is appropriately acknowledged.

Contents

List of Abbreviations **xiii**

1 Introduction **1**
1.1 Thesis Outline . . . 1
1.2 Hexagonal Boron Nitride . . . 4
1.3 Boron Nitride Nanotubes . . . 6
1.3.1 Properties & Applications . . . 7
1.3.2 Synthesis Landscape . . . 13
1.3.2.1 High Temperature Synthesis . . . 13
1.3.2.2 Low Temperature Synthesis . . . 14
1.3.3 Buckypaper Macroscopic Assemblies . . . 17
1.4 Ammonia Borane: an h-BN precursor . . . 19

2 Coating Multi-wall Carbon Nanotubes with Boron Nitride (MWCNT@BN) **24**
2.1 Introduction . . . 24
2.2 Synthesis of MWCNT@BN by Ammonia Borane pyrolysis . . . 33
2.2.1 Materials and Methods . . . 33
2.2.1.1 Decontamination procedures . . . 33
2.2.1.2 Chemical Vapour Deposition of h-BN . . . 34
2.2.1.3 Sample Preparation & Characterisation . . . 35
2.3 Results and Discussion . . . 37
2.3.1 Structure of MWCNT@BN . . . 37
2.3.1.1 Morphology . . . 38
2.3.1.2 Core-shell structure . . . 39
2.3.1.3 Nanotube dimensions . . . 46
2.3.1.4 Rate of h-BN deposition . . . 47
2.3.1.5 Crystallinity of MWCNT and MWCNT@BN . . . 48
2.3.2 Bond Speciation within MWCNT@BN . . . 59
2.3.2.1 XPS analysis of MWCNT and MWCNT@BN . . . 59
2.3.2.2 A Comparative Study: MWCNT@BN synthesised by H_3BNH_3 vs. $B_2O_3 + NH_3$ . . . 64

2.3.2.3 Oxygen Impurities in MWCNT@BN 68
2.3.3 h-BN Deposition Selectivity 74
2.4 Conclusion 75

3 Boron Nitride Nanotubes via Sacrificial Templating of Carbon Nanotubes 80
3.1 Introduction 80
3.2 Synthesising BNNTs by oxidation of CNT template 86
3.2.1 Materials and Methods 86
3.2.1.1 Oxidation treatment of MWCNT@BN 86
3.2.1.2 Synthesis of Larger Diameter MWCNTs 87
3.2.1.3 Sample Preparation & Characterisation 87
3.3 Results and Discussion 89
3.3.1 Thermal Oxidation of MWCNT template 89
3.3.1.1 Oxidation Resistance of MWCNTs 90
3.3.1.2 Oxidation Resistance of deposited h-BN 95
3.3.2 BNNT Structure 97
3.3.2.1 BNNT Morphology 97
3.3.2.2 BNNT Diameter Control 100
3.3.2.3 BNNT Crystallinity 103
3.3.3 BNNT Composition 112
3.3.3.1 EELS analysis of BNNTs 112
3.3.3.2 XPS analysis of BNNTs 114
3.3.3.3 UV-Vis Spectroscopy 118
3.4 Conclusion 120

4 Macroscopic sheet architectures of Boron Nitride Nanotubes 124
4.1 Introduction 124
4.2 Synthesis of BNNT buckypaper by sacrificial templating 133
4.2.1 Materials and Methods 133
4.2.1.1 Fabrication of MWCNT/h-BN heteronanotube buckypapers 133
4.2.1.2 Fabrication of BNNT buckypapers 134
4.2.1.3 Sample Preparation & Characterisation 135
4.3 Results and Discussion 136
4.3.1 Buckypaper Structure 136
4.3.1.1 Geometry, Cross Section Architecture & Nanotube Alignment 136
4.3.1.2 Thickness, Density & Pore Size 141
4.3.2 Buckypaper Composition 145

4.3.2.1 Probing Composition by EDX 145
4.3.2.2 Composition Depth Profiling by XPS 147
4.3.2.3 Adventitious Carbon & CO_2 Adsorption by BNNTs 153
4.3.3 Buckypaper surface platelet formation 155
4.3.3.1 Theory I: BNNT Oxidative Unzipping & Coalescence 157
4.3.3.2 Theory II: Spontaneous Boric Acid Crystallisation 160
4.3.3.3 Observed H_3BO_3 platelets 165
4.3.3.4 Platelet Composition by EDX analysis 168
4.4 Conclusion 176

5 Outlook **180**
5.1 Summary 180
5.2 Future Work 181
5.2.0.1 BNNT Structure 181
5.2.0.2 BNNT Buckypaper Architectures 182
5.2.0.3 Hierarchical Structure Assemblies 183
5.2.0.4 Buckypaper Composites and Properties 186
5.2.0.5 Heteronanotube Assemblies and Properties 186

Appendices

A Chapter 2 Appendix **189**
A.1 EELS Quantitative Analysis Parameters 189
A.2 Synthesis of MWCNT@BN by $B_2O_3 + NH_3$ precursors 193
A.2.1 Materials and Methods 193
A.2.2 Results 194
A.3 Nanocyl NC7000™ Impurities 197
A.3.1 Effects of Ammonia Borane CVD on Al_2O_3 198

B Chapter 3 Appendix **201**
B.1 Oxidation Rate Calculations 201
B.2 Additional BNNT Characterisation 202
B.2.1 EELS quantitative analysis parameters 202
B.2.2 BNNTs after 900°C 204
B.2.3 Catalysed BNNT growth 205
B.3 AACVD MWCNTs characterisation 206

C Chapter 4 Appendix **208**
C.1 Sonication and Vacuum Filtration of BNNT powder 208
C.1.1 Materials and Methods 209
C.1.2 Results 209
C.2 Measurement of hybrid Buckypaper Electrical Resistivity 212
C.3 Additional BNNT Buckypaper Characterisation 214
C.3.1 SEM & EDX 214
C.3.2 XPS 216
C.4 Predicting X-ray Generation Depth for EDX analysis 217
C.4.1 monte CArlo SImulations of electroN trajectory in sOlids: CASINO v2.51 217
C.4.1.1 Brief Introduction to principles of CASINO 217
C.4.1.2 Specimen Model and Microscope Settings 219
C.4.1.3 Results of Simulation 221
C.5 Additional Platelet SEM and EDX 223

References **225**

List of Abbreviations

1D, 2D, 3D . . One-, two-, three-dimensional

AB . . . . . Ammonia Borane

APCVD . . . . Atmospheric Pressure Chemical Vapour Deposition

AACVD . . . Aerosol Assisted Chemical Vapour Deposition

BNNT . . . . . Boron Nitride Nanotube

BOCVD . . . . Boron Oxide Chemical Vapour Deposition

BP . . . . . Buckypaper

CNT . . . . . Carbon Nanotube

CVD . . . . . Chemical Vapour Deposition

CCVD . . . . . Catalytic Chemical Vapour Deposition

DADB . . . . . Diammoniate of Diborane

DFT . . . . . Density Functional Theory

DTG . . . . . Derivative of Thermogravimertry

EELS . . . . . Electron Energy Loss Spectroscopy

ELNES . . . . Energy Loss Near Edge Structures

EPIC . . . . . Extended-Pressure Inductively-Coupled Plasma

FFT . . . . . Fast Fourier Transform

FTIR . . . . . Fourier Transform Infrared

HABS . . . . . Hydrogen Assisted BNNT synthesis

h-BN . . . . . Hexagonal Boron Nitride

HTP . . . . . High Temperature/Pressure

LPCVD . . . . Low Pressure Chemical Vapour Deposition

MWCNT . . . Multi-wall Carbon Nanotube

MWNCT@BN Multi-wall Carbon Nanotube coated in coaxial h-BN

PACVD . . . . Plasma Assisted Chemical Vapour Deposition

PPAB . . . . . Poly[2-n-propylamino-4,6-bis(methylamino)borazine

PVD . . . . . Physical Vapour Deposition

SEM . . . . . Scanning Electron Microscopy

SWBNNT . . Single Wall Boron Nitride Nanotube

SWCNT . . . Single Wall Carbon Nanotube

TEM . . . . . Transmission Electron Microscopy

t-BN . . . . . Turbostratic Boron Nitride

VLS . . . . . Vapour-Liquid-Solid

XRD . . . . . X-ray Diffraction

XPS . . . . . X-ray Photoelectron Spectroscopy

Chapter 1
Introduction

Contents

1.1 Thesis Outline 1
1.2 Hexagonal Boron Nitride 4
1.3 Boron Nitride Nanotubes 6
1.3.1 Properties & Applications 7
1.3.2 Synthesis Landscape 13
1.3.3 Buckypaper Macroscopic Assemblies 17
1.4 Ammonia Borane: an h-BN precursor 19

1.1 Thesis Outline

Chapter 1

This introductory chapter first highlights the structure of hexagonal boron nitride (h-BN) and graphitic carbon and their nano-dimensional morphology of interest to this thesis- *the nanotube*. This is followed by an overview of the unique properties of boron nitride nanotubes (BNNTs) in comparison to their carbon nanotube counterparts (CNTs). Next, the potential applications of BNNTs are presented to paint an attractive picture of this next-generation nanomaterial. The present synthesis landscape for BNNTs is then explored and the case is made for the synthesis methods presented in this work. Subsequently, the discussion evolves from nano to

macro, and the importance of fabricating nanotubes into macroscopic architectures is highlighted. Finally, ammonia borane is introduced as the advantageous precursor used for h-BN deposition in this thesis.

Chapter 2

This chapter begins with a review of the literature on the synthesis of heteronanotubes composed of CNT and h-BN, specifically in the configuration of h-BN coaxial shells around core CNTs. This puts into perspective the work explored here, which proposes the use of ammonia borane as the atmospheric pressure chemical vapour deposition (CVD) precursor for coating of h-BN onto multi-wall CNTs (MWCNTs). The as-synthesised nanotubes are subsequently characterised to determine whether this method is successful for the selective deposition of h-BN as coaxial shells, the quality of the deposited h-BN achieved (crystallinity, thickness *etc.*) and the purity of the heteronanotube product. The composition of nanotube bonds is also examined to determine whether the method is more favourable than others for the fabrication of true van der Waals heternanotubes, i.e with minimal covalent interaction between the core CNT and h-BN shells.

Chapter 3

It is proposed here that the heteronanotubes synthesised in Chapter 2 be subjected to thermal oxidation in order to sacrifice the MWCNTs whilst leaving BNNT shells. This can effectively be considered as a new ammonia borane CVD route to BNNTs (with MWCNTs as the template assistants) and adds to the very limited number of studies using this precursor for BNNT synthesis, as outlined in this chapter introduction. The dependence of this route on thermal oxidation of the carbon component requires that the MWCNT oxidation behaviour (both pristine and when encapsulated by h-BN) is investigated here. Nanotubes structures remaining after the oxidation process are scrutinised to determine the extent of carbon removal and to confirm their BNNT composition. The quality of BNNT achieved here, in terms

of crystallinity, wall thickness, and impurity levels (esp. oxygen) is assessed. The potential for diameter control of BNNTs by this method is also considered.

Chapter 4

In this final experimental chapter, methods described in the previous two chapters are evaluated to determine whether they are effective at the macroscopic scale, specifically for the fabrication of BNNT buckypaper sheet assemblies by the use of vacuum filtration in conjunction with sacrificial templating techniques. Two different BNNT buckypaper fabrication protocols are tested, their difference being the sequence in which h-BN CVD treatment and vacuum filtration occur prior to thermal oxidation. The resulting buckypaper structures are compared for their geometries, yield, cross sectional architecture *etc.* The composition of these BNNT buckypapers is also probe to determine again the extent of carbon removal during the thermal oxidation process from the dense assembly (relative to powdered forms) and question the influence of atmospheric, adventitious carbon as a contamination source. Furthermore, existing literature on the oxidation behaviour of the BNNT buckypaper themselves is re-assessed, and a new theory is developed to explain the appearance of polygonal, platelet crystal structures of the BNNT buckypaper surface.

Chapter 5

This chapter gives a brief summary of the research findings and outlines ideas for future work. This includes, for example, improvement of the BNNT crystallinity and purity, and fabrication of BNNT buckypapers with universal in-plane alignment, hierarchical structure buckypapers combining BNNTs with nanosheets, and buckypaper-polymer composites. Properties to be tested and applications are also discussed.

1.2 Hexagonal Boron Nitride

Hexagonal boron nitride (h-BN) is the inorganic, heteroatomic analogue to graphite, and is composed of a network of boron (B) and nitrogen (N) atoms that form stacked layers of honey-comb lattices.[1]

This in-plane honey-comb structure is emergent from the sp^2 bonding configuration, such that each B and N atom in the lattice has valence electrons ordered into three hybrid sp^2 orbitals (see Figure 1.1) that are oriented 120° apart. These orbitals are responsible for σ covalent in-plane bonds between B and N. Remaining electrons in the unhybridized $2p_z$ orbital of N can form a dative π bond with the empty $2p_z$ orbital of B.[2] However, because N is more electronegative than B (3.04 and 2.04 respectively on the Pauling scale), the B-N bond is also partially ionic in nature. This results in localisation of electrons around the N atomic centers, including the π bond electrons. In contrast, the homo-nuclear nature of graphite, i.e. non-polar C-C bonds, allows for the delocalisation of the π electrons. Thus, despite the isoelectronicity of h-BN and graphite, the former is electrically insulating, whilst the latter is conductive, one of the prominent differences between the two

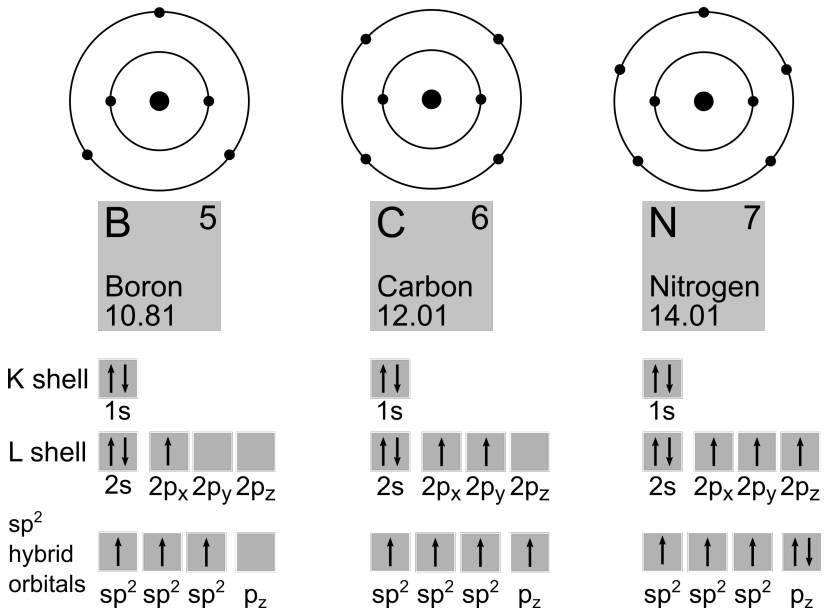


Figure 1.1: The elements of interest in this work: Boron, Carbon and Nitrogen. Ground state electron configurations are illustrated along with their sp^2 hybrid configurations relevant to the formation of graphitic carbon and hexagonal boron nitride.

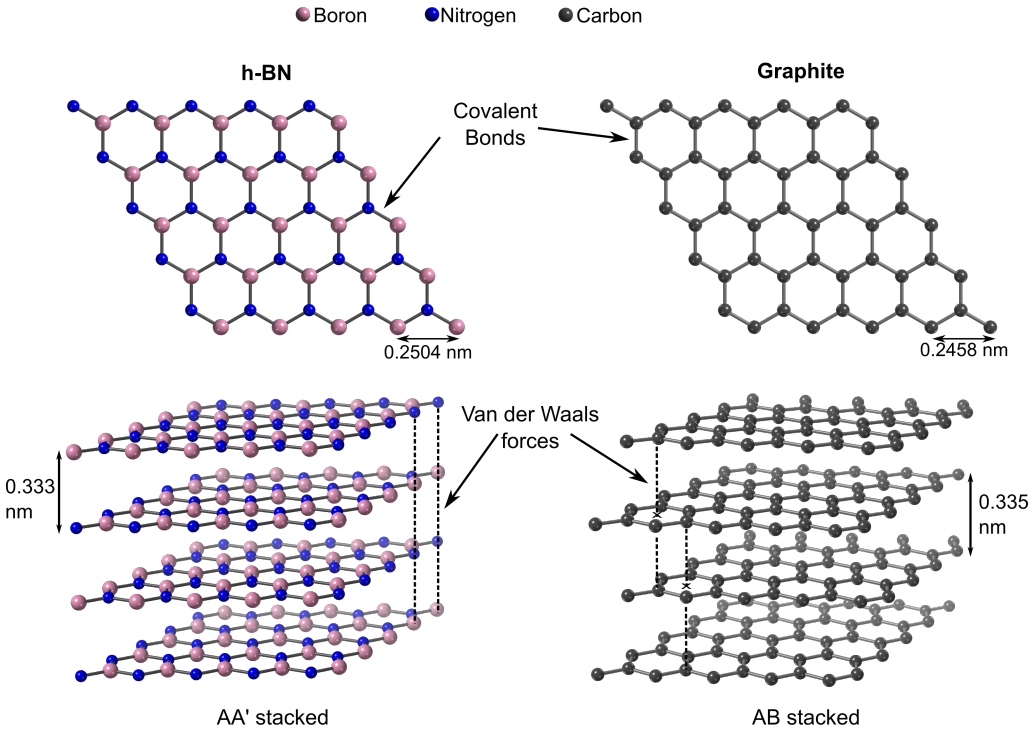


Figure 1.2: Illustration of the structure of h-BN and graphite, depicting their similar in-plane, covalent bonded honey-comb network and inter-layer van der Waals stacking. h-BN exhibits a few structural dissimilarities to graphite, most distinctly a different optimal stacking configuration.

materials.[3] These electronic properties directly influence the visual appearance of these materials, such that owing to the wide band gap of h-BN, light absorption only occurs within the UV range, making it appear white/colourless as opposed to the black (all-light absorbing) colour of graphite.

Whilst strong covalent bonds are found intra-layer, weaker van der Waals forces are responsible for inter-layer stacking of h-BN and graphite alike, which exhibit inter-layer distances of 0.333 nm and 0.335 nm respectively, as illustrated in Figure 1.2.[1] However, an inter-layer structural difference between h-BN and graphite is their symmetrical stacking mode. Graphite exhibits what is described as AB' stacking, whereby a C atom within one layer is positioned at the center of adjacent layer hexagons. On the other hand, to minimise electrostatic energy, the optimal stacking mode of h-BN is AA', such that B and N atoms are superposed on each other in succession along the crystal c-axis.[4]

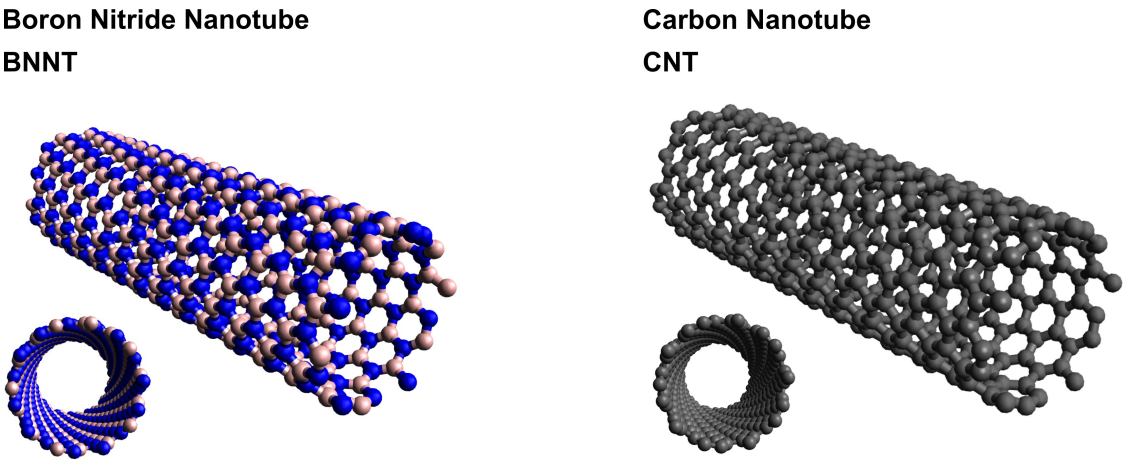


Figure 1.3: Illustration of a BNNT and a CNT. A nanotube can be imagined as a monolayer of h-BN or graphite wrapped into a hollow tube, with a nanoscale diameter much smaller than its length (high aspect ratio). For simplicity, only single-wall nanotubes are depicted here, but multi-wall nanotubes exist and are composed of multiple concentric nanotubes.

1.3 Boron Nitride Nanotubes

Given the as-described structure of h-BN and graphite, at the bulk scale these materials are most commonly produced as microscopic flakes with the thickness dimension corresponding to the layer stacking height. However, h-BN and graphite can also be synthesised into a a newer class of low-dimensional materials, whereby at least one dimension is reduced to the nanoscale.

Of particular interest here is the nanotube, often described as a 1-D nanomaterial because of the significantly smaller diameter (nanoscale) dimension in comparison to its length (otherwise known as a high aspect ratio). A single-wall BN nanotube (SWBNNT) can be conceptualised as a monolayer of h-BN (also called 2-D h-BN) rolled up into a cylinder.[5] This is illustrated in Figure 1.3, alongside the SWCNT counterpart. Accordingly, multi-wall BN tubes (MWBNNT) consist of concentric SWBNNTs of larger diameter enclosing those of smaller diameter and so on, similar to a Russian Doll model. These concentric tubes interact by van der Waals forces, just as described for the structure of h-BN and graphite above.[6]

Note that although only open tipped BNNTs and CNTs are modelled in Figure 1.3, both can also exhibit closed tip structures with varying curvature dependent

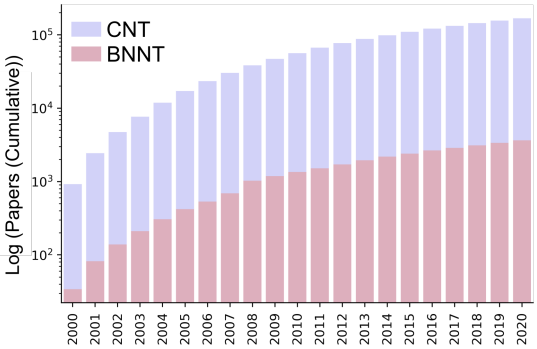


Figure 1.4: A graphical depiction of the cumulative research paper output for CNT and BNNT work within the last decade, based on a Scopus search. In comparison to the field of CNT research, the BNNT field is still nascent.

on the types of defects present at the ends, such as odd (e.g pentagons) vs. even numbered (e.g tetragon) rings.[7] Nanotubes can also exhibit structural variance amongst each other by their helicity, briefly described as the angle at which the tube is wrapped, i.e. the angle ϕ between the lengthwise tube axis and the nearest hexagonal row. For $0<\phi<30°$, the wrapping is chiral, and as such this BNNT and CNT structural feature is often referred to as chirality.[7,8]

Interestingly, whilst the first CNTs were synthesised in 1991[9] and the first BNNTs closely followed in 1995,[10] there is a remarkably significant difference in the progress and research output of the respective fields. This fact is highlighted in Figure 1.4, depicting the orders of magnitude greater extent of literature investigation of CNTs in comparison to that of BNNTs in the last decade up to now. This difference is primarily due to the greater accessibility of CNTs while, as will be outlined later in §1.3.2, there is still much progress to be made toward the viable fabrication of BNNTs. Indeed, the unique properties and applications of BNNTs, reviewed in the following section, decidedly justifies their continued exploration.

1.3.1 Properties & Applications

The properties of BNNTs in comparison to CNTs are summarised in Table 1.1.

In addition to sharing a low density (1.3-1.4 g/cm^3)[23,24] and high aspect ratio, both BNNTs and CNTs are excellent thermal conductors and have exceptional mechanical properties. Empirically measured values for thermal conductivity along

Properties	BNNTs	CNTs
Appearance	White	Black
Electrical Conductivity	Insulating, wide band gap (5-6 eV); independent of chirality [11]	Metallic or semiconducting (ca. 0.5-2 eV); dependent on chirality [12]
Mechanical Properties (Young's Modulus)	ca. 1.2 TPa [13]	1.09-1.25 TPa [14]
Thermal Conductivity	350 $Wm^{-1}K^{-1}$ [15]	300 $Wm^{-1}K^{-1}$ [15]
Thermal Stability (in air)	Stable up 800-900 °C [16–18]	Stable up to ca. 500-700 °C [19]
Optical Properties	Visible and infrared transparent; UV region absorption [20]	Full spectrum absorption; NIR fluorescence [20]
Piezoelectricity	Piezoelectric [21, 22]	Not piezoelectric
Neutron Absorption Cross section (barn= $10^{-24}cm^2$)	^{11}B: 767 barns, ^{10}B: 3835 barns [23] N: 1.9 barns	C: 0.003 barns

Table 1.1: A comparison of the properties of BNNTs versus CNTs.

the tube axis are as high as 300-350 $Wm^{-1}K^{-1}$ for both BNNTs and CNTs of the same diameter range (30-40 nm).[15] For smaller diameter CNTs, an even higher value of 3000 $Wm^{-1}K^{-1}$ was measured,[25] and theoretical studies predict this value to be even higher for smaller diameter BNNTs.[26] Both types of nanotubes have also exhibited remarkable Young's moduli reaching into the TPa magnitude.[13,14]

However, unlike CNTs that are metallic or semiconducting dependent on their chirality,[11] BNNTs are consistently electrically insulating.[12] This property, coupled with their superb elastic modulus, makes BNNTs the strongest known insulating fibre to date.[13] They also possess the incredibly rare duo of being a dielectric and a thermal conductor. Furthermore, in terms of thermal stability, BNNTs outperform CNTs, and can resist oxidation in air up to up to 800-900 °C[16–18] (and up to 1500 °C in inert atmosphere).[27] Other BNNT properties such as demonstration of a piezoelectric effect[21,22] and high neutron adsorption capacity (due to the large neutron adsorption cross section of boron[28]) are not presented by CNTs.

This combination of properties makes BNNTs relevant to a range of applications,[6,7,29–32] such as the examples included in Figure 1.5, for most of which the advantages bestowed by BNNTs are not possible with CNTs. Many of these applications involve use of BNNTs as fillers within a matrix material, forming a nano-composite.[32] Generally, the low-density of BNNTs is highly favourable, as they can confer improvements in properties to the composite without adding the burden of significant weight increases; in fact, weight reduction is an incentive for compositing, because improved material capabilities can decrease total material usage requirements.

Perhaps one of the most popularly considered uses of BNNTs is in novel heat dissipating materials for electronics packaging. Thermal management of waste heat generated from increasingly miniaturised but higher power density electronics is a very pressing challenge. Solutions are needed to quickly dissipate heat from active processors, so as to prevent hot-spots that compromise the performance and reliability of the electronics.[33] Polymers form an important class of electronics packaging material, used in substrates, encapsulants, adhesives, heat spreaders and heat sinks *etc.*[34] Nano-composites with BNNTs used as thermally conductive fillers within a polymer matrix are promising candidates to improve the efficiency of these packaging components in passive thermal management.[27,32,35–37] Next-generation electronics with flexible designs could also exploit such polymer nano-composites.[33] Importantly, BNNTs concomitantly maintain the electrical insulation of the polymers, precluding the possibility of short-circuiting with electrically active components.

Another highly desirable property of BNNTs is its transparency to visible light.[32] When added to materials such as polymers or glasses, the resulting composites maintain their transparency, or can be dyed. Even the addition of a small weight percentage of CNTs would otherwise render these materials opaque. BNNTs, because of their high strength, can simultaneously act as structural reinforcement fillers, allowing for the development of ultra-strength clear plastics[38] and glasses[39] that

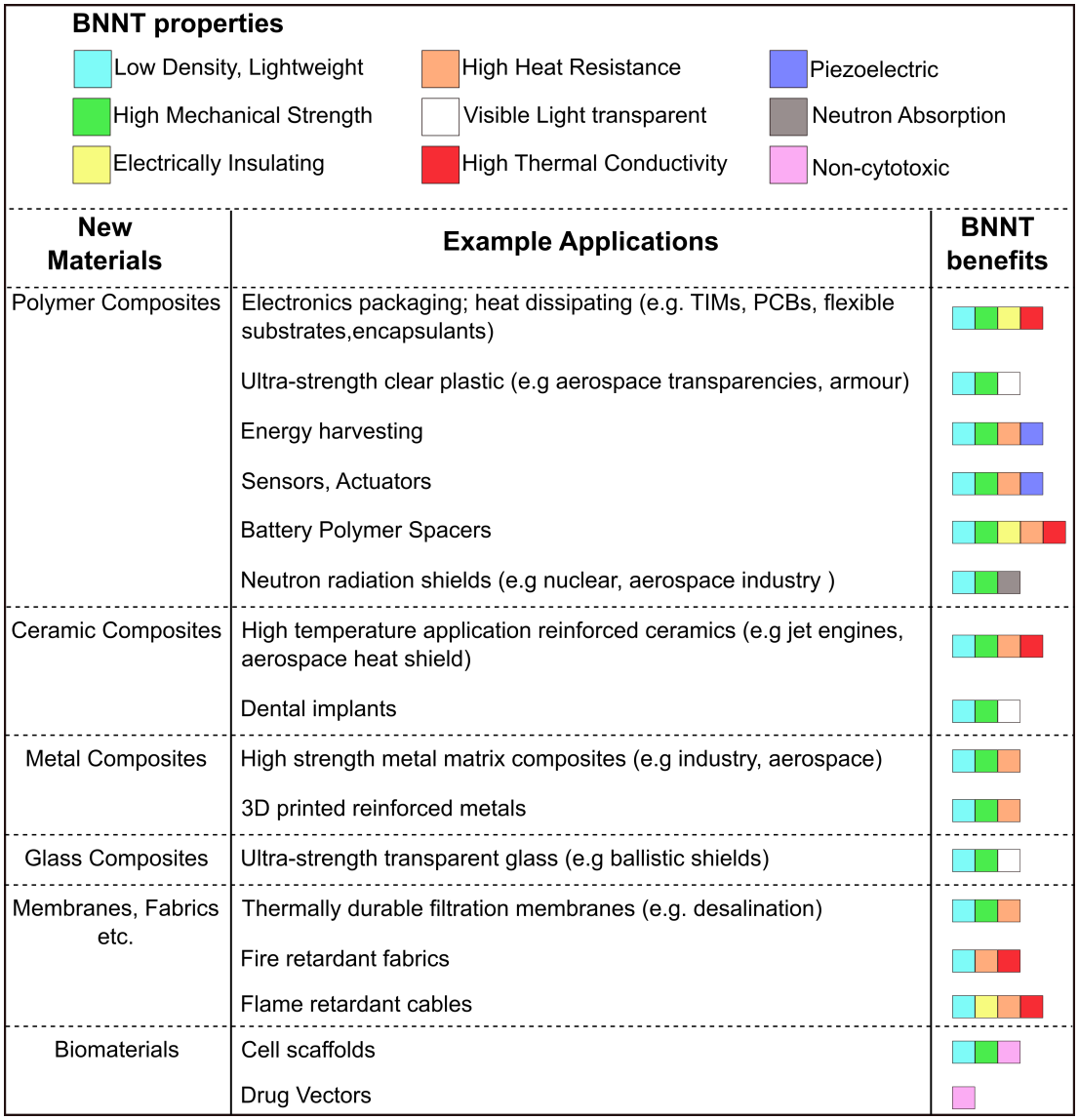


Figure 1.5: A compilation of potential BNNT applications, colour coded to highlight the specific properties of BNNTs that are advantageous to each application. As demonstrated here, the multi-functionality of BNNTs is an important factor of their appeal.

can be used as armour, ballistic shields, optical protection, aerospace transparencies *etc.*[40]

Structural reinforcement capabilities of BNNTs can also be extended to ceramic and metal matrix composites. As the processing temperatures of these materials are usually high, CNTs are not the ideal fillers because of their lower thermal stability; they begin to oxidise <700 °C thereby losing their structural integrity. BNNTs are more suitable to withstand high processing temperatures because of their

superior thermal stability.[32] The BNNT-metal (e.g aluminium,[41] titanium[42]) and BNNT-ceramic (e.g. alumina,[43] zirconia,[44] silicon nitride[45]) reinforced composites also have potential to be used in extreme environments e.g. heat shields, jet engines. Particularly for aerospace applications, the potential weight reduction offered by these composites is especially advantageous for cutting fuel usage, and consequently cost and environmental impact. The aerospace industry can also benefit from the high neutron shielding capability of BNNTs, making these highly attractive materials for spacecraft structural components that satisfy the multi-purpose of protecting astronauts against neutron radiation.[46,47]

Aside from the benefit of thermal stability for high temperature resilient structural composites, this heat resistance property makes BNNTs suitable as fire retardants, potentially in coatings, adhesives, fabrics and cabling insulation.[46] This flame-resistive property has also been recently proposed for exploitation by reusable ultrafiltration membranes, as BNNTs can withstand the high temperature used during membrane regeneration (i.e. removal of organic filtered impurities).[48]

BNNTs may also be used for piezoelectric energy harvesting, i.e. the generation of electric charge from deformation. The inverse effect facilitates fabrication of sensors and actuators. The appeal of BNNTs for such piezoelectric devices is also linked to their high thermal stability, allowing their effective operation at extreme temperatures (e.g. on space missions) that limit other electroactive materials.[49] Elsewhere in the field of energy research, BNNTs have been proposed for use in battery polymer spacers (e.g. Li-S batteries) to improve strength and thermal stability.[50]

Furthermore, preliminary evidence that suggests the non-cytoxicity[51] of BNNTs has prompted recent research into their use in biomedicine, for instance as cell scaffolds, drug carrier and biological channels.[52]

The overview presented here gives a non-exhaustive list of potential BNNT applications, aiming to highlight the scope of multi-functionality of this nanomaterial.

BNNT Synthesis Methods: Definitions Summary

High Temperature/High Enthalpy BNNT Growth Systems

Arc Discharge *~3000-4000 ºC*	Arc plasma is used to vaporise an anode material with a BN or B-containing component (e.g. metal borides (HfB_2, LaB_6, YB_6) or boron mixed with metals (Ni or Co) in an inert atmosphere, typically N_2. B undergoes nitridation and BNNT growth is catalysed by metal particles condensed from the arc plasma vapour.
Laser Ablation *> 4000 ºC*	A laser beam is irradiated upon a h-BN target which vapourises and decomposes into B and N_2. Condensed B nanoparticles undergo re-nitridation by N_2 to form BN seeds that grow into BNNTs. Elemental B is an alternative irradiation target, and under high pressure N_2 atmospheres (0.7-1.4 MPa), BNNTs are synthesised.
Thermal Plasma Jet *> 4000 ºC*	A plasma jet is generated from a gas feed (e.g. Ar, N_2, H_2) and is used to atomise an h-BN feedstock into B and N. Small B droplets nucleate upon cooling and undergo nitridation to form BNNTs. Large H_2 partial pressures (e.g. 18 vol. %) catalyse BNNT growth. Alternatively, elemental B vaporised by the plasma can form BNNTs under high pressure N_2 (>305 kPa).

Low Temperature BNNT Growth Systems

Ball Milling/ Annealing ~1000-1200 ºC	A ball mill is used to induce mechanical attrition of elemental boron, generating defective B nanoparticles. This is followed by thermal annealing. Both milling and annealing processes are carried out in NH_3 or N_2 atmospheres, which facilitate nitridation of the reactive B particles and subsequent BNNT growth. Metal nanoparticles from the mill ball/container or separately introduced (e.g. Fe) could also act as BNNT growth catalysts.
Chemical Vapour Deposition ~ <1700 ºC	Vapour phase precursors containing B,N are thermally reacted and deposited on a substrate in the form of BNNT. This typically involves transition metal nanoparticles that catalyse BNNT growth. Precursors, usu. decomposed from liquid/solid into vapour upon heating, can either be single-source (e.g. $B_3H_6N_3$, H_3NBH_3) or multi-source, the most common such route being boron+metal oxide which releases B_2O_3 that is reacted with NH_3 (BOCVD). Catalytic CVD can also be plasma-assisted. CVD BNNT growth without metal catalyst has also been demonstrated, and can include the use of templates for substitution/sacrificing.

Figure 1.6: A summary of BNNT synthesis according to methods characterised as high temperature (e.g.Arc Discharge,[10,53–57] Laser Ablation,[58–61] Plasma Jet[62–65]) vs. low temperature (e.g.Ball Milling/Annealing,[66–70] or CVD[71–80]).

1.3.2 Synthesis Landscape

BNNTs were first synthesised by Chopra *et al.,* in 1995 via an arc discharge method, adapted from an earlier system used for fullerene production.[10] Since then, there has been a diversification in the reported BNNT synthesis methodologies, the main concepts of which are concisely summarised in Figure 1.6. Based on explicit differences in temperature, these current methods can be dichotomised into high temperature (>3000 °C) versus low temperature (<2000 °C) BNNT growth systems.

1.3.2.1 High Temperature Synthesis

High temperature/enthalpy systems encompass methods that employ arc discharge,[10,53–57] laser ablation,[58–61] or thermal jet plasma[62–65] for BNNT synthesis. The fundamental objective of the high energy input of these systems is to overcome the energy barrier associated with the direct reaction of $2\,B + N_2 \longrightarrow 2\,BN$. Vaporisation and atomisation of one or both B and N precursors (e.g. h-BN or elemental B, and N_2) by a high energy heat source increases their reactivity and thus facilitates occurrence of this nitridation reaction.[20] Collectively, these methods tend to produce BNNTs characterised by high crystallinity, small outer diameters (<10 nm) and few walls. Whilst arc discharge has remained disadvantaged by the small reaction volume achievable and consequently the low BNNT yield, upscaled manufacturing processes have matured from laser ablation and thermal plasma methods. For example, the High Temperature/Pressure method (HTP), developed by the National Institute of Aerospace and the NASA Langeley Research Center, utilises a CO_2 laser to vapourise boron that is reacted with N_2 in a pressurised chamber at 0.7-1.4 MPa, which has to date achieved reported BNNT yield rates of 200 mg/hr.[61] Alternatively, according to an induction thermal plasma jet process, the National Research Council of Canada have designed a method with a larger fabrication capacity of 20 g/h that depends on a large partial pressure of H_2 (18 vol.%) amongst the atomised B and N reactants. These vapours are exposed to extreme plasma temperatures >8000 K at atmospheric pressure; now known as the Hydrogen assisted BNNT synthesis (HABS) method.[63] The Zettl group

similarly utilised an induction plasma system, but at high nitrogen pressure (> 305 kPa) without H_2, and were able to attain a 35 g/hr yield of BNNT; the Extended-pressure inductively-coupled plasma (EPIC) method.[65]

Whilst methods such as HTP, HABS and EPIC have set new records for the throughput of highly crystalline, small diameter BNNTs, there remains several factors in relation to production accessibility and BNNT purity that are acknowledged limitations. For instance, the requisite equipment is particularly specialised and is coupled with demanding operational conditions such as extreme temperatures, high pressures or large supplies of hazardous gases (e.g. H_2), which all contribute to costly setup and maintenance; necessarily, BNNTs manufactured by these routes are not yet economical. Furthermore, B nanoparticles, amorphous BN and other h-BN nanostructures (e.g. cages, nanoribbons, sheets) are common impurities prevalent in the BNNT products synthesised by these high temperature methods, sometimes lowering BNNT purity to as much as 40-50 wt.%. This thereby necessitates further purification steps which have the difficult task of differentiating amongst various polymorphs of chemically identical h-BN in order to extract BNNTs.[81,82]

1.3.2.2 Low Temperature Synthesis

On the other hand, low temperature BNNT synthesis methods (<2000 °C) such as ball milling/annealing and chemical vapour deposition (CVD) are more economically viable routes that require less specialised equipment. However, at these lower temperatures, B and N precursors are unlikely to be atomised, and so the direct nitridation of B and N is unfavoured. Yet, to effectively encourage B nitridation in the ball milling/annealing pathway, the reactivity of elemental B to N_2 or NH_3 is promoted by the introduction of multiple structural defects caused by mechanical attrition.[20] This though, is an especially time-intensive process (e.g. >150 hours) and by-products comprised of amorphous B and h-BN are typically found amongst the BNNTs.[66–70]

Instead, a process that is both more accessible and that has demonstrated the most selective control of BNNT growth, i.e fewer impurities, is CVD. Unlike other methods that rely on nitridation of elemental B, the CVD pathway depends on release of B, N molecular vapour species via chemical decomposition of precursors, which then react/deposit as h-BN. In the presence of molten catalyst nanoparticles, so far primarily transition metals, h-BN growth in the form of BNNT is promoted; this is the catalytic CVD route (CCVD).[71–80] Briefly, the most widely accepted theory for nanotube growth during CCVD is known as the vapour-liquid-solid (VLS) mechanism, involving the dissolution and supersaturation of vapour precursors in a liquid catalyst nanoparticle, resulting in the precipitation of a solid filament* to reduce the free energy of the system.[84,85] This mechanism is referenced for the CCVD growth of many 1D nanomaterial crystals, including nanowires (e.g. Si, Ge, GaN, ZnO & InP) and nanotubes, both CNTs and BNNTs alike.[76] Indeed, for CNTs, CCVD synthesis is the most widely investigated method of growth and is the most common method encountered on the CNT commercial market, indicating its economic viability.[20,31,77]

In comparison, the synthesis of BNNTs by CCVD faces several challenges that have limited its progression in parametric diversity and yield to the same extent as experienced by CCVD fabricated CNTs. For instance, according to the VLS mechanism, the growth component vapour must have a high solubility in the catalyst in order to optimise nanotube growth rate. Whilst metals such as Fe, Ni and Co have demonstrated a high solubility for a wide range of carbon precursors and are thus effective catalysts for CNT growth,[86] the situation is compounded for BNNTs because of its dual element nature, i.e. the most suitable catalyst must exhibit high solubility for both B and N simultaneously.[76] This is in fact a difficult criteria to satisfy, and to date further exploration of catalyst efficiency for BNNT growth is still required. Higher CVD processing temperatures for BNNT in comparison to CNTs, largely owing to differences in B, N vs. C precursor chemistry, also prompt

*The hollow nature of nanotubes grown by the VLS mechanism during CCVD, both CNTs and BNNTs, has been attributed to the anisotropy of graphite and h-BN, such that when precipitating from the catalyst, the basal plane forms the curved exterior for surface energy minimisation.[83]

the increased occurrence of catalyst thermo-agglomeration. This phenomenon is especially problematic for BNNT diameter control, as nanotube diameter is dependent on catalyst size by the CCVD synthesis route.[87]

1.3.2.2.1 Template Assisted CVD To circumvent some of the issues encountered by catalytic CVD whilst taking advantage of the general accessibility of the low temperature CVD, template-assisted CVD is proposed as a promising alternative. This involves the use of a template material that possesses a nanotubular structure that can act as a scaffold for BNNT growth.

Of particular interest here is the use of the CNT as a template for BNNT synthesis. There are several identified advantages to the use of CNT templates. Firstly, the similar lattice structure of graphitic carbon and h-BN indicates that CNTs and BNNTs are structurally compatible. Furthermore, the field of CNT synthesis has already progressed to commercialisation, and there exists a wide variety of CNT products with different dimensions and morphologies from which to select as template material.

Indeed, there are multiple conceptualised routes to BNNT synthesis by the use of CNT templating, as illustrated in Figure 1.7. One of the earliest explored routes involved substitution of carbon atoms in the CNT with B and N, using a carbothermal reaction of boron oxide and ammonia. This however favoured the formation of $B_xC_yN_z$ nanotubes with residual carbon content.[88,89] More recently, CNTs have been implemented as a nano-reactor, within which a gaseous precursor was trapped and converted into a BNNT when heat treated.[90] The BNNTs synthesised this way were limited to single walls and did not maintain their strucutral integrity upon removal of the CNT shell.

In this work, the third possible useability of CNT as a template for BNNT synthesis is explored, i.e. via the deposition of coaxial layers of h-BN onto the surface of a CNT (Chapter 2). As graphitic carbon has lower oxidative stability compared to h-BN, the CNT templates can be burnt off to leave the BNNTs as shells (Chapter 3). Here, ammonia borane is implemeneted as the precursor for

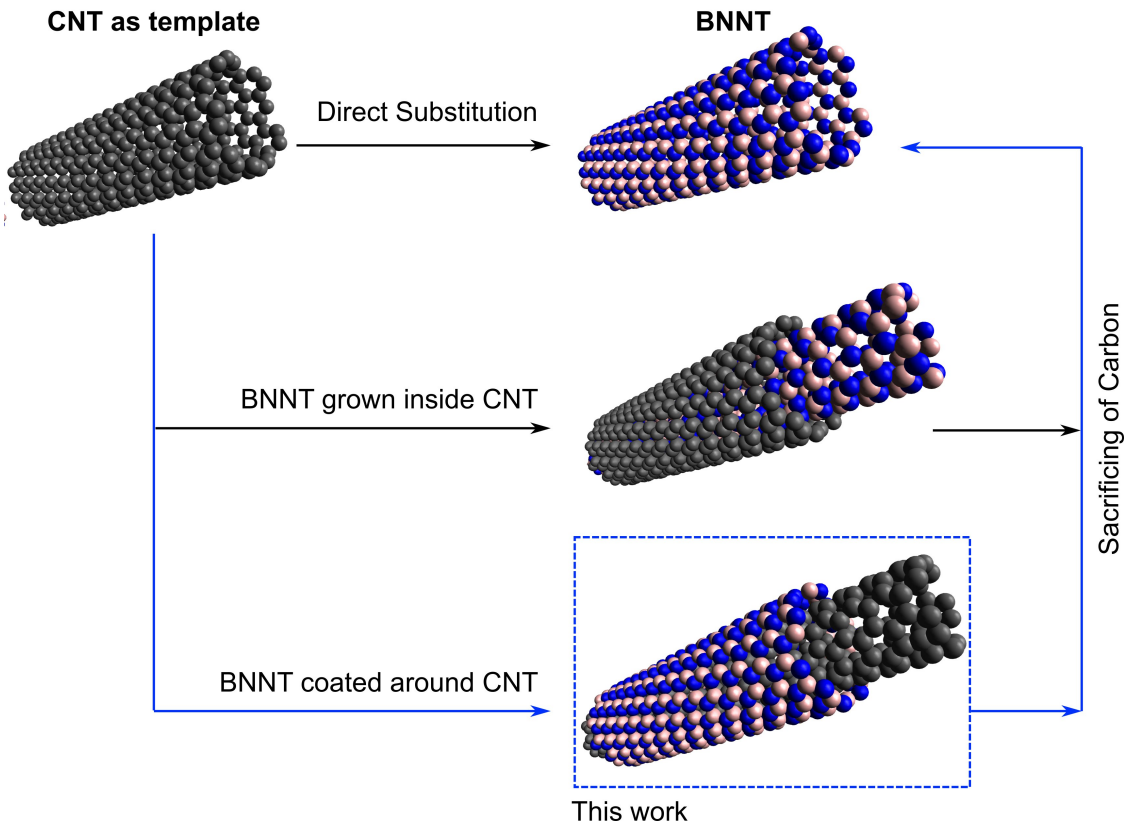


Figure 1.7: An illustration of the three possible uses of CNT as a template for growth of BNNT.

h-BN deposition. See §1.4 for an introduction to this precursor and its CVD decomposition pathway toward the deposition of h-BN.

1.3.3 Buckypaper Macroscopic Assemblies

The interest in macroscopic assemblies of nanotubes stems from their integrability into macroscale, real-world application components, either independently or as part of a high nanotube content composite. Of course, their attractiveness is also dependent on their ability to impart the unique properties of the individual nanotubes in the assembly.

To date, the research output on the fabrication of BNNT macroscopic assemblies is still overshadowed by that of their CNT counterparts, which is a consequence of earlier challenges associated to BNNT synthesis scalability and thus availability. However, as new techniques continue to emerge for larger-scale production of

BNNTs, so too will studies on their macroscopic assemblies.

BNNT assembly macro-architectures that have thus far been reported include substrate-supported thin films,[75,91,92] self-supporting yarns/fibrils,[61,63,93] aerogels/foams,[94,95] vertically aligned forests[96] and buckypapers, which are the focus of this chapter.

The term buckypaper was first coined in 1998 in reference to a 'free-standing mat of entangled SWCNTs', as SWCNTs of 'molecular perfection' belong to the fullerene family of carbon allotropes,[97] and are sometimes called buckytubes. Nowadays, the term is used more broadly to encompass all CNT (both SWCNT and MWCNT) paper-like assemblies[98,99] and has also been co-opted for similar architectures of non-carbon nanotube materials, e.g. BNNT buckypapers. Regardless of the type of nanotube, the similar feature shared by all buckypapers is that they are held together by the van der Waals forces acting between nanotubes tangled into a mesh-like, porous network.

Buckypapers, by nature of being a macroscopic assembly, are easier to handle than loose nanotube powders. This is particularly relevant to nano-composite manufacturing, e.g. BNNTs embedded in a polymer matrix. When mixed in with a liquid matrix during composite processing, powder nanotube additives have a tendency to agglomerate, whilst also increasing the viscosity of the mixture.[36] These factors can contribute to non-uniform distribution of the nanotubes in the matrix as well as a limited achievable nanotube content due to poor processability of highly viscous mixtures.[100] Buckypapers offer a competitive alternative path to nano-composite fabrication. Their pre-existing nanotube network is porous and can be impregnated with the matrix material, thus allowing a high content of nanotubes that are already homogeneously distributed to become part of the composite.[32] Indeed, BNNT polymer/epoxy composites with the highest nanotube load thus far attained (17-40 wt%) were fabricated by infiltration of the matrix into the preformed buckypaper.[27,35,37,49] These higher nanotube loads are promising for a more weighted contribution of nanotube properties to the overall composite,

e.g. greater improvements in thermal conductivity[27,35,37] or piezoelectric response of BNNT-polymer/epoxy composites.[49]

Besides being lightweight, as are all BNNT macro-assemblies, buckypapers present the advantages of being paper-like thin sheets that are usually flexible. These features make it a practical material for fashioning into a desired geometry or bending/folding to fit a form, otherwise not feasible with other macro-assemblies such as aerogels/foams or aligned carpets.

For its many advantages, BNNT buckypapers are of interest here and their fabrication is explored in this work by a combination of vacuum filtration and sacrificial templating techniques, as detailed in Chapter 4.

1.4 Ammonia Borane: an h-BN precursor

Ammonia borane is a molecular compound ($H_3N{-}BH_3$; AB), as pictured in Figure 1.8, that is used in this thesis as an h-BN precursor. At room temperature, ammonia borane is a molecular crystal, existing in a crystalline, white powder form.[101] Despite being isoelectronic to ethane, ammonia borane's solid occurrence at room temperature is attributable to dihydrogen bonding, whereby the polarity of the molecule causes hydrogens bonded to B to behave as hydrides, whilst those bonded to N are protonic; these hydrides and protons consequently interact to form a dihydrogen bonding network of ammonia borane molecules.[102,103]

Owing to the high hydrogen content of this compound (19.6 wt%),[104] it has increasingly been explored as a material for chemical hydrogen storage and release.

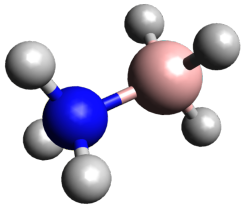


Figure 1.8: Ball & Stick model of Ammonia Borane. Chemical Formula: $H_3N{-}BH_3$. Other names: Borazane, Amminetrihydroboron. White crystalline molecular solid at room temperature.

However, within the last decade, growing interest in ammonia borane has also been motivated by its attractiveness as a precursor for h-BN, i.e. the end product ceramic after its complete dehydrogenation.[105]

As AB already has a 1:1 ratio of B:N that matches that of h-BN, it is inherently advantageous for h-BN stoichiometric control. Moreover, with hydrogen being the sole non-BN element in AB, the possibility of contamination (e.g. carbon, oxygen, halide) introduced from the precursor is also precluded.[106] Generally, besides AB, these two aforementioned properties can also describe borazine, the second most prominent single source precursor used for CVD synthesis of h-BN. However, borazine, isoelectronic to benzene, has some disadvantageous qualities that diminish its competitiveness relative to AB. A liquid at room temperature, borazine is hazardous (potentially pyrophoric) and decomposes rapidly at ambient conditions, making it more challenging to handle and store.[107] Furthermore, its high tendency for being hydrolysed into boric acid, ammonia and hydrogen upon exposure to moisture is well established.[108] In contrast, AB is a non-toxic solid and is stable under ambient conditions.[109,110] For example, it has a vapour pressure of ca. 10^{-4} Torr at room temperature, which is considerably lower than that of borazine (259.3 Torr).[111,112]

For an understanding of the context behind selection of h-BN synthesis parameters in this work, the decomposition pathway from ammonia borane to h-BN must first be reviewed (as illustrated in Figure 1.9).

Importantly, as CVD growth of h-BN is dependent on a vapour phase precursor feed, the first stage of AB transition must be from its room temperature solid state into a gas. This conversion to a vapour phase in fact involves the evolution of $N_xB_yH_z$-containing gases from the solid AB upon heating. To initiate this vapour phase evolution, a range of temperatures have been implemented in the literature when heating solid AB, e.g. 60-130 °C.[113] This temperature range largely corresponds to the temperatures at which the first stage of AB decomposition occurs, whereby AB undergoes dehydrogenation, losing 1 mole of H_2 per mole of AB .[103] The primary vapour product of this initial dehydrogenation is molecular (monomeric) aminoborane, which can also form polyaminoborane in a reversible reaction that

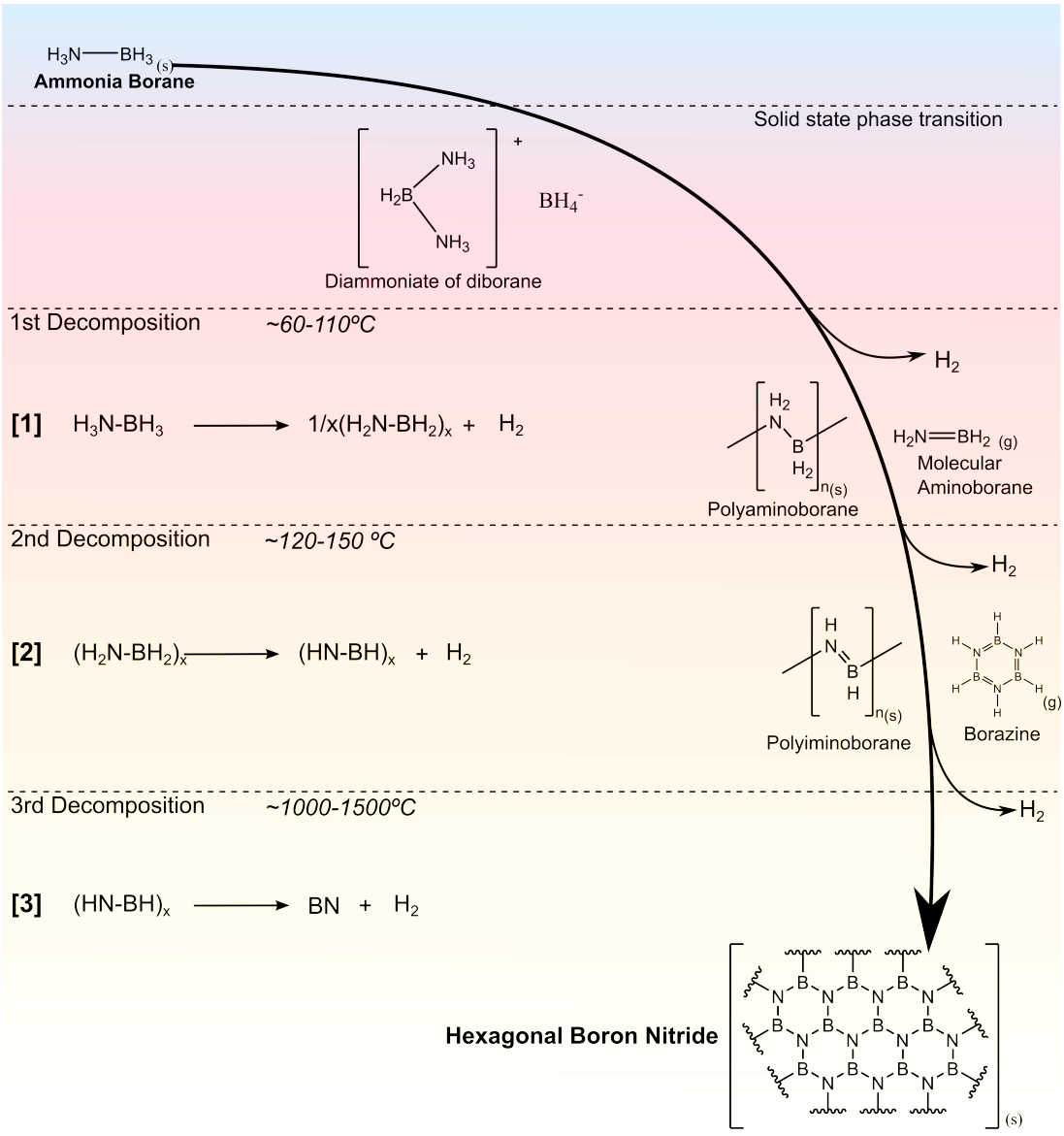


Figure 1.9: Summarised stages of ammonia borane (AB) thermal decomposition (pyrolysis) into h-BN. First, AB undergoes a solid state phase transition into its ionic isomer Diammoniate of diborane (DADB), followed by three stages of dehydrogenation, releasing 1 mole of H_2 per mole of AB at each stage.

favours the monomeric form as temperatures increase further.[104] Notably, the first decomposition stage of AB is likely facilitated by a solid state phase change during heating, such that AB is converted to its ionic isomer, diammoniate of diborane (DADB).[103,106,113] As demonstrated by Babenko *et al.*, 2017, after 30 minutes of heating solid AB at 90 °C, there was a spike in the total vapour flow, which was associated to completed AB conversion to the more 'mobile' DADB phase that is less restricted by dihydrogen bonds.[103,113]

Subsequently, at slightly higher temperature, ca. 120-150 °C, the second stage of dehydrogenation occurs as depicted in Figure 1.9, whereby again H_2 is released. At this stage, the aminoborane species begin decomposing into polyiminoborane and borazine.

At the final, third stage of decomposition, the preceding compounds become fully dehydrogenated. In the context of CVD reactions, this final stage of decomposition that results in the deposition of h-BN has been reported to occur above 1000 °C. Indeed, the pioneering studies that implemented AB as an h-BN precursor demonstrated 2D h-BN synthesis on copper[114] and on graphene[115] at 1000 °C growth temperatures.

In light of the appreciable difference in temperature between the first and final stages of AB pyrolysis, a two stage heating regime is often applied. Namely, this requires heating of the solid AB, to achieve its so-called initial sublimation, in a separate compartment that is upstream to a higher temperature reaction zone in which h-BN deposition is achieved. In this work, as will be outlined in Chapter 2, such a two stage regime was used, with 90 °C and 1000 °C set as the AB heating and h-BN deposition temperature respectively. Beyond consistency of these parameters with the accepted AB decomposition pathway, the selection of the particular AB heating temperature was also informed by previous work in our research group. Specifically, Babenko *et al.*, 2017 showed that at 90 °C and under atmospheric pressure conditions, there was sustained release of $N_xB_yH_z$-containing vapour species from the AB over a period of 2 hours.[113] This established vapour precursor flow

within an economic time-frame was thus considered accessible for experiments in this work involving deposition of h-BN onto CNTs.

Chapter 2

Coating Multi-wall Carbon Nanotubes with Boron Nitride (MWCNT@BN)

Contents

2.1 Introduction 24
2.2 Synthesis of MWCNT@BN by Ammonia Borane pyrolysis 33
2.2.1 Materials and Methods 33
2.3 Results and Discussion 37
2.3.1 Structure of MWCNT@BN 37
2.3.2 Bond Speciation within MWCNT@BN 59
2.3.3 h-BN Deposition Selectivity 74
2.4 Conclusion 75

2.1 Introduction

Presented in this chapter is the first reported demonstration of the use of ammonia borane precursor to synthesise h-BN coaxial coatings on MWCNTs under atmospheric pressure CVD conditions.

The nanotubes synthesised here belong to a pre-existing family of heteronanotubes, albeit a newly emerging one, with a core-shell configuration of carbon/h-BN.

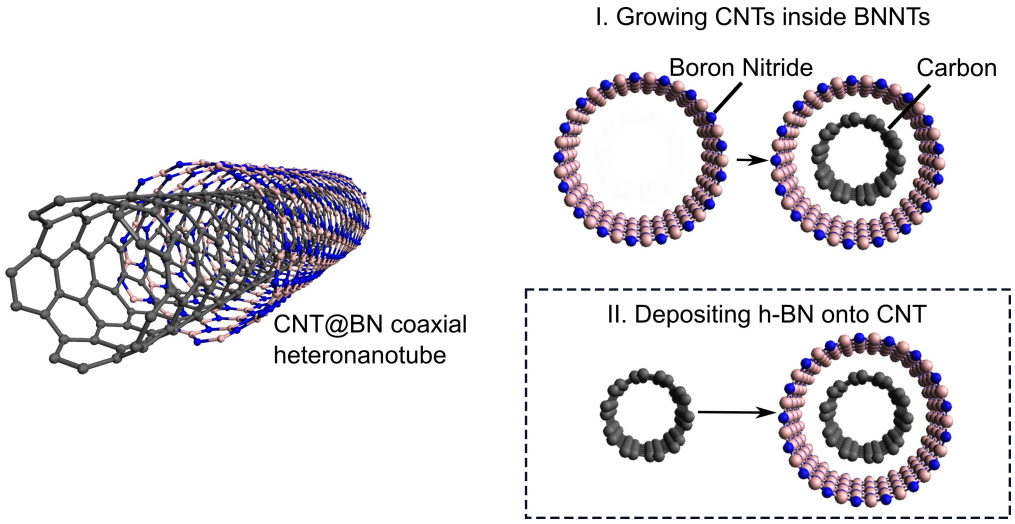


Figure 2.1: Schematic depiction of CNT@BN coaxial heteronanotube and methods of synthesis by a) growing CNTs inside BNNTs or b) depositing h-BN onto CNT, as demonstrated in this chapter. Only SWCNT and single layer h-BN are depicted here for simplicity.

The two strategies towards synthesis of core-shell nanotubes of CNT@BN are by a) growth of CNTs inside a BNNT or b) deposition of coaxial h-BN onto the CNT surface, as summarised in Figure 2.1. Each of these strategies present their own advantages and limitations. In Table 2.1, the properties and accessibility of the CNT@BN hybrids synthesised by these two different approaches are compared.

Briefly, if BNNTs are available as the starting material, it is possible to synthesise coaxial heteronanotube structures by confining C_{60} fullerenes or amorphous carbon inside the BNNTs, and then restructuring the carbon into SWCNTs.

Coalescence of C_{60} molecules into SWCNTs inside a BNNT was achieved by Mickelson *et al.*, (2003)[116] and Walker *et al.*, (2017)[117] by electron beam irradiation (120 keV) and heat treatment (1200 °C) respectively. In both cases, only BNNTs with a low diameter (< 2 nm) could successfully restrict the fullerenes to fuse into SWCNTs. A crucial step to these methods is the introduction of C_{60} into the BNNTs, which first requires opening of the BNNT tips by BNNT air oxidation at 800 °C and/or hydrolysis with ammonium hydroxide solution. However, these steps can also cause significant length reduction to the BNNTs, e.g. from ca. 200 μm to ca. 0.55 ± 0.22 μm.[117] Consequently, the growing CNT's length dimension

Characteristics	**Growing CNT inside BNNT[116–118]**	**Coating h-BN onto CNT[94,96,119–135]**
h-BN crystallinity	Highly crystalline BNNTs used; made by plasma arc discharge,[55] laser vaporisation,[136] or HTP[61]	h-BN usually less crystalline; dependent on factors such as CNT surface crystallinity[121]
h-BN number of walls	Single or double wall BNNTs used	Single or multi-wall concentric h-BN, or polycrystalline h-BN; controlled by deposition parameters
h-BN diameter restriction	<2 nm BNNT diameter needed to restrict C_{60} to coalesce	No restriction as deposited h-BN can encapsulate CNTs of variable diameter
CNT number of walls	Single-wall CNTs coalesced from C_{60} or restructured from amorphous C	Single or multi-wall; dependent on CNT source
CNT length	Short (e.g. ca. 5 nm) SWCNTs 'tubules' formed by C_{60} coalescence or amorphous C restructuring	Variable; dependent on CNT source
Scalability	Microscope electron irradiation methods limited to small quantity of nanotubes; heat induced C_{60} coalescence more scalable	CVD, PVD techniques accessible to coat larger quantities of CNTs with h-BN

Table 2.1: A comparison of the CNT@BN nanotube structural properties and yield scalability related to two differing direct growth strategies.

is also restricted by the BNNT template length.

Amorphous carbonaceous material trapped inside a single or double wall BNNT can also be restructured into a crystalline SWCNT by electron beam irradiation (80 keV), as demonstrated by Arenal *et al.*, (2014).[118] It appeared that a low concentration of carbon favoured crystallisation to a graphitic nanotube, whilst a high concentration of carbon was not crystallised during irradiation. The irradiation was also observed to shrink and cut the BNNT.

Notably, restructuring of carbon allotropes (C_{60} or amorphous C) into a SWCNT tends to result in multiple short (e.g. ca. 5 nm), close ended SWCNTs that are encapsulated within the BNNT,[117] rather than μm scale long SWCNTs.

The focus of this chapter is on the deposition of h-BN onto the surface of CNTs. Generally, for CNT@BN heteronanotubes, this approach allows (i) more flexibility with regard to controlling the dimensions of both the starting CNT and deposited h-BN, and (ii) more scalability, as vapour deposition techniques are more accessible than microscope electron irradiation techniques often required to restructure carbon whilst it is encapsulated inside a BNNT (see Table 2.1) More specifically, the h-BN deposition approach is selected for this work given that the objective is not to synthesise CNTs inside pre-existing BNNTs, but indeed to synthesise BNNTs by later removing the CNT onto which the h-BN was originally deposited (Chapter 3).

Both chemical and physical vapour deposition (CVD, PVD) techniques have been implemented to synthesise h-BN coatings on CNTs. PVD techniques involve the vaporisation of a solid target h-BN source to coat h-BN onto CNTs whilst CVD relies on decomposition and reaction of chemical precursors. CVD, further categorised into atmospheric pressure (APCVD), low pressure (LPCVD), autoclave and plasma assisted (PACVD), offers more control than PVD over the structure and crystallinity of the h-BN coating.

The most often used method is APCVD involving the use of separate boron (boron oxide B_2O_3 or boric acid H_3BO_3) and nitrogen (nitrogen N_2, ammonia NH_3, urea $CO(NH_2)_2$) precursors. These precursor routes are adopted from economical industry methods for fabrication of h-BN.[137] Other precursors explored in the

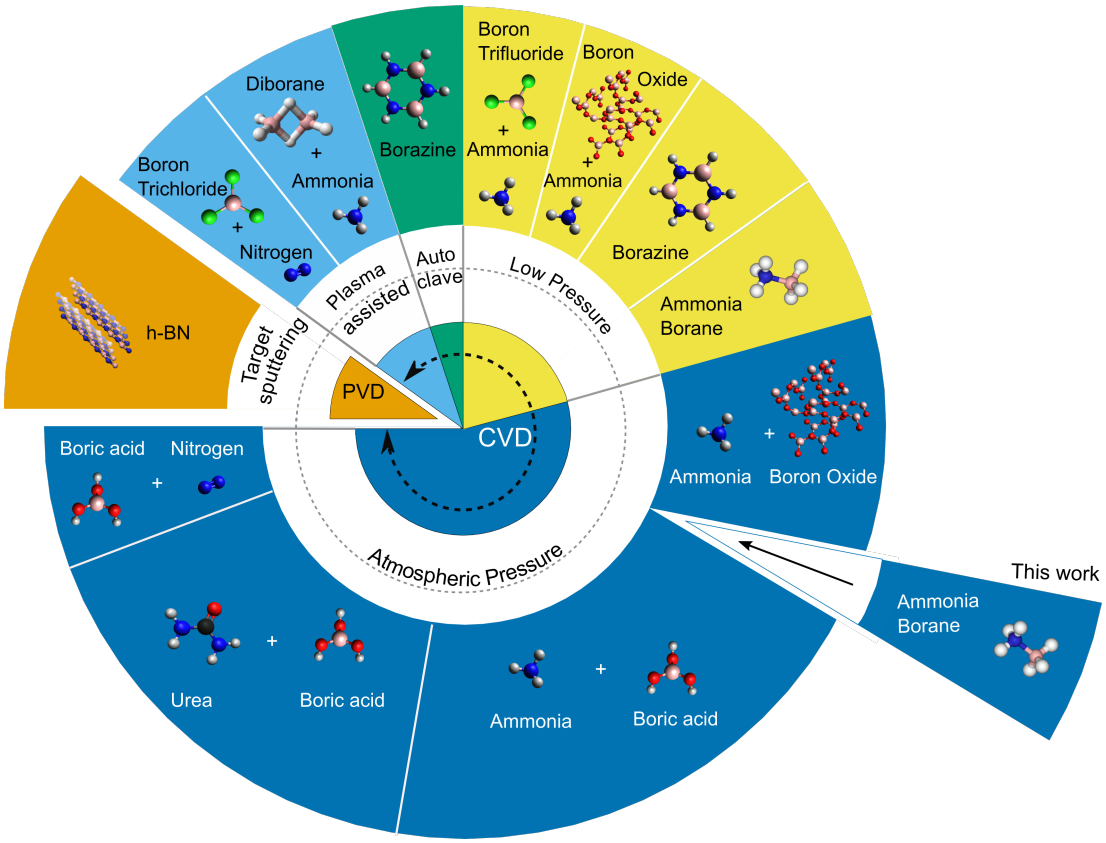


Figure 2.2: Summary of Chemical Vapour Deposition CVD (atmospheric pressure, low pressure, autoclave and plasma assisted) and Physical Vapour Deposition PVD precursor pathways used to deposit h-BN onto CNTs. Sections of the pie plot are proportionately allocated to represent the percentage occurrence of each method in the reviewed literature. Precursor structures are depicted as molecular or lattice compounds (the latter case for solid h-BN or Boron Oxide (B_2O_3). Adapted from by Jones *et al.*, 2020, Ref.[138].

variety of CVD techniques include boron trihalides (boron trichloride BCl_3 and boron trifluoride BF_3) with N_2 or NH_3, diborane B_2H_6 with NH_3, and single source precursors borazine $B_3H_6N_3$ or ammonia borane H_3NBH_3. The Figure 2.2 pie plot summarises the PVD/CVD methods and associated precursors used to deposit h-BN on CNTs, and the accompanying Table 2.2 reviews the structural properties (e.g. CNT diameters, number of CNT walls, deposited h-BN thickness) and certain deposition parameters (temperature, time) achieved by all PVD/CVD studies on CNT@BN in the literature.

The ideal CNT@BN van der Waals heteronanotube consists of single crystal h-BN layer(s) forming an outer concentric BNNT shell that encapsulates the core CNT, as illustrated in Figure 2.1. In reality, this ideal case has only been rarely

achieved by deposition of h-BN onto CNTs.[131] Jones *et al.*, 2020 categorised the morphologies of h-BN coating that have so far been synthesised.[138] Generally, the deposited h-BN coatings can be dichotomised into two descriptive categories: rough or smooth, visualised in the (Figure 2.3) compilation of transmission electron microscope (TEM) images of CNT@BN tubes synthesised by various CVD methods and their precursors. Rough h-BN coatings are non-uniform and exhibit unevenness

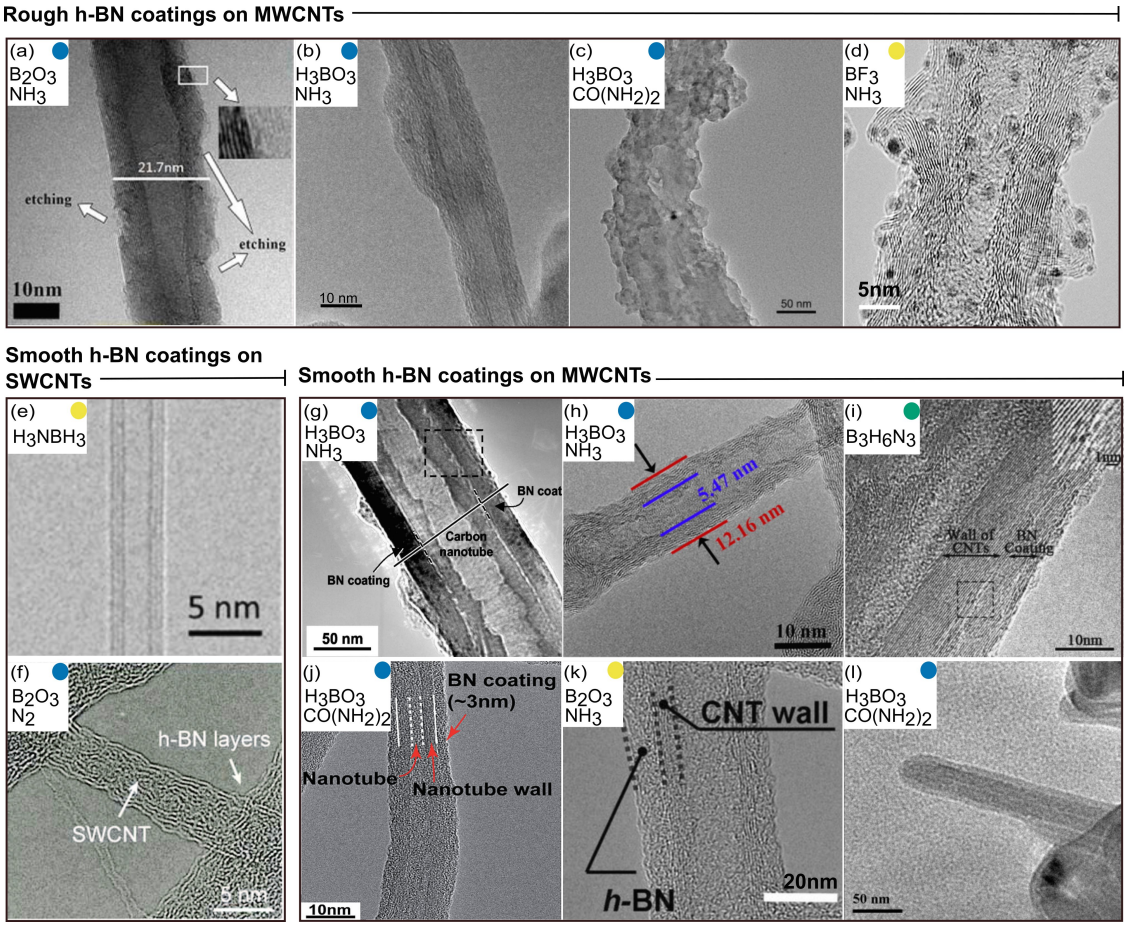


Figure 2.3: Catalogue of Transmission Electron Microscopy images grouped according to morphology of the deposited h-BN coating. Colour codes are matched to types of CVD in Figure 2.2 and precursor pathways are noted in insets. (a-d) Rough h-BN on MWCNTs. Reproduced with permission from Refs. [119, 122, 128, 130] Copyright 2015, American Chemical Society. Copyright 2011, Elsevier Ltd. Copyright 2014, Elsevier Ltd. Copyright 2018, American Chemical Society. (e-f) Smooth h-BN coatings on SWCNTs. Reproduced with permission from Refs.[125, 131] Copyright 2020, American Association for the Advancement of Science. Copyright 2015, Royal Society of Chemistry. (g-l) Smooth h-BN coatings on MWCNTs. Reproduced with permission from Refs. [96, 121, 126, 127, 129, 133]. Copyright 2004, The American Ceramic Society. Copyright 2015, American Chemical Society, Copyright 2010, Elsevier Ltd. Copyright 2016, Royal Society of Chemistry. Copyright 2015, Wiley-VCH. Copyright 2008, Elsevier Ltd.

		Carbon Nanotube Templates			h-BN coating			Ref
B Precursor	**N Precursor**	**Type**	**Outer Diameter (nm)**	**Wall Thickness (nm)**	**Deposition time (min)**	**Temperature (°C)**	**Thickness (nm)**	
Atmospheric Pressure CVD								
B_2O_3	NH_3	MWCNTs	15	-	60	1200	4-18	[119]
		MWCNTs	20	2-3	240	1200	2	[120]
H_3BO_3	NH_3	MWCNTs	100	18	50	1100-1200	15-20	[121]
		MWCNTs	9.5	3	60	1027	1-2	[122]
		VA-MWCNTs	8-9	1-2	60	900	2	[96]
		VA-MWCNTs	8-9	1-2	60	900	1-2	[123, 124]
H_3BO_3	N_2	SWCNT aerogel	1	-	60	1000	1-3	[125]
H_3BO_3	$CO(NH_2)_2$	MWCNTs	25	-	180	1000	10	[126]
		MWCNTs	9.5	3	180	900	3	[127]
		MWCNTs	20-40	<20	120	1000	10-25	[128]
Low Pressure CVD								
B_2O_3	NH_3	VA-MWCNTs	<10 nm	1-2	3	900	3-8	[129]
BF_3	NH_3	VA-MWCNTs	20	5	180	1100	ca. 5	[130]
$B_3H_6N_3$		MWCNT aerogel	12-13	3-4	30-120	900	2	[94]
H_3BNH_3		SWCNT film	1-2	-	180	1100	2-3	[131, 132]
Autoclave								
$B_3H_6N_3$		MWCNTs	50-70	ca. 20	600	600	<10	[133]
Plasma Assisted CVD								
BCl_3	N_2	MWCNTs	8-12	-	1.5 - 4	650	3 - 8	[134]
B_2H_6	NH_3	VA-MWCNTs	50	-	0.5	900	5-50	[135]
Magnetron Sputtering PVD								
h-BN sputter target		VA-MWCNTs	50	-	1-3	Room	15-30	[135]
h-BN sputter target		VA-MWCNTs	50	-	-	Room	3-20	[139]

Table 2.2: Summary of Chemical and Physical Vapour Deposition pathways for h-BN deposition onto CNTs. Core CNT diameter dimensions are summarised along with h-BN coating parameters (temperature, time) and thickness.

parallel to the surface of the underlying CNT.[119,122,128,130] Smooth h-BN coatings are uniform and can range from highly crystalline[121,131] to partially crystalline[96,125,133] to polycrystalline.[127,129,134]

Ammonia borane emerges as a particularly promising precursor for the CVD synthesis of h-BN as it is a stable solid at room temperature (safe for storage) and is also non-hazardous (easy to handle). Therein lies one of its advantages over many other precursors such as boron trihalides, diborane and borazine which themselves present risks associated with being toxic, highly flammable or corrosive, or produce harmful by-products.[113]

Moreover, in the common scenario whereby two separate B and N precursors are used, and at least one is in an aqueous state (e.g.H_3BO_3 or $CO(NH_2)_2$),[96,121,123–128,140] a pre-reactor procedure is necessary to infiltrate the precursor onto the surface of the CNTs prior to CVD. Additional steps to de-tangle and disperse CNTs in solution, often involving sonication and stirring, are used to obtain a more extensive, uniform precursor coating. However, this also explains why methods that use aqueous precursors are overall highly time extensive (several hours to days) and non-gentle.[120,125,127] Additional procedures might include CNT functionalisation with hydroxyl and carboxyl groups to improve the dispersibility of CNTs in aqueous solutions.[126–128,141]

A single source precursor such as ammonia borane already has a desirable 1:1 stoichiometric ratio of B:N matching that of h-BN and can simultaneously deliver both B and N in the vapour phase (evolved from its solid state upon heating). As such, laborious steps associated with aqueous state precursors are avoided. Until very recently, ammonia borane had not been explored for CVD growth of h-BN on CNTs. In 2020, Xiang *et al.* reported using ammonia borane to deposit highly crystalline coaxial h-BN onto SWCNTs under low pressure CVD conditions (Figure 2.3e).[131]

The work presented in this chapter contributes to the nascent exploration of ammonia borane as a precursor for CVD of h-BN on CNT on three fronts.

As exemplified by the upscaled CVD production of graphene to continuous processes, e.g. roll-to-roll,[142,143] atmospheric pressure conditions are favourable,

both for economic and technical feasibility. To address the prospective upscaling of CNT@BN production, the viability of ammonia borane for h-BN deposition onto CNTs under APCVD conditions is investigated here.

Secondly, as summarised in our review (Jones *et al.,* 2020),[138] several APCVD precursor routes, particularly the most frequently studied, e.g. B_2O_3 and NH_3 (and similar variants such as H_3BO_3 and $CO(NH_2)_2$), promote the formation of covalent interactions between the h-BN and CNT such that the resulting CNT@BN is not a true core-shell van der Waals heteronanotube. In this work, the effects of ammonia borane versus the aforementioned precursors on the nature of bonding between the deposited h-BN and CNT are explored.

Finally, ammonia borane APCVD is employed to coat MWCNTs rather than SWCNTs here. The justification for this is relevant to the Chapter 3 objective of implementing sacrificial templating to obtain BNNTs from the MWCNT@BN synthesised in this chapter. As a sacrificial template, SWCNTs offer a limited range of outer diameters (usu. 1-2 nm), which is not the case for MWCNTs, thus introducing more flexibility to the templating method for BNNT synthesis.

2.2 Synthesis of MWCNT@BN by Ammonia Borane pyrolysis

2.2.1 Materials and Methods

Name	Purity	Supplier
Reactants		
Solids		
MWCNT Nanocyl NC7000™	90%	Nanocyl SA
Ammonia Borane Complex	97%	Sigma-Aldrich
h-BN powder grade 015	>98.5%	3M
Gases		
Argon/Hydrogen (97.5 : 2.5 %)	-	BOC
Solvents		
Acetone		Sigma Aldrich
Isopropanol		Sigma Aldrich
Methanol		Sigma Aldrich

Table 2.3: Summary of reactants implemented in this chapter for synthesis of CNT@BN, and solvents used for cleaning of substrates, sample holders *etc.*

2.2.1.1 Decontamination procedures

Prior to use of the reactants and reactant vessels, decontamination procedures were conducted as summarised here.

Ammonia borane and h-BN powder were vacuum treated for 5 days prior to use. This treatment was introduced to remove any residual organic solvent, such as tetrahydrofuran (THF) in the 97(%) grade of Sigma Aldrich product. Such extensive vacuum treatment has been previously found to be effective at carbon decontamination.[144]

Nanocyl MWCNT powder was also vacuum treated and stored in a dessicator prior to use to ensure absence of residual solvents and moisture.

The support apparatus for containing the powder nanotubes (quartz slide) was cleaned by solvent rinsing (in order: Acetone, Methanol, Isopropanol), followed by drying with the nitrogen gun. This support apparatus was heat treated inside the quartz tube growth environment up to 1000 °C in air flow to oxidise any carbon contaminants present on the supports or in the reactor prior to the experiment. Glass precursor reservoir flasks were also cleaned following the same solvent wash, and subjected to UV/ozone treatment for 30 minutes prior to each experimental run.

2.2.1.2 Chemical Vapour Deposition of h-BN

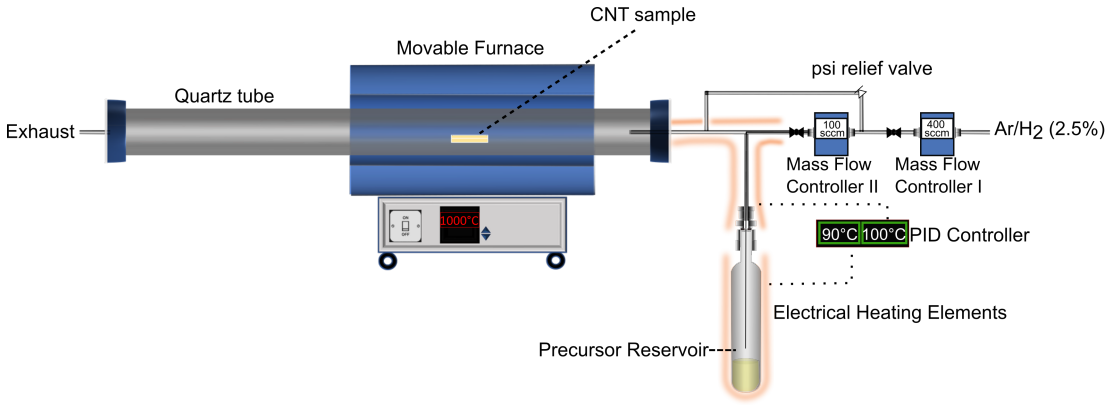


Figure 2.4: Illustration of CVD setup for h-BN depoisition onto MWCNTs by Ammonia Borane pyrolysis. Furnace: Elite Model TSU/12/38/500. Quartz tube dimensions: Length =1.8 m, inner diameter=29 mm .

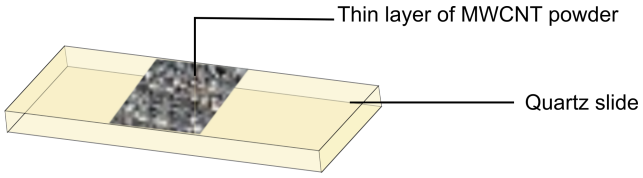


Figure 2.5: Illustration of CNT sample setup inside the reactor, i.e. layer of CNT on quartz slide.

Ammonia borane powder was mixed with inert h-BN filler in the weight ratio of 1:10 (100 mg and 1000 mg) to separate the ammonia borane granules and prevent global polymerisation of volatile gases emitted upon heating. This precursor

mixture was transferred into a reservoir flask that was connected upstream to the horizontal quartz tube furnace.

Nanocyl NC7000 MWCNTs (2-3 mg) was spread flat to form a roughly 2x2 cm square at the centre of a cleaned quartz slide (Figure 2.5). This slide was then inserted into the quartz tube at a room temperature position, and the system was sealed and purged with Ar/H_2 (2.5%) for 25 minutes.

To begin the synthesis (see Figure 2.4), an electronically heated jacket was raised to envelop the precursor reservoir flask. This cover was pre-heated to a set temperature of 90 °C before synthesis was initiated. Once the precursor flask began heating, the furnace-on-wheels was shifted over the region of growth, ensuring that the pre-heated 1000 °C centre of the furnace aligned with the centre of the growth sample. The connecting stainless steel manifold between the reservoir and the reactor quartz tube was also heated to 100 °C to prevent gas condensation inside the connector. Synthesis was conducted for 2 hours in Ar/H_2(2.5%) net carrier gas flow of 400 sccm. Gas flow through the precursor flask was set to 100 sccm. After this set time, the furnace was shifted downstream, allowing the sample to cool to room temperature within 15 minutes in Ar/H_2 (2.5%) flow. The system was then unsealed and the powder sample was then retrieved and stored in a glass vial.

2.2.1.3 Sample Preparation & Characterisation

For characterisation by scanning electron micrscopy (SEM), nanotube powders were deposited onto a sticky carbon tab. Nanotube samples with insulating properties were coated with ca. 8 nm of platinum prior to SEM imaging to prevent charging. SEM images were taken with the Zeiss Merlin SEM at acceleration voltage 3 kV.

For characterisation by transmission electron micrscopy (TEM), scanning TEM (STEM) and Electron Energy Loss Spectroscopy (EELS) , <1 mg of nanotubes were added to a small volume of ethanol solution in a glass vial. This was sonicated briefly for <5 minutes to gently break up nanotube agglomerates. A glass pipette was then used to deposit a few drops of solution onto a lacey carbon grid. This was placed into a vacuum oven overnight to remove residual solvent prior to imaging. High resolution

TEM (HRTEM) images were taken on the JEOL JEM-3000F with acceleration voltage set at 300kV. STEM images and EELS spectra, linescans and maps were obtained on the JEOL ARM-200F, with beam energy 200kV. The convergence and collection semi-angle were set to 30 and 40 mrad respectively. All EELS spectra were analysed by the Gatan Digital Micrograph® software, with spectra fitting models set as follows: Power Law (Background Model), Hartree Slater (Partial Cross Section Atomic Model), and Fitted Logarithm (Zero-loss Model). Full EELS quantitative analysis parameters for all included spectra are detailed in Appendix A, §A.1.

Nanotube samples analysed by Raman were positioned on a glass slide. All Raman spectra were acquired using the LabRam Aramis with green laser at wavelength 532 nm.

Powder samples analysed by X-ray photoelectron spectroscopy (XPS) and X-ray diffraction (XRD) were secured on carbon sticky tape. XPS analysis was conducted using the Thermo Scientific K-Alpha spectrometer under a microfocused, monochromated Al K-α X-ray source, operating at 12 keV with a 400 μm spot size. All samples were charge neutralised using a low energy ion flood source. Collected survey scan spectra achieved binding energy resolution of 1 eV, whilst high resolution scans had 0.1 eV resolution. These spectra were analysed using CasaXPS software and the Gaussian-Lorentzian product lineshape was used to model synthetic symmetrical peaks unless otherwise stated.

Nanotube sample XRD patterns were collected using the Bruker D8 Advanced Eco powder diffractometer with Cu K-α radiation paired with a LYNXEYE XE detector. Samples were scanned between the 2θ range 10-80°, with a step size of 0.02°.

Besides, XPS and EELS spectra, all plot-type data was analysed in OriginPro.

2.3 Results and Discussion

This section is divided into three themed subsections for discussion.

Firstly, in §2.3.1, the structure of the as synthesised MWCNT@BN is analysed to (i) determine the effectiveness of the APCVD method (described in §2.2.1.2) in introducing coaxial shell layers of h-BN onto the surface of MWCNTs, and (ii) to facilitate comparison of the quality and quantity of MWCNT@BN structural parameters with those in the literature.

Next, in §2.3.2, the suitability of this method to synthesise van der Waals type heteronanotubes, such that the h-BN has minimal covalent interactions with the underlying carbon, is examined. Here, the source and distribution of oxygen contamination are also considered.

Finally, in §2.3.3, the selectivity of the method to coaxial deposited h-BN and not other 0D to 3D nano-morphologies is discussed.

2.3.1 Structure of MWCNT@BN

Here, the results of structural analysis are presented in the following order:

- Introduction of the morphology of the nanotubes before and after the CVD process (SEM, TEM)
- Confirmation of the deposition of h-BN as coaxial shells encapsulating the MWCNTs (STEM, EELS)
- Measurement and calculation of the thickness of deposited h-BN sheath and the rate of deposition achieved (TEM)
- Determination of the crystallinity (crystal defect density, interdefect distance, d_{002} spacing) of the starting MWCNTs and the deposited h-BN (XRD, Raman, TEM)

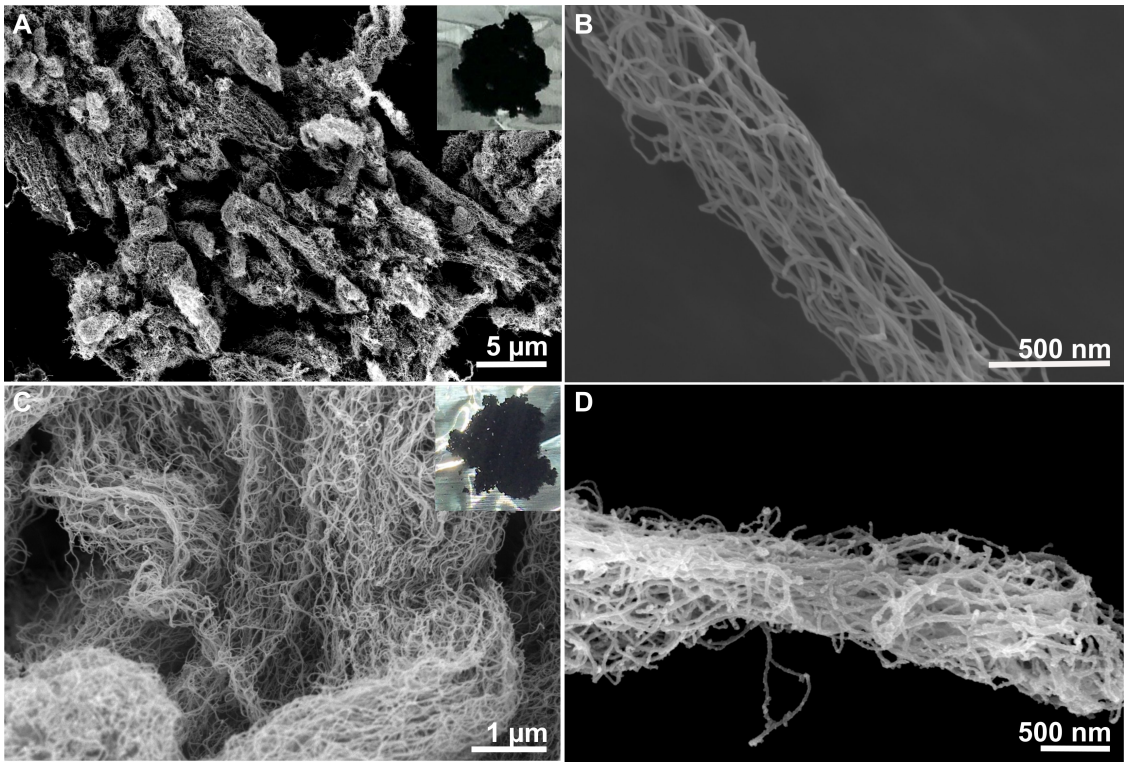


Figure 2.6: SEM images of (A,B) Nanocyl MWCNTs and (C,D) Nanocyl MWCNTs after h-BN coating CVD process. Inset pictures show optical appearance of black and dark grey nanotube powders.

2.3.1.1 Morphology

The as-received black powder Nanocyl NC7000 MWCNTs are visualised by SEM in Figure 2.6A. As expected, this powder is composed of microscopic agglomerates of MWCNTs ranging from 10μm to 1 mm in diameter.[145] At higher magnification, the MWCNTs are observed as entangled in ropes, e.g. Figure 2.6B.

After the CVD process, the nanotubular form of the materials is still intact (Figure 2.6C), with no deformation or collapse of the walls. This is an indication that the integrity of the MWCNT structure, which has been shown to undergo damage during processes such as carbon/h-BN substitution reactions,[146] has not been compromised by the h-BN coating process here. The higher magnification SEM images of the post-CVD nanotubes (e.g. Figure 2.6D) show that the walls of nanotubes remain relatively smooth with no protruding structures.

HRTEM images taken of the Nanocyl MWCNT prior to and subsequent to the CVD process (e.g. Figure 2.7A & B respectively) reveal that the post-CVD

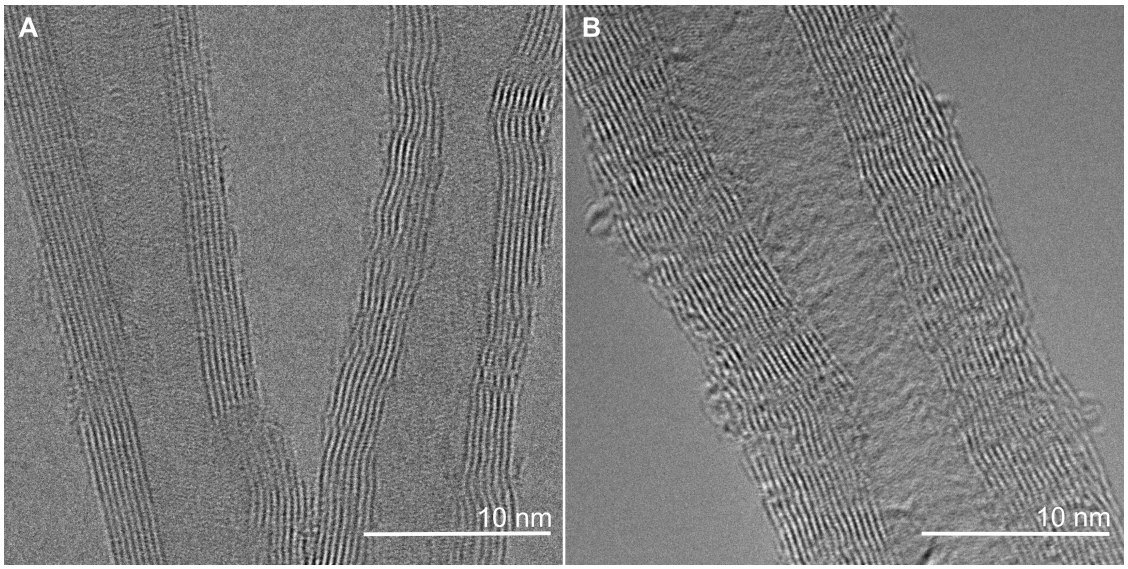


Figure 2.7: Example High Resolution TEM images of (A) Nanocyl NC7000 MWCNTs and (B) Nanocyl MWCNT after CVD h-BN deposition process; increased outer diameter and number of coaxial layers relative to pristine MWCNTs.

nanotube maintained a lamellar wall structure, but had an increased number of walls (dimensions are explored later in §2.3.1.3).

Both the SEM and HRTEM images of the post-CVD nanotubes provide evidence consistent with successful h-BN deposition onto the MWCNTs walls, with the basal plane of h-BN growing parallel to the basal plane surface of the MWCNT (i.e. in coaxial core-shell heterostructure.) This is further validated by STEM EELS analysis below.

2.3.1.2 Core-shell structure

EELS spectral images were obtained to visualise individual nanotube elemental composition and spatial distribution relative to the nanotube z-axis.

In Figure 2.8A-C, a typical as-received Nanocyl MWCNT is shown, as imaged in STEM mode and subsequently mapped for a EELS spectral image at a higher magnification. The corresponding EELS high-loss spectrum corroborates the known graphitic carbon composition of the nanotube.

Subsequent to the CVD treatment, collected EELS spectral images confirmed the co-location of B and N in an encapsulating shell around the MWCNTs, as exemplified in Figure 2.9. The EELS spectrum of the mapped area includes B-K and

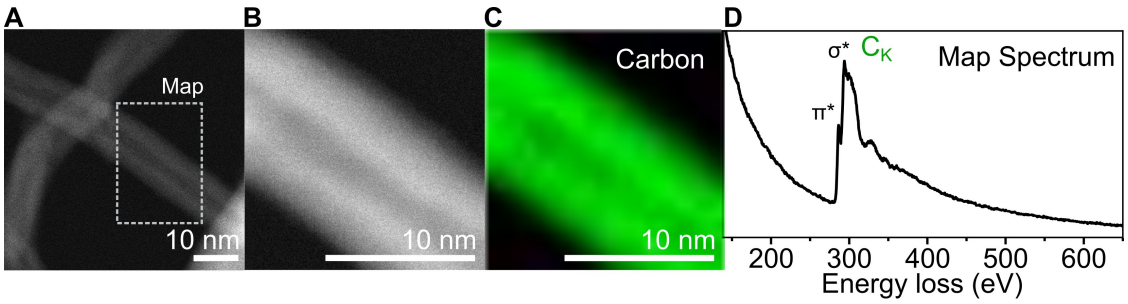


Figure 2.8: Nanocyl™ MWCNT observed by (A-B) Dark Field STEM and (C) EELS spectral imaging. (D) Corresponding EELS spectrum that exhibits a C-K edge typical of graphitic carbon. EELS collection parameters are summarised in Appendix Table A.1

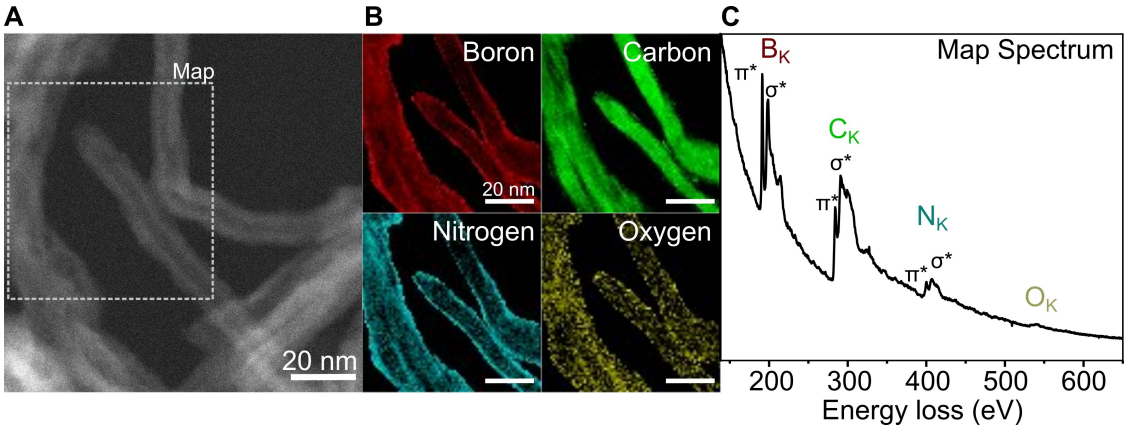


Figure 2.9: Example of MWCNT@BNs observed by (A) Dark Field STEM and (B) EELS spectral imaging, which reveals a BN shell around a C core. Elements detected, including oxygen, are summarised in (C) the corresponding EELS map spectrum.Fine edge structures of B/N and C exhibit π^* and σ^* feature typical of hexagonal BN and grahitic C. EELS collection parameters are summarised in Appendix Table A.2.

N-K edges with π^* and σ^* fine features which indicate that the deposited B and N are structured in the hexagonal polymorph, h-BN. Oxygen is also detected (see §2.3.2.3).

It is noticeable in Figure 2.9B that the h-BN coating also encapsulates the tip of the MWCNT. This is again observed on another mapped specimen, seen in Figure 2.10. High magnification EELS spectral images of the tip show a clearly defined core MWCNT surrounded by h-BN, with a closed cap. Such examples of full h-BN encapsulation, not just along the external layers but also at the nanotube ends, have not been previously demonstrated by other CVD-based coating methods. Analysis of the EELS spectra extracted from specific locations on the nanotube (Figure 2.10D) validates the spectral image elemental distributions. At locations 1,2 and 4, corresponding to nanotube outer layers at the tip end , left and right walls

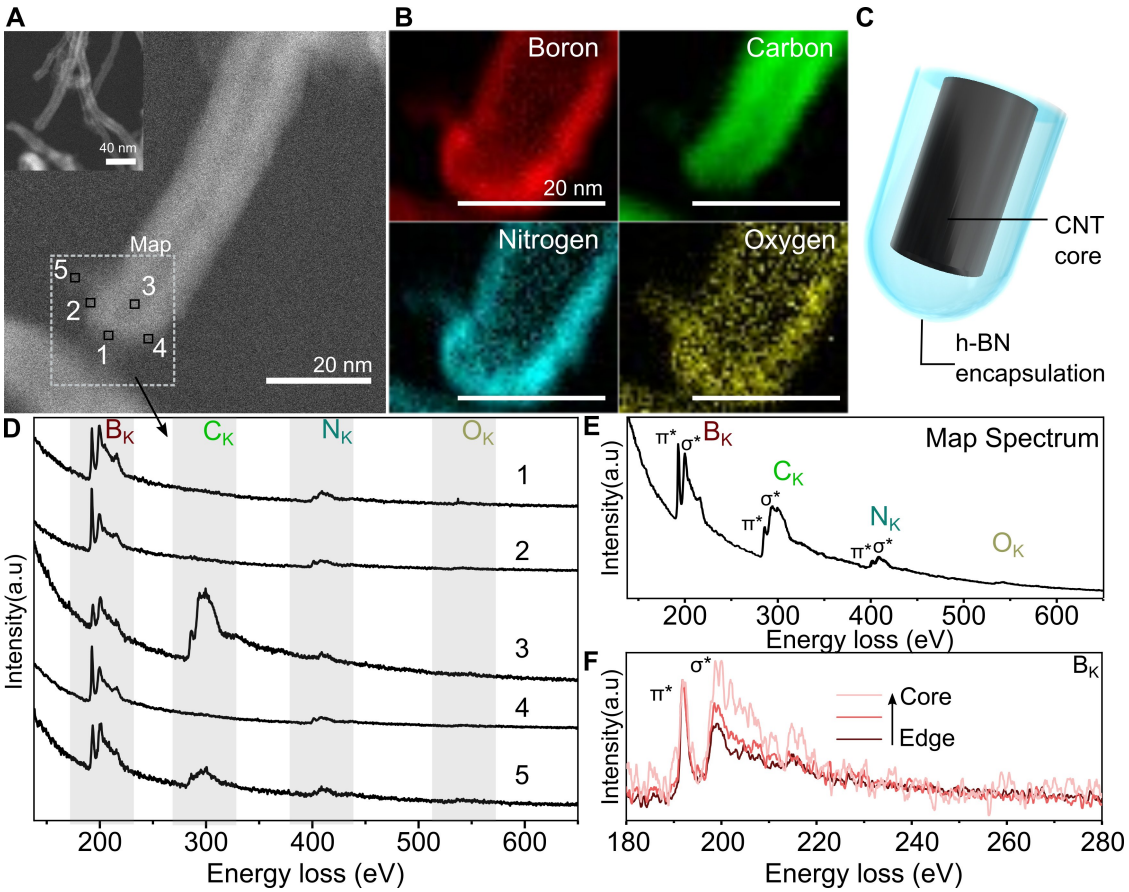


Figure 2.10: MWCNT@BN specimen observed by (A)Dark Field STEM with the nanotube tip mapped by (B) EELS spectral imaging. Complete tip encapsulation by BN is illustrated in (C). EELS spectra are extracted from the coordinates labelled 1-5 (D), indicating the h-BN composition of the outer shell. An atypical appendage is observed at coordinate 5. Increasing intensity of B-K edge σ^* peak relative to π^* (outer shell to inner core) indicates 360° h-BN encapsulation (F).

respectively, only B-K and N-K core-loss edges are visible. C-K losses are detected only within the core of the nanotube (at coordinate 3). Whilst the B-K edge is also identified along the spectrum of coordinate 3, the π^* peak of this edge is noticeably lower in intensity relative to that of other B-K edges from spectra collected at the edge of the nanotube. The B-K signal at site 3 is not due to h-BN presence within the core MWCNT, but to the h-BN outer shell that is oriented with basal plane perpendicular to the electron probe beam. At the nanotube edges, the basal plane (i.e. walls) are parallel to the beam. In Figure 2.10F, EELS spectra of the B-K edge collected from the outer nanotube edge toward the core (normalised to the π^* peak), show increasing relative intensities of the σ^* peak. This is a sign of the

changing orientation of h-BN relative to the probe beam,[147] and is therefore direct evidence of the 360° encapsulation of the h-BN around the MWCNT.

An atypical appendage to the nanotube, observable in the coloured spectral images, and associated with the collected EELS spectrum at coordinate 5, has co-located B,C,N and O. Apart from this feature, the core-shell relationship of MWCNT and h-BN suggests primarily van der Waals interactions between the two materials. The potential existence of covalent interactions, perhaps the scenario in the appendage, is discussed in §2.3.2.

Another specimen MWCNT@BN nanotube is analysed by EELS, as depicted in Figure 2.11. Alongside spectral mapping, line profiles were obtained for this specimen at two sites, located as marked in Figure 2.11A. As with previous specimens, B,C,N and O are detected and the h-BN outer coating is discernible from the spectral maps. In both line profiles 1 and 2, there is an evident spatial anti-correlation between C and B/N. The oxygen profile, albeit with its lower relative intensity, can be roughly superposed onto the matching B and N profiles, suggesting that oxygen is also present at the BN outer walls. The potential sources of this oxygen are discussed in §2.3.2.3.

A small peripheral peak is observed in the linescan 2 B-K, C-K and N-K profiles close to the onset of the MWCNT@BN nanotube left wall. Interestingly, this ca. 1 nm feature exhibits anti-correlated B/N and C peaks with BN on the outer surface. This feature is thus postulated to be a protruding fragment of a defective CNT wall that has similarly been coated on its outer surface with h-BN during CVD.

For further verification of the h-BN composition of the outer layers of the MWCNT@BN specimen, EELS spectra were extracted at the outer walls and inner core positions of the linescans (ranges indicated by the grey panels in Figure 2.11 D-E). These extracted spectra, shown in Figure 2.12, confirm that the outermost nanotube walls layers are indeed h-BN; for this specimen the h-BN shell extends ca. 1 nm inwards before a C-K edge is detected in the spectra.

The possibility that electron beam irradiation had induced damage to the nanotube walls to cause the small torn-off fragments observed in Figure 2.10 and Figure 2.11 cannot be neglected here, but is also not conclusive as before and

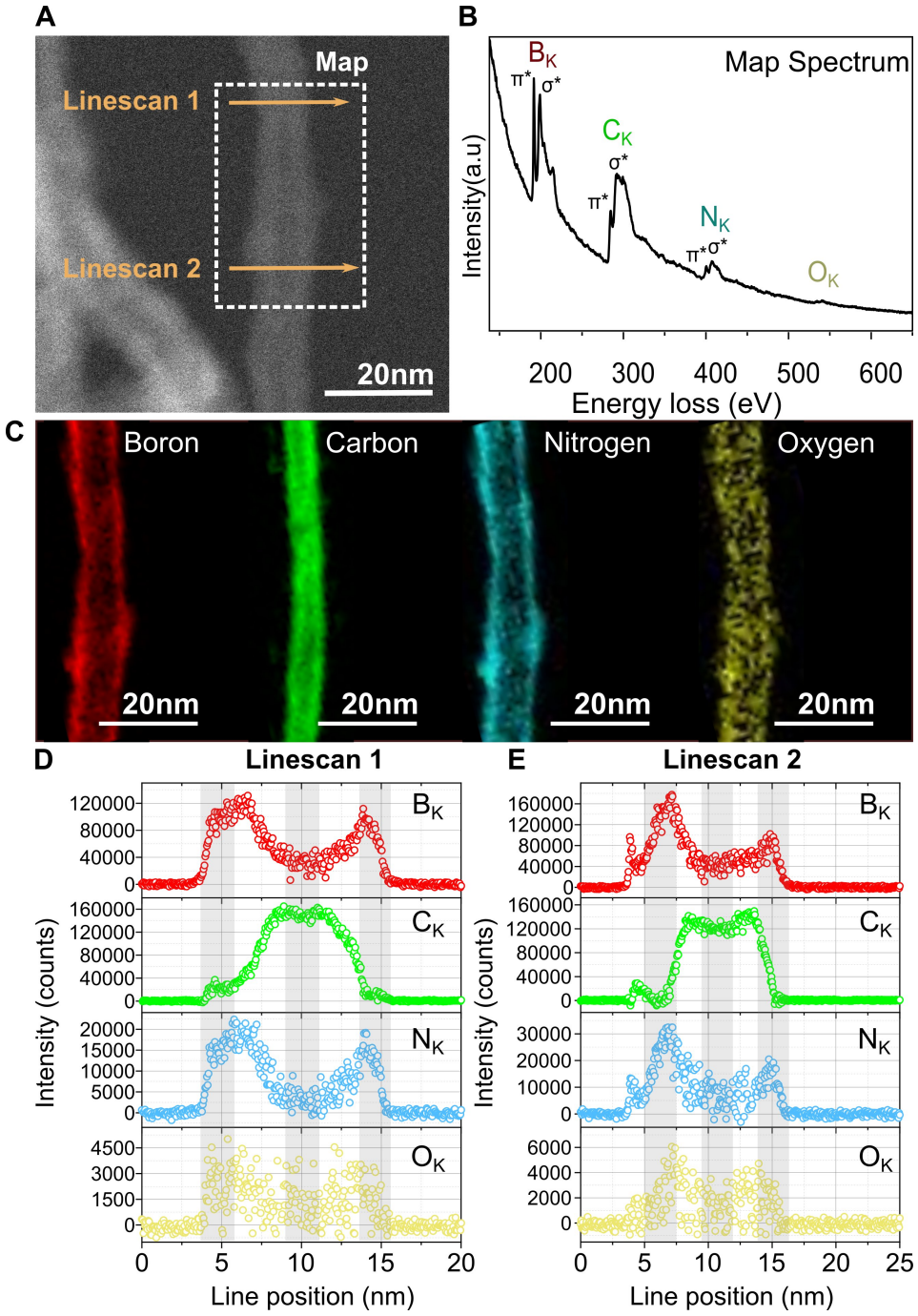


Figure 2.11: MWCNT@BN specimen observed by (A) STEM and mapped by (B-D) EELS spectral imaging which confirm the core-shell BN-C configuration. EELS linescans (D-E) were conducted at the indicated lateral positions along the nanotube. These profiles show distinct BN rich outer layers. The anomaly observed in line profile 2 is addressed in the text. Grey areas outlined in the linescan profiles correspond to line positions of extracted profiles in Figure 2.12. EELS collection parameters are summarised in Appendix Tables A.4, A.5 & A.6.

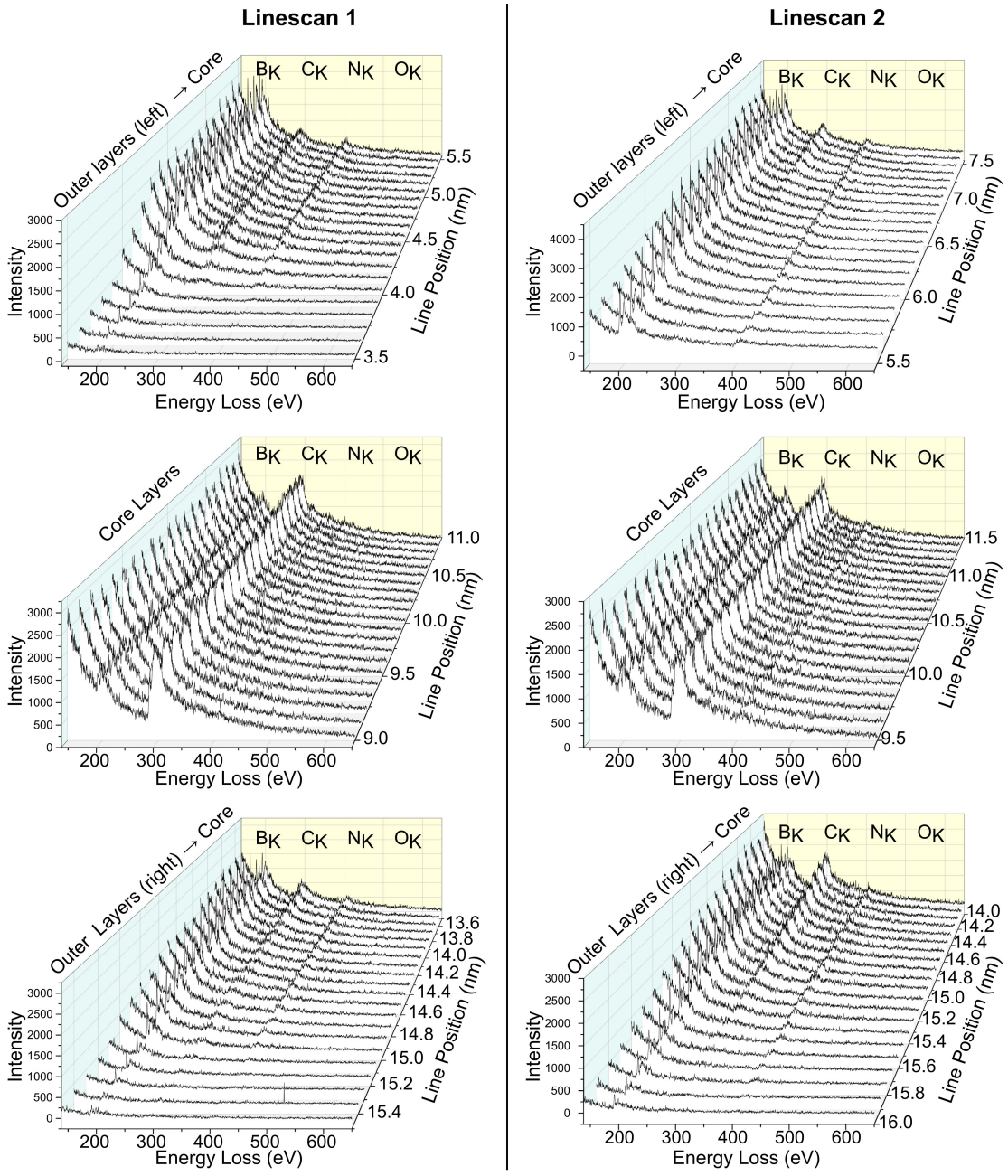


Figure 2.12: EELS spectra extracted from Linescan 1 and Linescan 2 located along a MWCNT@BN as shown in 2.11. Spectra represent regions on outer layers of the nanotube (on both sides of line scan) and its core. Spectra collected from the outer layers reveal the h-BN nature of the outer walls, whilst carbon is evidently in the nanotube core.

after irradiation images were not recorded. Electrons can cause displacement damage in the irradiated specimen, especially when it consists of light elements, whereby knock-on collisions of electrons and nuclei can prompt ballistic ejection of atoms. Defects induced by electron irradiation have been observed in SWCNTs, with structural changes including e.g. nanotube shrinkage, wall distortion, amorphisation.[148–151] MWCNTs have also undergone structural collapse subsequent to electron irradiation,[152,153] but as is the case with SWCNTs, the onset of these damages is dependent on irradiation factors such as beam energy and irradiation time. Similarly, nanotube shortening by tearing and detaching of tube ends has been observed on irradiated BNNTs.[154] For the MWCNT@BN nanotubes imaged here, the 200 keV electron beam used is also routinely implemented for high-resolution imaging of carbon and boron nitride nano-structures.[152] For many of the above mentioned irradiation induced damages, particularly on MWCNTs, intense electron irradiation was necessary, e.g. 800 keV, as generally the multi-wall structure is more stable against atom displacement compared to single-wall nanotubes.[148,150] The irradiation conditions applied here, including minute time-scale irradiation, are thus not expected to induce significant damage to the multi-wall CNT@BN structures. However, there is no existing study on electron irradiation effects on CNT@BN type hybrids, including types of induced defects and displacement thresholds, leaving this as an open area for future research.

Discussion on EELS has hitherto been focused on the qualitative composition and structure of the hybrid nanotubes. Quantitative EELS analysis has also been implemented here to assess the stoichiometric composition of the MWCNT@BN nanotubes, i.e. the relative ratios of B,C,N and O. Elemental quantification for each of the EELS analysed specimens aforementioned is summarised in Table 2.4. Procedures for quantification are briefly outlined in §2.2.1.3. Elemental atomic ratios relative to carbon (calculated in DigitalMicrograph®) reveal an approximately 1:1 stoichiometric ratio of B:N (within propagated error). This is in keeping with the stoichiometry expected for h-BN. Oxygen content is discovered to be on average 6 at.% (averaged from spectral images).

	Atomic Ratio (/C)				Percent Content %			
Spectral Images	B	C	N	O	B	C	N	O
2	0.44 ± 0.063	1.00	0.39 ± 0.055	0.13 ± 0.019	22.61	50.8	19.74	6.85
8	0.38 ± 0.054	1.00	0.35 ± 0.050	0.10 ± 0.014	20.9	54.48	19.3	5.32
18	0.35 ± 0.050	1.00	0.32 ± 0.046	0.10 ± 0.014	19.77	56.38	18.25	5.60
Linescans								
1	0.32 ± 0.045	1.00	0.29 ± 0.040	0.08 ± 0.012	18.78	59.39	16.97	4.86
2	0.39 ± 0.055	1.00	0.36 ± 0.051	0.07 ± 0.009	21.33	55.23	19.74	3.69

Table 2.4: Quantitative analysis of EELS spectral images and line scans. Atomic ratios are presented relative to carbon areal density. Percent contents are presented based on absolute areal density comparisons. Quantification parameters for each set of data is detailed in Appendix Tables A.2, A.3, A.4, A.5 & A.6.

2.3.1.3 Nanotube dimensions

According to the Nanocyl NC7000 MWCNT technical data sheet, these MWCNTs have an average outer diameter of 9.5 nm and length of 1.5 μm. This was verified for the sample of MWCNTs used for this study. The inner and outer diameters of 50 MWCNTs were measured from their HRTEM images similar to Figure 2.7A. This raw data is summarised in the Figure 2.13A histogram.

The same nanotube diameter measurements were collected from HRTEM images of MWCNT@BN nanotubes (e.g. Figure 2.7B) , and are compiled in the Figure 2.13B histogram.

The wall thickness of the nanotubes was calculated as the difference between the measured inner and outer diameters, as schematically depicted in Figure 2.13. The box plot in Figure 2.13C shows the calculated wall thickness of the MWCNTs before and after h-BN coating. There is a statistically significant wall thickness increase (as verified by the Mann-Whitney U test; $p = 2.43 \times 10^{-7}$) observed in the MWCNT@BN sample. As interpreted from the box plots, the coating method implemented here has introduced ca. 2-3 nm of h-BN on the surface of the MWCNTs.

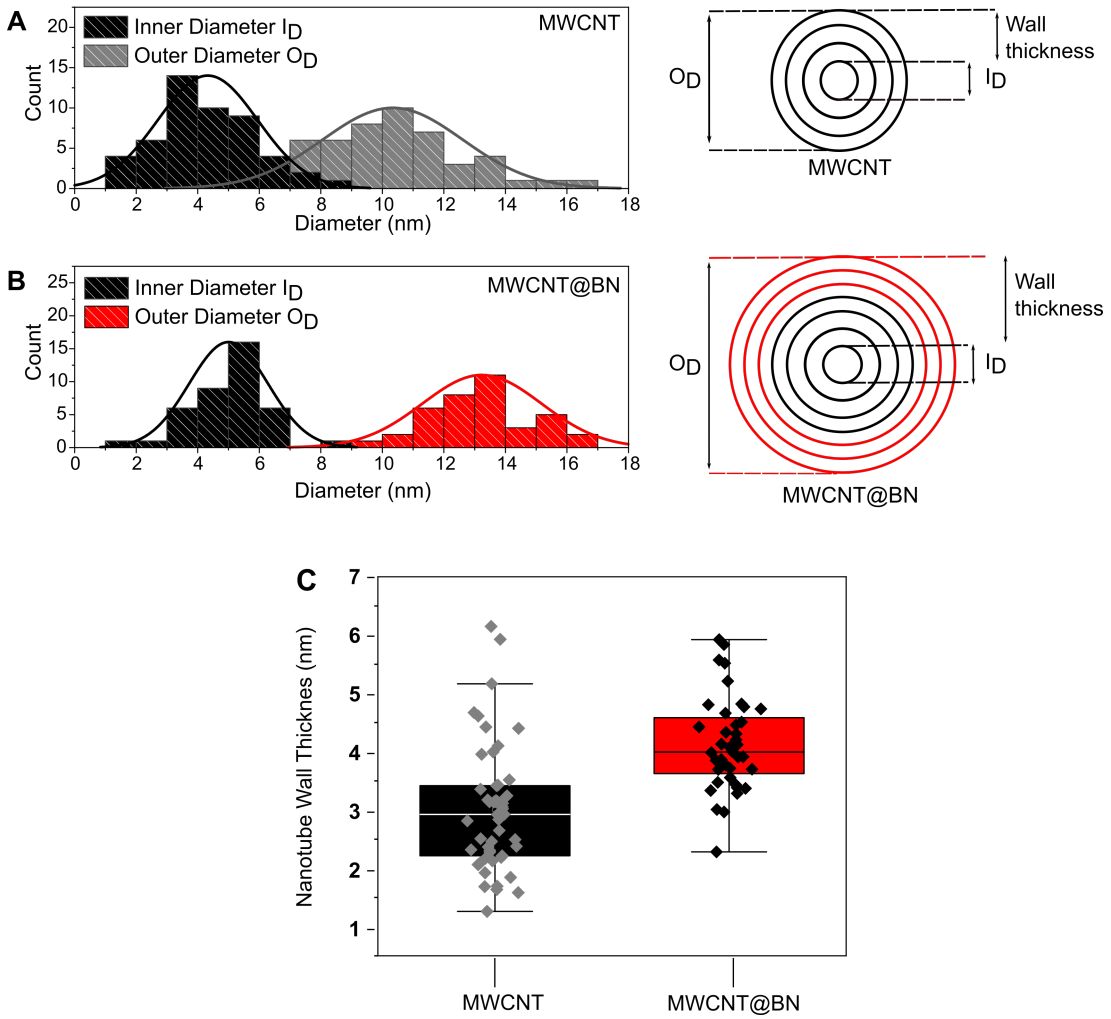


Figure 2.13: Distributions of the nanotube inner and outer diameters for (A) MWNCT and (B) MWCNT@BN as measured from HRTEM images, similar to those shown in 2.7A & B. The method of calculating the wall thickness of individual nanotubes is illustrated in the accompanying schematics. These wall thickness results, summarised in (C) box plot graphs, indicate an evident increase attributable to ca. 2-3 nm of deposited h-BN.

2.3.1.4 Rate of h-BN deposition

Based on the known synthesis time of 2 hours and the measured thickness of the h-BN layers, it was possible to calculate the achieved h-BN deposition rate for this work. Using the h-BN thicknesses and growth times reported in the literature, i.e. time within reactor at maximum temperature/plasma power *etc.*, it was also possible to calculate h-BN deposition rates achieved in the literature. Figure 2.14 shows the rates of h-BN deposition thus far attained in the literature, grouped according to categories of CVD and PVD. The rate of ca. 1 nm/hour achieved in this

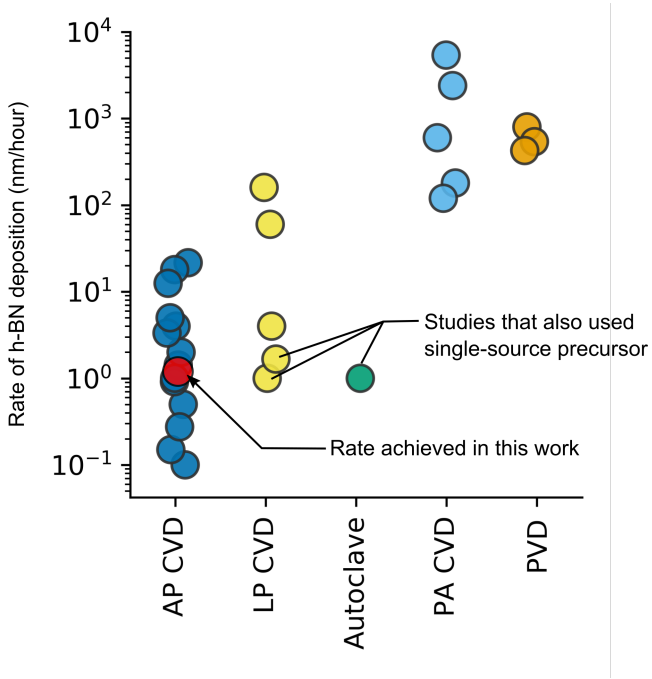


Figure 2.14: Calculated h-BN deposition rate (nm/hour) amongst the various methods of CVD (atmospheric pressure[96,119–123,125,126,128,155], low pressure,[94,129–131], autoclave,[133] plasma assisted[134,135]) and PVD.[135] Rates are shown on a log10 scale. The deposition rate achieved for this work is on the order of 1 nm/hour.

work fits within the range of rates typically observed for atmospheric pressure CVD techniques of h-BN deposition. This rate is similarly observed in other studies that implemented single source precursors (ammonia borane or borazine), albeit under different CVD conditions (i.e. low pressure CVD or autoclave). This may suggest a rate on this magnitude is characteristic of the single-source precursor pathway.

Whilst plasma assisted CVD,[134,135] PVD[135,139] and a few low pressure CVD techniques[129] show deposition rates that are 2-3 orders of magnitude higher than other CVD techniques, including the work reported here, such time-efficiency is often at the expense of h-BN crystallinity, i.e. h-BN is polycrystalline or amorphous. This can be observed in Figures 2.3 k,l.

2.3.1.5 Crystallinity of MWCNT and MWCNT@BN

The CNT surface crystallinity is a factor previously demonstrated to influence the crystallinity of the CVD deposited h-BN, as first reported by Chen *et al.,* (2004).[121] They found that pyrolytically stripped CNTs (PS-CNTs) with an etched, disordered

and turbostratic surface, had a similarly rough, polycrystalline h-BN coating. Contrastingly, heat treated CNTs (HT-CNTs), which became highly graphitised, appeared to be encapsulated by a uniform cylindrical h-BN tube. Both grades of MWCNTs had been infiltrated with H_3BO_3, and subjected to 1100-1200 °C heat in a horizontal quartz tube furnace with NH_3 flow. The difference in quality of h-BN coating on the PS-CNTs versus the HT-CNTs was attributed to the difference in surface structure of the CNTs; a disordered surface would facilitate multiple h-BN nucleation sites whilst an ordered surface has rarer nucleation. Thus, the difficulty of h-BN nucleation on a highly crystalline CNT surface facilitates single crystal h-BN growth rather than polycrystalline growth.

Consequently, the crystallinity of the h-BN as deposited in this work is investigated in parallel to the crystallinity of the template Nanocyl NC7000 MWCNT, given the established direct relationship amongst the two. The discussion on crystallinity involves examination of nanotube defect density, crystallite size and wall spacing (*vide infra*).

2.3.1.5.1 Crystal Defect Density For graphitic materials, including nanographites such as MWCNTs, one descriptor of crystallinity is the qualitative measure of structural defect density, which can be assessed by Raman spectroscopy. Pristine MWCNTs exhibit most distinctly the Raman D band (ca. 1350 cm^{-1}) and G band (ca. 1582 cm^{-1}). Whilst the G peak is attributed to first order phonon emission from the in-plane sp^2 carbon, the D peak is disorder-induced and originates from second order phonon scattering from defects, including broken sp^2 bonds or sp^3 bonds in carbonaceous impurities.[156–158] The ratio of D to G peak intensities (I_D/I_G) is a conventional means of describing MWCNT defect density, such that highly graphitised CNTs have low I_D/I_G and increasing the defects/amorphous carbon contributes to higher I_D/I_G. The D peak overtone, termed the 2D peak, originates from a double resonance process. As such , the 2D/G ratio has also been considered as an indicator of crystallinity, as increased order is expected to better facilitate the phonon coupling resonance event, thereby increasing the 2D peak

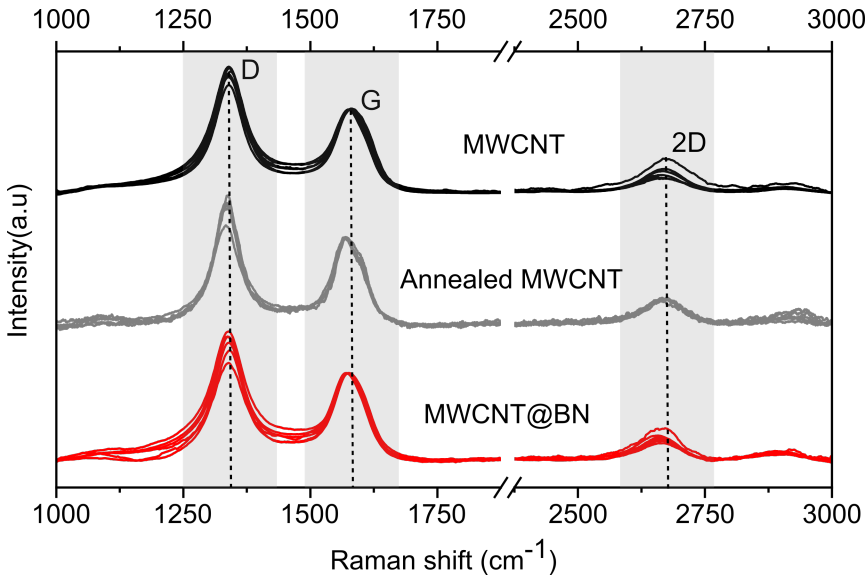


Figure 2.15: Raman spectra of Nanocyl NC7000™ MWCNTs as received, post annealing to 1000 °C in Ar/H_2, and post h-BN coating. Six spectra were taken from each sample using a 532 nm wavelength laser. D, G and 2D band positions are highlighted. See Table 2.5 and Figure 2.16 for spectra analysis.

intensity and the 2D/G ratio and vice versa.[157] Ferrari *et al.* have also reported that increasing disorder in graphitic carbon leads to broader full width at half maximum (FWHM) of all Raman peaks.[159]

Raman spectra were collected from the raw Nanocyl NC7000 MWCNTs and the MWCNT@BN. Additional spectra were collected from the MWCNTs subjected to the same temperature and carrier gas conditions used during the h-BN deposition process, but without introduction of the ammonia borane precursor. This acts as a control and is referred to here as annealed MWCNTs. These collected spectra are depicted in Figure 2.15. The D, G and 2D peak descriptors (Raman shift and full width at half maximum (FMHM)), along with the I_D/I_G and I_{2D}/I_G ratios for MWCNTs, annealed MWCNTs and MWCNT@BN are summarised in Table 2.5.

The noticeable D peak and I_D/I_G ratio of 1.43 ±0.08 in the MWCNT spectra facilitates the qualitative assessment that the Nanocyl NC7000 indeed has disordered graphitic content. This result corresponds with the visible kinks and wavy characteristics of the MWCNT walls as seen by TEM (Figure 2.7A). Otherwise, highly graphitised MWCNT would exhibit discernibly straight and concentric walls.

	D peak		G peak		2D peak	
	Position (cm^{-1})	**FWHM (cm^{-1})**	**Position (cm^{-1})**	**FWHM (cm^{-1})**	**Position (cm^{-1})**	**FWHM (cm^{-1})**
MWCNT	1340±1	80±6	1578±4	71±3	2666±5	111±13
Annealed MWCNT	1335±2	60±6	1569±2	62±4	2671±6	100±8
MWCNT@BN	1339±1	80±10	1574±2	69±4	2664±6	98±5

	Peak ratios	
	$\mathbf{I_D/I_G}$	$\mathbf{I_{2D}/I_G}$
MWCNT	1.43±0.08	0.25±0.09
Annealed MWCNT	1.35±0.11	0.29±0.02
MWCNT@BN	1.33±0.12	0.27±0.06

Table 2.5: Measured average D,G and 2D Raman peak parameters (Raman shift, FWHM) and intensity ratios of I_D/I_G and I_{2D}/I_G for MWCNTs, Annealed MWCNTs and MWCNT@BN. Errors are standard deviations.

Notably however, upon annealing at 1000 °C in Ar/H_2 atmosphere for 2 hours, there was an observable decrease in the average I_D/I_G ratio of the MWCNTs, as visualised in Figure 2.16. Simultaneously, the average I_{2D}/I_G ratio increased, and FWHM of the D,G and 2D peaks narrowed subsequent to annealing (Figure 2.16). These results denote that the MWCNT defect density has reduced upon heat treatment relative to the raw MWCNTs, i.e. the MWCNTs have become more graphitised.

Consequently, it is expected that the crystallinity of the MWCNT core in MWCNT@BN is on par with the annealed MWCNT, having undergone the same temperatures during the h-BN coating process. This is corroborated by the similarly decreased I_D/I_G ratio observed from the MWCNT@BN Raman spectra and its slightly increased average I_{2D}/I_G ratio, relative to the MWCNT spectral data. These results also confirm that the graphitic structure of the core MWCNT is preserved during the h-BN coating process, i.e. h-BN coat did not disrupt the CNT structure. Indeed, if B or N were primarily covalently doped into the MWCNT, a increase in defect density, as detected by Raman, would be expected.[160,161] That this is not the case here substantiates that the CVD process in this work

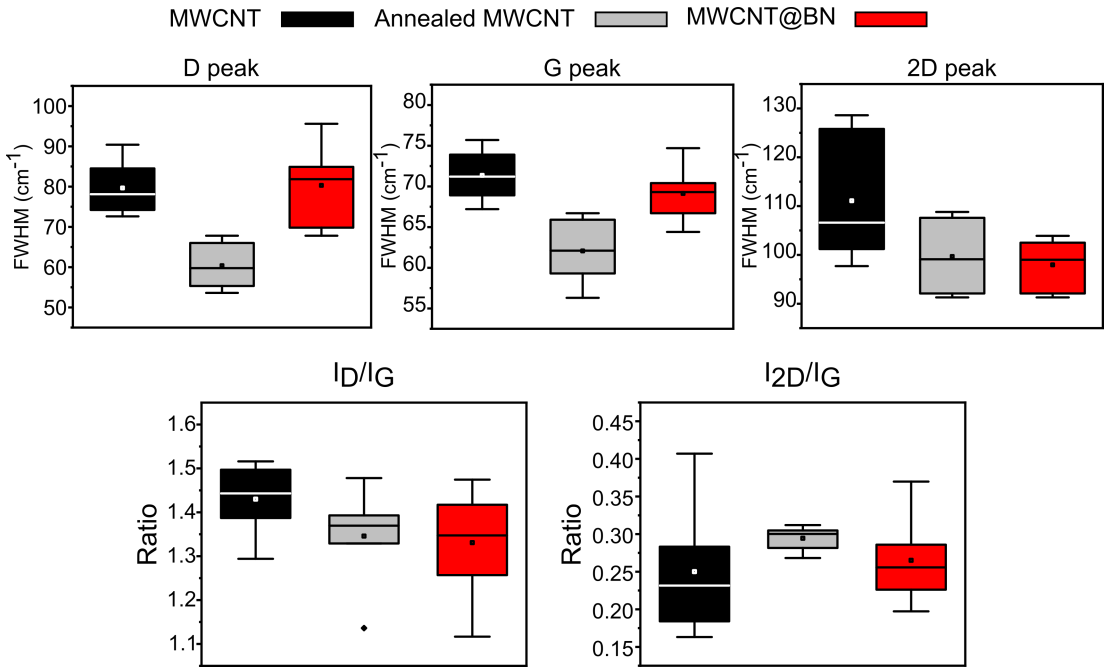


Figure 2.16: Box plot visualisations of D,G and 2D FWHM, and I_D/I_G and I_{2D}/I_G ratios for MWCNTs, Annealed MWCNTs and MWCNT@BN. Errors are propagated from I_D/I_G ratio standard deviations.

is in favour of h-BN deposition onto the MWCNT surface and not B and/or N substitution into the graphitic lattice.

The E_{2g} mode of h-BN from in plane B-N vibrations, which is situated at ca. 1366 cm^{-1} - 1370cm^{-1},[162,163] sits close to the D peak contributed by the MWCNT and as a result is is rarely delineated in Raman spectra of MWCNT@BN. Only in a small number of reports has it been possible to deconvolute the D+E_{2g} peaks to show the core-shell contributions made by carbon and boron nitride respectively.[94,119,130] Here, albeit no h-BN E_{2g} peak is observed, the D peak FWHM of MWCNT@BN is broadened relative to the annealed MWCNT, suggesting a contribution from h-BN E_{2g}.

2.3.1.5.2 Interdefect distance and d_{002} spacing To obtain an alternative assessment of crystallinity that is more quantitative, an estimate is made here of the average interdefect distance along the basal plane (graphitic nanotube walls) of the MWCNTs and is referred to as the average crystallite size, L_a (see Figure 2.17) . Increased L_a is synonymous with lower defect density and vice versa.

The relationship between I_D/I_G with L_a, that is dependent on Raman laser energy (or wavelength λ_{laser}), was first proposed and empirically validated by Cançado *et al.*,(2006) as shown in equation 2.1,[165] according to which both L_a crystallite size and λ_{laser} are expressed in nanometer units.

$$L_a(nm) = (2.4 \times 10^{-10})\lambda_{laser}^4 \left(\frac{I_D}{I_G}\right)^{-1} \tag{2.1}$$

The calculated L_a crystallite sizes for the MWCNTs, annealed MWCNTs and MWCNT@BN are summarised in Table 2.6. In keeping with the observed I_D/I_G trends, the MWCNT L_a interdefect distance increases upon annealing without or with the introduction of h-BN (i.e. annealed MWCNT or MWCNT@BN respectively).

An estimation of interdefect distance L_a can also be made by X-ray diffraction (XRD) analysis of the nanotubes. XRD patterns collected for the raw Nanocyl MWCNTs, annealed MWCNTs and MWCNT@BN are depicted in Figure 2.18.

The most distinct diffraction peak for graphitic carbon is due to the (002) reflection , followed by (100). Diffuse maxima that correspond to these reflections are observed in all the collected XRD patterns. By the well-known Scherrer equation, it is possible to extract values of L_a from the (100) peak parameters. The formula

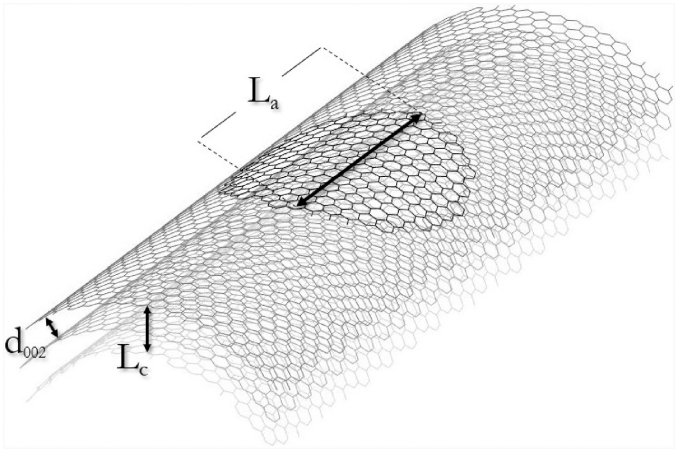


Figure 2.17: An illustration of a crystallite region (highlighted in black) and the orientation of crystallite size definitions L_a and L_c relative to this region in a MWCNT. Interlayer spacing of the MWCNT is also shown (d_{002}). Reproduced with permission from [164]. Copyright 2019, Elsevier Ltd.

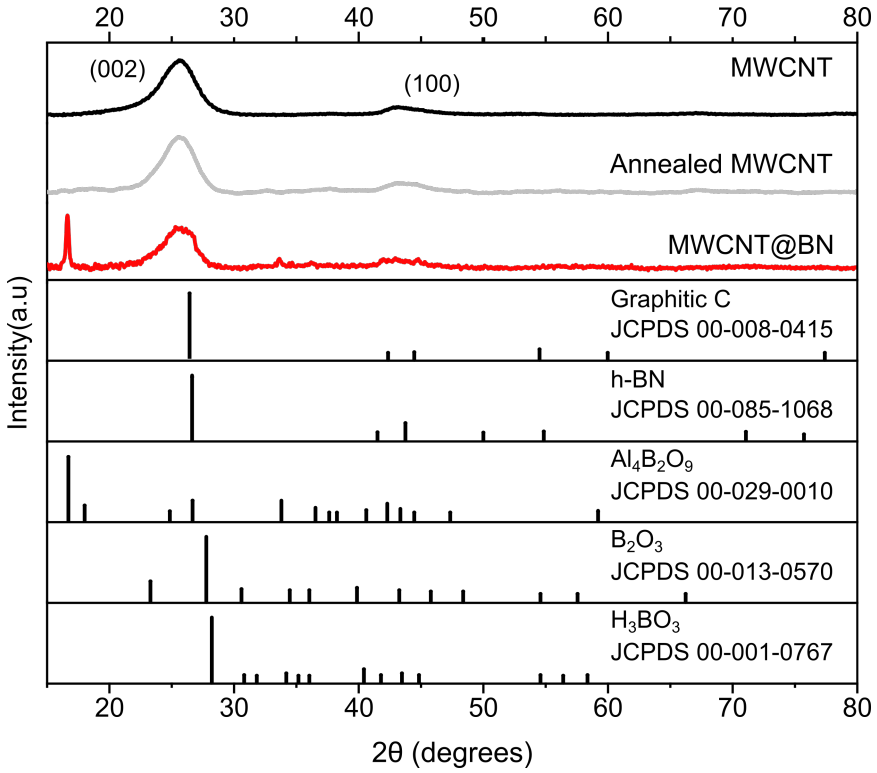


Figure 2.18: Collected XRD patterns of MWCNT, Annealed MWCNT and MWCNT@BN are shown alongside reference XRD patterns for graphitic carbon, h-BN, aluminium borate. Further discussion on the identified $Al_4B_2O_9$ impurity is included in §A.3. Reference XRD patterns for B_2O_3 and H_3BO_3 do not indicate the presence of these impurities in the MWCNT@BN.

for L_a (see equation 2.2) consists of a Warren modified k constant of 1.84,[166] X-ray wavelength $\lambda = 0.154$ nm for a Cu K-alpha source, β as the FWHM in radians of the diffraction peak, and θ as the Bragg angle. A similar calculation can be done for L_c, which is an estimate of the average stacking height of the lamellar crystallite (Figure

	Interdefect Distance [L_a **crystallite size (nm)**]
MWCNT	13.4 ± 0.8
Annealed MWCNT	14.2 ± 1.2
MWCNT@BN	14.5 ± 1.3

Table 2.6: Calculated crystallite size along the basal plane of the MWCNT walls in MWCNTs, Annealed MWCNTs and MWCNT@BN. This is an estimation of the interdefect distance based on the Raman I_D/I_G ratios. Laser wavelength λ_{laser} applied is 532 nm.[165]

	2θ (degrees)		**FWHM (degrees)**		**Crystallite Size (nm)**		**Layer spacing (nm)**
	(002)	(100)	(002)	(100)	L_a	L_c	d_{002}
MWCNT	25.5	43.7	3.6	3.4	5.1	2.3	0.349
Annealed MWCNT	25.6	43.7	3.2	3.0	5.8	2.5	0.348

Table 2.7: L_a, L_c interdefect distances (crystallite sizes) and d_{002} spacings for MWCNT and Annealed MWCNT, as calculated from data derived from the XRD patterns in Figure 2.18 and equations 2.2, 2.3 and 2.4.

2.17), using the (002) diffraction peak parameters and k=0.9.[167] See equation 2.3.

$$L_a = \frac{1.84\lambda}{\beta cos\theta} \tag{2.2}$$

$$L_c = \frac{0.9\lambda}{\beta cos\theta} \tag{2.3}$$

$$d_{002} = \frac{n\lambda}{2sin\theta}, n = 1 \tag{2.4}$$

Calculated values of L_a and L_c for MWCNTs and annealed MWCNTs are summarised in Table 2.7. Albeit the absolute values of L_a are smaller than compared to those calculated using the Raman relationship (Table 2.6), the same trend is observed whereby the L_a interdefect size is increased subsequent to annealing. This thereby corroborates that MWCNT exposure to 1000 °C in Ar/H_2 measurably increases its relative crystallinity. L_c is a lesser recognised indicator of crysatllinity as the lamellar stacking height is not a comprehensive descriptor of the order in stacking.[164] Noticeably however, the estimated L_c values match closely with the MWCNT wall thickness ca. 3 nm (Figure 2.13).

The XRD patterns also reveal information regarding stacking order along the crystal c-axis, i.e. lamellar orientation relative to each other. A high degree of graphitic three-dimensional ordering is consistent with a characteristic upshift and narrowing of the (002) peak, alongside the appearance of higher resolved peaks e.g. (101), (102), (004), (110), (112) *etc.* For the MWCNTs here, the absence of

the higher resolved peaks, alongside the broadened (002) peak and its downshifted position (2θ =25.5°) relative to the graphitic C reference (2θ=26.4°; JCPDS 00-008-0415), indicate the typically more turbostratic nature of ordering amongst the MWCNT walls;[164] the layers may be parallel but are more randomly stacked (translated and rotated) along the c-axis and not perfectly AB' stacked as in highly crystalline graphite.[168] The calculated d_{002} layer spacings for the MWCNTs and annealed MWCNTs (Table 2.7), according to Bragg's law (equation 2.4), reveals an interlayer separation of 0.349 nm , which is larger than that of highly crystalline graphite (0.335 nm). A broader interlayer spacing is generally observed in MWCNTs compared to bulk graphite crystals due to a combination of turbostratic ordering and wall curvature in MWCNTs.[158,168,169]

The interpretation of h-BN crystallinity based on the XRD pattern of MWCNT@BN is compounded by the fact that graphitic carbon and h-BN have very similar diffraction patterns (see reference peaks for graphitic C and h-BN in Figure 2.18). For this reason, the L_a,L_c and d_{002} values for MWCNT@BN are not calculated from its corresponding XRD pattern. As the graphitic C and h-BN (002) peak positions are slightly displaced from one another, respectively 2θ=26.426 (JCPDS 00-008-0415) and 2θ= 26.627 (JCPDS 00-085-1068), a common interpretation of XRD patterns for h-BN coated CNTs is that the (002) peak should be slightly upshifted and asymmetric relative to that of the pristine CNT.[119,127,130,133] The (002) peak on the MWNCT@BN sample does appear slightly more asymmetric to higher 2θ values as compared to the MWCNT and annealed MWCNTs. However, this is likely also influenced by an $Al_4B_2O_9$ impurity contribution, further discussed in §A.3.

With regard to h-BN crystallinity, as with the previously discussed graphitic MWCNT, a highly ordered crystal structure would be manifested by the appearance of higher resolved peaks e.g. (101), (102), (004), (110), (112) on its diffraction pattern as exemplified in the XRD patterns of increasingly crystalline h-BN in Figure 2.19 A-D.[170] As these higher resolved peaks are not evident on the MWCNT@BN pattern, it can be inferred that the ordering of the CVD deposited h-BN is similarly turbostratic in nature to its underlying MWCNT. Figure 2.19 E-F illustrate perspective models

of turbostratic BN (t-BN) with parallel layers randomly oriented within the c-axis, compared to highly crystalline h-BN that shows AA' stacking.

For further quantification of the d_{002} spacing in both the MWCNTs and the deposited h-BN layers, line profile analysis was conducted on the of HRTEM

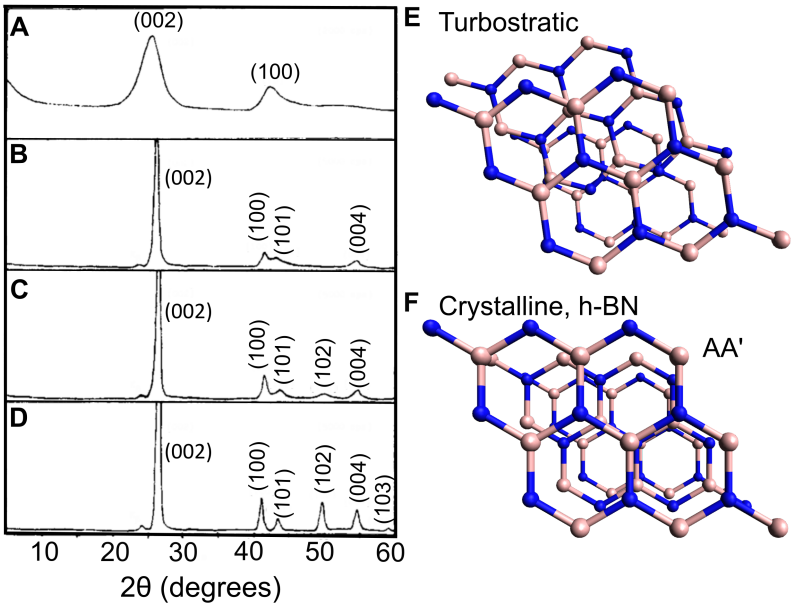


Figure 2.19: (a)-(d) XRD patterns of h-BN with increasing crystallinity from turbostratic to crystalline forms. Reproduced with permission from Ref. [170]. Copyright 1962, American Chemical Society (e) Model of turbostratic BN with random alignment along the c axis. (f) Perspective model of crystalline h-BN whereby B and N atoms are superposed on each other in succession (AA' stacked) along the crystal c-axis.

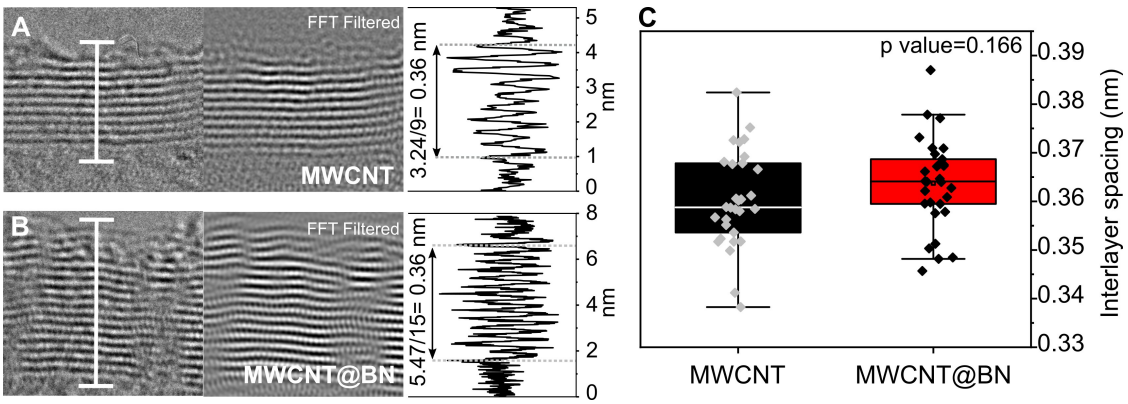


Figure 2.20: HRTEM line profile analysis of (A) MWCNT and (B) MWCNT@BN for estimation of the d_{002} spacings, found to be ca. 0.36 nm . Repeated analysis of multiple specimens, plotted in (C), reveals that that there is no significant difference between the d_{002} of MWCNT and MWCNT@BN.

images of nanotube walls. As shown in Figure 2.20 A-B, line profile intensity maxima correspond to individual nanotube walls in the bright field HRTEM images. Interlayer distance can be more accurately averaged from the distance separating multiple walls. For the examples shown of MWCNT and MWCNT@BN in Figure 2.20 A-B, the averaged d_{002} for both is 0.36 nm. To be more conclusive of the d_{002} spacings, line profile measurements as seen in Figure 2.20 A-B were repeated for across 30 separate wall areas for MWCNT and MWCNT@BN each. The collected data is summarised in the box plots in Figure 2.20 E. Statistical analysis of the normally distributed datasets reveals that they are not significantly different (p value = 0.166) and have average d_{002}= 0.36 nm. In the scenario that the deposited h-BN spacing was greater/lesser than that of the MWCNT, this would be represented by a statistically significant increase/decrease in the average d_{002} spacing of MWCNT@BN relative to that of MWCNT. That this is not the case here indicates that the deposited h-BN interlayer spacing is on par with that of the core MWCNT. Considering that the d_{002} spacing of highly crystalline h-BN is 0.333 nm, the deviation to a larger spacing (ca. 0.36 nm) observed here is an indicator of the non-optimal c-axis ordering of lamellae in the deposited h-BN (i.e. mirroring that of the underlying MWCNT), along with possible curvature effects, as in the case of increased interlayer spacings observed in CNTs relative to graphite crystals.[168,169]

In summary of §2.3.1 on the structure of synthesised MWCNT@BN, the hetero-nanotube core-shell configuration of carbon and h-BN was verified. Importantly, it was observed that the introduction of h-BN did not disrupt the crystal structure of the MWNCTs, which was actually discovered to undergo graphitisation under the operated CVD conditions. These results lend support to the minimal occurrence of covalent bonding between the shell h-BN and core MWCNT, which is further investigated below in §2.3.2.

2.3.2 Bond Speciation within MWCNT@BN

In this section, the nature of chemical bonding between h-BN and MWCNT in the MWCNT@BN is probed by XPS, a powerful technique for analysis of nanomaterial chemical composition. Owing to the several hundred μm spot size of the X-ray probe, a large number of nanotubes are encompassed in the probe area, so acquired results are more statistically significant than possible via electron microscopy techniques.

The main objective here is to determine the suitability of the method in this work for synthesising van der Waals hybrids of MWCNT@BN, i.e. with few covalent interactions between the deposited h-BN and CNT.

The subsequent discussion is presented in the following order:

- Detailed XPS analysis of the pristine MWCNT and the synthesised MWCNT@BN
- Comparison of bond speciation deduced by XPS in MWCNT@BN synthesised in this work versus that of MWCNT@BN synthesised from the most frequently used precursors in the literature.
- Consideration of the source, distribution and bonding of oxygen contaminant in the MWCNT@BN structure.

2.3.2.1 XPS analysis of MWCNT and MWCNT@BN

First, XPS survey spectra of MWCNT and MWCNT@BN reveal their respective qualitative and quantitative overall elemental composition.

The MWCNTs exhibit a high purity of carbon (98.4 at.%) and a low concentration of oxygen (1.6 at.%). By deconvolution of the high resolution XPS C1s peak, this native oxygen in the MWCNT is attributed to C-O functional groups (see Figure 2.22 & Table 2.8).

The XPS survey scan of MWCNT@BN (Figure 2.21B) confirms the presence of boron (26.9 at.%) and nitrogen (20.4 at.%), alongside carbon (46.6 at.%) and oxygen (6.1 at.%). Thus, the calculated B:N atomic ratio is 1.3:1, slightly biased to a higher B content than the ideal 1:1 stoichiometric ratio expected of pristine

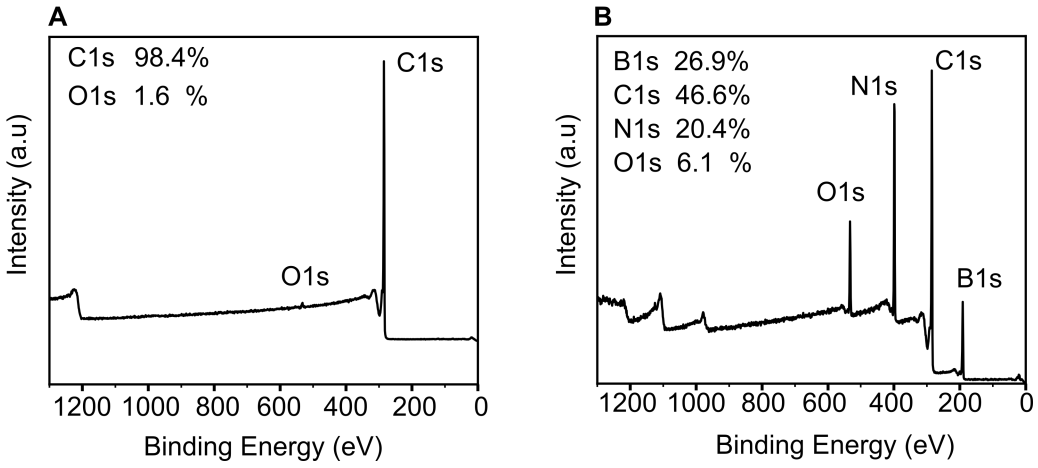


Figure 2.21: XPS survey spectra of (A) Nanocyl MWCNTs and (B) MWCNT@BN.

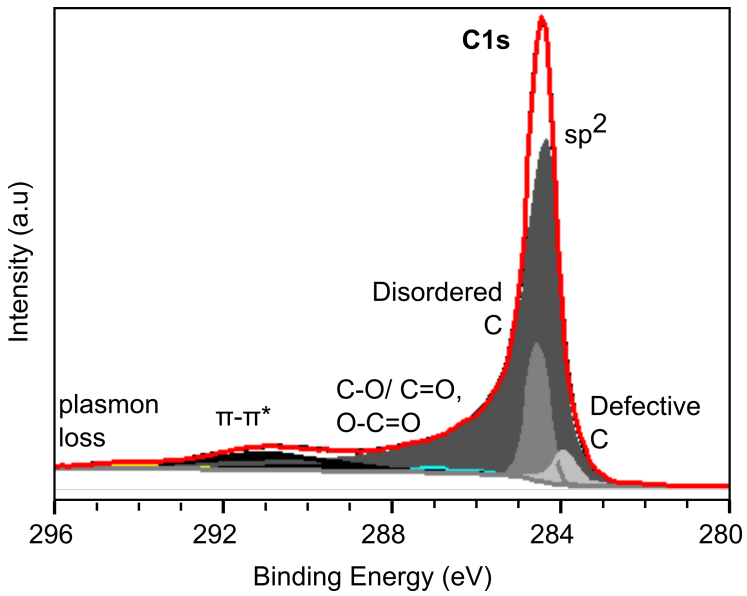


Figure 2.22: XPS High Resolution C1s spectra of Nanocyl NC7000 MWCNT fitted in CasaXPS with synthetic peaks as further summarised in Table 2.8. Line shapes for peaks are Gaussian-Lorentzian, with the exception of the asymmetric modified Lorentzian LF lineshape for fitting sp^2 carbon due to it XPS final state effects.[171]

h-BN. The increased oxygen content relative to that of the MWCNTs suggests incorporation of oxygen impurity into the h-BN, as previously also detected by EELS in §2.3.1.2. This is addressed in the later discussion on the high resolution XPS B1s and N1s peaks of the MWCNT@BN as well as in the §2.3.2.3.3 review on oxygen distribution within the MWCNT@BN.

As exemplified by the high resolution XPS C1s peak of the MWCNTs in

Bond	Binding Energy (eV)	FWHM	% Area
Defective carbon	283.9	0.60	3.56
sp^2 carbon	284.4	0.65	74.26
Disordered carbon	284.6	0.56	11.88
C-O	286.0	0.6	0.24
C=O	287.0	0.75	0.50
O-C=O	288.0	0.75	0.25
π-π^*	290.9	3.37	8.61
Plasmon loss	294.4	1.68	0.72

Table 2.8: Summarised description of synthetic peaks fitted to the high resolution XPS C1s spectrum of Nanocyl NC7000 MWCNTs as shown in Figure 2.22. Bond identification is referenced from Blume *et al.*, (2015).[171] and Zielke *et al.*,(1996).[172]

Figure 2.22, the overall spectrum shape results from accumulative contribution of photoelectron energy peaks associated to the various chemical environments of C (i.e. different bonds). As both MWCNT and MWCNT@BN share a graphitic carbon component, it is possible to compare their high resolution XPS C1s spectra to infer if the deposited h-BN caused any changes to the chemical environment of the carbon atoms in the MWCNT lattice, especially involving new covalent bonds such as C−B or C−N.

Figure 2.23 displays the superposed C1s spectra of MWCNT and MWCNT@BN, which show no significant difference, as summarised in the accompanying difference spectrum. The lack of peaks in the difference spectrum in the region associated with C−B and C−N bonds[146,160,173–175] suggests that there are minimal covalent interactions between the MWCNT and h-BN coating and the core MWCNT structure maintains its chemical integrity. However, this must be validated by the B1s and N1s XPS spectra.

The B1s and N1s high-resolution XPS spectra for MWCNT@BN are shown in Figure 2.24A and B respectively. Deconvoluted peaks identified in the B1s spectrum correspond to photoelectron energies emitted from B atoms involved in B−N (190.49 ev), B−N_2O (191.71 eV) and B−NO_2 (192.76 eV) bonds. There is no

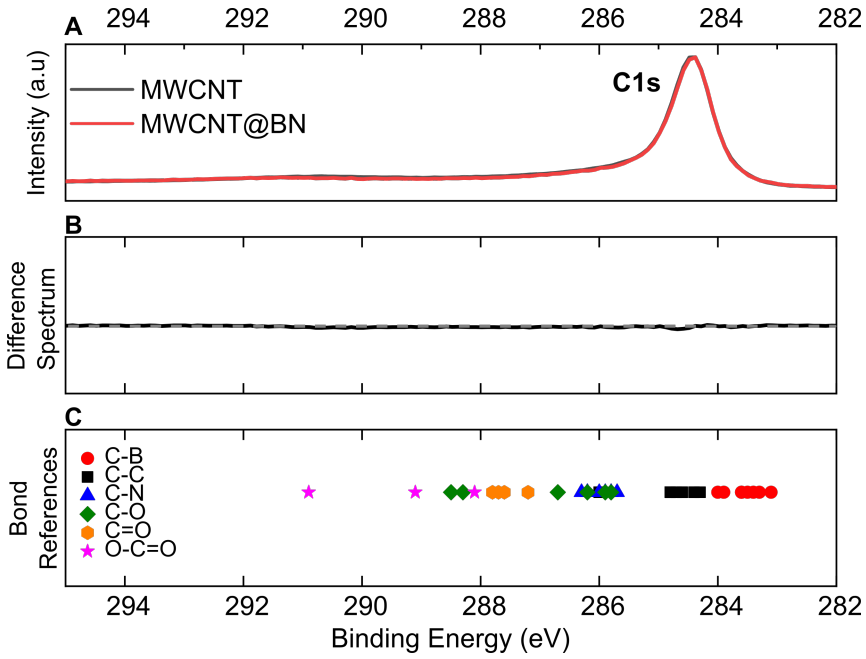


Figure 2.23: (A) Superposed High Resolution XPS C1s spectra of Nanocyl NC7000 MWCNTs and MWCNTS after h-BN coating.(B) The difference spectrum shows no noticeable peaks in the C-B or C-N regions, as referenced to (C) previous literature.[96,119,125–128,133,141,146,160,173,176]

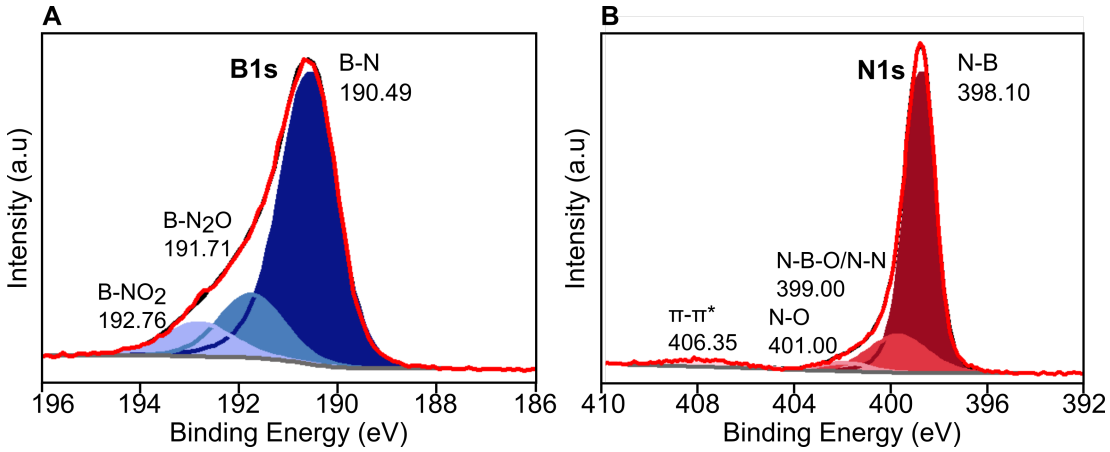


Figure 2.24: High resolution XPS (A) B1s and (B) N1s spectrum for MWCNT@BN. High resolution peaks fitted in CasaXPS with a GL-T lineshape for the B-N bonds[177] and GL lineshapes for other bonds.

B1s				N1s			
Bond	**Binding Energy (eV)**	**FWHM (eV)**	**% Area**	**Bond**	**Binding Energy (eV)**	**FWHM (eV)**	**% Area**
B-N	190.49	1.15	73.01	N-B	398.10	1.10	74.91
B−N_2O	191.71	1.5	17.47	N-B-O/ N-N	399.00	2.5	17.48
B−NO_2	192.76	1.61	9.52	N-O	401.00	1.97	3.23
				π-π^*	406.35	3.23	4.38

Table 2.9: Summarised description of synthetic peaks fitted to the high resolution XPS B1s and N1s spectrum of MWCNT@BN as shown in Figure 2.24. Bond identifications are referenced from [178].

evident B−C contribution at ca. 189 eV.[125,146,174] The synthetic B−O peaks fitted here are associated with oxygen adsorbates that preferentially bond at N vacancy sites of the h-BN.[178] The adsorbance of O at N vacancy sites could account for the skewed B:N stoichiometric ratio (1.3:1) in favour of B, as demonstrated in Figure 2.21. Alternative B−O type bonds, such as hydroxylated B−OH[179] or B_2O_3[119] have peak positions that overlap with the B−NO_2 and B−N_2O region.*

Finally, the N1s spectrum (Figure 2.24B) is fitted with peaks associated to N−B (398.10 eV), N−B−O/N−N (399 eV) and N−O (401 eV) bonds.[178] As oxygen is detected both in the survey scans of MWCNT@BN as well as in the B1s spectrum, it is anticipated that oxygen will also alter some of the N atom chemical environments to some extent. As such, the small shoulder of non-h-BN bonds are ascribed to primarily oxygen related bonds. Notably however, N−C bonds have been previously associated with peaks of electron binding energy ca. 399-400 eV,[119,127,146] i.e. within the same vicinity as N−B−O/N−N and N−O. Thus, it is not possible to be absolutely conclusive regarding the absence of N−C covalent bonds. Nevertheless, the absence of any apparent changes to the C1s spectra of the MWCNT subsequent to h-BN deposition, and the evident presence of oxygen in the h-BN layer, arguably

*Note that $Al_4B_2O_9$ impurities were detected in the MWCNT@BN, as discussed in §A.3. Consequently, this could potentially also contribute to the peaks associated to B−O type bonds in the high resolution B1s spectrum, although the much higher content of nanotubes is expected to contribute more dominant signals.

favours identification of the non h-BN peaks in the N1s spectrum as dominantly N−O related as opposed to N−C related.

In summary, albeit the occurrence of covalent interactions between the deposited h-BN and MWCNT (particularly N−C interactions) cannot be undeniably excluded, it is conclusive that the dominant interaction is van der Waals hybridisation between the shell h-BN and core MWCNT.

In section §2.3.2.2, this conclusion is scrutinised from a comparative perspective: are the MWCNT@BN synthesised in this work more represenative of true van der Waals heteronanotubes compared to MWCNT@BN synthesised by other methods in the literature?

2.3.2.2 A Comparative Study: MWCNT@BN synthesised by H_3BNH_3 vs. $B_2O_3 + NH_3$

Notable from an assessment of the research literature on the CVD synthesis of CNT@BN heteronanotubes is the variation in starting CNT material, as exemplified in Table 2.2. There has to date been no comparative study whereby the same CNT template is subjected to different precursor routes for h-BN deposition.

To better highlight the effects of each precursor pathway on the quality (structure, composition *etc.*) of the deposited h-BN and overall CNT@BN heteronanotube, it is necessary to maintain the CNT starting materials as a controlled variable when subjecting it to the different precursor routes. This eliminates the influence of the CNT sample purity or structure, for example, its crystallinity, which is known to influence the crystallinity of the resulting h-BN coating.

Of interest in the comparative study presented here, using MWCNT Nanocyl NC7000™ as the controlled variable, is whether the ammonia borane decomposition pathway for h-BN deposition on CNTs is indeed more favourable than the predominantly used $B_2O_3 + NH_3$ pathway for minimising the occurrence of covalent linking between the h-BN coating and the CNT core, i.e. preferential synthesis of van der Waals hybrids.

To draw this comparison, MWCNT@BN nanotubes were also synthesised according to the method reported by Chang *et al.,* (2015),[119] using $B_2O_3(s) + NH_3(g)$

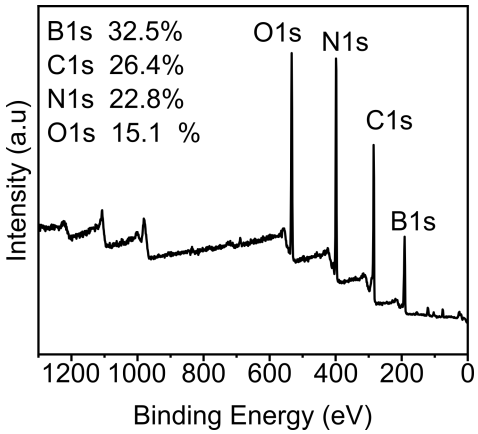


Figure 2.25: XPS survey spectrum of MWCNT@BN synthesised by the $B_2O_3 + NH_3$ CVD precursor pathway based on the method by Chang *et al.*,(2015).[119]

as detailed further in Appendix A. As evidenced by TEM images collected and as reported by Chang *et al*, this method also generates coaxial outer layers of h-BN on the CNT surface.

XPS analysis is used here to compare the MWCNT@BN sample purity and the repertoire of bond species as achieved by CVD using H_3BNH_3 vs. $B_2O_3 + NH_3$. The XPS survey scan of MWCNT@$BN_{(B_2O_3+NH_3)}$ (Figure 2.25) reveals the presence of boron (32.5 at.%), carbon (26.4 at.%),nitrogen (22.8 at.%) and oxygen(15.1 at.%). The ratio of B:N (1.4:1) is higher than as detected in the MWCNT@$BN_{(H_3BNH_3)}$ (1.3:1 ; See Figure 2.21). This suggests the existence of more non B−N boron bond species within the MWCNT@$BN_{(B_2O_3+NH_3)}$ sample, likely to be boron oxide as inferred from the simultaneously increased oxygen atomic composition. Inherently, the $B_2O_3 + NH_3$ pathway has a higher tendency to leave B_2O_3 impurity in the MWCNT@BN sample due to unreacted precursor. Steps to remove this residual solid B_2O_3, involving dissolution in boiling water, as implemented by Chang *et al.* and followed here (see Appendix A.2) are time-consuming and inefficient, an issue than can be avoided by using a single source gaseous precursor.

The high resolution XPS C1s spectrum of the MWCNT@$BN_{(B_2O_3+NH_3)}$ superposed on the starting Nanocyl MWCNT C1s spectrum is shown in Figure 2.26 , as similarly done in Figure 2.23 for MWCNT@$BN_{(H_3BNH_3)}$. A small difference is present in the electron binding energy ranges associated with C−B bonds as well as

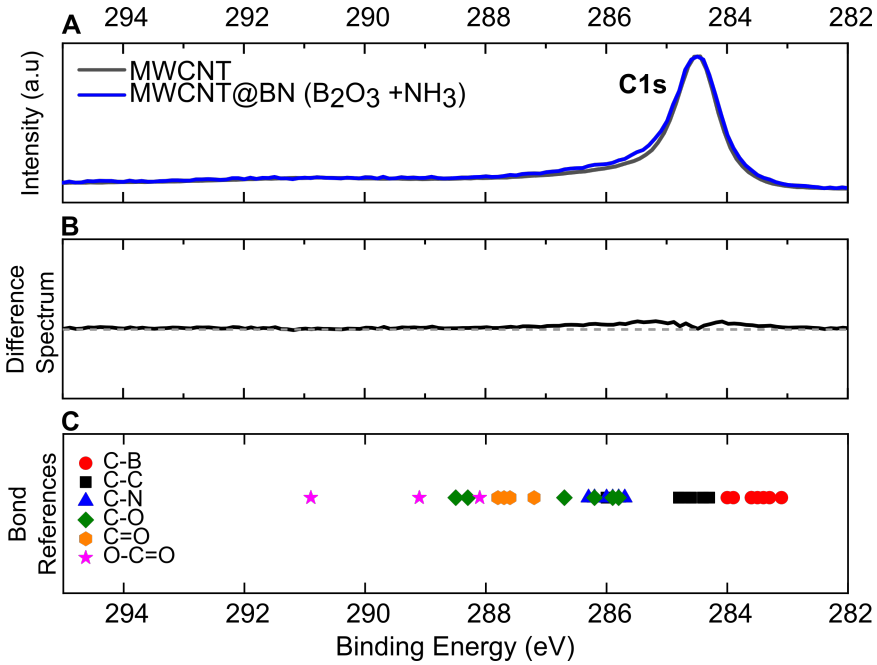


Figure 2.26: (A) Superposed High Resolution XPS C1s spectra of Nanocyl NC7000™ MWCNTs and MWCNTS after h-BN coating via CVD route with $B_2O_3 + NH_3$ precursors. (B) Calculated difference spectrum with peaks in the range of binding energies associated with C-B bonds and C-N and/or C-O bonds in the MWCNT@BN, according to (C) the collected literature references.[96,119,125–128,133,141,146,160,173,176] See Figure 2.23 for comparison.

in the overlapping C−N AND C−O region, which is unlike the null difference depicted in Figure 2.23.

Further direct comparison of MWCNT@BN$_{(H_3BNH_3)}$ and MWCNT@BN$_{(B_2O_3+NH_3)}$ was achieved by superposing their respective high resolution B1s and N1s XPS spectra, as depicted in Figure 2.27. More prominent shoulders at higher binding energies are visible in the B1s and N1s spectra of MWCNT@BN$_{(B_2O_3+NH_3)}$, associated with considerable presence of B−O bonds and N−C and/or N−O bonds.

At the lower binding energies, the B1s spectrum of MWCNT@BN$_{(B_2O_3+NH_3)}$ also exhibits a difference to the B1s spectrum of MWCNT@BN$_{(H_3BNH_3)}$, attributable to a contribution from B−C bonds in the former. Similarly, the N1s spectra of the two grades of MWCNT@BN show a detectable deviation from one another in the range of lower binding energies associated with the N-B bond. This suggests

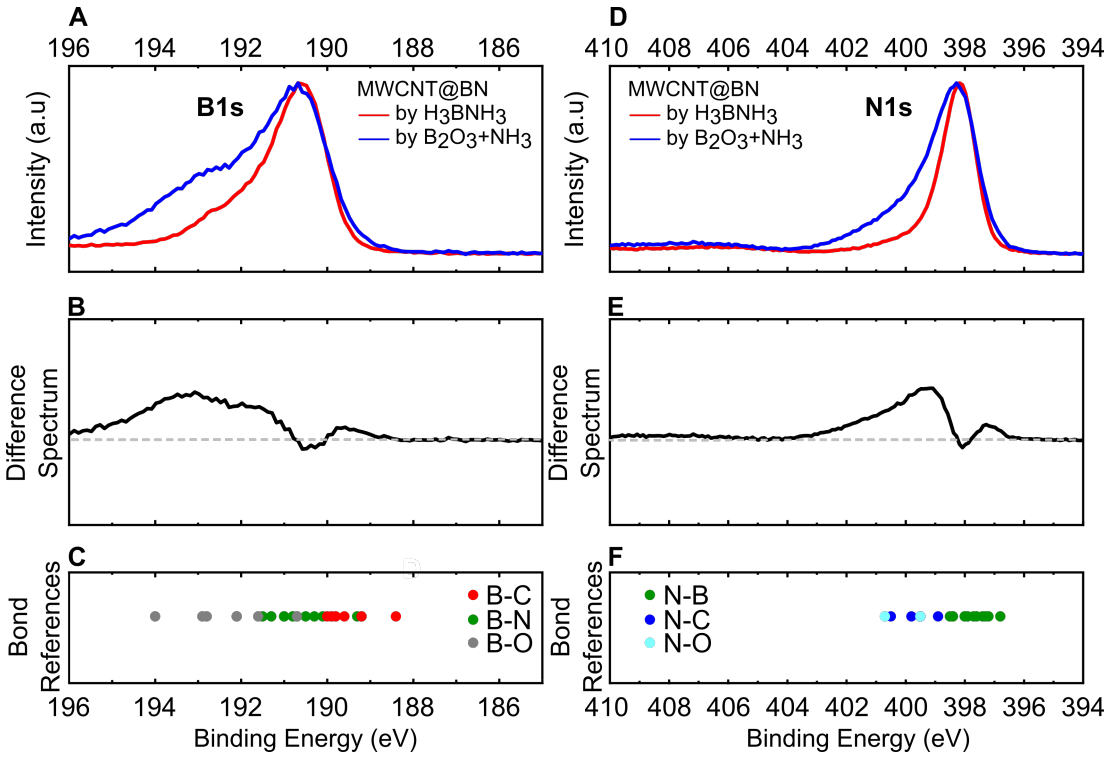


Figure 2.27: High resolution XPS B1s and N1s spectra of MWCNT@BN as synthesised by the H_3BNH_3 pathway vs. the $B_2o_3 + NH_3$ pathway. Dissimilarities exist between the spectra, most prominently at higher binding energies associated with B-O bonds and N-C and/or N-O bonds in the MWCNT@$BN_{(B_2O_3+NH_3)}$. Small peaks detected in the difference spectrum at higher binding energies suggest the occurrence of B-C and altered N-B bonds in the MWCNT@$BN_{(B_2O_3+NH_3)}$. Literature bond references are as cited.[96,119,120,127,128,146,160,173,174,180,181]

that some N-B bonds in the MWCNT@$BN_{(B_2O_3+NH_3)}$ have bonding environments altered by neighbouring covalent linking with carbon.

The above XPS analysis of bond speciation within MWCNT@BN as synthesised using H_3BNH_3 or $B_2O_3 + NH_3$ with the same Nanocyl NC7000 MWCNT templates demonstrates that the $HBNH_3$ single source CVD precursor pathway is more advantageous for achieving the following:

- High concentration of B-N bond purity within the deposited h-BN
- Low degree of covalent bonding between the h-BN and carbon, i.e. h-BN and carbon interact by van der Waals hybridisation.

The comparison evidence presented here corroborates earlier studies that suggested a link between the use of B_2O_3 and NH_3 precursors with the high

occurrence of boron oxide species as well as covalent bonds, B-C and N-C, between the h-BN coating and underlying CNT.[96,119,120,125,127] This duo of precursors, and variants of this pathway including H_3BO_3, that is dehydrated to B_2O_3 at elevated temperatures in the reactor,[121] and $CO(NH_2)_2$, which decomposes *in situ* to NH_3,[126] promotes covalent bond formation due to its associated mechanism of h-BN growth.

The reaction of B_2O_3 and NH_3, the so called 'amide route' (reaction R 2.1) is thermodynamically less favourable than reaction R 2.2, the carbothermic reduction of B_2O_3.[121,182] h-BN formation occurs preferentially with the involvement of C from the CNT itself, which acts a B_2O_3 reducing agent (reaction R 2.2).

$$B_2O_3 + 2\,NH_3 \longrightarrow 2\,BN + 3\,H_2O \qquad \text{(R 2.1)}$$

$$B_2O_3 + 3\,C + 2\,NH_3 \longrightarrow 2\,BN + 3\,CO + 3\,H_2 \qquad \text{(R 2.2)}$$

$$B_2O_3 + 2\,C + 2\,NH_3 \longrightarrow 2\,[BN{-}C] + 3\,H_2O \qquad \text{(R 2.3)}$$

A consequence of reaction R 2.3 is the 'etching' of the underlying CNT, whereby the CNT structure is altered by the removal of C atoms.[119,140] These C atoms are removed as a gaseous oxide or are incorporated into the growing h-BN layers, as in reaction R 2.3. Reaction R 2.3 is often referenced as a means of substituting C with h-BN to form ternary $B_xC_yN_z$ hybrid nanotubes.[181,183,184]

2.3.2.3 Oxygen Impurities in MWCNT@BN

As observed from the XPS measurements detailed above , there is a non-negligible quantity of oxygen detected in the MWCNT@BN heteronanotubes that is increased relative to the MWCNTs. Specifically, according to the XPS survey scans, the oxygen content increases from 1.6 at.% in MWCNTs to 6.1 at.% in MWCNT@BN. This higher oxygen content in the MWCNT@BN is corroborated by EELS analysis, as detailed in §2.3.1.2, whereby measured oxygen at.% of MWCNT@BN, taken from spectral images, is within a similar range of 5-7 at.%. Given that there is no

intentional introduction of oxygen during the CVD process of coating h-BN onto the MWCNTs, the introduced oxygen must originate from a contaminant source.

The following discussion on oxygen contamination is subdivided into three sections:

- The identity of the oxygen source and the time at which the MWCNT@BN nanotubes are exposed to it are considered in §2.3.2.3.1.
- The potential routes to incorporation of oxygen into the MWCNT@BN structure are considered in §2.3.2.3.2.
- The evidence of oxgyen incorporation in the MWCNT@BN structure is reviewed in §2.3.2.3.3 in view of the hypotheses outlined in the two preceding sections.

2.3.2.3.1 On the Source of Oxygen Impurities In the lifetime of a MWCNT@BN heteronanotube as synthesised here, it is hypothesised here that there are two different stages at which an oxygen-containing contaminant could be introduced: (i) in the quartz tube reactor during CVD and post-CVD cooling, and/or (ii) out of the quartz tube reactor, i.e. during sample storage.

According to the first of these theories, an oxygen-containing contaminant is present in the quartz tube reactor, despite the measures taken to decrease this probability. Particularly, Ar/H_2 was streamed through the CVD system (including the quartz tube reactor and precursor reservoir vessel) prior to the initiation of the CVD process to purge all atmospheric gases.[†] Furthermore, materials used during CVD, including the MWCNT powder and inert h-BN powder used as filler in the precursor reservoir were stored in a dessicator prior to use to reduce their content of adsorbed atmospheric oxygen and moisture. [‡] Although these deliberate steps

[†]The conducted purging regime accounted for the calculated volume ($V_{reactor}$) of the quartz tube reactor and the time required (T) to replace this volume when flowing Ar/H_2 at 400 sccm. When $V_{reactor}$ = 1189 cm^3 (see quartz tube dimensions in §2.2.1.2), T= 2.97 mins. Therefore, a purge time of 25 minutes is more than eight-fold times the minimal required purge time.

[‡]The ammonia borane precursor itself was stored in a tightly sealed container, but was not stored in the dessicator as a precaution against sublimation caused by the warmth generated within the dessicator's vacuum chamber.

were taken to reduce the probability of atmospheric gas presence within the reactor during CVD, a 0% probability was not indisputably guaranteed. Considering that the implemented Atmospheric Pressure CVD (APCVD) system is always open to air in intermission periods between uses, and that there is no complex vacuum pumping regime prior to use, it is likely, even described as inevitable,[185] that residual atmospheric gases are present in the system after purging. This is a compromise made for the time and cost-saving simplicity of the APCVD system. Hence, oxygen-containing atmospheric gases, e.g. residual O_2 and/or H_2O, could be present within the CVD reactor during use.

Alternatively, and perhaps in addition to oxygen contamination within the reactor described above, oxygen impurities could be introduced to the MWCNT@BNs during sample exposure to ambient atmosphere when stored.

The potential routes for oxygen, from a source either within or outside the reactor, to become incorporated into MWCNT@BN sample are explored below.

2.3.2.3.2 Incorporation of Oxygen into MWCNT@BN (I): Theory

Whilst the potential instances of when MWCNT@BN could be exposed to oxygen contaminants have be defined above, exposure alone does not explain how oxygen could become incorporated into a MWCNT@BN heteronanotube.

Within the reactor atmosphere during CVD, oxygen-containing residual gases could act as oxidising agents, henceforth referred to as oxidising impurities.[185,186] At a sufficiently high reactor temperature, these oxidising impurities could oxidise the MWCNT templates or h-BN being deposited onto the MWCNT surface. In this case, the reactor temperature of 1000°C is above the oxidation onset temperature of both the graphitic carbon in MWCNTs (400-700°C)[19] and h-BN (800-900°C).[16–18] However, given that MWCNTs are less resistant against oxidation in comparison to h-BN (for reasons outlined in Chapter 3, §3.3.1), it is anticipated that oxidising impurities in the CVD reactor would result in a higher rate of oxidation of the MWCNT components relative to that of the h-BN components. A high rate of MWCNT oxidation could also compete against the rate of h-BN deposition onto

the surface of the MWCNTs, such that exposed MWCNT surface becomes oxidised prior to being coated by h-BN. In such a scenario, the MWCNT surface becomes oxidised (functionalised with C-O type covalent bonds) and the oxygen consequently exists at the interface between the MWCNT outer surface and h-BN coating. It is possible that h-BN could itself form covalent bonds to the interfacial oxygen at defect sites. Otherwise, oxidising impurities could also functionalise the outer surface of the h-BN coating with covalently bonded O, either after the h-BN has been deposited or via oxidation of B,N-containing vapour precursor molecules that later become incorporated into the deposited h-BN lattice.

However, just as preventative measures were implemented to minimise the occurrence of oxidising impurities within the reactor, measures in the CVD method were also in place to counteract the effects of oxidising impurities. Specifically, 2.5% H_2 was present to the carrier gas alongside inert Ar. Typically, H_2 is a constituent of carrier gas used during CVD of graphene or h-BN onto metal substrates (e.g. copper or nickel) to reduce oxides on the substrate surface.[113,115,187] According to Reckinger *et al.*, (2013), H_2 also has the supplementary role of reducing oxidising impurities within an APCVD system, such that the potential for these impurities to 'oxidatively etch' vulnerable materials in the system is minimised. In their study, deposited graphene exhibited the least oxidative etching when exposed to H_2 during both the deposition and cooling stages of CVD.[185] In this work, H_2 is similarly expected to limit the effects of oxidising impurities on the MWCNT@BN. The fate of an oxidising impurity, e.g. O_2, instead of being oxidation of the MWCNT@BNs, is likely to be reduction by H_2 to form H_2O that is subsequently evacuated by the continually replenished Ar/H_2 carrier gas. Therefore, the addition of H_2 is a counteractive measure that should result in interception of potential oxidising impurities from oxidising MWCNT@BNs. Nevertheless it is still possible that some oxidising impurities persist, as no conclusions can be drawn here on the reduction efficiency of the 2.5 vol% H_2 flow at 400 sccm, otherwise selected for being non-flammable and consequentially beneficial to safety of operation.[113]

Alternatively, according to the second hypothesis described above, oxygen contamination occurs during exposure of the MWCNT@BN to ambient atmosphere during storage. Given that room ambient temperature is significantly below the oxidation onset temperature of MWCNT and h-BN, the route to oxygen incorporation into the MWCNT@BN at ambient conditions would not be the same as within the CVD reactor, i.e. high temperature oxidative etching by oxidising impurities.

In support of this theory, it is established in the literature that exposure of h-BN to ambient atmosphere results in the appearance of oxygen-containing impurities over time.[188–194] Specifically, this phenomenon has been attributed to the hydrolytic attack of h-BN by ambient moisture, with evidence showing that h-BN hydrolytic stability has a direct relationship with h-BN crystallinity. As the crystallinity of h-BN decreases, synonymous with increasing d_{002} interlayer spacing and the density of defects, moisture sensitivity also increases.[188,195] Accordingly, it has been postulated that that ambient H_2O, initially physisorbed onto the h-BN, subsequently interacts with h-BN primarily at reactive defect sites such as dangling bonds to covalently incorporate oxygen, e.g. by bonded hydroxyl groups.[193,194]

As detailed in §2.3.1.5, the h-BN deposited here does not match theoretically ideal crystallinity. Thus, in the context of h-BN moisture sensitivity being determined by its crystallinity, the h-BN deposited in this work could be unstable under ambient conditions and susceptible to reaction with H_2O.

2.3.2.3.3 Incorporation of Oxygen into MWCNT@BN (II): Evidence

The two potential routes to incorporation of oxygen into the MWCNT@BN structure proposed above are likely to result in different distributions of oxygen in the nanotube wall. During CVD, oxidising impurities could become integrated (i) into the MWCNT surface layers and thereby also be present at the interface between the MWCNT and h-BN coating, and/or (ii) throughout the h-BN layers, i.e. distributed homogeneously in the h-BN coating. On the other hand, exposure of the MWCNT@BN to ambient moisture during storage is likely to result in

high oxygen concentration at the surface of the h-BN layers, i.e. oxygen will be distributed in a gradient. Therefore, interpretation of oxygen distribution from the data acquired on MWCNT@BN composition may allow identification of the source of oxygen contamination.

Looking at the EELS spectral images and line scans of the MWCNT@BN in §2.3.1.2 (e.g. Figures 2.9, 2.10 & 2.11) oxygen appears to be co-located with B and N in the h-BN coating layers. However, it is difficult to ascertain from the achieved EELS spatial resolution whether this oxygen (at low concentration relative to B,C and N) is distributed homogeneously or in a gradient across the h-BN layers, and whether or not it is also present at the interface between the MWCNT core and h-BN coating.

XPS analysis provides further insight into oxygen distribution. Particularly, no significant change was noticed in the C1s spectrum of MWCNT@BN relative to that of the MWCNT. If oxidising impurities had primarily etched the MWCNT core, this would be detected in the C1s spectrum as a broadening of the C1s peak to higher binding energies (e.g. C-O, C=O or O-C=O contributions at 286-288 eV). That this was not the case suggests that the majority of introduced oxygen contaminant is not bonded to the MWCNT component. Instead, high resolution XPS spectra of the h-BN components, particularly the B1s spectrum shows conspicuous broadening to the higher binding energies associated with the formation of B-O covalent bonds. This result points to the distribution of oxygen primarily within the h-BN coating.

Furthermore, Raman spectra of both the annealed MWCNT and MWCNT@BN samples showed decreases in their I_D/I_G ratio relative to that of the pristine MWCNT. If oxidation of the MWCNT components had occurred within the CVD reactor, the I_D/I_G ratios would instead be expected to increase relative to that of the pristine MWCNTs as a result of an increase in defect density arising from the oxidation. The Raman results corroborate the XPS results in the finding that the oxygen contaminant is not bonded to the MWCNT component of MWCNT@BNs, thereby leaving the h-BN component as the primary site of oxygen distribution.

It is inferred from these results that the introduction of oxygen contaminant is less likely to have occurred within the CVD reactor, but instead mainly during ambient storage of the MWCNT@BN. This is because the hypothesis on moisture sensitivity of the h-BN component more suitably explains the detection of oxygen principally within the h-BN coating layers and not also within the MWCNT component. Nevertheless, additional analysis, e.g. higher spatial resolution EELS, is essential for making conclusions on the homogeneity of oxygen distribution within the h-BN and its potential presence at the MWCNT/h-BN interface.

It is proposed that future experiments could be carried out to better identify the source of oxygen contamination. For example, MWCNT@BN samples could be transferred to a controlled, low moisture environment, e.g vacuum storage, immediately after synthesis. Hypothetically, by reducing exposure to ambient moisture, any detected oxygen contamination in the MWCNT@BN could then be attributed with more confidence to oxidising impurities within the CVD reactor. Additionally, experiments could also be conducted with the MWCNT@BN duration of ambient atmosphere exposure as the independent variable, such that the susceptibility of h-BN to ambient moisture destabalisation over time is investigated. Similarly, controlled MWCNT@BN storage atmospheres with varied relative humidity might also assist in determining the moisture sensitivity of the h-BN component.

2.3.3 h-BN Deposition Selectivity

Of interest is whether the ammonia borane APCVD parameters used in this work are selective for h-BN deposition onto the MWCNT surface, and selective against the synthesis of by-products, particularly other h-BN nanostructures including nanospheres or nanosheets *etc.*

Whilst most studies on ammonia borane pyrolysis have demonstrated synthesis of h-BN as thin films, few studies have also reported generation of nanospheres by a self-catalysed growth mechanism.[196,197]

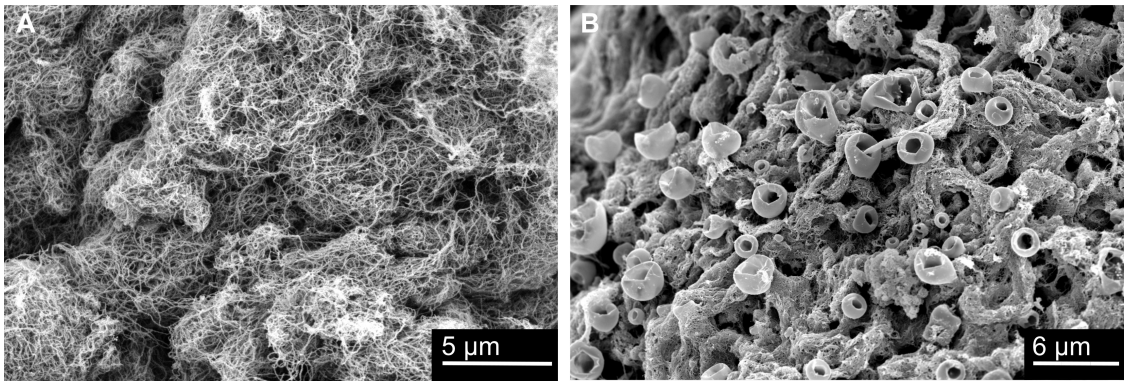


Figure 2.28: SEM images show the absence of non-nanotube structures observed in (A) MWCNT@BN$_{(H_3BNH_3)}$, whilst hollow microspheres are observed in (B) MWCNT@BN$_{(B_2O_3+NH_3)}$.

No such impurities were observed in the MWCNT@BN samples synthesised here, suggesting that the method and reaction parameters implemented are highly selective to the deposition of h-BN onto the MWCNTs.

Interestingly, the MWCNT@BN as synthesised by the $B_2O_3 + NH_3$ pathway (described in Appendix A.2 and §2.3.2.2) showed a high frequency of hollow spherical microstructures (Figure 2.28B) which were not reported in the prior work from which the synthesis method was adopted.[119] See Appendix A.2 for further characterisation of the microspheres by EDX which suggests their BN-inclusive composition. The potential sphere growth mechanisms from boron oxides and ammonia CVD are considered elsewhere.[198,199]

With regard to the effect of ammonia borane on impurities already intrinsic to the MWCNT sample, i.e. the Nanocyl NC7000™ grade, it was discovered that Al_2O_3 catalyst supports changed into $Al_4B_2O_9$. This is outlined in Appendix A.3.

2.4 Conclusion

In this chapter, an APCVD method coupled with the single source precursor ammonia borane has been demonstrated for the selective deposition of coaxial layers of h-BN onto the surface of MWCNTs.

The resultant core-shell MWCNT@BN structure is corroborated by electron microscopy characterisation, including SEM, TEM, and EELS. Specifically, the

nanotubular morphology of MWCNT@BNs is confirmed by SEM. An increased outer diameter of the MWCNT@BNs relative to the pristine MWCNT, as measured from TEM images, reveals the introduction of an outer coating with a thickness of 2-3 nm. The observed lamellar nature of these outer layers of the MWCNT@BNs confirms their h-BN polymorph structure, further evidenced by the collected EELS high-loss spectra, which depict B-K and N-K edges with fine features associated with h-BN. Additionally, EELS spectral maps and line scans clearly depict the superposition of B and N in an outer shell encapsulating a core MWCNT.

Other spectroscopic techniques, including Raman and XPS, provide further evidence in support of the core-shell structure of the synthesised MWCNT@BNs. For instance, in an alternative scenario in which B and N had become primarily covalently incorporated into the graphitic lattice of the MWCNT, an increase in defect density would be detected in the Raman spectra of the MWCNT@BN as an increase in the I_D/I_G ratio relative to that of the pristine MWCNTs. However, I_D/I_G of MWCNT@BN Raman spectra do no exhibit such an increase, thereby substantiating that this synthesis technique favours h-BN deposition as a shell around the MWCNT core, the latter which maintains it graphitic lattice structural integrity. Similarly, turning to XPS, high resolution C1, B1s and N1s XPS spectra of the MWCNT@BNs reinforce that the MCNT and h-BN components are ordered in core-shell layers interacting by van der Waals forces. Particularly, the MWCNT@BN C1s spectrum does not deviate from that of the pristine MWCNT, suggesting that the core graphitic lattice remains largely intact and without appreciable covalent bonding with B/N, as corroborated by corresponding B1s and N1s spectra which reveal that B and N are predominantly bonded in an h-BN lattice.

In addition to confirming the core-shell structure of the MWCNT@BN, EELs and XPS were also implemented to interrogate the purity of the heteronanotubes. Specifically, quantitative analysis of XPS survey spectra and EELs spectral images reveal consistent results regarding the B:N stoichiometric ratio (1.3:1 $_{[XPS]}$ & 1.1:1 $_{[EELS]}$) and oxygen content (6.1 at.%$_{[XPS]}$ & 5.9 at.%$_{[EELS]}$) of MWCNT@BN. These slight differences can be reasonably accounted for by errors in measurement/analysis,

e.g. 10% accuracy of XPS atomic concentrations[200] and 5-10% systematic error associated with computation of EELs K-edge cross sections.[201] The obtained B:N ratios almost align with the ideal 1:1 stoichiometry of h-BN, albeit with a small bias to B. These B:N ratios, in the context of the non-negligible oxygen content and alongside evidence of B-O covalent bond contributions in the B1s XPS spectrum, indicate the covalent incorporation of contaminant oxygen into the h-BN lattice likely at N vacancy sites. The possibility that this oxygen is present as a free oxide is not supported by XRD analysis of the MWCNT@BN. It is hypothesised here that the deposited h-BN is moisture sensitive and thereby exposure of the MWCNT@BN to ambient moisture, instead of oxidation by residual oxidising impurities within the CVD reactor, is the more likely source of oxygen contamination. However, future experiments are proposed to investigate this further.

Turning to crystallinity of the MWCNT@BN product, characterisation by Raman, XRD and TEM concludes the imperfect crystallinity of both the MWCNT core and the deposited h-BN. From TEM analysis of the pristine MWCNTs and the MWCNT@BN, it is possible to make the qualitative assessment that the walls of the Nanocyl NC7000 MWCNTs have a turbostratic ordering that limits the consequent ordering of the deposited h-BN. Quantitative descriptors of crystallinity were also considered, particularly crystallite size (L_c, L_c) and interlayer spacing d_{002}. Although the d_{002} interlayer spacing of the turbostratic MWCNT and h-BN layers is estimated via XRD (0.35 nm) and TEM (0.36 nm) to be greater than that of ideal graphite or h-BN, it must be acknowledged that their turbostratic nature lends to a degree of invalidity of the absolute values of this metric as a quantifier of crystallinity. The same can be said for L_c crystallite size. However, L_a (in plane) crystallite size is considered the most valid for quantifying crystallinity of nanotube walls.[164] Here, analysis of Raman spectra and XRD patterns help in assessing changes in crystallinity of the as-obtained MWCNT and the MWCNT after 1000°C treatment in the CVD reactor, specifically highlighting the trend of increasing L_a size in the latter. This observed trend has important implications for the interpretation of MWCNT@BN oxidative stability in the literature and in the Chapter 3 discussion.

Specifically, the improving crystallinity of the MWCNT core during high temperature CVD is rarely considered when explaining the difference in oxidative stability between the MWCNT@BN product and the original MWCNT. Whilst Raman and XRD based calculations of L_a follow the same trends, the absolute values of L_a differ, e.g. 13.4 nm (MWCNT) $\rightarrow$ 14.2 nm (annealed MWCNT) according to Raman, and 5.1 nm (MWCNT) $\rightarrow$ 5.8 nm (annealed MWCNT) according to XRD. One potential justification of this discrepancy is the sensitivity of the MWCNT XRD pattern's peak widths to factors other than crystallite size, e.g. the number of graphitic layers, the nanotube orientations and lattice distortions.[164,202] Such factors that lead to broadening of the (100) peak could therefore result in underestimation of L_a crystallite size.

Finally, the new synthesis method and MWCNT@BN product presented in this chapter are not discussed in isolation, but also from a comparative perspective in relation to pre-existing methods for synthesis of MWCNT@BN heteronanotubes. For example, after calculating and compiling the rates of h-BN deposition achieved in the literature, it is apparent that the 1 nm/hr rate achieved here closely matches the rate achieved when using single source precursors under LPCVD or autoclave conditions. Therefore, the efficiency of coating in this accessible and safe APCVD method is on par with that of more complex LPCVD or autoclave systems. Also, to the best of our knowledge, this work is the first to report the encapsulation of the tip of a CNT by CVD deposited h-BN. Beside comparisons made to the literature, experimental repeat of the prominent amide route ($B_2O_3 + NH_3$) for h-BN deposition on MWCNT was conducted. With the MWCNT source as a controlled variable, it was possible to make a reliable comparison for the first time between the MWCNT@BN synthesised by the amide route and those synthesised here, using ammonia borane under APCVD. This empirical comparison demonstrates significant advantages of the ammonia borane route, which are (i) a higher purity, i.e less oxygen contamination (6.1 at.% O in MWCNT@$BN_{(H_3BNH_3)}$ vs. 15.1 at.% O in MWCNT@$BN_{(B_2O_3{}^{+}NH_3)}$, (ii) less risk of etching the underlying MWCNT to form B-C or N-C covalent bonds and (iii) high selectivity to deposition of h-BN onto

the MWCNT walls, without formation of other h-BN by-product nanostructures such as nanospheres or nanosheets.

Chapter 3

Boron Nitride Nanotubes via Sacrificial Templating of Carbon Nanotubes

Contents

3.1 Introduction 80
3.2 Synthesising BNNTs by oxidation of CNT template . 86
3.2.1 Materials and Methods 86
3.3 Results and Discussion 89
3.3.1 Thermal Oxidation of MWCNT template 89
3.3.2 BNNT Structure 97
3.3.3 BNNT Composition 112
3.4 Conclusion 120

3.1 Introduction

In this chapter, BNNT synthesis is explored by way of sacrificial templating of the MWCNT@BN heteronanotubes described in Chapter 2.

This work is an original study that is subsumed under the sparsely investigated BNNT synthesis category involving ammonia borane as the h-BN precursor. Within this category, the method presented here belongs to the template assisted synthesis subcategory, which is an alternative to catalyst assisted techniques. The as described categorisation is depicted in Figure 3.1. In Table 3.1, prior studies implementing

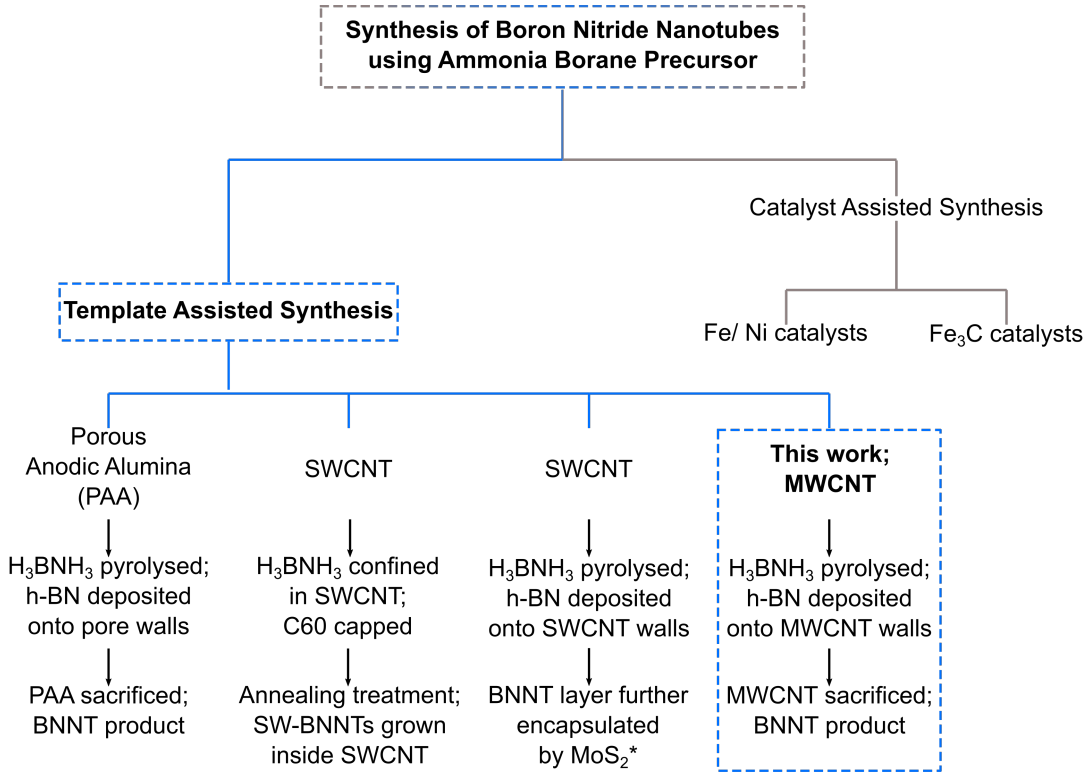


Figure 3.1: A hierarchical tree diagram of the methods implemented thus far to synthesise BNNTs using ammonia borane as the h-BN precursor.[90,131,203–205] See also Table 3.1. [*Note: Only preliminary evidence has been provided of sacrificing of SWCNT core templates to leave pure BNNT product.[131]]

ammonia borane for BNNT synthesis (both catalyst and templated assisted) are summarised to primarily highlight the BNNT characteristics thus far achieved and their corresponding synthesis parameters.

Noticeably, based on the catalyst assisted studies summarised in Table 3.1,[203,204] and even more generally for such studies involving alternative h-BN precursors,[77,78,206,207] BNNTs synthesised via this route tend to have large diameters, broad diameter distributions and heterogeneous nanotube morphologies (e.g. both cylindrical and bamboo nanotubes). These outcomes are directly associated to the behaviour of the implemented nanoparticle catalysts, usually transition metal based, in the high temperature BNNT growth environments. Nanotubes are theorised to grow from nanoparticle catalysts according to the VLS mechanism, whereby precursor vapours become dissolved into the liquid nanoparticles. The eventual supersaturation of these nanoparticles with precursor vapours eventually

	BNNT Characteristics			Synthesis parameters				Refs.
Starting catalyst OR template material	**Morphology**	**Diameter (nm)**	**Length (um)**	**H_3BNH_3 heating temperature(°C)**	**BNNT growth temperature(°C)**	**Growth Atmosphere**	**Synthesis times**	
				Catalyst Assisted Methods				
Fe/Ni nanoparticles	MWBNNTs; Cylindrical	most 100-300; few 3-30	<1	300	1050	N_2	1 hour	[203]
Ferrocene; Fe_3C	MWBNNTs; Cylindrical and Bamboo	Cylinders: 100 Bamboo: 100-500	Cylinders: 100s Bamboo: 10s	same as BNNT	900-1600; highest yield at 1450	N_2; lower yield in Ar	1 hour	[204]
				Template Assisted Methods				
Porous Anodic Aluminum (PAA)	MWBNNTs; Cylindrical; BNNT vertical arrays after PAA removed	200-300 & 70-80	<60	250	550 followed by two cycle heat program: 1300 and (1400-1700)	N_2 or NH_3	>24 hours	[205]
SWCNTs	SWBNNTs; Cylindrical; encapsulated in SWCNT	0.7±0.1	-	550	1400	vacuum	6 days	[90]
SWCNTs	single-few wall BNNTs around SWCNTs; Cylindrical; also encapsulated in MoS_2	< 2	up to 2	70-90	1000-1100	Ar/3% H_2	30 mins-6 hours	[131]

Table 3.1: Summary of the few studies that have used ammonia borane, in conjunction with either catalysts or templates, to grow BNNTs. The implemented synthesis parameters and achieved BNNT characteristic are included here.

results in the precipitation of filamentous nanotubes.[83–85] Whilst melting of the nanoparticles into the prerequisite liquid state is more easily attained because of nano-size dependent melting point depression,[208–211] their increased mobility in this state favours their agglomeration into larger sized particles, i.e. by sintering. This coarsening in catalyst size, by mechanisms such as particle migration and coalescence or Ostwald ripening, is thermally activated, and as such is sometimes referred to as thermo-agglomeration.[212,213] For BNNT growth systems, where the temperatures are usually higher than for CNT growth systems, one reason being the higher precursor decomposition temperatures, the involved catalysts experience greater mobility, inevitably making the phenomenon of sintering more predominant.[87] Given that catalyst-grown nanotubes have diameters correlated to their nanoparticle catalyst size, larger nanoparticles predictably cause the precipitation of larger diameter nanotubes.[206] Furthermore, non-uniform catalyst sintering and the phenomenon of catalyst reshaping during nanotube growth are responsible for the occurrence of broad BNNT diameter distributions and bamboo morpholophy nanotubes respectively.[204,206,214] As such, catalyst size and shape control are still challenges that warrant addressing in order to achieve BNNT diameter and morphology fine tunability via this synthesis route.

Alternatively, a catalyst free route for BNNT synthesis could be adopted. In fact, via the ammonia borane precursor pathway, there have been very few studies, as outlined in Figure 3.1 and Table 3.1, that have investigated catalyst free BNNT synthesis. More specifically, these studies have made use of templates to guide h-BN growth into a BNNT form. For example, Wang *et al.*, (2008), demonstrated that porous anodic alumina (PAA), which has cylindrical, vertically aligned pores, can be used as a template for synthesis of vertically aligned arrays of BNNTs.[205] Pyrolysed ammonia borane vapours were deposited as amorphous h-BN onto the walls of the PAA pores, and subsequent to additional steps involving heating up to 1700 °C in NH_3, the PAA template was itself dissolved in a NaOH etching solution. Whilst there is potential to tune BNNT outer diameters using PAA of varying pore size (e.g. 200-300 nm commercial PAA and 70-80 nm 'homemade' PAA in the study),

the PAA material itself has no advantageous effect on the crystallinity of the BNNT, and very high temperature input was necessary to improve the as-synthesised BNNT crystallinity. Instead, a template material with a structural affinity to h-BN would promote crystalline BNNT formation. As introduced in Chapter 1 and 2, graphitic CNTs are structurally analogous to BNNTs, and so are highly suitable templates for BNNT growth. In this context, Nakanishi *et al.*, (2013) leveraged SWCNTs as both nano-reaction vessels and as nano-templates, whereby ammonia borane molecules were encapsulated inside the SWCNTs and subsequently thermally converted at 1400 °C into SWBNNTs.[90] Although the resulting SWBNNTs exhibited especially narrow diameter distributions (0.7±0.1 nm) because of the constrictive diameter of the SWCNTs, this method has inherent limitations to the range of achievable BNNT diameters and number of walls. Additionally, the requirement for a capping agent, e.g. C_{60} molecules, to trap the ammonia borane molecules inside the SWCNT, entails increased material and time expenditure. Ensuing attempts to remove the SWCNT template, by thermal oxidation at 700 °C, indeed resulted in their removal, but also lead to the collapse of the internal SWBNNT structures. As such, this templating method proved successful for the fabrication of heteronanotubes of SWBNNTs encapsulated inside SWCNTs, but has yet to be proven feasible as a sacrificial templating method for BNNT synthesis.

In the work presented here, MWCNTs were used as the template of choice, and an accessible APCVD process involving ammonia borane was implemented to deposit coaxial h-BN on the MWCNT outer walls, as fully detailed previously in Chapter 2. In this present Chapter, the synthesised MWCNT@BN heteronanotubes are subjected to thermal oxidation treatment that relies on a differential in oxidation resistance to sacrifice the MWCNT core templates while leaving BNNT shells (Figure 3.2). Only very recently, Xiang *et al.,* (2020) also demonstrated synthesis of coaxial shells of h-BN on CNTs, but specifically on SWCNT and via a low pressure CVD ammonia borane precursor route.[131] Notably, that study was also supplemented by a cursory description of sacrificial templating of SWCNTs to make single to few-wall BNNTs. Instead, it is proposed here that MWCNTs are

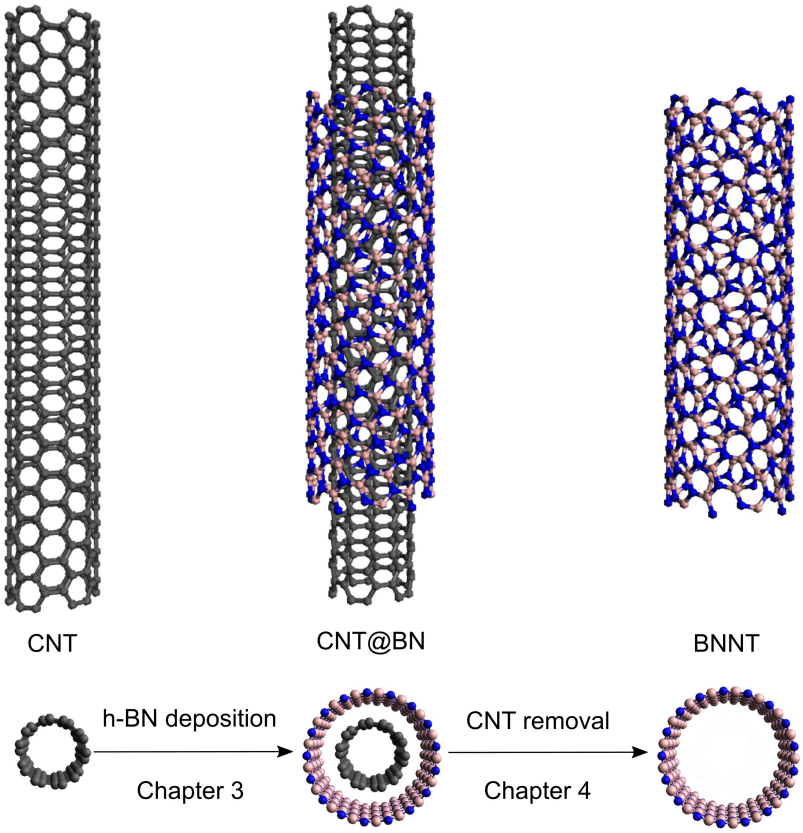


Figure 3.2: Schematic of progression in nanotube composition, from CNT to CNT@BN and finally to BNNT, realised in this work. Single-wall CNT and BNNT are shown for simplicity.

more versatile templates than SWCNTs for the fabrication of BNNTs with a wider range of potential diameters and morphologies.

As such, presented here is the first detailed investigation of BNNTs synthesised using MWCNTs as sacrificial templates in conjunction with APCVD and ammonia borane precursor as the single-source of h-BN. To the best of our knowledge, this study is also the first to explore BNNT diameter control by utilising MWCNTs templates of varied diameter. Alongside BNNT quality assessment, new insights are also gained on the thermal oxidation behaviour of the MWCNTs when composited in MWCNT@BN heteronanotubes, which contributes to a better understanding of the sacrificial templating process.

3.2 Synthesising BNNTs by oxidation of CNT template

3.2.1 Materials and Methods

Name	Purity	Supplier
Reactants		
Solids		
MWCNT@BN	-	As synthesised in Chapter 2
Ammonia Borane Complex	97%	Sigma-Aldrich
h-BN powder grade 015	>98.5%	3M
Liquids		
Ethylbenzene	99.5%	Sigma-Aldrich
Ferrocene	98%	Sigma-Aldrich
Gases		
Argon	99.998%	Air Products
Air	-	Standard Room
Solvents		
Acetone		Sigma Aldrich
Isopropanol		Sigma Aldrich
Methanol		Sigma Aldrich

Table 3.2: Summary of reactants implemented in this chapter and solvents used for cleaning of substrates, sample holders *etc.*

3.2.1.1 Oxidation treatment of MWCNT@BN

MWCNT@BN heteronanotubes samples produced according to the method detailed in Chapter 2 were subjected to a heat treatment at 700 °C in air flow (1.8 L/min from an air pump) to oxidise the carbon nanotube templates. All equipment previously described in Chapter 2 were retained for this process. The pre-heated furnace was wheeled over to the location of the supported powder samples along the quartz tube. After 1 hour, the remaining white powder samples were allowed to cool and then collected into a glass vial.

3.2.1.2 Synthesis of Larger Diameter MWCNTs

To explore diameter control of BNNTs by the sacrificial templating method, MWCNT templates of different diameter compared to the Nanocyl NC7000™(ca. 9.5 nm) were required. These larger diameter MWCNTs were synthesised in house according to an aerosol-assisted CVD (AACVD) technique developed in our lab group by Meysami *et al.*[215–217]

An ethylbenzene with a 5 wt.% ferrocene solution was used as the carbon and catalyst source respectively. These precursors were simultaneously introduced into the reactor by an piezo-based aerosol generator. At 800 °C and under 1000 sccm Ar flow, vertically aligned MWCNT carpets were deposited on the quartz reactor tube wall. After a reaction time of 30 mins, the furnace was left to cool, and the MWCNT material was carefully scraped of the quartz walls and collected into a glass vial. The specific experimental conditions used here are expected to produce MWCNTs with an average outer diameter of 45.1±24.1 nm.[216]

3.2.1.2.1 Coating AACVD MWCNT with h-BN and Oxidation treatment AACVD MWCNTs were ground with a mortar and pestle to separate MWCNT bundles from the the densely packed vertically aligned carpets. This powder was then treated to the coating process described in Chapter 2 to coat the MWCNTs with coaxial h-BN layers. The as-synthesised MWCNT@BN heteronanotubes* were then subjected to thermal oxidation, as described in §3.2.1.1 to sacrifice the MWCNT templates while leaving BNNT shells.

3.2.1.3 Sample Preparation & Characterisation

Synthesised nanotube samples were characterised by SEM, TEM, STEM, EELS, XPS and XRD according to the setups already described in Chapter 2, §2.2.1.3. Note that EELS quantitative analysis parameters are given in Appendix B, §B.1.

*Note that when MWCNT or MWCNT@BN are discussed in the results sections of this thesis, it refers to nanotubes involving Nanocyl NC7000™. If the AACVD produced MWCNTs are involved, this will be clearly stated as AACVD MWCNTs or AACVD MWCNT@BN.

For Raman spectroscopy, both the 532 nm green laser and 632.8 He-Ne laser were used (separately) as irradiation sources.

Thermo-gravimetric analysis (TGA) was also conducted on as prepared powdered samples using a Perkin Elmer Pyris TGA at a heating rate of 20 °C/min, under air flow of 80 mL/min; the scanned temperature range was 50-900 °C.

As synthesised samples were also characterised by Fourier Transform Infrared Spectroscopy (FTIR) using the Varian Excalibur FTS 3500 FT-IR Spectrometer. Transmission spectra were collected in the range of 500- 4000 cm^{-1}.

For UV-Visible (UV-Vis) Spectroscopy, nanotubes were added to ethanol (to form ca. 0.025 mg/mL solutions) and briefly sonicated (<5 minutes) prior to transfer of these solutions to a quartz cuvette. These liquid samples were then characterised by a Varian Cary 5000 UV-Visible-NIR spectrometer for the wavelength range 200-800 nm.

3.3 Results and Discussion

This section is divided into three themed subsections for discussion.

Firstly, in §3.3.1, the thermal oxidation behaviour of the MWCNT@BN heteronanotubes is investigated in order to determine the suitable temperature for targeted removal of MWCNT templates whilst preserving the h-BN component

Next, in §3.3.2, the BNNT product synthesised by the sacrificial templating process is characterised for its morphology, dimensions and degree of crystallinity. The potential for BNNT diameter control is also explored.

Finally, in §3.3.3, the h-BN purity of the BNNT product is analysed.

3.3.1 Thermal Oxidation of MWCNT template

This sacrificial templating method leverages the difference in oxidation resistance of h-BN compared to graphitic carbon. h-BN has characteristically higher thermal oxidation resistance than graphite because of the larger activation energy barrier for oxidation to occur. The oxidation reactions for graphitic carbon and h-BN are as follows:

$$\mathrm{C} + \mathrm{O_2} \longrightarrow \mathrm{CO_2} \tag{R 3.1}$$

$$2\,\mathrm{BN} + \frac{3}{2}\,\mathrm{O_2} \longrightarrow \mathrm{B_2O_3} + \mathrm{N_2} \tag{R 3.2}$$

The elementary oxidation reaction of carbon requires the formation of a sole vacancy in a graphitic lattice while multiple B and N vacancies must be formed for the elementary oxidation of h-BN. The initial vacancy formation energy (H_{vac}) for carbon is ca. 7.5eV[218]and the estimated H_{vac} for two BN divancancies is at ca. 15eV[219]; see Figure 3.3A. Empirically measured oxidation activation energies for highly graphitized carbon and commercial h-BN were found to be 152 kJ/mol and 298-330 kJ/mol respectively.[195]

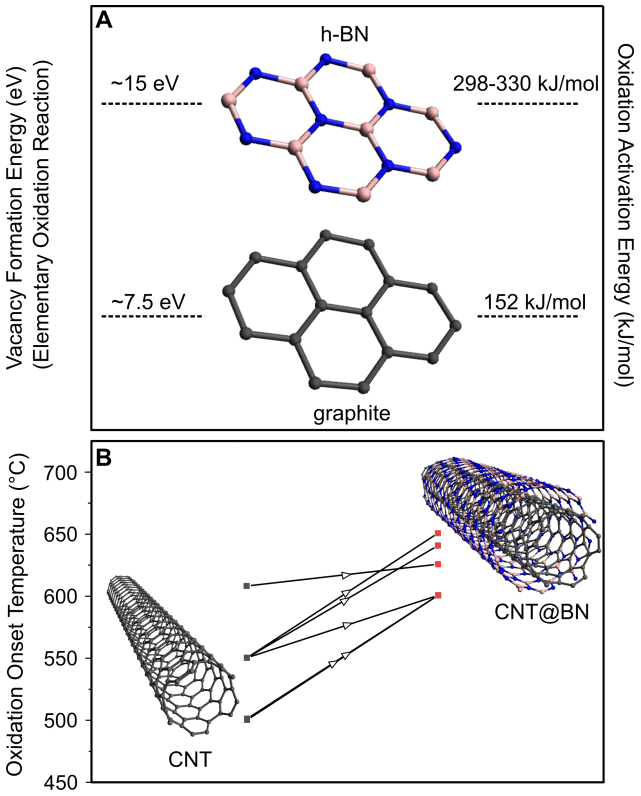


Figure 3.3: (A) Vacancy formation energy[218,219] and oxidation activation energy[195] of h-BN vs. graphitic carbon, justifying why h-BN is more oxidatively stable at high temperatures than graphitic carbon. (B) Compiled oxidation onset temperature values from studies that reported TGA results on CNTs prior to h-BN coating and after h-BN coating,[96,119,122,123,133,141] suggesting that h-BN was effective at improving oxidation resistance.

In the following discussion, TGA and FTIR results are presented to describe the thermal stability of the as synthesised MWCNT@BN and its independent components.

3.3.1.1 Oxidation Resistance of MWCNTs

In order to sacrifice the core MWCNT templates by thermal oxidation, their oxidation resistance had to be determined. Of particular interest is the temperature of oxidation, when carbon in the MWCNTs becomes reactive to oxygen and then proceeds to be volatilised.

It is well established that CNTs begin oxidising in air in the temperature range of ca. 400-700 °C, depending on factors such as crystallinity,[220–223] nanotube diameter,[224] number of walls,[220,225,226] and metal catalyst content.[220,227,228] In this

work, an additional factor is also expected to influence the oxidation resistance of the MWCNT, i.e. the presence of the protective h-BN outer coating. Indeed, previous studies have reported that oxidation onset temperature of MWCNTs increased after deposition of h-BN outer layers, in some cases by up to 100 °C, as summarised in Figure 3.3B. Whilst this is beneficial to the thermal stability of the CNT and suggests that CNT@BN heteronanotubes present better potential for high temperature applications (e.g metal/ceramic nanocomposites),[138] it implies that targeted removal of the core CNT for sacrificial templating requires a tailored, higher oxidation temperature.

To study the oxidation behaviour of the synthesised MWCNT@BN nanotubes, TGA was conducted to measure sample weight loss over the temperature range 50-900 °C. This was similarly repeated for the pristine MWCNTs and annealed MWCNT for comparison. The weight losses observed in all these TGA curves (Figure 3.4A) is attributable to carbon volatilisation upon its oxidation. In the case of the MWCNT@BN, the other potential oxidation candidate is the h-BN, but its oxidation product B_2O_3 has negligible volatilization below 1100 °C because of a low vapour pressure,[195,229–231] so any observed weight loss in the implemented TGA temperature regime must be due to volatilisation of the CNT component.

As shown in Figure 3.4A, the onset of oxidation of the MWCNT@BN occurs at a higher temperature than the pristine MWCNTs, as anticipated. Interestingly however, the annealed MWCNT (Ar/H_2; 1000 °C; 2 hours) which is a control for the MWCNT@BN (treated to all the same reaction conditions without the introduction of h-BN precursor) also exhibits an increase in oxidation onset temperature, albeit not as much as the MWCNT@BN. This result represents the first time that an annealed MWCNT control sample was also analysed by TGA alongside the as-received pristine MWCNT and the MWCNT@BN product. According to the Raman analysis done on the annealed MWCNTs in Chapter 2, it appeared that they had undergone graphitisation. This might also explain their elevated oxidation onset temperature relative to the raw MWCNTs, as the more crystalline graphitic structures better resist oxidation.[220,221,223] The implication of this finding

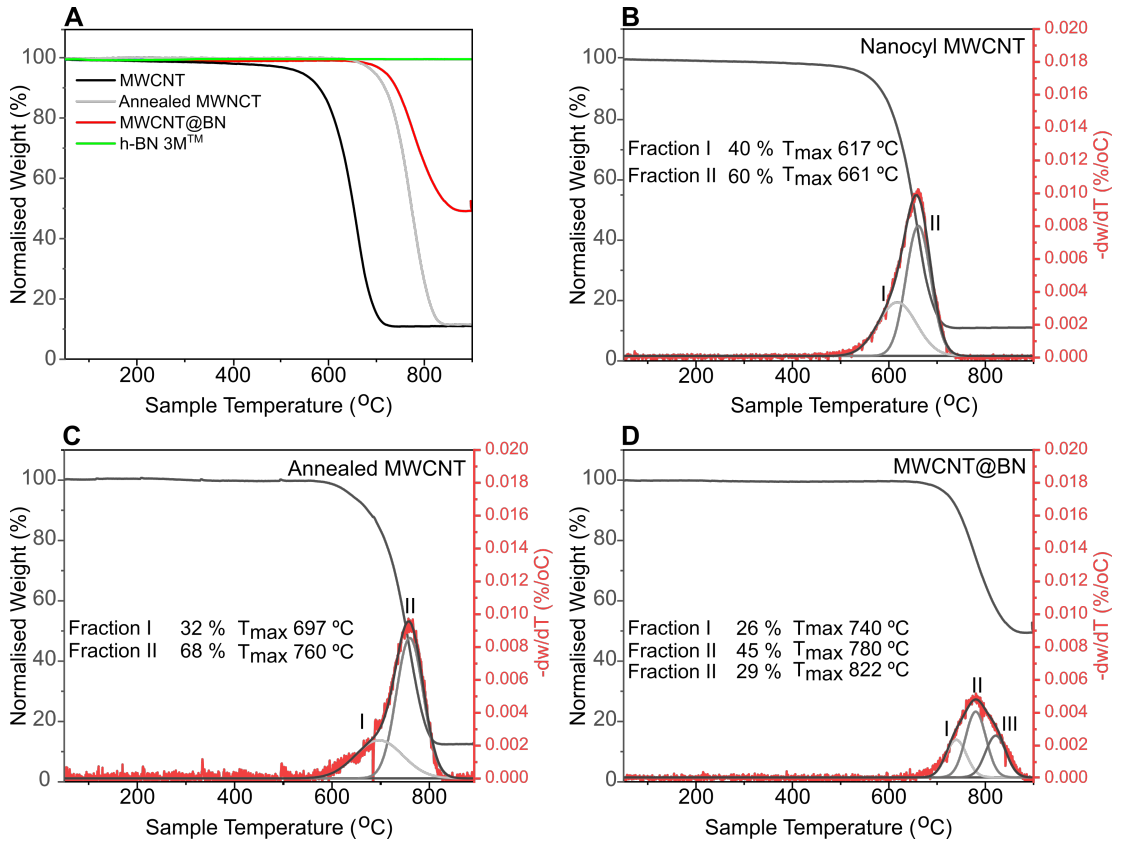


Figure 3.4: (A) TGA graphs showing normalised weight % vs. temperature for Nanocyl MWCNTs, annealed MWCNTs and MWCNT@BN compared to h-BN reference (3M™ powder). TGA scan rate: 20 °C/min. (B-D) Individual TGA curves for MWCNT, annealed MWCNT and MWCNT@BN are shown alongside their 1st-order derivative (wt%/°C) graphs -dw/dT. Gaussian distributions are fitted to the derivative curves to identify oxidation fractions, their temperatures at maximum combustion rate (T_{max}) and composition contribution (area %).

is that the attribution of improved MWCNT@BN oxidation stability relative to pristine MWCNTs solely to the presence of the h-BN coating, as stated in previous studies,[96,119,122,123,133,141] needs to be reassessed; changes to the carbon graphitic lattice itself during high temperature CVD processes must also be considered.

For a more quantitative evaluation of the TGA curves, their 1st-order derivatives were also plotted (also known as derivative of thermogravimetry curves; DTG curves), as depicted in Figure 3.4B-D. Such DTG curves have often been used to extract the temperature of maximum oxidation rate, T_{MAX}, of CNT materials based on the temperature at the well-defined DTG curve peaks.[145,220,232] This is considered a precise descriptor of oxidation behaviour and is frequently quoted as the oxidation

temperature, T_O.[220,228] As shown in Figure 3.4B-D, it is also possible to fit DTG curves with Guassian distribution components. The physical significance of these deconvoluted peaks is that they represent different fractions in the CNT sample which have their own oxidation reactivity.[225] A carbonaceous fraction's oxidation reactivity, and thus thermal stability, is inversely related to the structural defect content, i.e. fewer defects are favourable for higher oxidation resistance.[228,232,233] Consequently, DTG curves are useful to analyse CNT homogeneity, e.g. uniformity of types of nanotubes or graphitic versus amorphous carbon content.

For the DTG curves of MWCNTs and annealed MWCNTs, Figures 3.4B-D respectively, there are two step-wise weight loss fractions identified (I & II). Their chemical identities are likely associated to MWCNTs of different defect densities, with fewer defects in Fraction II. Other potential carbonaceous components, e.g. amorphous carbon, usually exhibit T_{MAX} oxidation fractions <400 °C, which are not observed here.[225,233,234] Subsequent to annealing, both fractions' T_{MAX} values increased; for Fraction I, $\Delta\ T_{MAX_I} = 80$ °C (from 617 °C to 697 °C) and for Fraction II, $\Delta\ T_{MAX_{II}} = 99$ °C (from 661 °C to 760 °C). Based on the discussion above, these increases correspond to an overall reduction of Nanocyl MWCNT sample defect density upon annealing, corroborating the results of Raman analysis in Chapter 2, §2.3.1.5. Alongside the observed T_{MAX} changes resulting from annealing, changes in fraction peak area were also noticed. Each peak area is used as a quantitative measure of the wt. % content of an oxidation species.[225,233,235] In both the MWCNT and annealed MWCNT samples, Fraction II is the predominant component. However, upon annealing, there is a slight increase (+8%) in the Fraction II % and a concurrent Fraction I % decrease (-8%), which might indicate a transferal of a portion of Fraction I to Fraction II MWCNT oxidation reactivity as a result of annealing induced graphitisation.

An entirely different DTG profile is observed for MWCNT@BN, as depicted in Figure 3.4D. It is immediately distinguiable from the DTG profiles of MWCNT and MWCNT@BN for its smaller intensity, signifying a slower rate of oxidation. Specifically, the maximum rate achieved is -0.005%/°C, compared to the -0.01%/°C

for the pristine and annealed MWCNTs. This is a convincing indication of the protective role of the h-BN outer coating, whereby it can effectively decrease the oxidation rate of the core MWCNT by as much as 50%.

In addition to the rate reduction, the DTG profile for MWCNT@BN has a noticeably different shape that is more symmetric compared to the asymmetric DTG peaks exhibited by pristine and annealed MWCNTs. This symmetric DTG profile is fitted with three Guassian fractions I-III (Figure 3.4D). The exact identification of the oxidation species within each of these fractions (with substantial overlap) is challenging, given that both the MWCNT crystallinity as well as the h-BN outer coating can influence thermal stability in the MWCNT@BN system. Furthermore, there are no references in the literature for comparison, as DTG analysis has not been applied for CNT@BN until now. Despite this ambiguity, it is clear that the reactivity of the carbon in these fractions is altered by the presence of h-BN, as measured T_{MAX} values are relatively higher. For instance, between the highest T_{MAX} observed for annealed MWCNT (760 °C) and the highest observed for MWCNT@BN (822 °C), there is a 62 °C oxidation temperature enhancement.

Thus far, oxidation temperature has been discussed in terms of the T_{MAX} descriptor. Whilst this is well accepted in the literature on CNTs, it is obviously overlooked in the CNT@BN literature to date. Instead, oxidation behaviour has been more cursorily treated, such that the region at which the TGA graph changes from plateau to steep decline is used to estimate oxidation initiation/onset temperature (not always explicitly stated). By this interpretation (and approximating the point at which the DTG curves starts rising from zero), oxidation onset temperature increases as follows: 500 °C (MWCNT) < 600 °C (annealed MWCNT) < 700 °C (MWCNT@BN).

All of the above results considered, a temperature of 700 °C was selected as the oxidation temperature to sacrifice the core MWCNTs, leaving h-BN skeletons as BNNTs. At this temperature, oxidation of CNTs has initiated in the MWCNT@BN sample, but is not at the maximum rate. Thus, the implemented oxidation regime was intentionally mild, but done over a 1 hour period, so as to account

for CNT removal, albeit slower, whilst reducing the probability of oxidation of the h-BN itself. Using the tangential oxidation rate (%wt/mins) measured at 700 °C from the MWCNT@BN TGA curve (see Appendix Figure B.1) and assuming consistency, it was estimated that a total of 32 minutes was sufficient to achieve the same carbon weight loss as the final oxidised product at 900 °C. The 1 hour oxidation period applied is thus justified as a precaution to sufficiently exceed the calculated requisite time.

3.3.1.2 Oxidation Resistance of deposited h-BN

FTIR spectra were collected to confirm the preservation of h-BN after the oxidation treatment of MWCNT@BN and to probe the oxidation resistance of h-BN up to 900 °C.

As shown in Figure 3.5A, there are absorption peaks present in the FTIR transmission spectra of MWCNT@BN and the BNNT that are not present in the spectrum of the Nanocyl MWCNT.

When compared to the characteristic FTIR profile of h-BN, as depicted in Figure 3.5B, it is evident that prominent absorption peaks observed in MWCNT@BN and

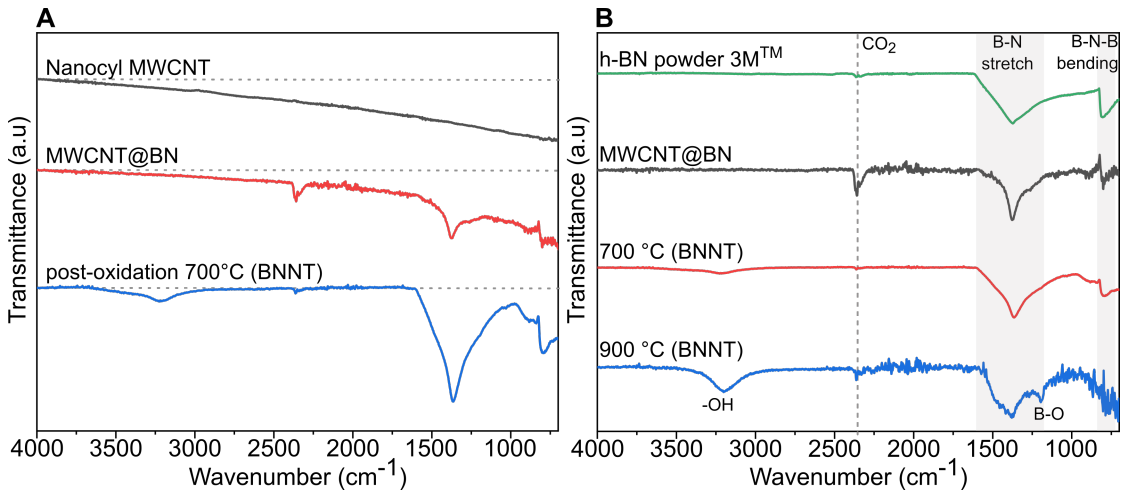


Figure 3.5: FTIR transmission spectra (A) as-collected from Nanocyl MWCNTs, MWCNT@BNs and BNNTs (made by 700 °C oxidation of MWCNT@BN templates). The featureless MWCNT spectrum is in contrast to the MWCNT@BN and BNNT spectra, which both show absorption peaks associated with h-BN. (B) Normalised FTIR spectra comparing BNNTs (synthesised from 700 °C and 900 °C sacrificial templating) to MWCNT@BN (baseline substracted) and an h-BN reference (3M™ powder).

FTIR Frequencies (cm^{-1})					
h-BN 3M™	**MWCNT@BN**	**BNNT (700 °C)**	**BNNT (900 °C)**	**Vibration**	**Molecule/ Functional group**
-	-	3217	3196	O-H stretching	H_2O; B-OH
2362	2359	2361	2360	C-O asymmetric stretching	CO_2
1373	1377	1363	1380	B-N in-plane stretching	h-BN
-	-	-	1187	B-O stretching	B-O stretching
804	798	787	-	B-N-B out-of-plane bending	h-BN

Table 3.3: Summary of FTIR absorption peaks recorded from spectra of MWCNT@BN, BNNT (700 °C), BNNT (900 °C) and reference h-BN powder from 3M™ (shown in Figure 3.5B). Note that the peak at ca. 2360 cm^{-1} is a result of atmospheric and/or adsorbed CO_2.

post-oxidation BNNT samples are indeed associated with h-BN (ca. 1373 cm^{-1} for B-N in-plane stretching and ca. 793 cm^{-1} for B-N-B out-of-plane bending). Exact FTIR peak frequencies for all spectra are compiled in Table 3.3.

These results confirm the high oxidation resistance of the deposited h-BN given that it is still detected after 700 °C. However, if the MWCNT@BN is treated to 900 °C oxidation for 1 hour, the h-BN undergoes appreciable oxidation, as revealed by the corresponding FTIR spectrum in Figure 3.5B. A noticeable peak at 1187 cm^{-1} appears that is attributable to B-O stretching vibrations from oxidised boron species. Additionally, the B-N-B bending absorption peak becomes less visible whilst the the -OH stretching peak becomes more prominent. This -OH is related to adsorbed water or B-OH bond formation that occurs from hydrolytic instability of h-BN as it becomes more defective during oxidation;[195] see also Chapter 4, §4.3.3. These are all characteristic changes observed as h-BN becomes more susceptible to oxidation at higher temperatures.[236,237] Given that there is also a visible, albeit small intensity, -OH absorption peak found on the FTIR spectrum of the 700 °C BNNT product, there is likely partial oxidation of the h-BN at this temperature.

3.3.2 BNNT Structure

Here, the results of structural analysis are presented in the following order:

- Introduction of the morphology and dimensions of the BNNTs synthesised (SEM, TEM)
- Demonstration of achieved diameter control of the BNNTs (TEM)
- Quantitative assessment of the BNNT crystallinity (Raman, XRD)

3.3.2.1 BNNT Morphology

Subsequent to the 700 °C oxidation treatment, indeed nanotube structures are still present, as observed by SEM in Figure 3.6. Compared to the MWCNT and MWCNT@BN powders, which are black to dark grey (See Chapter 2, Figure 2.6), the post oxidised product is off-white in colour, as visible in the inset of Figure 3.6B. This result is in line with the BNNT composition of these nanotubes and the effective removal of the graphitic carbon component during the oxidation process.

The removal of the MWCNT templates is also supported by TEM analysis of the post-oxidised nanotubes. As exemplified in Figure 3.7A, there is an clear transition in the wall thickness and diameter dimensions of the nanotubes subsequent to oxidation. The larger inner diameter of the BNNTs in comparison to its precursor MWCNT@BN is in accordance with sacrificing of the original MWCNT core.

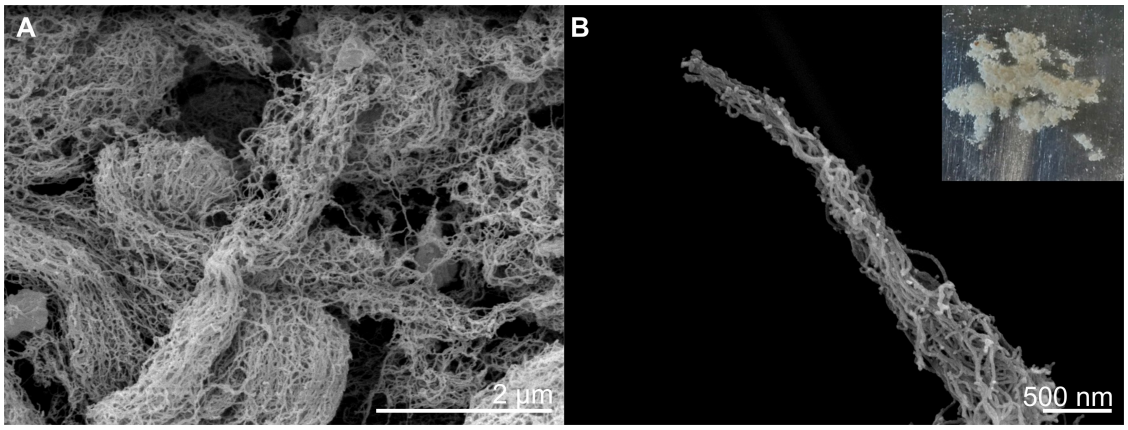


Figure 3.6: (A-B) SEM images of BN nanotubes remaining after 700 °C oxidation treatment of MWCNT@BN. Inset image shows optical photo of off-white coloured BNNT residual powder.

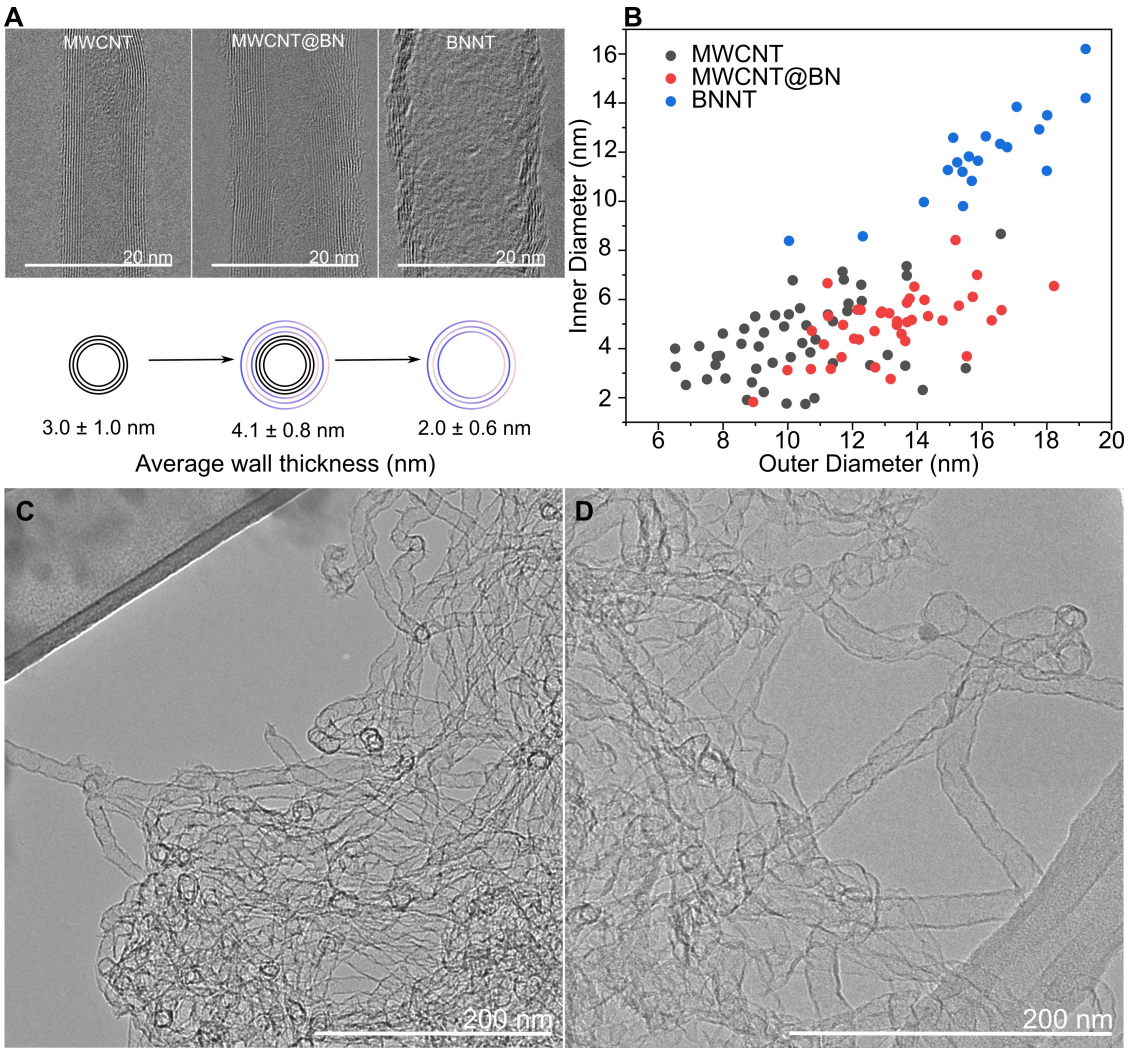


Figure 3.7: (A) HRTEM images highlighting the transformation of Nanocyl MWCNT to MWCNT@BN and BNNT achieved here. Average wall thicknesses of each nanotube species are summarised in the accompanying illustration. (B) Scatter plot of nanotube inner diameter vs. outer diameter for MWCNT, MWCNT@BN and BNNT. Evidently the inner diameter of BNNTs is significantly increased- an indication of core MWCNT removal during oxidation of MWCNT@BN. (C-D) TEM images showing the uniformity of BNNTs synthesised by the sacrificial templating method.

Meanwhile, the BNNT wall thickness matches with the thickness of CVD deposited h-BN determined in Chapter 2 from the MWCNT@BN heteronanotubes (i.e. ca. 2-3 nm). A compilation of inner and outer diameters of MWCNT, MWCNT@BN and BNNT, as measured from HRTEM images, is included in Figure 3.7B. Additional TEM images, depicted in Figure 3.7C-D, evidence the homogeneity of the BNNT structures achieved by the sacrificial templating method.

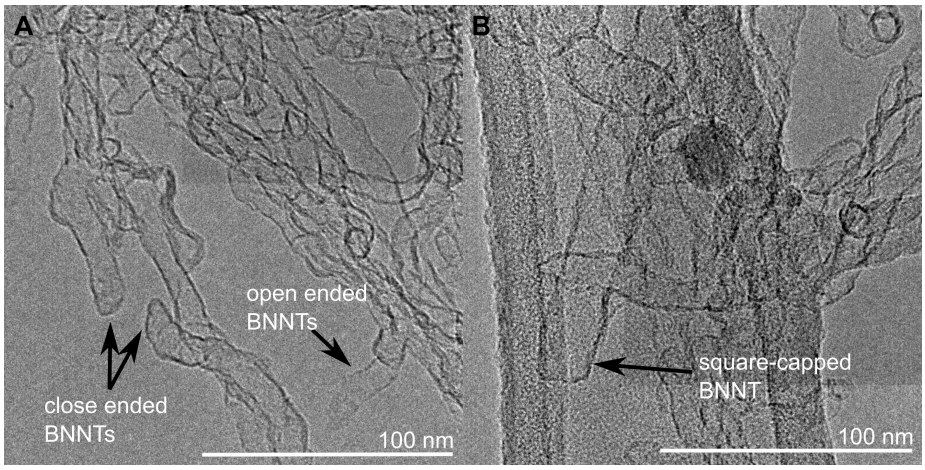


Figure 3.8: TEM images depicting BNNTs with different tip structures, e.g. closed vs open ended.

Whilst diameters were measureable from the TEM images, precise BNNT lengths were more difficult to assess due to the entanglement of nanotubes. However, by general observation, BNNTs synthesised by this sacrificial templating method are several hundred nanometers in length (i.e.<1 μm). The subject of length also brings to question the path of oxygen access into the MWCNT core. If the MWCNTs were completely enveloped along their entire lengths and around their ends by h-BN, the core MWCNTs would be protected against oxidation at 700 °C. Otherwise, partial coating of the MWCNTs by h-BN would leave areas of exposed MWCNT that would be the starting point of MWCNT oxidation. This is theorised to be the case here, whereby exposed regions either along the length of MWCNTs or at their tips were not protected by h-BN. The occurrence of close-ended BNNTs would indicate oxygen penetrated into the core at a point along the length of the nanotubes, whilst open ended BNNTs would support oxygen access at the tips. Both of these scenarios are possible, as evidenced by the TEM images of closed and open-ended BNNTs in Figure 3.8.

From HRTEM images of the BNNTs, as exemplified in Figure 3.9, it is apparent that their walls are not highly crystalline, but are instead disordered. Further analysis of crystallinity, discussed in §3.3.2.3, corroborates the turbostratic nature of the as synthesised BNNTs. A combination of factors are likely responsible for the low crystallinity achieved, including the defective MWCNT templates used, the

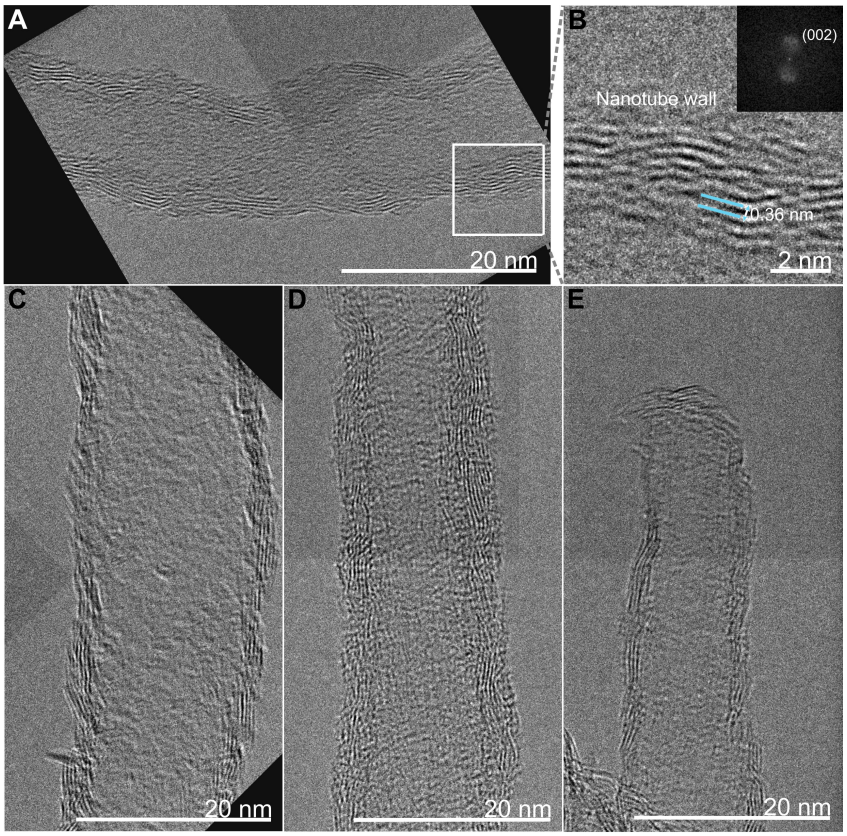


Figure 3.9: Example HRTEM images of BNNTs synthesised here by sacrificial templating. These images evidence the disordered structure of the BNNT walls. The achieved turbostratic BNNT wall structure is magnified in (B), showing the disordered h-BN lamellae and a broad (002) spacing of ca. 0.36 nm.

1000 °C temperature at which the h-BN was synthesised, and potential thermal oxidation induced damage. Note that the selection of the h-BN synthesis variables was initially justified by the Nanocyl NC7000™ MWCNT template availability and the favourable growth rate of h-BN at 1000 °C, above which rate decreases due to increased gas-phase nucleation of the CVD precursor.[238] Nevertheless, there is potential for later post-synthesis improvements to BNNT crystallinity, e.g. by thermal transformation,[170] which is recommended as a future course of investigation.

3.3.2.2 BNNT Diameter Control

To demonstrate diameter control of the BNNTs from the sacrificial templating method, alternative MWCNT templates with a larger outer diameter than the Nanocyl NC7000 MWCNT were also employed. These alternative MWCNT

templates, synthesised by AACVD, as described in §3.2.1.2, exhibit, on average, approximately 4-fold wider outer diameters than the Nanocyl MWCNTs, as well as a much higher variance. This difference is evident from the outer diameter histograms compiled in Figures 3.10A & C, which are based on measurements taken

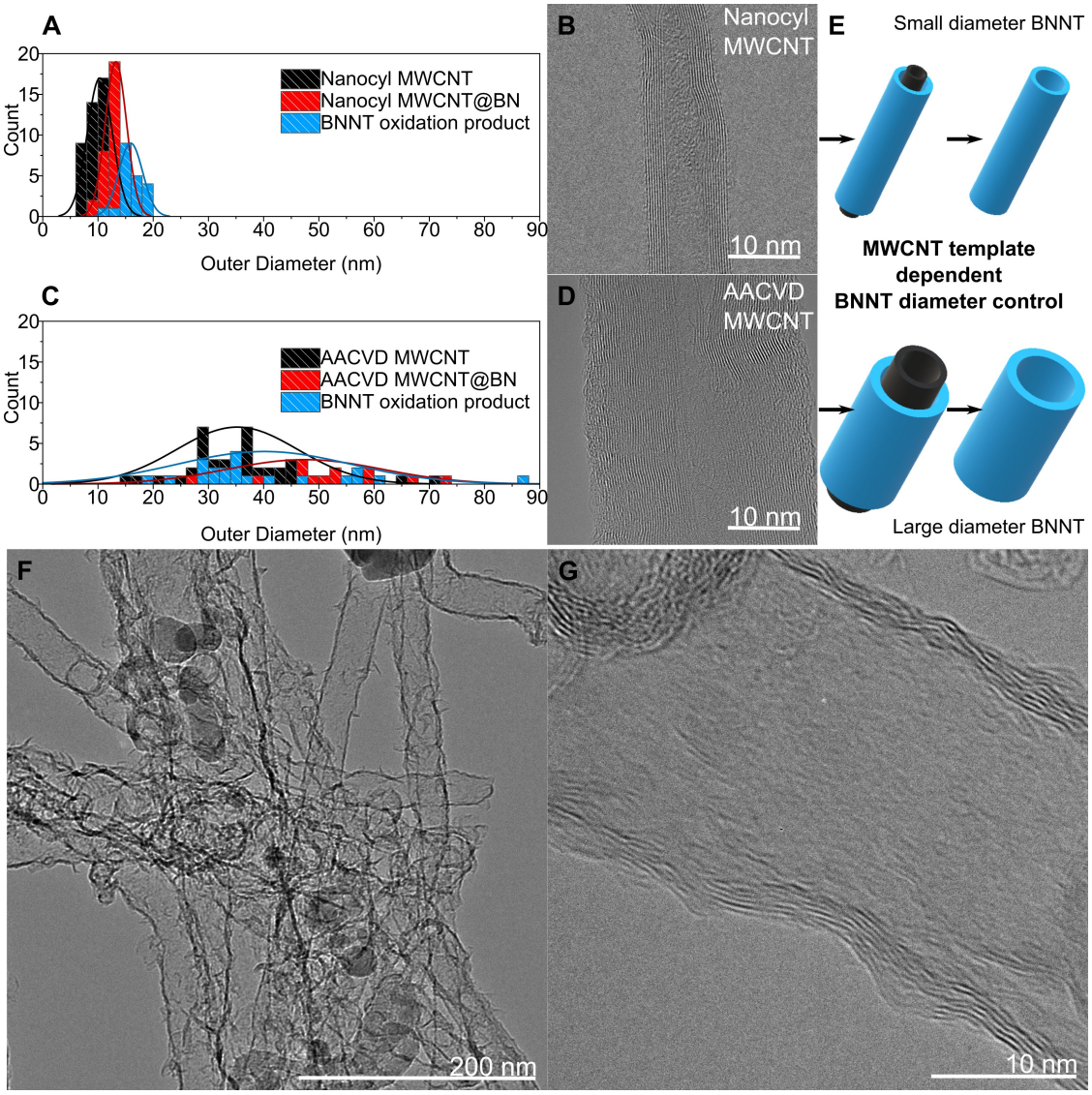


Figure 3.10: (A) Collected outer diameter distributions of Nanocyl MWCNTs and its MWCNT@BN and BNNT derivatives. For comparison, the analagous measurements are compiled in (C) for the wider diameter AACVD synthesised MWCNTs and its derivatives. For visual comparison, HRTEM images of (B) Nanocyl and (D) AACVD MWCNTs show their distincly different nanotube diameters. (E) The diameter of the resulting BNNT is expected to be dependent on the MWCNT template diameter. (F) TEM image depicting BNNTs synthesised from the sacrificial templating of the AACVD MWCNT templates. (G) HRTEM image exemplifying structure of large diameter BNNTs achieved.

from TEM images of MWCNTs typified in Figures 3.10B & D for Nanocyl and AACVD MWCNT respectively. As the outer diameter of the BNNT synthesised here are dependent on the diameter of the starting MWCNT template, larger diameter MWCNTs are predicted to facilitate growth of larger diameter BNNTs, a concept summarised in the Figure 3.10E schematic.

By implementing the same CVD method described in Chapter 2 to coat the AACVD MWCNTs with coaxial h-BN, followed by thermal oxidation, indeed larger diameter BNNTs were obtained, as shown in Figure 3.10F. Similar to their narrower counterparts, these broader BNNTs have thin (ca. 2-3 nm), disordered h-BN walls, as observed from HRTEM images such as Figure 3.10G.

Additional characterisation of these BNNTs, and their precursor AACVD MWCNTs and MWCNT@BNs is included in Appendix B, §B.3. Notably, alongside the BNNTs synthesised by sacrifical templating, other bamboo morphology BNNTs appeared frequently during TEM observations, as shown in Appendix Figure B.7. It is hypothesised here that these bamboo BNNTs grew from ferrocene derived catalyst nanoparticles present in the AACVD MWCNT samples, as has been previously demonstrated.[204] In fact, ca. 10 wt.% non-graphitic residue was detected in the AACVD MWCNT template material, all of which is likely attributable to Fe-based catalysts; see TGA plots in Appendix Figure B.5A. So in comparison to the Nanocyl MWCNTs, which had 10 wt.% catalyst support material (Al_2O_3) and only <1wt.% of transition metal oxide catalysts, the AACVD MWCNTs were found to have a higher active catalyst content. Consequently, the high frequency of Fe-derived catalyst nanoparticles are deduced to be responsible for the prevalence of bamboo morphology BNNTs amongst the sacrificial templated BNNTs. In light of this, further detailed characterisation of BNNTs in this thesis focuses only on those derived from the Nanocyl NC7000 MWCNT templates. The BNNTs sythesised as such exhibit greater homogeneity of cylindrical BNNT morphologies resulting from sacrificial templating and not from catalyst-assisted mechanisms, and are more suitable for characterisation to specifically investigate the results of the templating technique.

3.3.2.3 BNNT Crystallinity

3.3.2.3.1 Investigating crystallinity by Raman Spectroscopy As exemplified earlier for the analysis of MWCNT@BN in Chapter 2, Raman spectroscopy is useful for investigations of nanotube structure because of the technique's sensitivity to material crystallinity. For the BNNTs synthesised in this Chapter, Raman spectroscopy was again conducted to probe the degree of crystallinity achieved at bulk scale.

The two Raman active non-polar E_{2g} modes of h-BN are located at ca. 51.8cm $^{-1}$ and ca. 1370 cm^{-1}. The former is attributed to rigid shear vibration between layers whilst the higher frequency mode is due to intralayer B and N counter-phase vibrations.[162] This intralayer mode is most commonly observed in the literature on h-BN and so is the only mode considered here.

In Figure 3.11A(i), the Raman spectrum of commercially available h-BN powder shows a prominent high frequency E_{2g} peak at 1364.8 cm^{-1} with a FWHM of 8.9 cm^{-1}, typical of highly crystalline h-BN. In comparison, for the same laser irradiation wavelength of 532 nm, the collected spectrum for the as-synthesised

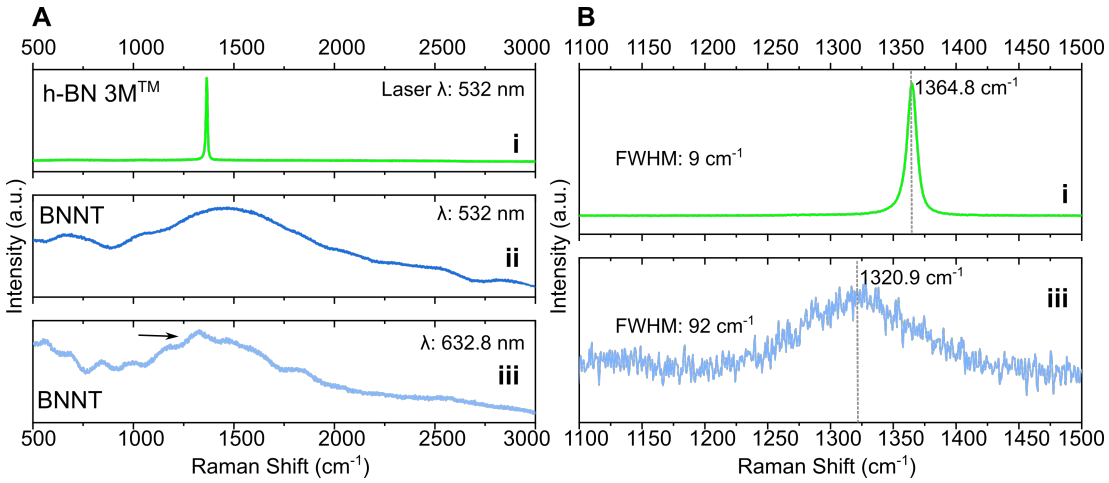


Figure 3.11: (A) Raman spectra collected from (i) a reference crystalline commercial 3M™ h-BN sample and (ii-iii) BNNTs synthesised by sacrificial templating. Laser wavelength used for (i-ii) was 532 nm, but 632.8 nm for (iii) to test fluorescence suppression. (B) A magnification of the E_{2g} mode for (i) reference h-BN powder and (iii) the BNNTs (laser λ 632.8 nm) for clearer comparison of peak position and FWHM. FWHM are calculated from Lorentz peak fittings.

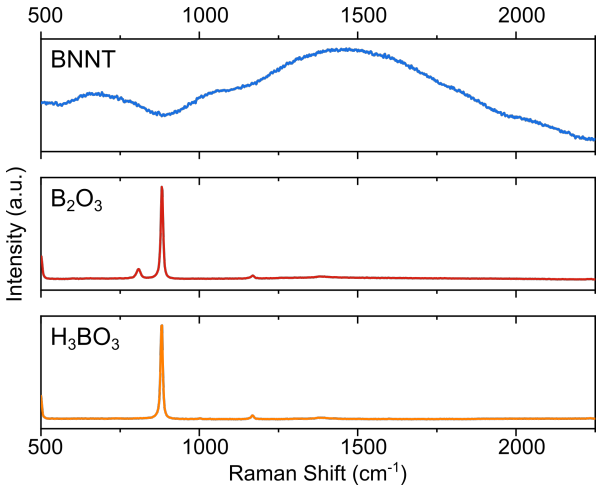


Figure 3.12: Raman Spectra collected from as synthesised BNNTs are compared to spectra of B_2O_3 and H_3BO_3 in order to determine potential Raman spectral contributions from these impurities. Reference Raman spectra, also collected at 532 nm excitation wavelength, were obtained from the Raman Open Database, entry card numbers 3500002 and 3500052.[239]

BNNTs is considerably different (Figure 3.11A(ii)). Instead of a narrow E_{2g} peak, there is a significantly broad feature (FWHM: ca. 780 cm^{-1}) centered at ca. 1450 cm^{-1} with a notable slope background. To eliminate the potential for Raman spectral contributions from oxidation impurities such as B_2O_3 and/or H_3BO_3, the BNNT spectrum was also compared to reference Raman spectra for these materials, as shown in Figure 3.12. The features of the collected BNNT Raman spectrum do not correspond with either of these reference spectra. Several explanations are considered below to explain the broad peak of the BNNT spectrum, as discussed below.

In the wider scope of literature on h-BN materials, a few reports were discovered that presented similarly anomalous broad Raman spectral features which they associated with the small crystallite sizes of their synthesised h-BN products. For instance, Zhong *et al.*, made turbostratic BN (t-BN) films on SiO_2/Si substrates using ammonia borane at 1350 °C, and found a very broad feature (FWHM: 400 cm^{-1}) centered at 1381 cm^{-1} in the associated Raman spectrum.[240] A similarly broad Raman peak with FWHM of ca. 600 cm^{-1}, centered at 1370 cm^{-1} was observed for BN nanocapsules made by nitridation of the outer layers of boron nanoparticles at 1100 °C.[241] Finally, polycrystalline (amorphous) BN fibres synthesised via the

pyrolysis of poly[2-n-propylamino-4,6-bis(methylamino)borazine] (PPAB) in NH_3 at 1000 °C exhibited a diffuse peak at 1500 cm^{-1} and FWHM of more than 500 cm^{-1}.[242] Noticeably, in these studies, the descriptor 'small' is used rather informally to address h-BN crystallite size, with little to no quantitative interpretation. Consequently, their association of the exceptionally broad Raman peaks in the vicinity of the h-BN E_{2g} mode to 'small' crystallite size is inconclusive.

Nonetheless, their interpretation is inspired by the seminal observations by Nemanich *et al.*, 1981, who demonstrated a quantifiable dependence of h-BN's Raman E_{2g} mode peak FWHM ($\Gamma_{1/2}$) and peak shift (Δ) on the h-BN basal plane L_a crystallite size.[163] As h-BN L_a crystallite size decreased, the Raman higher frequency E_{2g} mode $\Gamma_{1/2}$ was found to widen whilst the peak shifted to higher frequencies. These relationships are expressed according to equations 3.1 and 3.2. Calculations use L_a expressed in angstroms Å.

$$\Gamma_{1/2} = \frac{1417}{L_a} + 8.70 \tag{3.1}$$

$$\Delta = \frac{380}{L_a} - 0.29 \tag{3.2}$$

Notably, these models were formulated for h-BN with L_a sizes from 4.4 ± 0.5 nm to 78.5 ± 13.0 nm, which had corresponding Raman E_{2g} peak ($\Gamma_{1/2}$) values in the range of 50 cm^{-1} to 10 cm^{-1} respectively. The greatly broadened peaks observed in Figure 3.11A(ii) and in the aforementioned studies[240–242] exhibit ($\Gamma_{1/2}$) values significantly larger, i.e. by an order of magnitude greater than investigated in the original study. It is thus controversial whether equation 3.1 is still relevant for the extremely broad ($\Gamma_{1/2}$) values so far outside the range of the Nemanich *et al.* study.

An alternative explanation that more likely accounts for the very broad Raman spectral feature observed in Figure 3.11A(ii) is that there is a considerable fluorescence background. Whilst Raman spectra are generated as a result of scattered photons that have transferred energy to rotational or vibrational energy of the irradiated molecules, fluorescence (a form of photo-luminescence) occurs when the incident monochromatic photon energy is resonant with a molecular

	h-BN powder 3M™	**As synthesised BNNTs**
E_{2g} frequency (cm^{-1})	1364.8	1320.9
FWHM $\Gamma_{1/2}$ (cm^{-1})	9	92
L_a crystallite size (nm)	472	2

Table 3.4: Comparing the high frequency E_{2g} Raman peak parameters (position and FWHM) of commercial h-BN powder to that of the as synthesised BNNTs. See Figure 3.11B). L_a is calculated from the Nemanich *et al.* expression linking FWHM and L_a in equation 3.1.

electronic transition, such that it is absorbed and re-emitted as a lower energy photon during a relaxation process. It is possible, and an inconvenience commonly encountered in Raman spectroscopy, for Raman scattering and fluorescence emission to occur concurrently from an illuminated sample.[243] This is likely the case if there are any materials within the illuminated sample, even minority impurities, that have an absorption spectrum corresponding with the laser excitation wavelength. Given that Raman scattering is already a weak phenomenon, fluorescence can easily overwhelm the Raman spectrum with characteristically broad bands which can have intensities on the order of 10^4 greater than the Raman signal.[244] In such a scenario, Raman signals could become entirely masked.

Given that the Raman spectrum obtained in Figure 3.11A(ii) closely resembles the features expected for a strong fluorescence band, it was hypothesised that this intense fluorescence was obscuring any Raman signals of interest, particularly the h-BN E_{2g} peak. Furthermore, it has been reported previously that some BNNT samples produce strong fluorescent backgrounds dependent on their synthesis route and final composition,[245] perhaps resulting from impurities and defects. One approach to fluorescence suppression was subsequently investigated in order to test this hypothesis. This involved using a longer laser excitation wavelength, e.g. 632.8 nm as opposed to the originally used 532 nm. Selection of a longer excitation wavelength is a traditional protocol for fluorescence suppression, based on the theory that a longer wavelength, lower energy photon source usually has reduced adsorptivity, so a diminished probability of fluorescence excitation is

expected.[243,244,246] The BNNT Raman spectrum collected at excitation wavelength 632.8 nm is depicted in Figure 3.11A(iii). Indeed, a weak peak is revealed at 1320.9 cm^{-1} that was previously hidden, thus providing evidence in support of the fluorescence hypothesis and furthermore, indicating that fluorescence was slightly mitigated at the longer excitation wavelength.[†]

It is subsequently assumed that the peak at 1320.9 cm^{-1}, highlighted in Figure 3.11B(iii), is indeed attributable to the h-BN intralayer E_{2g} mode of the BNNTs. This peak exhibits characteristics more suitable for analysis according to the Nemanich *et al.*, equation 3.1 presented above, which associates h-BN L_a crystallite size to the E_{2g} peak width ($\Gamma_{1/2}$). By this estimation, for $\Gamma_{1/2}$= 92 cm^{-1}, the L_a crystallite size of the synthesised BNNTs is 2 nm. This is significantly smaller than the L_a calculated for the highly crystalline h-BN powder, as summarised in Table 3.4, suggesting that the BNNTs synthesised here are not very well crystallised. In the BNNT literature, particularly in the small subset that recorded Raman spectra and analysed the h-BN E_{2g} peak, reported $\Gamma_{1/2}$ have been as narrow as 13 cm^{-1},[247] close to 20 cm^{-1},[248,249] or approaching a broader 30 cm^{-1}.[250,251] Yong Bae *et al.,* have also reported a broad 38 cm^{-1} value of $\Gamma_{1/2}$ for bamboo-like BNNTs synthesised at 1050 °C.[250] As one of the highest reported $\Gamma_{1/2}$ for BNNT, that would correspond to L_a crystallite size of ca. 5 nm according to equation 3.1. By comparison, these literature $\Gamma_{1/2}$ values appear to confirm the low crystallinity of the BNNTs synthesised here.

There is however a possibility that the crystallite size of BNNTs is underestimated by the Nemanich *et al.* expression (Equation 3.1). This is in light of evidence revealing that the crystallite size effect is not the exclusive determinant for $\Gamma_{1/2}$ of the h-BN E_{2g} peak. Indeed, peak width of the E_{2g} mode can also be influenced by anharmonic effects such as temperature dependence, whereby higher temperatures have been demonstrated to induce peak broadening, e.g in pyrolitic h-BN.[252] In the absence of other heat sources, the laser used for Raman spectroscopy can be responsible for local temperature increases in an illuminated sample. The extent

[†]Although there is evidence of fluorescence suppresion achieved here, it is recommended that to further improve the Raman signal-to-noise , Resonance Raman Spectroscopy should be used to characterise the BNNTs.

of this temperature rise is dependent on the laser power and the ability of the illuminated sample to dissipate heat, i.e. its thermal conductivity. In this context, laser heating has been proposed to be more pronounced in BNNT agglomerates compared to bulk h-BN, as the former's thermal conductivity is usually limited by the thermal contact resistance between non-aligned nanotubes.[253,254] As such, the generally broader E_{2g} peak of BNNTs relative to bulk h-BN is suggested by Arenal *et al.* to be due to laser heating induced anharmonicity.[255] In support of the laser heating effects, Arutyunyan *et al.*, found that increasing the laser power caused marked E_{2g} peak broadening of irradiated BNNTs.[256] Given that laser heating efficiency is increased by any factors that reduce thermal conductivity, e.g impurities or BNNT defects/disorder[254,256] it is postulated here that thermal effects contribute towards the E_{2g} peak broadening witnessed for the defective BNNTs synthesised here (Figure 3.11B(iii)).

Besides peak broadening, there is also a noticeably down-shifted (red-shifted) frequency of the BNNT E_{2g} peak relative to that of the h-BN (Figure 3.11B); specifically the frequency shift Δ is -43.9 cm^{-1}. This red-shifting is in fact in keeping with anharmonic thermal effects,[257] such as caused by laser heating; both Arutyunyan *et al.* and Lu *et al.* found that BNNT E_{2g} peaks exhibited peak broadening accompanied by red-shifts as laser irradiation power increased.[254,256] Returning to the expression formulated by Nemanich *et al* that associated E_{2g} frequency shift Δ to L_a (equation 3.2),[163] it is evident that red-shifting is not predicted. Instead, blue-shifting is expected for h-BN of decreasing crystallite size. That a red-shift was observed for the BNNTs synthesised here could be an indication that thermal effects had a more dominant effect than size effects in this scenario.

3.3.2.3.2 Investigating crystallinity by X-ray Diffraction To confirm the degree of crystallinity of the as-synthesised BNNTs, XRD analysis was also conducted.

In Figure 3.13A, the collected XRD pattern (10-80°) of the BNNTs is compared to that of commercial h-BN powder. Evident from this comparison is the presence

of non-h-BN impurities in the BNNT sample. These impurities are indexed to B_2O_3/H_3BO_3 and $Al_4B_2O_9$. The inclusion of the B_2O_3 reference pattern is based on the fact that it is the oxidation product of h-BN.[‡] As B_2O_3 is readily converted to H_3BO_3 upon exposure to moisture (as later elucidated in Chapter 4), the latter

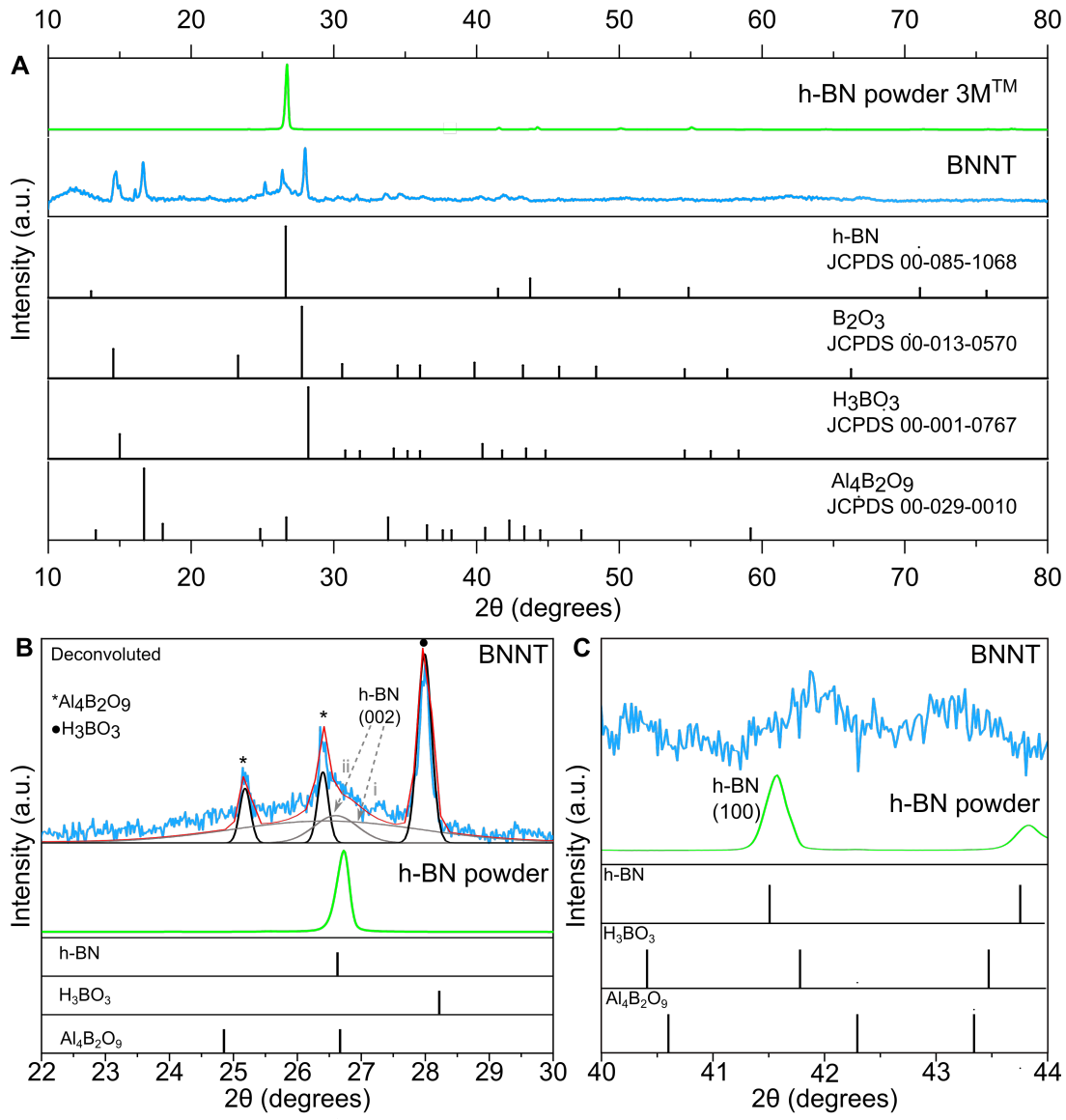


Figure 3.13: (A) X-ray diffraction patterns (10-80°) of commercial h-BN 3M™ and the as-synthesised BNNTs. Reference XRD patterns for h-BN, B_2O_3, H_3BO_3 and $Al_4B_2O_9$ are included for indexing.(B) Deconvoluted XRD pattern (22-30°) of BNNT; diffuse Gaussian fitted curves associated to the h-BN (002) reflection are identified by arrows. (C) XRD patterns of BNNT and h-BN powder 3M™ between 40-44 °, alongside references for h-BN, H_3BO_3 and $Al_3B_2O_9$. The h-BN (100) reflection is difficult to discern on the BNNT XRD pattern due to low signal to noise ratio, and possible overlapping contributions from H_3BO_3.

reference pattern was also included for indexing. As identified in Chapter 2, $Al_4B_2O_9$ is a residual contaminant resulting from a reaction between the boron-containing CVD precursor and the Al_2O_3 catalyst supports present in the original Nanocyl MWCNT templates.

The XRD maxima associated with these aforementioned impurities, particularly in the range of 22-30°, as highlighted in Figure 3.13B, complicate direct analysis of the BNNT (002) reflection. Accordingly, this region of the XRD pattern was deconvoluted by Guassian fitted curves, resolving three narrow peaks and two diffuse peaks. The two narrow peaks at 25.18°, 26.40° are indexed to the (311) and (231) reflections of $Al_4B_2O_9$ respectively, while the prominent peak at 27.99° is attributed to the (002) reflection of H_3BO_3. Notably, the (231) reflection of $Al_4B_2O_9$ overlaps closely with the position of the (002) peak of h-BN, giving rise to the possibility of peak misattribution. However, the narrowness of the 26.4° peak (FWHM: 0.2°) precludes its identification as the (002) reflection of the BNNTs. As already suggested by TEM and Raman analysis, the synthesised BNNTs are less crystalline relative to the commercial h-BN flakes. It is thus expected that the (002) XRD peak of the BNNTs must be broader than that of the crystalline h-BN powder reference, i.e. FWHM >0.2°.

In fact, two broad peaks are revealed after deconvolution at 26.44° & 26.60°, with FWHM of 0.8° and 3.5° respectively. These two peaks are interpreted as originating from the (002) h-BN plane in the BNNTs, and are analysed to calculate the L_c crystallite stacking height of h-BN in the BNNTs, based on the Scherrer equation previously described in Chapter 2 (see §2.3.1.5.2, equation 2.3). Calculated crystallite sizes are summarised in Table 3.5. Effectively, L_c should give a close approximation of the BNNT wall thickness. Indeed, for the most diffuse peak, the calculated L_c is 2.3 nm, which is on par with the BNNT wall thickness as measured from TEM images. The presence of a second (002) contribution with a

[‡]Whilst B_2O_3 is an oxidation product of h-BN, it does not readily crystallise at ambient pressures;[258–260] so crystalline B_2O_3 is not anticipated to occur here. However, H_3BO_3 formed from B_2O_3 interaction with ambient moisture has a well-defined crystal structure at ambient conditions. See Chapter 4, §4.3.3.2

	2θ (degrees)		**FWHM (degrees)**		**Crystallite Size (nm)**		**Layer spacing (nm)**
	(002)	(100)	(002)	(100)	L_c	L_a	d_{002}
h-BN powder 3M™	26.72	41.58	0.232	0.226	35	77	0.333
BNNT (curve i)	26.44	-	3.5	-	2.3	-	0.337
BNNT (curve ii)	26.60	-	0.8	-	10	-	0.335

Table 3.5: Crystallite sizes and d_{002} spacings calculated from 2θ and FWHM data derived from XRD patterns in Figure 3.13B & C for the reference 3M™ commercial h-BN powder and as synthesised BNNTs. See equations 2.2, 2.3 and 2.4. Note that whilst L_c, crystallite stacking height, is calculated for the BNNTs based on the deconvoluted (002) reflections, L_a is not calculable due to poor (100) peak resolution.

narrower FWHM suggests that larger L_c crystallite sizes (calculated as 10 nm) are also present in the sample. Larger diameter, thicker wall BNNTs, rarely observed by SEM in the sample (see Appendix B, Figure B.4) could be the source of this peak; these are not BNNTs synthesised by sacrificial templating but instead are BNNTs likely grown from exposed catalysts during the Ammonia Borane CVD process.

Whilst the BNNT L_c crystallite size was determined from the (002) peak, the crystallite basal plane size/ basal plane interdefect distance (L_a) is associated with the (100) reflection. See again Figure 2.17 for an illustration of L_c and L_a in the context of a nanotube. For the commercial h-BN powder reference, the (100) reflection is distinct, as shown in Figure 3.13C. However, the BNNT XRD pattern within this same 2θ range (40-44°) exhibits an evident low signal-to-noise ratio, and any (100) peak is also compounded by potential contribution from H_3BO_3. Consequently, it is not possible to analyse with confidence the (100) reflection of the BNNTs from this acquired XRD pattern. Nevertheless, both TEM and Raman analysis indicate that the L_a crystallite size of the BNNTs is on the order of magnitude <10 nm, which is smaller than the average circumference of these nanotubes ($2\pi \cdot radius \approx 60$ nm), thereby demonstrating a high defect density in the BNNTs synthesised here.

3.3.3 BNNT Composition

In this section, (i) EELS, (ii) XPS and (iii) UV-Vis spectroscopy characterisations of the synthesised BNNTs are examined to determine BNNT composition purity in terms of the extent of (a) graphitic carbon removal during the thermal oxidation treatment of the MWCNT@BN and (b) the introduction of oxygen impurities.

3.3.3.1 EELS analysis of BNNTs

As similarly done for the MWCNTs and MWCNT@BN specimens in Chapter 2, EELS was also conducted on the BNNTs here to determine their localised elemental composition.

Figure 3.14A shows the STEM image of a BNNT along with its EELS elemental maps for B,C,N and O. The corresponding EELS spectrum confirming the presence of these elements is depicted in Figure 3.14B. Whilst the hollow nature of the BNNTs is evident from TEM images (e.g. Figure 3.7), this is not as easily visible from the STEM image EELS maps presented here. This is a result of issues such as sample charging and drifting during the EELS mapping, which negatively affected the achieved spatial resolution. Indeed, the EELS maps in Figure 3.14 are of the more presentable of those collected from the BNNTs, with the least encountered specimen drift. It must thus be acknowledged that future work is needed to optimise the EELS collection parameters for these thin-wall, insulating BNNT samples.

Nevertheless, the preliminary EELS analysis of these BNNTs confirms that B and N are present, and remain in their sp^2 bonded networks expected of h-BN. This is based on the B-K and N-K edge profiles that have retained their π^* and σ^* features after the oxidation process, as highlighted in Figure 3.14C

Interestingly, the presence of carbon could indicate the incomplete removal of the MWCNT cores during sacrificial templating. However, further inspection of the C-K edge profile reveals that it closely resembles that of amorphous carbon,[63,261] with noticeably weaker π^* and σ^* features than apparent on the C-K edge of graphitic carbon; see Figure 3.14D. This thus implies that the detected carbon does not

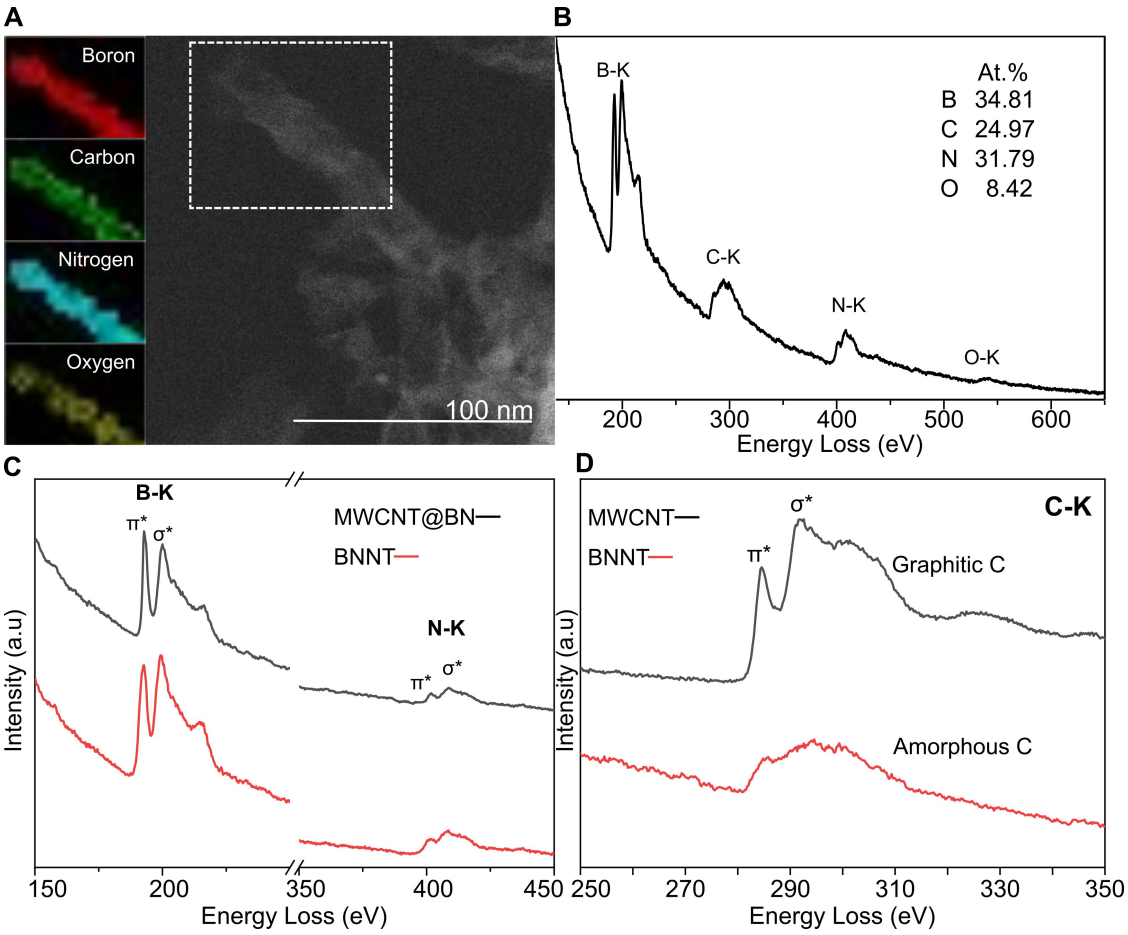


Figure 3.14: (A) EELS elemental maps for B,C,N and O of a single BNNT, from the region highlighted on the accompanying Dark Field STEM image. (B) EELS spectrum collected from the same BNNT shows B-K, C-K, N-K and O-K edges; calculated atomic composition is included. (C) The B-K and N-K edges of the BNNT and MWCNT@BN profiles are compared. (D) The C-K edges of the BNNT and MWCNT profiles are compared; the BNNT C-K edge profile is unlike that of graphitic carbon and most similar to amorphous carbon. EELS collection parameters are summarised in Appendix Table B.1

originate from unoxidised MWCNT, but instead most likely from contamination sources.

Meanwhile, the increased oxygen content detected on the BNNT, in comparison to its precursor MWCNT@BNs, is believed to be due to partial oxidation of the BNNTs themselves. This is further explored by XPS in the section below.

3.3.3.2 XPS analysis of BNNTs

XPS analysis was conducted to assess the purity of the synthesised BNNTs, particularly with regard to residual carbon content as well as oxygen impurities.

According to the XPS survey spectrum shown in Figure 3.15A, there is considerable reduction in the carbon content down to <1 at.%. Recall from the XPS survey spectrum of MWCNT@BN heteronanotubes (Figure 2.24) that the measured carbon content was 46.6 at.%. For further comparison, as shown in Figure 3.15B, the C1s spectrum intensity of the post-oxidation BNNTs is markedly reduced relative to that of the MWCNT@BN precursor, thus substantiating the targeted removal of carbon during the oxidation treatment. The residual low carbon content is reasonably assumed to originate from adventitious carbon, as also suggested by the EELS analysis (see also Chapter 4, §4.3.2.3).

Concurrently, there is also an increase in the cumulative B and N atomic % contribution in the analysed BNNT sample (77.4%) relative to that of the MWCNT@BN (47.3%), which is expected given that these are the dominant elements remaining after carbon is sacrificed. Noticeably however, the B:N atomic ratio has changed from 1.32:1 for MWCNT@BN, to 1.67:1 for the BNNT sample. This inflated bias toward B is likely associated with the partial oxidation of the h-BN, whereby N oxidation product, N_2, is more easily volatilised than B oxidation product B_2O_3. Moreover, O more preferentially substitutes with N sites instead of B sites because of a more similar electronegativity with the former.[178,262] The higher oxygen at.% content in the post-oxidised BNNT sample suggests the presence of oxygen functionalities on the BNNTs. Furthermore, peak broadening, particularly to higher binding energies, as witnessed for the B1s spectrum (see Figure 3.15C), corroborates the partial oxidation of BNNTs.

To further evaluate the chemical bond composition of the BNNTs, their high resolution B1s and N1s spectra are deconvoluted, as depicted in Figure 3.16A & B respectively. Fitted peak parameters are summarised in Table 3.6. In the B1s spectrum, the fitted synthetic peaks are attributed to photoelectrons emitted from B atoms in the following chemical environments: B-N (190.52 eV), B$-N_2O$ (191.7

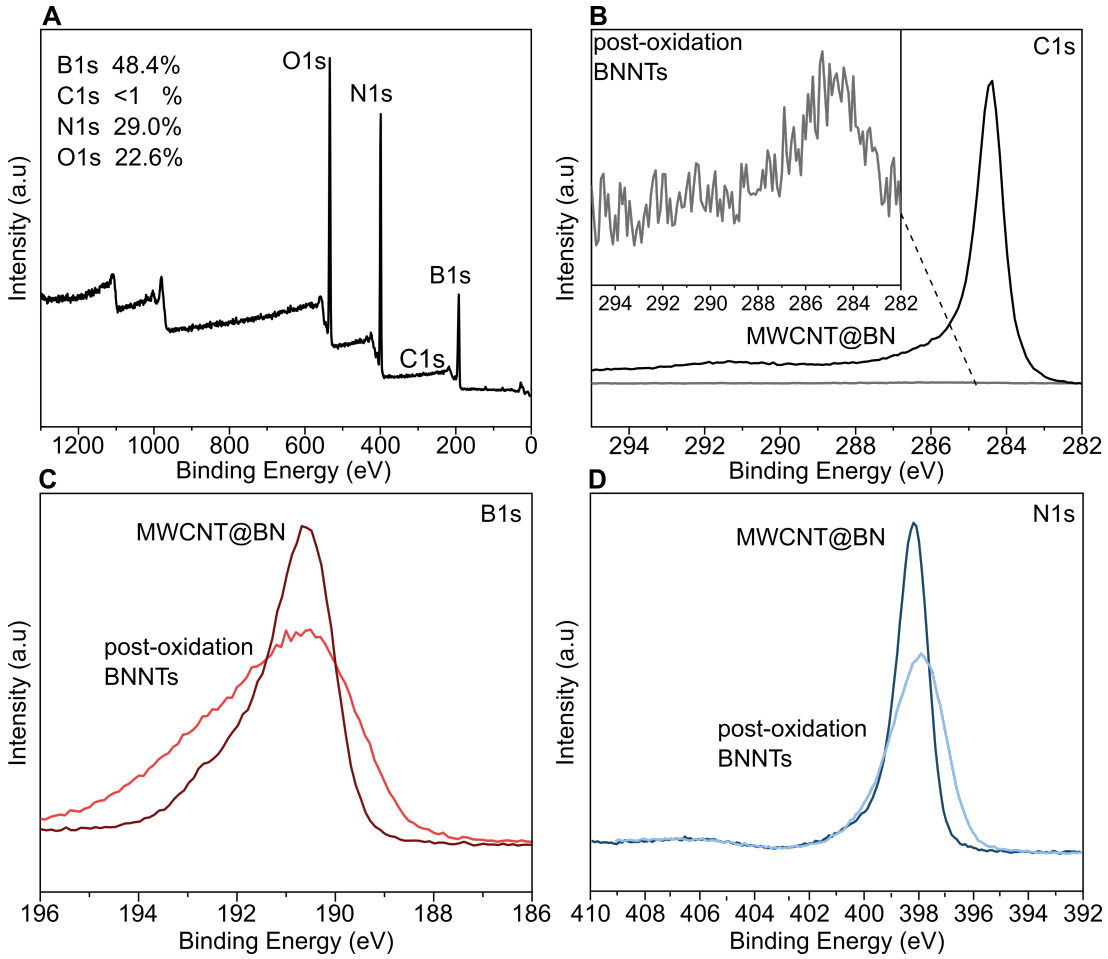


Figure 3.15: (A) XPS survey spectrum of BNNTs synthesised by 700 °C oxidation treatment of MWCNT@BN. (B-D) High resolution C1s, B1s and N1s spectra of BNNTs normalised to respective spectra of their precursor MWCNT@BNs. The low intensity C1s spectrum collected from the BNNTs is magnified in the inset of (B).

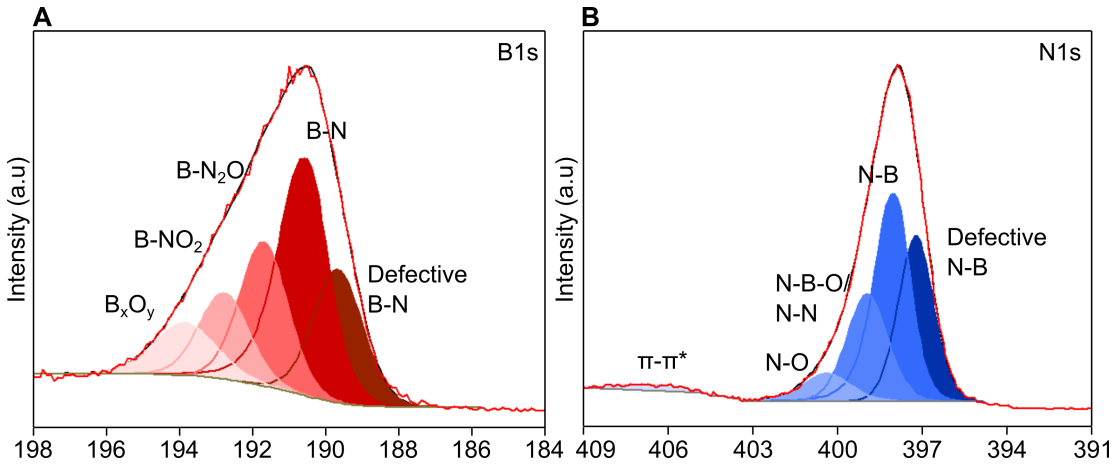


Figure 3.16: High resolution XPS (A) B1s and (B) N1s spectrum for BNNTs. High resolution peaks were fitted in CasaXPS with a GL-T lineshape for the B-N bonds and GL lineshapes for other bonds as previously demonstrated in Figure 2.24 for MWCNT@BNs.

B1s				N1s			
Bond	**Binding Energy (eV)**	**FWHM (eV)**	**% Area**	**Bond**	**Binding Energy (eV)**	**FWHM (eV)**	**% Area**
Defective B-N	189.67	1.58	19.65	Defective N-B	397.26	1.45	29.35
B-N	190.52	1.40	37.04	N-B	398.00	1.30	39.55
B−N_2O	191.7	1.55	20.74	N-B-O/ N-N	398.97	1.69	22.23
B−NO_2	192.78	1.60	12.85	N-O	400.40	1.98	6.71
BxOy	193.84	2.00	9.73	π-π^*	406.57	2.91	2.15

Table 3.6: Summarised description of synthetic peaks fitted to the high resolution XPS B1s and N1s spectrum of BNNTs as shown in Figure 3.16. Bond identifications are referenced from [178, 263–266].

eV), B−NO_2 (192.78 eV) and B_xO_y (193.84 eV). An additional synthetic peak at 189.67 eV is assigned to defective B-N, which accounts for the B1s peak broadening to lower binding energies visible in Figure 3.15C. This assignment of defective B-N could encompass single/double nitrogen vacancies and/or B-H bonds.[263,264] The presence of such defects is in line with the detected low crystallinity of the BNNTs after oxidation as outlined previously in §3.3.2.3. In comparison to the deconvoluted B1s spectrum of the MWCNT@BN (Figure 2.24 and Table 2.9), there is reduced B-N purity (56.69%; including defective B-N) in the BNNT product, alongside increases in contribution of the B−N_2O and B−NO_2 bonds which are associated with O substitution at N sites. Furthermore, the free oxide B_xO_y (e.g B_2O_3) component at high binding energies[263–265] is unique to the BNNT sample and is not detected in the B1s spectrum of the MWCNT@BN precursor.

In the BNNT N1s spectrum, synthetic peaks are assigned as follows: N-B (398.00 eV), N-B-O/N-N (398.97 eV), N-O (400.40 eV) and $\pi - \pi^*$ (406.57 eV). Notably, the cumulative contribution of oxygen-based impurities in the N1s spectrum is less than that found in the B1s spectrum, supporting the case of preferential substitution of O at N sites rather than B sites of the BNNT upon partial oxidation. As evident from Figure 3.15D, there is broadening of the N1s spectrum of the BNNTs to lower binding energies. In the deconvoluted N1s spectrum in Figure 3.16, this

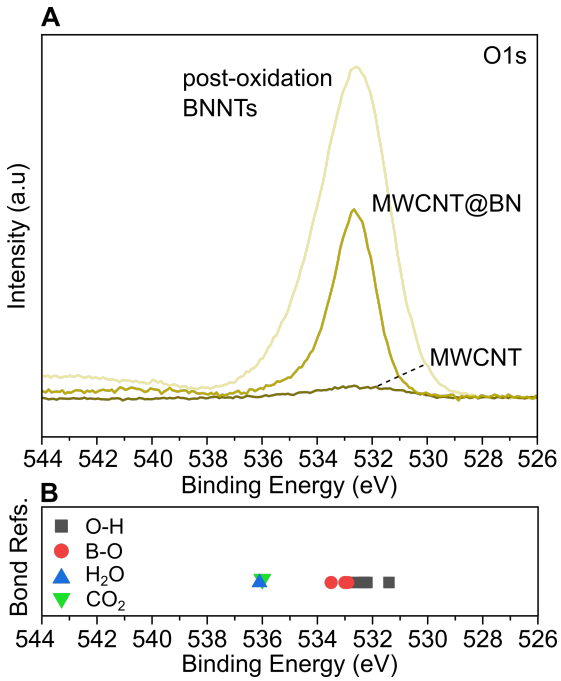


Figure 3.17: (A) XPS high resolution O1s spectrum collected from MWCNT, MWCNT@BN and BNNT samples. Spectra are normalised to the MWCNT O1s peak intensity. Increasing peak intensity and broadening to higher binding energies are likely associated with more B-O type bonds and physisorbed H_2O and/or CO_2, coinciding with literature binding energies compiled in (B). Bond references from [172, 179, 267–271].

broadening (fitted with a synthetic peak at 397.26 eV) is associated with lower crystallinity, defective h-BN bond environments.[266]

To support the attribution of oxygen related impurities in the B1s and N1s spectra, the O1s spectra was also inspected. As summarised in Figure 3.17, the intensity of the O1s peak increases from the original Nanocyl MWCNT, to MWCNT@BN and finally to the post-oxidation BNNTs as a result of increased atomic % contribution: 1.6%, 6.1% and 22.6 % respectively. The broadening of the BNNT O1s peak likely corroborates the occurrence of more B-O type bonds in the BNNTs, as well as the presence of adsorbed moisture.[§] This is inferred from summarised literature findings (Figure 3.17B) that O emitted photoelectrons exhibit increased energies in the following bond order: O-H< B-O< H_2O/CO_2.[172,179,267–271] However, a clear distinction between O impurities bonded to h-BN or present in

[§]The contribution of $Al_4B_2O_9$ impurities to the O1s spectrum, and also to the B1s spectrum of the BNNTs, is not considered here. The justification for this is the negligible Al 2p and/or Al 2s signals detected in the survey scan, thereby indicating low borate content in the analysed specimen region.

free oxide still remains nebulous in the reports on O1s spectra, as is the case for physisorbed species such as H_2O or CO_2. Generally, O1s spectra deconvolution is considered a non-straightforward task and as evident in the literature, O1s spectra are less commonly analysed for determining oxygen chemical states in BNNTs, whilst B1s and N1s are more favoured.

Overall, these XPS results point to the presence of oxygen impurities in the BNNT product, predominantly as O substituted into the h-BN lattice, as well as in the form of free boron oxides. There are two proposed times at which this oxygen is introduced. Firstly, the BNNTs themselves could become partially oxidised during oxidation treatment at 700 °C to remove carbon. This would suggest that the CVD deposited h-BN was not sufficiently crystalline to fully resist oxidation itself at this temperature. Secondly, low crystallinity h-BN is more susceptible to hydrolytic attack from ambient moisture at room temperature[195] (e.g.during sample storage), thereby contributing to further oxygen impurities. Consequently, this second phase likely exaggerates the extent of oxidation of the as-synthesised BNNTs.

3.3.3.3 UV-Vis Spectroscopy

To further confirm that (i) the MWCNT component of MWCNT@BN heteronanotubes was removed during the oxidation treatment and (ii) the residual nanotubes were indeed composed of h-BN, UV-visible absorption spectroscopy was conducted.

The UV-Vis absorption spectra of the Nanocyl MWCNT, followed by that of synthesised MWCNT@BN and BNNT samples are shown in Figure 3.18A-C respectively. For the pristine MWCNT, the broad absorption band in the UV wavelength range of the spectrum (<400 nm) is characteristic of π plasmon resonance (collective excitation of π electron).[272] This strong absorption feature is typical for all graphitic carbon nanomaterials. The split nature of the band, i.e. the presence of two peak maxima at 236 nm and 266 nm, is likely associated to optical anisotropy of the CNTs.[273] Notably, the π plasmon absorption peaks are still observable in the MWCNT@BN spectra (Figure 3.18B), but disappear in the BNNT spectrum (Figure 3.18C), thereby strongly supporting prior evidence that the core MWCNTs

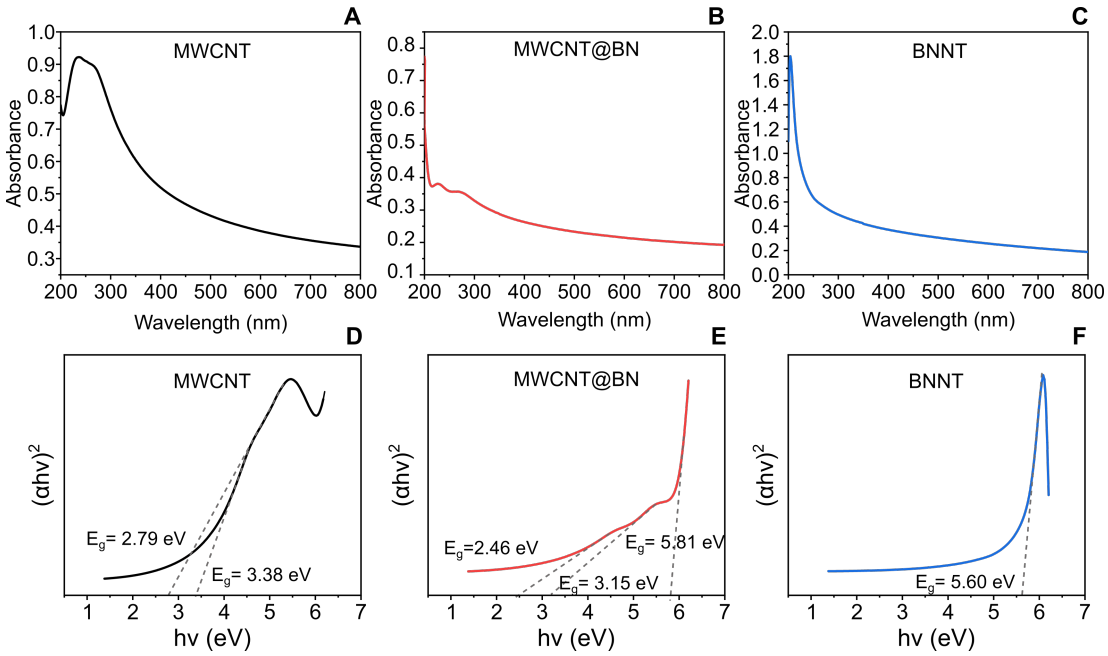


Figure 3.18: (A-C) UV-Vis absorption spectra of raw Nanocyl NC7000 MWNCT, and synthesised MWCNT@BN and BNNTs. (D-F) Corresponding Tauc plots with extrapolated optical band gap values shown.

were indeed removed by the oxidation treatment. The residual BNNT absorption spectrum has a distinct, narrow peak at 204 nm which is attributable to the excitonic absorption of h-BN.[274,275] Indeed, this h-BN excitonic peak is also present in the MWCNT@BN spectrum, thus corroborating its heteroatomic composition.

These UV-Vis spectra were further interpreted to estimate the optical band gap of the MWCNTs, MWCNT@BN and BNNTs according to Tauc plots, as shown in Figure 3.18D-F. These plots are generated according Equation 3.3, whereby α is the absorption coefficient,¶ h is Planck's constant, ν is photon frequency, C is a proportionality constant and E_g is the optical band gap.[276–278]

Accordingly, from the plots of $(\alpha h\nu)^2$ vs. hν, optical band gaps are estimated by extrapolating from the linear segments of the plots to the x-axis, where $(\alpha h\nu)^2$=0 and so E_g=hc/λ_g.

$$\alpha h\nu = C(h\nu - E_g)^{1/2} \tag{3.3}$$

¶The absorption coefficient α is calculated according to α=2.303A/l, such that A is absorbance and l is the cuvette pathlength.[279,280] This term for α is derived from the following two equations:[281,282] A=$\log\frac{I_o}{I}$ and I=$I_o e^{-\alpha l}$.

Of particular interest is that the estimated 5.6 eV band gap extrapolated for the BNNTs is in the range of the anticipated wide band gap for bulk h-BN and BNNTs (ca. 6 eV).[275,283,284] Notably, this E_g value for the BNNTs is slightly lowered compared to the 5.81 eV h-BN band gap component of the MWCNT@BN, which could be result of more oxygen impurities/defects present in the post-oxidised BNNTs.[285] Additionally, given that the multiple different band gaps extrapolated from the Tauc plot of MWCNT@BN can be individually matched to both the MWCNT and h-BN components, the van der Waals hybridisation of these nanotubes is further corroborated. Otherwise, for covalent hybrids with homogeneous single-phase domains of of $B_xC_yN_z$, individual band gap identities of h-BN and graphitic carbon are less likely to be retained and would be replaced by a single optical band gap.[175,181]

3.4 Conclusion

In this chapter, a method has been demonstrated for the synthesis of BNNTs via the thermal oxidation of MWCNT@BNs previously fabricated using APCVD and ammonia borane precursor (according to Chapter 2).

To begin, thermal oxidation conditions had to be tailored in order to achieve targeted sacrificing of the core MWCNT whilst maintaining the outer h-BN layers as a BNNT shell. This required the oxidation temperature to be at or beyond the onset oxidation temperature (T_O) of the MWCNT component, but below the T_O of the h-BN component. Via TGA, it was discovered that two factors influence the oxidative stability of the MWCNT core when it is part of the heteronanotube. Specifically, graphitisation of the MWCNT core itself occurs during the 1000°C CVD process and causes a 100°C increase in T_O temperature relative to the raw MWCNT, from 500°C to 600°C. This graphitisation factor, corroborated by XRD and Raman results in Chapter 2, has not previously been considered during analysis of the oxidation behaviour of MWCNT@BN heteronanotubes, and is recommended here as a requisite to interpretation of oxidation behavior in both the literature and in future works. Secondly, the presence of the h-BN layer has a protective capacity and further increases T_O of the MWCNT by 100°C, to 700°C. The temperature at

maximum oxidation rate (T_{MAX}) is another metric obtained from the 1st derivative of the the TGA plots, which similarly showed an upward trend in value from MWCNT, to annealed MWCNT and MWCNT@BN. In addition to increasing the oxidation onset temperature of the MWCNT core, the h-BN sheath was also found to reduce the rate of oxidation by 50%. The above summarised quantitative understanding of oxidation behaviour of the MWCNT@BN was important in informing the selection of conditions, i.e. temperature and duration of oxidation, for targeted removal of the MWCNT core.

The post-oxidised product was examined to essentially address the following: (i) the extent of graphitic carbon removal, (ii) the extent of h-BN preservation, specifically in a nanotube morphology i.e. as a BNNT, and (iii) the resultant quality of the BNNT, e.g. its crystallinity and h-BN purity.

The immediate indication of graphitic carbon removal during oxidation is the off-white colour of the product, which is in stark contrast to the black/dark grey appearance of the MWCNT and MWCNT@BN precursors. Examination of this off-white powder by SEM and TEM revealed its constituent nanotubes. Considering the visual change alongside the detection of h-BN signatures in collected FTIR, EELS and XPS spectra, the residual nanotubes are identified as the BNNT shells remaining after sacrificing of the MWCNT core. This conclusion is further corroborated by the dimensions of the BNNTs as measured from TEM images. Specifically, the thickness of the BNNT walls corresponds with the thickness of deposited h-BN, and the inner diameters of the BNNTs are close to the outer diameters of the previously encapsulated MWCNT template, i.e the MWCNT core was removed, leaving the BNNT shell.

The full extent of graphitic carbon removal was further supported by XPS, EELS and UV-Vis. Particularly, neither XPS or EELS spectra of the BNNTs showed evidence of graphitic carbon components, and the UV-Vis spectrum of the BNNTs exhibits only the h-BN excitonic peak without π plasmon peaks associated with graphitic carbon. However, despite the evidence of graphitic carbon removal, carbon was still detected in the post-oxidised product. According to XPS, the BNNTs

have residual carbon content <1 at.%, with the C1s spectrum a peak characteristic of amorphous carbon. Similarly, the EELS C-K edge profile of BNNT exhibits weak π^* and σ^* features, which is in line with amorphous carbon. However, 25 at.% carbon content was detected by EELS, which is different to the low residual carbon content as detected by XPS. It must be acknowledged that the statistical significance of the single presented EELS map and elemental quantification of BNNTs is not arguable, and further sampling would be ideal. This was however limited by issues encountered during STEM/EELS analysis of the BNNTs, including significant sample charging and sample drift. As the XPS technique can probe a much larger number of nanotubes, elemental quantification is likely to be more representative of the overall sample. In any case, the presence of amorphous carbon in the BNNT sample might be accounted for by adventitious carbon contamination, as previously demonstrated in other BNNT products in the literature, and which is prevalent on all surfaces exposed to air. An alternative hypothesis is that the carbon may be residual from the MWCNT, but no longer graphitic due to oxidative damage, and bonded to the BNNTs in such a way to avoid volatilisation during the oxidation process. Given that there was limited evidence of bonding between the h-BN and MWCNT components in Chapter 2, the adventitious carbon hypothesis is preferred here and is further expounded in Chapter 4.

There is also evidence, according to XRD, XPS, and FTIR that the BNNTs produced here are partially oxidised. Primarily, XRD characterisation of the BNNTs reveals free oxide derived impurities, e.g. H_3BO_3 derived from B_2O_3, which is an oxidation product of h-BN. Broadening of the B1s XPS spectrum to higher binding energies also points to an increase in B-O related bonds in the BNNT structure, which justifies the increase in XPS surveyed oxygen content to 22.6 at.%. A weak hydroxyl peak was also present in the FTIR spectrum. Because oxygen was already present in the MWCNT@BN for reasons hypothesised in Chapter 2, this oxygen would also be residual in the BNNTs. Additional oxygen contamination is likely introduced by oxidation of the BNNT at h-BN defect sites, and also during moisture adsorption under ambient storage.

As for nanotube crystallinity, characterisation by TEM and XRD confirm that the BNNTs have disordered, turbostratic walls. Owing to the low intensity of the (100) XRD peak as well as the presence of oxide impurity contributions, a quantitative estimation of BNNT L_a crystallite size based on the XRD data size was not possible. However, extracted L_c crystallite size and d_{002} interlayer spacing values, albeit not as valid descriptors of crystallite size in comparison to L_a for a turbostratic nanotube structure, are on the magnitude expected of a disordered h-BN material. Furthermore, an estimation of L_a crystallite size (2 nm), based on an empirical relationship between the Raman E_{2g} FWHM of h-BN and L_a, also aligns with the magnitude as observed by TEM.

In comparison to BNNTs synthesised by other CVD techniques, the BNNTs synthesised here have the advantage of being highly selective to cylindrical morphologies, i.e. are structurally homogeneous and not composed of a mix of bamboo, cylindrical and/or other morphology tubes. Furthermore, whilst other CVD fabricated BNNTs tend to have larger outer diameters >100 nm owing to size dependency on thermoagglomerated catalysts, it is possible to achieve by this method not just smaller, but also tunable BNNT diameters based solely on the diameters of the starting MWCNT template. The BNNTs synthesised here are also uniquely turbostratic, which may explain their lower thermal stability relative to highly crystalline BNNTs. Further research to improve the crystallinty of BNNTs as synthesised by this method is proposed in Chapter 5.

Chapter 4

Macroscopic sheet architectures of Boron Nitride Nanotubes

Contents

4.1 Introduction 124
4.2 Synthesis of BNNT buckypaper by sacrificial templating 133
4.2.1 Materials and Methods 133
4.3 Results and Discussion 136
4.3.1 Buckypaper Structure 136
4.3.2 Buckypaper Composition 145
4.3.3 Buckypaper surface platelet formation 155
4.4 Conclusion 176

4.1 Introduction

In this chapter, a new fabrication route for BNNT buckypapers is explored, involving translation of the syntheses detailed in Chapters 2 and 3 to the macroscale.

In view of the composite and integration opportunities offered by BNNT buckypapers discussed in the introduction (see Chapter 1, §1.3.3), this specific macro-assembly is selected here as a high priority for investigation into new methods of accessible and versatile synthesis. To begin however, the already existing methods of BNNT buckypaper fabrication must be reviewed, as done here for the first

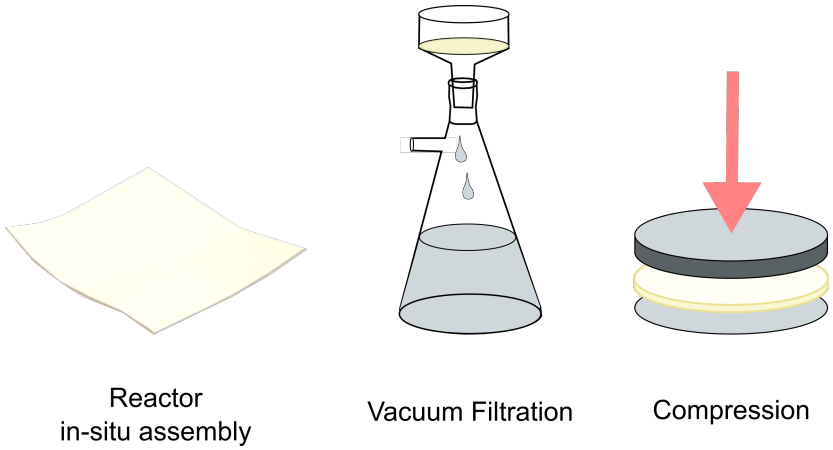


Figure 4.1: Illustration of the present methods used to synthesise BNNT macroscopic sheet assemblies in the literature.

time. These methods are categorised below into three groups: *in situ* growth, filtration and compression. Summarised in Table 4.1 are all reported examples of BNNT self-supporting sheet-like macro-assemblies, including all buckypapers and similar architectures that have been alternatively named (due to non-standardised nomenclature), e.g. mats, pellets, cloth-like deposits, and free-standing thin films.

***In situ* synthesis** The manufacturing of macroscopic BNNT assemblies most often involves post-processing steps, with pre-made BNNTs then compacted into sheets. Fewer methods exist that allow growth of BNNTs into as-synthesized macroscopic free-standing sheets. The most productive of such a method is Hydrogen-assisted BNNT synthesis (HABS), whereby BNNT sheets are formed inside the induction thermal plasma reactor.[63] Although the quality of BNNT is consistent, there appears to be diversity in the morphology of BNNT sheet-like materials generated by HABS. 'Cloth-like' deposits of up to 20×50 cm have been reported, which could also be delaminated into diaphanous thin films/membranes.[63] Other thicker sheets which could not be delaminated were also synthesized, either with random[37] or partially aligned[27] BNNTs with reported continuous areal dimensions of up to ca. 13×11 cm. HABS produced BNNT macro-assemblies (also including aerogels, webs, yarns) do however have as-synthesized impurities

Types of BNNT Freestanding Sheet Macroassemblies	BNNT synthesis method	BNNT characteristics: Diameter (nm)	No. of walls	Length (μm)	Processing Steps	Assembly Characteristics: Thickness (μm)	Density (g/cm^3)	Ref
In Situ Growth Techniques								
a. BNNT cloth-like deposits	HABS[63]	ca. 5	2-5	Few	Formed in HABS reactor	Few mm (thin film layers peeled off e.g. 0.2 μm)	0.15	[37, 63]
b. Partially aligned BNNT Buckypaper	HABS	ca. 5	2-5	Few	Deposited on rotating cylinder inside HABS reactor	–	0.16	[27]
c. Bamboo BNNT thin film	N-ISC+CVD[286]	60-80	>30	–	Substrate spraycoated w/ boron+catalyst ink; Heat treated in N_2 +H_2, Peeled off with blade	20-50	0.12	[286]
Filtration Techniques								
d. BNNT Buckypaper, BNNT+CNT hybrid Buckypaper (Sandwich, Janus)	HABS	ca. 5	2-5	Few	Purification,Stirring, Horn/Bath Sonication Filtration (Water/Methanol)	15-150	0.3-0.5	[37, 63] [27, 287]
e.BNNT Buckypaper, Sandwich Buckypaper (SWCNT/BNNT/SWCNT)	HTP[61]	1-10	2-5	ca. 200	Sonication, Filtration (N-methyl-pyrrolidone)	ca. 10 (in sandwich)	–	[49]
f. BNNT films, thicker mats	HTP	1-10	2-5	ca. 200	Mixing, Centrifugation Supernatant Extraction Filtration (Chlorosulfonic Acid)	<1-1.5 & thicker mat	–	[81]
Compression Techniques								
g. BCNNT mats, BNNT mats	Substitution/ Oxidation[88,89,288]	6-8	<10	–	BCNNTs Pressed, Annealed, Oxidized	700	–	[289]
h. Cylinder BNNT pellet,	BOCVD[71]	10-80	ca. 10	ca. 10	Pressed with 40 MPa	1000-2000	–	[253]
Bamboo BNNT pellet,	BBO+NH_3 CVD[290]	10-100	>100	–				
Collapsed BNNT pellet	BOCVD+Pt catalysis[291]	10-80	-	ca. 10				
i. BNNT mat	HTP	1-10	2-5	ca. 200	Pressed with 5.8 kPa	2300-6300	0.02	[292]
j. BNNT mat	HTP	1-10	2-5	ca. 200	Pressed 0.47-22.97 MPa	145-706	0.11-0.51	[293]

Table 4.1: Summary of BNNT macroscopic sheet assemblies reported in the literature, sorted according to the method of fabrication. The dimensions of BNNTs in the assemblies are compiled, along with the macroscopic assemblies' processing steps and overall thickness and density.

including amorphous boron particles encapsulated in h-BN, contributing around 20-30% mass of product.

The other method of *in situ* BNNT sheet manufacturing is via the use of nanocatalyst-assisted ink spray coating (N-ISC) onto stainless steel substrates, which are then exposed to a furnace environment.[286] The yield is considerably smaller scale than that of the HABS method, with sheets (referred to here as free-standing films) less than 100 μm thick with small surface area. N-ISC is very selective to larger diameter tubes of bamboo morphology, which has been used as an argument in favour of HABS because small diameter, highly crystalline cylindrical BNNTs 'fully take advantage of the distinct phenomena occurring at nanoscales'.[63] Notable is that the films do not separate from the substrate spontaneously, but must be forcibly peeled off with a blade, indicating there is the likelihood of damage in film continuity during the peeling process. Whilst the HABS process is entirely metal catalyst free, the N-ISC produced films will inherently have encapsulated catalysts (Fe_2O_3) nanoparticles as impurities.

Generally, the *in situ* produced BNNT sheets/films have low density and have properties less versatile to control in comparison to macro-assemblies made by other methods as discussed below.

Filtration Vacuum filtration of nanotubes in liquid suspension is one of the earliest methods of bulk sheet synthesis of CNTs, and was the method used for the first ever coined 'bucky paper'.[97] The nanotube bulk material is compacted into a sheet by the pressure gradient acting on the filtrate. Due to the historically lower availability of BNNTs, manufacturing of BNNT buckypaper by filtration has always been precluded. However, with the emergence of higher yield processes that can produce 200 mg h^{-1}[61] via the High Temperature and Pressure method (HTP) or even 30 g h^{-1} via HABS[27,63], BNNT buckypaper synthesis by filtration is now possible. Buckypapers of up to 30×1 m have been synthesized via an in-house made vacuum filtration setup, which is the largest reported scaling up effort for a BNNT buckypaper assembly.[27]

The vacuum filtration methods implemented to date involve a purification step prior to filtration of the BNNTs. HABS synthesized BNNTs undergo an extensive 3-day oxidation treatment followed by solvent washing to remove amorphous boron and B_2O_3 respectively,[27,63] as inspired by Chen *et al.*[294] This appeared to remove the majority of boron impurities, as evidenced by thermogravimetric analysis of the purified product,but h-BN flakes and shells remain alongside the BNNTs. Following purification, the BNNTs are subjected to a multi-step process of stirring and sonicating to disperse them in water/methanol. Details on the BNNT concentration and the duration of the dispersing regime are not given in publication.

HTP BNNT buckypapers have been purified by an alternative process that does not involve sonication, which has been shown to damage/shorten BNNTs even in aqueous solutions.[295,296] BNNTs were mixed with Chlorosulfonic Acid (CFA- a 'true solvent')[297] via speed stirring and after centriguation, a supernatant of purified BNNTs was extracted and washed with ethanol and water.[81] Removed impurities include elemental boron, B_2O_3 and $B_xN_yO_z$, as characterised in the precipitate. Non BNNT h-BN polymorphs were still found in the purified product, but in smaller ratios to BNNT structures than before purification.

HTP BNNTs have also been sonicated in N-methylpyrrolidone and filtered to form part of a sandwich buckypaper made of filtered SWCNT/BNNT/SWCNT in the sequence.[49] This ability to form these layered hybrid buckypapers of CNTs and BNNT is a advantage of the filtration technique and has only been demonstrated this way as of yet. Sandwich buckypapers of a BNNT core layer with CNT outer layers or CNT core layer insulated by BNNT layers have been fabricated via vacuum filtration, as well as so-called Janus, two sided BNNT/CNT buckypapers.

Besides the diversity in solvents used, another filtration parameter than can be varied is the filter membrane material and pore size. Filter membrane materials reported to date for pure BNNT buckypaper synthesis are 20μm pore sized polycarbonate[63] and 20 nm pore sized alumina filter paper.[81] As the affinity of the BNNT buckypaper to the membrane should be low in order for it is peel off easily, membrane selection necessitates further investigation and discussion in the literature.

Besides just filtering, Adnan *et al.* also transferred their HTP BNNT 'thicker films' from the alumina filter paper onto a perfluroalkoxy alkane (PFA) substrate before peeling off with tweezers; as to why a transfer process was required is not addressed.[81]

Filtration produced BNNT buckypapers tend to be more dense than BNNT assemblies produced otherwise. An example of this is given by the comparison of HABS BNNTs buckypapers made *in situ* versus vacuum filtration (as seen in Table 4.1); filtration facilitates the production of buckypapers that are up to around 3 times more dense than possible via *in situ* growth. Of course, this difference is partly due to the fact that a more significant quantity of BNNT material can be filtered to make a buckypaper. For example, BNNTs extracted from 300 mg of raw material were filtered to make only 1-1.5 μm thickness films with apparently centimeter scale area.[81] In terms of buckypaper microstructure, filtration tends to give rise to a mutlilayered architecture[287] and facilitates more uniform macroscopic thicknesses in comparison to *in situ* grown sheets.[37]

The filtration technique is inherently adaptable, allowing control of BNNT buckypaper dimensions , both areal size and thickness, which can be determined by the quantity of material used and the filtration setup measurements. The starting BNNT can technically be sourced from any manufacturer, so there is potential to make a diverse range of BNNT buckypaper materials with various BNNT morphologies. However, this potential is not realized because only a few production methods exist that can supply enough material to satisfy the requirements of the filtration process to produce free-standing buckypapers (i.e. seemingly more than 100 mg even for a lab scale filtration setup).

The challenge of dispersing BNNTs such that there are more individualized, non-agglomerated tubes in a stable suspension is not heavily featured in the BNNT buckypaper literature mentioned above. Using sonication and particular solvents such as CFA were explored to address this issue. Interestingly, surfactants were not introduced to assist with the BNNT dispersal, but their implementation can potentially benefit the production of macroscopic assemblies of BNNT made via filtration as BNNTs exhibit poor dispersibility in most solvents.[298] So the

issue of dispersion is an unfavourable factor of the filtration technique as it is an added consideration in buckypaper production that does not exist for non-liquid processing techniques.

Compression Whilst filtration uses a negative pressure to compact BNNTs, it is also possible to use weights/pistons to compress BNNTs into free-standing assemblies. The scale to which this has been accomplished has been notably small in comparison to methods discussed above. Literature on such methods of production tend to refer to the BNNT macroassemblies as pellets or mats instead of buckypapers, perhaps because of the considerable thicknesses produced, some reaching several mm dimensions (See Table 4.1). The area of these mats/pellets is on the mm-cm scale, with the largest being 31.8 mm in diameter[292] and the smallest at 4×1.5 mm.[289] The control offered by using compression is that both quantity of BNNT material and pressure applied can be manipulated to vary the sample thickness and density.[292,293] Although density is not consistently reported for all cases of using this method, it appears that very uniquely low densities can be made,[292] as well as densities crossing the range that is possible by *in situ* fabrication and filtration techniques.[293]

Unsurprisingly, BNNTs sourced to make the largest of compressed mats are from a high yield product, i.e. HTP BNNTs. The smaller mats/pellets are made using alternative BNNT sources, with one study producing pellets of three types of BNNTs (cylindrical, bamboo and collapsed).[253]

Synthesis by Sacrificial Templating Common to all *in situ*, filtration and compression methods described above is that the the BNNTs are first synthesised and subsequently assembled. An alternative approach would be to pre-fabricate the macroscopic assembly with a precursor material, e.g. CNTs, and then convert all the precursor into BNNTs whilst preserving the the original assembly architecture. Such a conversion entails multi-scale sacrificial templating, as both the nano-scale CNTs and their macro-scale assembly act as templates that determine the (i) structure of individual BNNTs and their (ii) arrangement.

There have been very few studies that have demonstrated CNT based multi-scale sacrificial templating for the fabrication of BNNT macro-assemblies.

The earliest study that implemented this strategy reported synthesis of a mm-scale BNNT mat (smaller than $4 \times 1.5 \times 0.7$ mm^3) that was tested for thermal conductivity.[289] In this case, the original template mat (made by compression of powders) was composed of $B_xC_yN_z$ nanotubes synthesized via a substitution reaction; MWCNTs were reacted with B_2O_3 and N_2 at 1600 °C.[88,89] According to characterisation of the substituted $B_xC_yN_z$ nanotubes, it appeared that there was strong radial phase separation of the C and BN into inner and outer coaxial layers respectively.[249] Subsequent oxidation treatment to 650 °C of the $B_xC_yN_z$ nanotubes led to removal of the carbon core, leaving few wall BNNTs (as analysed from converted powders and not from the mat itself).[288] This study thus presented a cursory description of the BNNT mat product, with no optical/microscopic visualisation or further detailed composition analysis at the macroscale.

More recently, the sacrificial templating concept has been demonstrated for the formation of BN aerogels (composed of BN nanotubes and nanosheets) from MWCNT-graphene composite aerogel templates (cm-scale),[94] and vertically aligned BNNT forests from VA-MWCNTs templates (mm-scale).[96] In both of these cases, instead of implementing a substitution reaction and depending on phase separation of BN and C, h-BN was introduced as a outer coating layer on the CNTs by CVD,

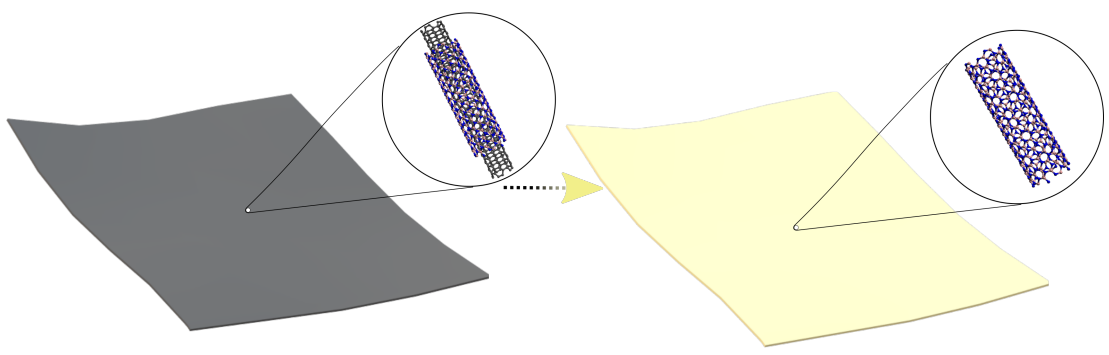


Figure 4.2: Illustration of sacrificial templating concept at the macro-scale for fabrication of BNNT buckypaper.

via the borazine and B_2O_3+NH_3 precursor routes respectively. The CNTs were then removed by thermal oxidation.

As demonstrated in this work, it is also possible to synthesise BNNTs by first synthesising coaxial coatings of h-BN onto CNTs via the ammonia borane precursor pathway (Chapter 2), followed by oxidative treatment to selectively sacrifice the core CNT (Chapter 3).

In this chapter, the syntheses investigated in Chapters 2 & 3 are extended to the macro-scale in order to evaluate their effectiveness in fabricating BNNT buckypapers; see Figure 4.2.

There are several advantages that motivate this direction of study. As documented in relation to high-yield commercially available BNNT sources most often used for buckypaper fabrication, there are usually other BN polymorphs present (e.g. spheres) that are difficult to completely purify from the product. A sacrificial templating method presents high selectivity to one specific BN polymorph, e.g. BNNTs, if the template itself has a high purity of that polymorph, e.g CNTs. Secondly, templating is predicted to be a very versatile technique for BNNT buckypaper fabrication. The more mature field of CNTs and their assemblies presents a wide range of templates (both in terms of CNT dimensions and buckypaper architecture) to potentially use for BNNT buckypaper conversion. This diversity could open up new areas for investigation of BNNT buckypaper properties. In comparison, buckypapers made from commercially available BNNT sources are currently limited to only a few types of BNNTs with fixed dimensions. Finally, the method presented here is accessible on the lab scale and has potential for upscaling, with no requirement for highly specialised equipment.

4.2 Synthesis of BNNT buckypaper by sacrificial templating

4.2.1 Materials and Methods

4.2.1.1 Fabrication of MWCNT/h-BN heteronanotube buckypapers

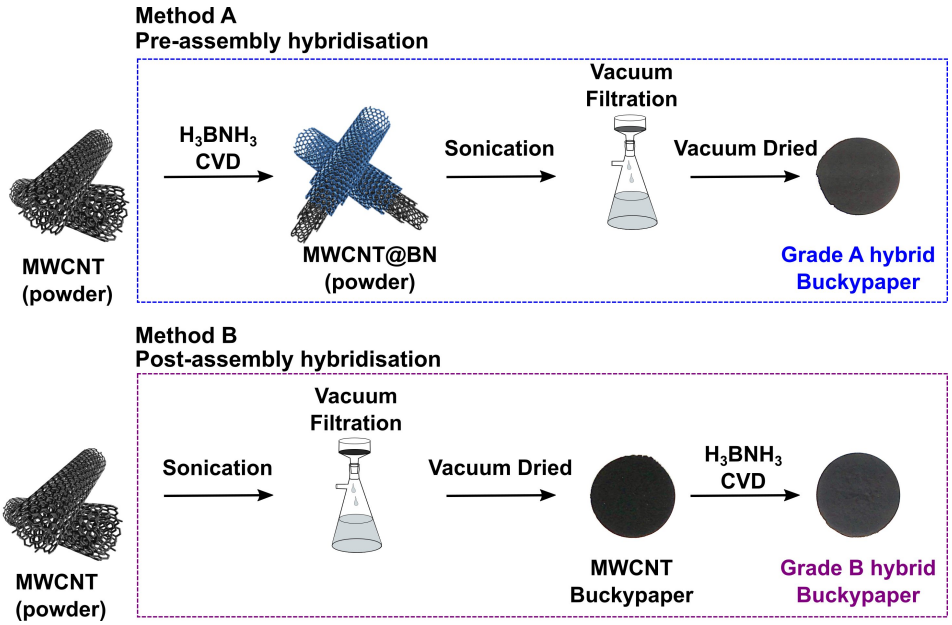


Figure 4.3: Schematics of hybrid buckypaper production for two investigated methods A and B. In Method A, MWCNT are coated with h-BN prior to buckypaper assembly, i.e. pre-assembly hybridisation. Alternatively, post-assembly hybridisation in practised in Method B, whereby already assembled MWCNT buckypapers were coated with h-BN. Buckypapers (17 mm diameter) shown are real optical images of fabricated samples.

Two grades of heteronanotube buckypapers were fabricated according to two different methods A and B outlined in Figure 4.3.

Method A involved first subjecting the MWCNTs to CVD h-BN coating according to the method described in Chapter 2. This was then followed by the buckypaper fabrication steps, involving sonication, vacuum filtration and finally vacuum drying. As the h-BN is introduced onto the MWCNTs prior to buckypaper fabrication, the Grade A buckypaper produced is referred to here as pre-assembly hydridised.

Alternatively, in Method B, the buckypaper was first fabricated using pristine MWCNTs, which was then subjected to the same CVD h-BN coating procedure. As such, the Grade B buckypaper is referred to here as post-assembly hybridised.

At the stage of buckypaper fabrication in both Method A and B, nanotube powder ca. 4 mg was dispersed into 20 mL of ethanol solution in a glass vial. These solutions were then sonicated in an ultrasonic bath at room temperature for 4 hours at a frequency of 20 kHz. Following sonication, the dispersions were vacuum filtered onto Whatman's Cyclopore track etched, polycarbonate filter paper with 0.4 µm pore size. The buckypaper and filter paper samples were vacuum treated overnight and then the buckypaper was carefully peeled off the filter paper.

Due to the diameter of the filtration cylinder in contact with the filter paper, all buckypapers synthesised were 17 mm in diameter.

4.2.1.2 Fabrication of BNNT buckypapers

4.2.1.2.1 Oxidation of hybrid buckypaper templates Both Grade A and B hybrid buckypapers, fabricated according to methods outlined in §4.2.1.1 above, were used for sacrificial templating synthesis of BNNT buckypapers.

For the 'sacrificing' step, a hybrid template buckypaper was positioned horizontally on a quartz slide, which was placed into the quartz reactor tube inside the furnace (same setup used for CVD in Figure 2.4). The buckypaper was subsequently oxidised under air flow (1.8 L/min from an air pump) at 700 °C for 1 hour for selective removal of graphitic components while leaving residual h-BN in the buckypaper.

4.2.1.2.2 Sonication and Vacuum Filtration of BNNT powder Attempts were also made to fabricate BNNT buckypapers via the direct sonication and vacuum filtration of the BNNT powders as synthesised in Chapter 3. Details and discussion of this fabrication route, which did not result in free standing BNNT buckypapers, are included in Appendix C, §C.1.

All further discussion in this chapter is therefore related to the new BNNT buckypaper fabrication methods involving the use of hybrid buckypaper templates as presented in §4.2.1.1 and §4.2.1.2.1.

4.2.1.3 Sample Preparation & Characterisation

Pieces of buckypaper were cut/broken off from the as synthesised samples for characterisation by SEM, FTIR, TGA and XPS (same equipment and settings used in Chapter 2, §2.2.1.3). Additionally, these samples were analysed by Energy Dispersive X-ray spectroscopy (EDX) utilising the Oxford Instruments Xmax 150 EDX system installed on a Zeiss Merlin SEM. Specific EDX spectral acquisition details are given for each individual spectrum included in the results.

In preparation for SEM/EDX analysis, buckypaper pieces were secured onto carbon sticky tabs and subsequently sputter coated with 8 nm of platinum. In some cases, silver paint was dabbed onto an edge of the buckypaper to establish a better conductive point of contact between it and the SEM tab. These steps were necessary to prevent charging of electrically insulating buckypaper samples during electron microscopy. Several samples were also prepared with the buckypaper directly secured on the stainless steel SEM stub using only the silver paint as glue.

Surface structures observed on the buckypapers were collected for further TEM analysis by carefully dragging a TEM copper grid across the surface of buckypapers (NB: not platinum coated).

XPS depth profiles were also acquired from buckypaper, using an EX06 ion source on the Thermo Scientific K-α system as the sputter beam. This ion gun was operated at 2 kV , whilst the X-ray beam size used was 100 μm.

Mass measurements of buckypapers, used in calculating their mass density, were obtained on the Mettler Toledo Balance, which has a resolution of 0.01 mg. Thickness measurements of buckypapers were obtained by analysing SEM buckypaper cross sections and by use of Mitutoyo digital thickness gauge that has a resolution of 0.001 mm. Resistivity measurements were conducted using a four-point probe, as detailed further in Appendix C, §C.2.

4.3 Results and Discussion

This section is divided into three themed subsections for discussion.

Firstly, in §4.3.1, the macroscopic structures of the BNNT buckypapers as synthesised according to two different fabrication protocols are analysed and compared.

Next, in §4.3.2, the purity of the BNNT buckypapers is probed with particular attention to carbon, both graphitic and adventitious.

Finally, in §4.3.3, platelet structures observed on the surface of BNNT buckypapers are characterised to determine their chemical identity and to understand their growth mechanism.

4.3.1 Buckypaper Structure

Here, buckypaper structure is described by characterisation of the following parameters:

- Geometry, cross sectional architecture, nanotube alignment (Optical imaging, SEM)
- Thickness, density and pore size (Thickness guage, SEM & ImageJ image analysis tools).

Additionally, TGA and electrical resistivity measurements help in evaluating hybrid MWNCT@BN buckypaper h-BN content prior to their subjection to thermal oxidation for BNNT buckypaper production; this is relevant to establish a link between h-BN content and the final BNNT buckypaper structure.

4.3.1.1 Geometry, Cross Section Architecture & Nanotube Alignment

Buckypaper structural parameters such as geometry, cross-sectional architecture, and nanotube alignment are investigated here for both the original templates and their post-oxidation products.

In Figure 4.4, SEM images of the Grade A and Grade B hybrid buckypapers are shown. Evident from these images is the layered architecture of both types of

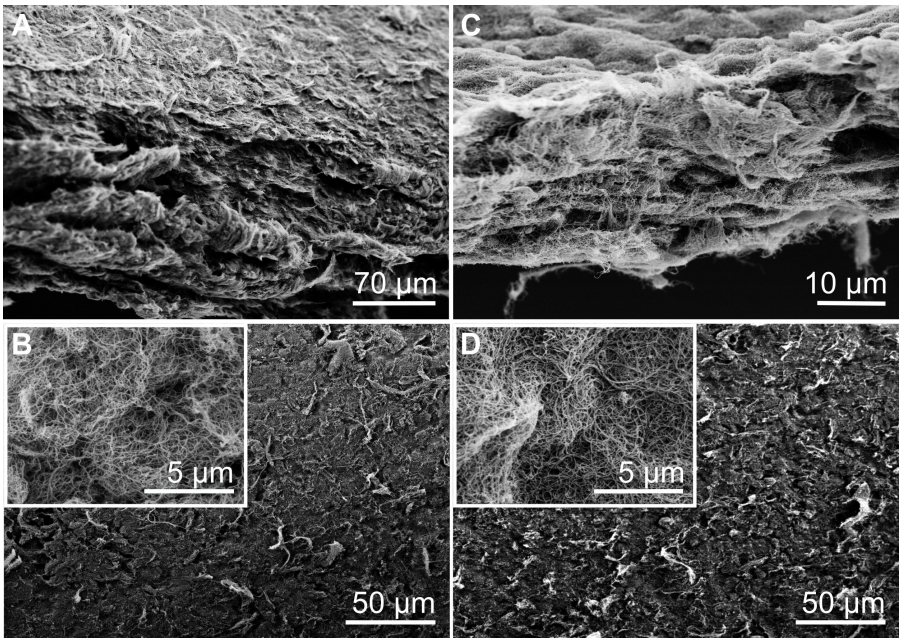


Figure 4.4: SEM of h-BN coated MWNCTs manufactured into buckypapers according to pre-assembly hybridisation (Grade A) and post-assembly hybridisation (Grade B) (See Figure 4.3). Layered cross sections, surface roughness and the random alignment of nanotubes (inset) are shown for for Grade A (Figures A-B) and Grade B (Figures C-D) buckypaper respectively. Acceleration voltage: 3 kV

buckypaper, which is typical of vacuum filtered nanotube sheet assemblies.[299,300] Some nanotube agglomerates are still visible on the buckypaper surface images, indicating that individual nanotube dispersion were not achieved by the implemented sonication procedure. This gentle dispersion procedure, involving use of a sonication bath instead of sonication probe and without the use of surfactant, was intentionally designed to preclude the possibility of exfoliation and damage to the h-BN coating on the MWCNT surface. This is more relevant to Grade A hybrid buckypapers whereby the MWCNT@BN are sonicated prior to assembly into buckypaper. As anticipated, random alignment of nanotubes is achieved from this process for both Grade A and Grade B hybrid buckypapers, as shown in the high magnification inset SEM images in Figure 4.4.

Subsequent to the oxidation process, changes in buckypaper structure are observed. At the macroscopic scale, the BNNT buckypapers undergo visible changes in colour, size and shape compared to their original hybrid templates, as shown in Figure 4.5. The BNNT buckypaper produced by sacrificing the Grade A hybrid

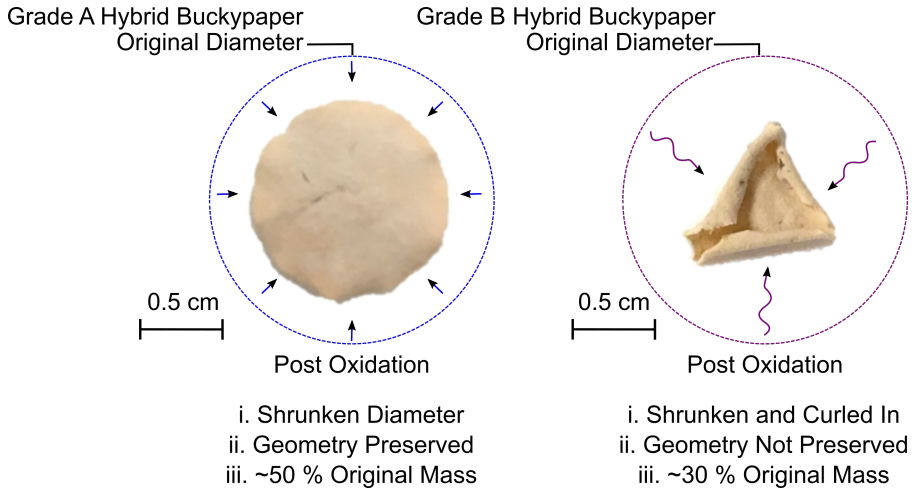


Figure 4.5: Macroscopic optical top view of BNNT buckypaper products made by thermal oxidation of Grade A and Grade B hybrid buckypapers. The changes to buckypaper geometry and size are illustrated to scale.

shrinks in diameter, yet preserves its original geometry, in this case a circular shape. However, the BNNT buckypaper produced by sacrificing the Grade B hybrid shrinks in size and curls towards the center, thereby not preserving its template's original flat, circular shape, and becoming less practical for application. The distinct difference in macroscopic geometry of the Grade A and Grade B product is also captured in SEM images in Figure 4.6A (flat) and 4.7A (curled) respectively.

Also apparent in Figure 4.6B,C and Figure 4.7B,C is a more cliff-edge type cross section of the BNNT buckypapers in comparison to the lesser defined, layered cross section observed in the original hybrid buckypapers (Figure 4.4A,B). Noticeably, there are still randomly entangled nanotubes in the oxidised buckypapers (Figure 4.6E and Figure 4.7E), in addition to large and prevalent platelet-type structures growing on the both surfaces. These platelets are discussed in detail later in §4.3.3.

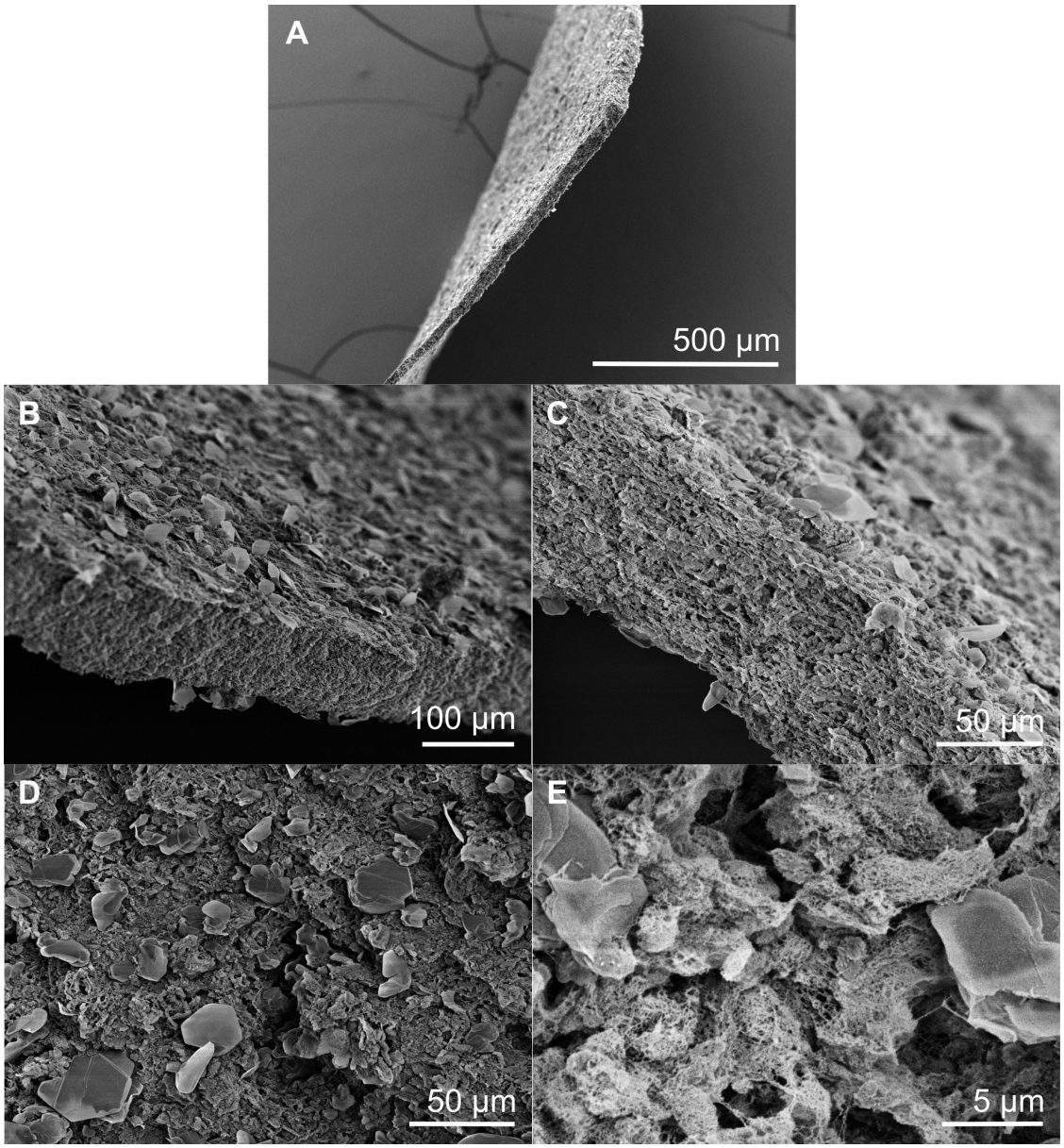


Figure 4.6: SEM images of BNNT buckypaper produced by oxidation treatment of Grade A hybrid buckypaper. The flat shape is depicted in (A), and cliff type edges are shown in (B-C). Platelet structures were discovered on the buckypaper surfaces, as depicted in (B-D). Nanotubes were still preserved in a random orientation, visible in (E). Acceleration voltage: 3 kV

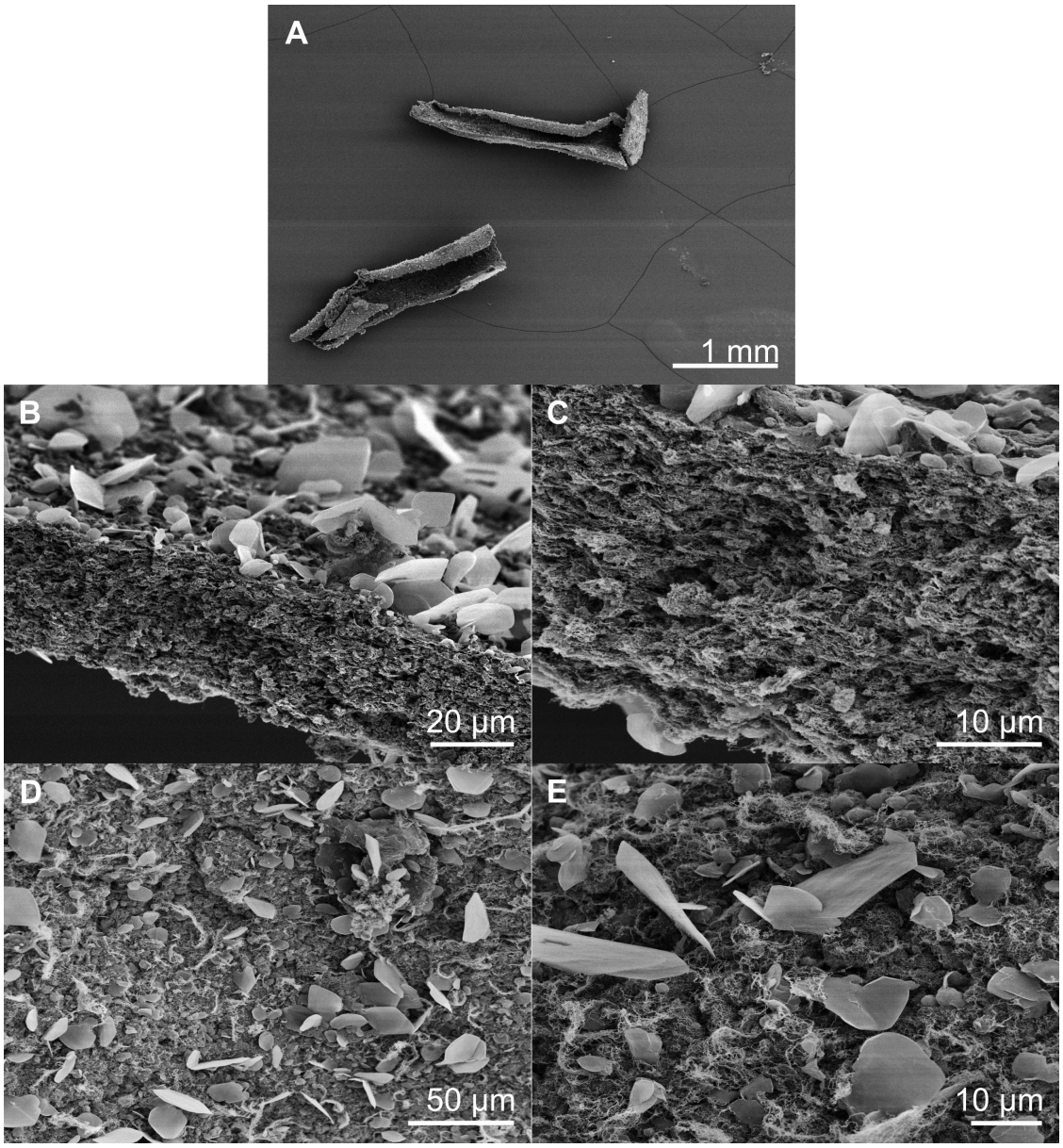


Figure 4.7: SEM images of BNNT buckypaper produced by oxidation treatment of Grade B hybrid buckypaper. Compared to the flat assembly seen in Figure 4.6A, this product undergoes edge curling as depicted in (A). Cross sectional architecure is shown in (B-C). Platelet structures were again discovered on the buckypaper surfaces, as depicted in (B-E). Nanotubes were still preserved in a random orientation, visible in (E). Acceleration voltage: 3 kV

4.3.1.2 Thickness, Density & Pore Size

The thickness achieved for the BNNT buckypaper was also found to be dependent on the route of synthesis, i.e. Grade A vs. Grade B oxidised.

For the equivalent starting hybrid buckypaper mass of ca.4 mg, average thicknesses achieved (prior to oxidation) were in the range of 115-140 μm for Grade A hybrids, and 110-120 μm for Grade B hybrids (See Figure 4.8A). Within both grades, each buckypaper itself also exhibited thickness variation at different points of measurement (by thickness gauge)*, with a standard deviation between ca. 5-10 μm. Subsequent to thermal oxidation, the BNNT buckypapers obtained from Grade A retained average thickness of 80-90 μm whilst Grade B was much thinner at around 30-40 μm (See Figure 4.8A).

The shallower residual thickness of BNNT buckypapers obtained from the Grade B hybrid suggests a lower composition of h-BN compared to that of Grade A. This is corroborated by thermogravimetric analyses of Grade A and Grade B hybrids, such that the Grade B hybrids only had a 30% residual weight subsequent to oxidation up to 900 °C, whilst the Grade A hybrids had 50% (Figure 4.8C). As the Grade B hybrid is manufactured by coating an already pre-formed MWCNT buckypaper, the higher density of the buckypaper relative to the loose powder MWCNT likely contributes to decreased gas permeability and more tortuous gas flow, and thus a lower efficiency of h-BN precursor vapour infiltration and deposition onto the MWCNT walls, as summarised in Figure 4.8C. Indeed, the inverse relationship between nanotube assembly density and the efficiency of a CVD h-BN coating process has been demonstrated by Tay *et al.*, 2015 when infiltrating h-BN into VA-MWCNT forests.[96] The lower efficiency of h-BN precursor vapour infiltration into the Grade B buckypaper might also result in less uniform h-BN coating amongst the MWCNT, thus accounting for uneven shrinkage during oxidation, and thus the curling observed in the BNNT buckypaper product.

*Whilst the thickness of hybrid buckypapers of MWCNT@BN were measured using a thickness gauge, this was not possible for the BNNT buckypapers primarily due to their brittleness (compared to their more flexible starting templates). All BNNT buckypaper thicknesses were thus measured from SEM images of buckypaper cross sections.

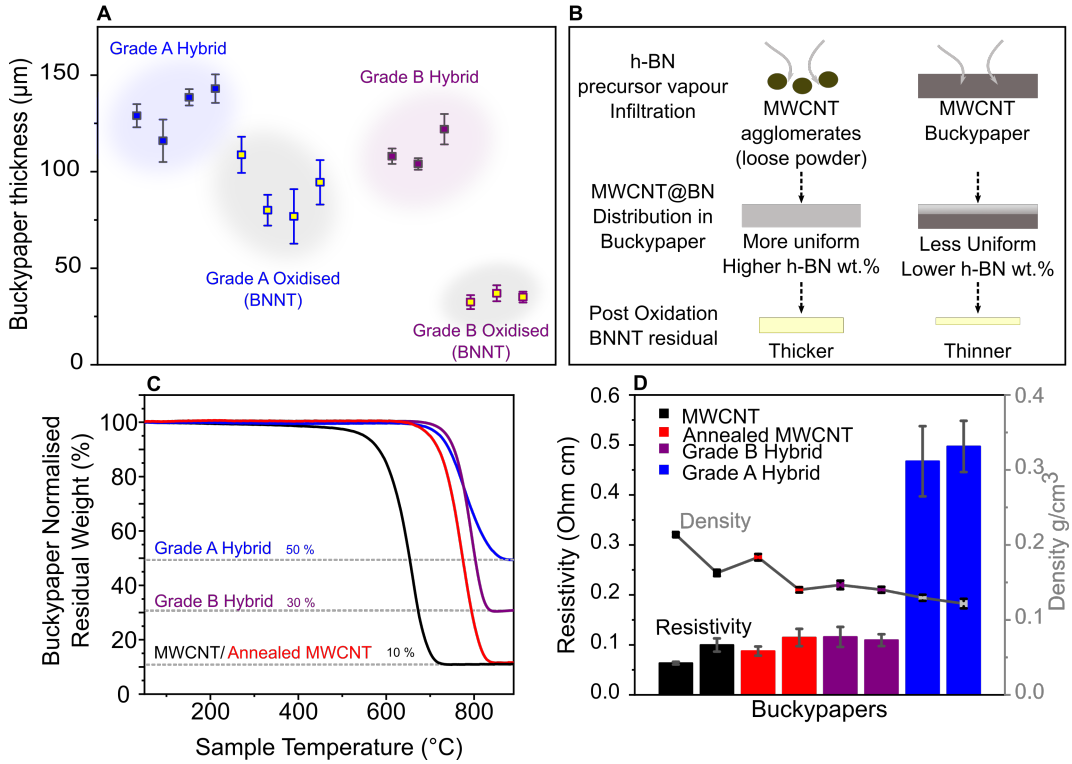


Figure 4.8: (A) Buckypaper thickness measurements for Grade A and Grade B Hybrids and their respective oxidised BNNT products. (B) The observed thickness difference for the two grades of BNNT buckypaper is explained by the accompanying schematic. (C) Thermogravimetric analysis of buckypapers confirms the increased residual weight of Grade A buckypapers (higher h-BN composition) relative to Grade B and control buckypapers after oxidation. (D) Resistivity measurements reveal increased resistivity of Grade A buckypaper, confirming a higher and more uniform composition of h-BN.

The improved uniformity of h-BN coating in the Grade A hybrid buckypapers is further confirmed by their increased electrical resistivity (ca. 0.5 Ω·cm) relative to Grade B, as well as to control MWCNTs buckypapers without any h-BN (all ca. 0.1 Ω·cm; See Figure 4.8D). Resistivity was measured using a four point probe, as described in Appendix §C.2. As h-BN is a wide band gap electrical insulator, it can behave as a dielectric spacer at CNT-CNT junctions within the buckypaper, thereby lowering junction resistance and the strongly correlated overall nanotube network resistivity of the buckypaper.[301,302] It is possible to eliminate the contribution of density factors[303] to the resistivity increase of the Grade A hybrid, as it shares a similar density to the control data. Therefore, the relative increase of the Grade A hybrid buckypaper electrical resistivity is attributable to the presence of h-BN

coating on the MWCNTS, such that within the fabricated nanotube network, many junctions are insulated by h-BN. In the scenario that fewer junctions are insulated due to a reduced efficiency of h-BN coating, then the buckypaper resistivity is likely to show a smaller or no increase in resistivity. This is the case for the Grade B hybrid buckypapers, whereby there are two postulated causes for fewer h-BN insulated junctions. Firstly, there is a lower h-BN content present in Grade B due to more limited precursor vapour infiltration into a denser sheet assembly compared to a loose powder. Secondly, CNT junctions in a buckypaper are pre-established, so infiltrating h-BN precursor at this stage results in wrapping of h-BN around the entirety of the existing CNT-CNT junctions, leaving the contact area as exposed CNT. This later point has been demonstrated in SWCNT network aerogels and thin films treated with CVD of h-BN, whereby negligible increase in electrical resistivity was recorded.[125,132] Here, the detectable difference in electrical resistivity between the Grade A and Grade B hybrid buckypapers illustrates their different degrees of h-BN coating uniformity and distribution within the MWCNT networks. This further justifies why these starting sacrificial template assemblies inherently lead to different BNNT buckypaper products after oxidation.

Quantitative assessment of buckypaper densities was made by modelling them as cylinders with regular, circular top and bottom faces and even depth. As this estimate includes the material pores, it is in fact the bulk density and not the true density.[304] For the hybrid buckypapers both Grade A and Grade B, the estimated bulk density is low, within the range of 0.12-0.15 g/cm^3. This method of density approximation was more challenging for the BNNT buckypapers, particularly those with irregular geometries. However, for BNNT buckypapers which maintained regular geometry (and thus more estimatable surface area and volume), bulk density was approximated from one sample to be ca. 0.17-0.2 g/cm^3, which is within the similarly low density range as other BNNT buckypapers fabricated in the literature (See Table 4.1).

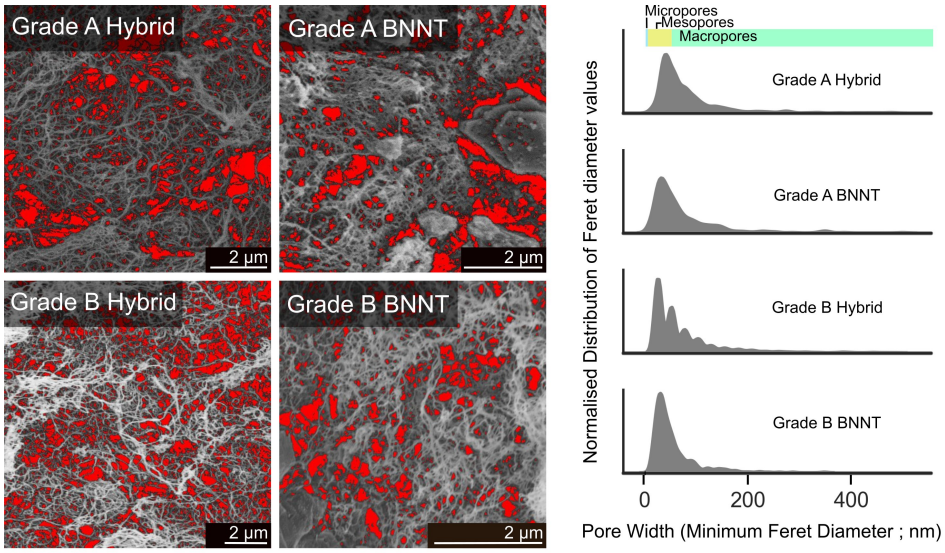


Figure 4.9: (A) SEM images of surfaces representing different grades of buckypaper fabricated here, with pore spaces identified in red by image threshold adjustment in ImageJ software. (B) Apparent pore sizes are measured according to minimum Feret diameter. The obtained distributions show that all buckypapers exhibit apparent meso/macroporosity (2-50 nm and >50 nm pore diameters.)

Another microstructural property of any buckypaper assembly is its pore-size distribution. The porosity of a nanotube assembly strongly influences its permeability to liquids/gases. This is relevant when considering such assemblies as liquid purification or gas separation membranes,[305] or as network fillers to be impregnated, e.g by a polymer matrix, for composite fabrication.

Estimates of pore sizes for all buckypaper types fabricated here were obtained from SEM image analysis of buckypaper surfaces. This method only allows for apparent pore size measurement, given that the buckypaper depth dimension is not examined.[306–309] As shown in Figure 4.9A, images were processed to highlight void areas. These areas were then analysed for their size, particularly the minimum Feret diameter, † used here as a representation of the pore width for the irregular shapes. According to the IUPAC categorisation of pore size, micropores are <2 nm, mesorpores are 2-50 nm and macropores are >50 nm.[304] As such, based on the typical SEM surfaces images shown in Figure 4.9A, both Grade A and Grade B hybrid

†The Feret diameter is often used for image analysis measurement of irregularly shaped particles (in this case pores), and describes the distance between two parallel tangential lines on the outline of the particle. The minimum Feret Diameter is the smallest such distance.

and post-oxidised BNNTs buckypapers largely exhibit mesoporous/macroporous structure (Figure 4.9B). Whilst a general magnitude of apparent pore sizes and distribution is achieved by this method, further work could obtain more accurate distributions for detailed comparison between buckypapers, perhaps by mercury intrusion porosimetry[310] or the Barret–Joyner–Halenda calculation based on N_2 adsorption isotherms.[306,307,309]

4.3.2 Buckypaper Composition

This section provides insight into the BNNT buckypaper chemical composition by (i) EDX and (ii) XPS analysis.

4.3.2.1 Probing Composition by EDX

Of interest here is the h-BN purity of the BNNT buckypapers synthesised by sacrificial templating. This purity is dependent on the presence of inherent impurities in the starting material, the extent to which carbon is effectively removed from the macroscopic buckypaper assembly during the oxidation process, as well as the introduction of new impurities during oxidation, particularly oxygen.

In terms of inherent impurities, Al_2O_3 and/or $Al_4B_2O_9$ are expected, given that this is present in the original MWCNT templating material before and after the h-BN coating process respectively (as detailed in Appendix §A.3.)

Whilst graphitic carbon appeared to be effectively removed from the MWCNT@BN powders subjected to oxidation (Chapter 3), this is not immediately assumed to be the case for the buckypaper assemblies and is thus further investigated.

EDX analysis of BNNT buckypaper samples (e.g. Figure 4.10) appeared to reveal residual carbon content after the oxidation treatment, alongside the principle B and N constituents that collectively account for ca. 60 at.%. Carbon compositions of less than 20 at.% (e.g Figure 4.10 and Appendix Figure C.4) or less than 10 at.% (e.g. Appendix Figure C.5) were detected. This inconclusive carbon residual content is made more nebulous by the fact that the EDX technique does not facilitate identification of the type of carbon, i.e. amorphous, graphitic *etc.* Thus, adventitious

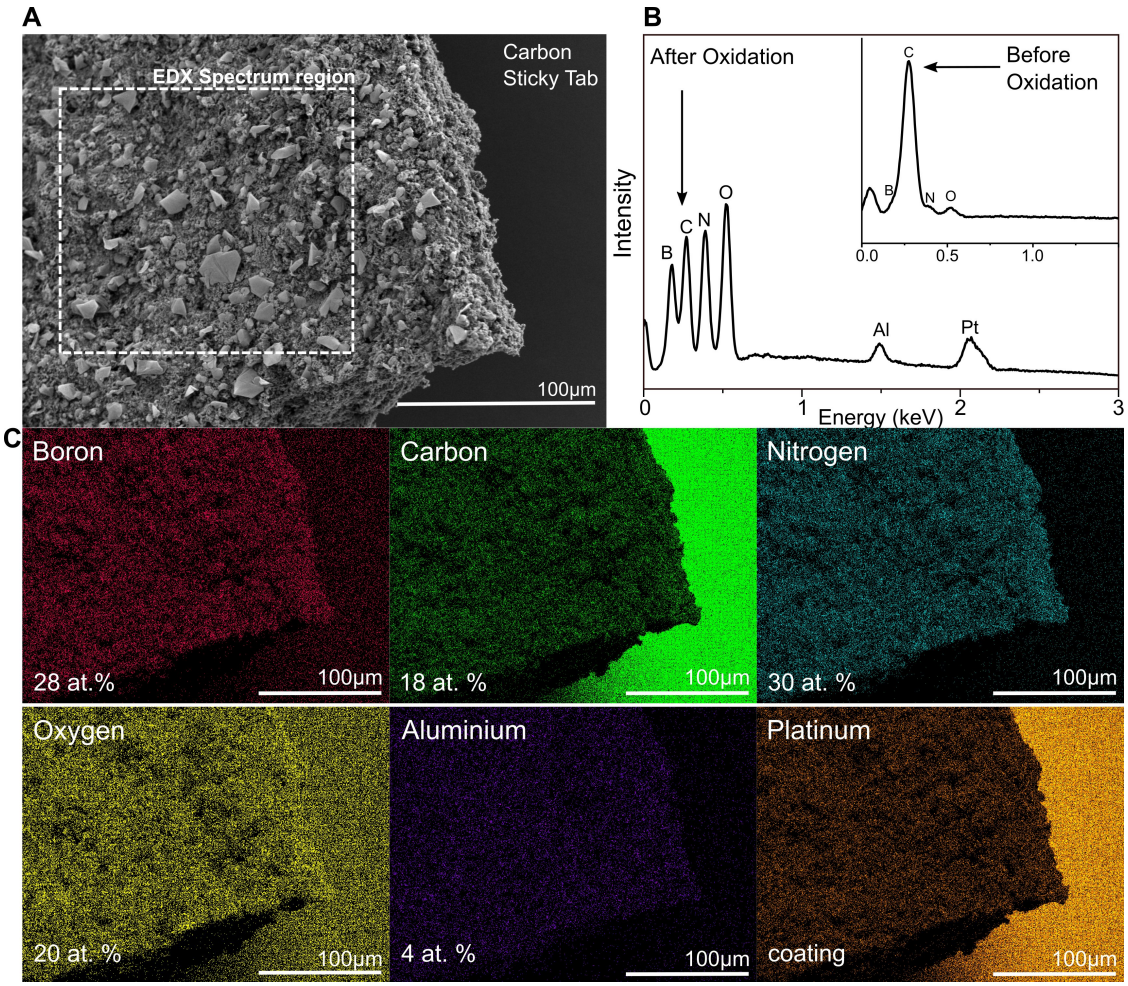


Figure 4.10: (A) SEM image of a buckypaper after thermal oxidation treatment to remove MWCNTs, leaving BNNT shells in the macroscopic assembly. The accompanying EDX spectrum for the outlined region is shown in (B), along with EDX elemental maps in (C). B and N are the main components, collectively accounting for ca. 60 at.% . Carbon content has indeed decreased compared to pre-oxidation buckypaper (see inset of (B)), but is still present in a form unidentifiable by EDX (i.e. graphitic, amorphous, hydrocarbon contamination *etc*). Oxygen impurity is also present in the buckypaper. EDX acquisition details (Acceleration Voltage: 3 kV, Pixel Size: 0.293 μm, Energy per channel: 5 eV, Dwell time: 176 μs, Stage Tilt: 0 °, Detector Elevation: 30 °)

carbon or even hydrocarbon contaminants introduced during Pt sputter coating (see §4.3.2.3 and §4.3.3.4.2) are non-eliminatable as contributing sources of EDX-detected carbon in the buckypapers. Further exploration of the nature and distribution of buckypaper residual carbon, specifically by XPS analysis, is discussed in §4.3.2.2.

Aside from considerations of carbon, it is evident that the buckypaper oxygen content increases upon oxidation. As highlighted in Chapter 3, the oxidation

treatment at 700 °C also leads to partial oxidation of the CVD deposited h-BN, giving rise to B-O type impurities such as B_2O_3. As exemplified by the EDX analysis in Figure 4.10 and Appendix Figure C.4, oxygen content reached ca. 20 at.%. Notably, for an oxidised buckypaper sample left in storage for a much longer period (several months), oxygen content detected was relatively higher, e.g. approaching 40 at.% in Appendix Figure C.5. This spike in oxygen hints towards the BNNT buckypaper instability under atmospheric conditions during extended storage. This phenomenon is explored to greater detail in §4.3.3 when explaining the evolution of large platelet structures on the buckypaper surface.

4.3.2.2 Composition Depth Profiling by XPS

In this section, XPS depth profiling conducted on a BNNT buckypaper is detailed, with one of the primary objectives being interrogation of the extent of carbon removal from the hybrid template buckypaper macroscopic assembly subsequent to oxidation treatment.

On its own, XPS is a surface analysis technique usually probing to depths of 10 nm of the specimen. However, paired with a sputtering ion beam, the surface can be etched at intervals, as illustrated by the schematic in Figure 4.11A, thus facilitating XPS analysis of the specimen composition with a depth resolution.

The XPS atomic % composition depth profile of a probed BNNT buckypaper area is shown in Figure 4.11B for the elements B, C, N and O. Here, 21 levels were scanned, including the buckypaper surface, from etch time 0-1200s at 60s intervals. According to software settings, the etch rate achieved was 5nm/s (and hence total etch depth of 6000 nm or 6 μm). However given the non-calibrated sputter rate for this novel material, the exact depth of probing is not precisely quotable and as such depth is henceforth considered qualitatively in relation to increasing etch time.

4.3.2.2.1 Carbon Depth Profile Regarding the carbon depth distribution, the measured atomic % composition indicates a decrease from 26 at.% on the buckypaper surface to 9 at.% after 1200s etch time, at which point this at.% appears to already be plateauing (Figure 4.11B). In the context of oxidative removal

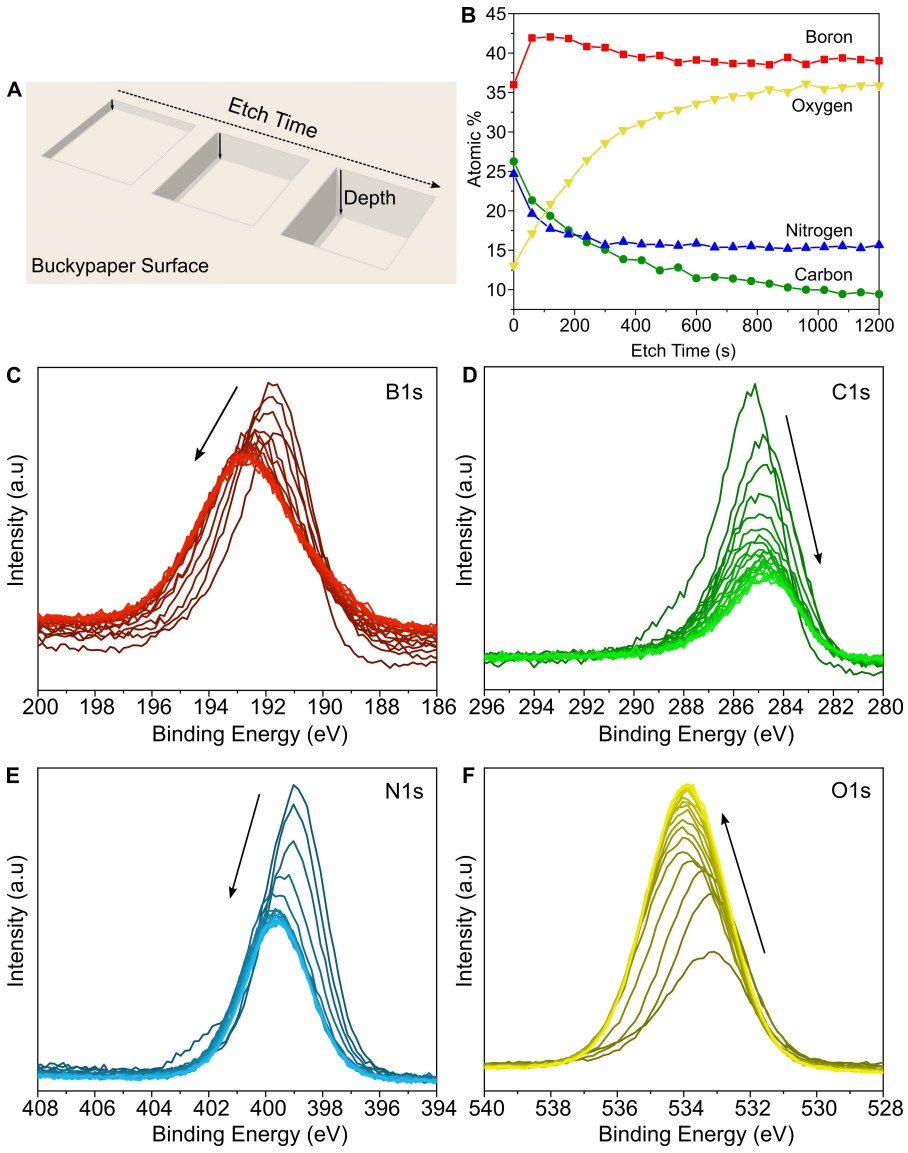


Figure 4.11: (A) Schematic of buckypaper depth profile experiment by ion beam etching. (B) BNNT buckypaper XPS depth profile composition results for B,C,N and O at 21 probed depth levels (60s etch intervals) and 1200s total etch time. (C-F) High resolution XPS of B1s, C1s, N1s and O1s at increasing depth, corresponding to each etch time data point in (B). Arrows point in direction of peak shift and change in intensity with increasing etch time. Peaks are normalised to their respective maximum intensities obtained at etch time 0s. Depth profile parameters: EX06 Ar ion beam at 2 kV; X-ray beam area 100 μm.

of graphitic carbon from the buckypaper, this result appears counter-intuitive given that the more accessible place for oxygen to attack is the buckypaper surface; the surface should have lower carbon content compared to the buckypaper interior, but the opposite is measured here. The most probable explanation for the high surface carbon content is that it is mainly adventitious, i.e. introduced from external

sources to the buckypaper surface and not native to the buckypaper itself.

Considering that the presence of adventitious carbon is a well established phenomenon and is practically ubiquitious on samples exposed to air,[311] and even on cleaned samples exposed to vacuum conditions in the XPS chamber,[312] the presence of adventitious carbon on the BNNT buckypaper is highly likely and evidence of this is discussed here.

Typically, adventitious carbon is formed in a thin layer (few nm) and is comprised of a diverse mix of oxidised carbon species and hydrocarbons. In most cases, the ratio (R) of oxidised carbon to hydrocarbon species is ca. $0.1<R<0.3$ such that the C1s XPS spectrum of adventitious carbon is usually dominated by a narrow hydrocarbon peak (ca. 285 eV) and small shoulder to the higher binding energies associated with oxidised carbon species.[311,313] However, it is also possible for the adventitious carbon to exhibit a heavily oxidised signature, whereby there are significant quantities of oxidised species relative to the hydrocarbon. In this scenario, the C1s spectrum becomes broadened to the binding energy range >285 eV.[311] As such, the C1s spectra collected from the BNNT buckypaper surface (and interior) match the signature of heavily oxidised adventitious carbon, given their rather broad peak widths, as exemplified in Figure 4.12A in comparison to the narrow graphitic C1s peak of a Nanocyl MWCNT reference spectrum. However, it does appear that the C1s peak position at etch time 0s (buckypaper surface) deviates further to higher binding energies compared to the C1s peak at etch time 1200s (as also evident in the C1s spectral evolution with depth depicted in Figure 4.11D). This difference is further explored to highlight its implications regarding the nature of carbon on the buckypaper surface compared to carbon in the buckypaper interior.

Deconvolution of the buckypaper high resolution C1s peaks at etch time 0s (Figure 4.12B) and 1200s (Figure 4.12C) reveals that significant synthetic peak contributions in the higher binding energy shoulder are attributable to oxygen-containing carbon species, such as hydroxyl/phenol groups (C−O), keto/quinone groups (C=O) and carboxylic groups (O−C=O).[172] Collectively, these oxygen-containing functionalities, typical of adventitious carbon and common in the observed

quantitative order C−O > C=O,[311] are present at a higher percentage at the buckypaper surface (56%) compared to its interior (34%), as calculated from the peak areas summarised in Table 4.2

To conform with the previous C1s XPS peak fitting done on graphitic MWCNT (see Figure 2.22), the buckypaper C1s spectra were fitted with synthetic peaks for defective C, sp^2 carbon and disordered C for components with binding energies $\leqslant$ 285 eV (Figure 4.12B-C and Table 4.2). These fittings presuppose that there is residual carbon of the graphitic nature in the BNNT buckypaper that was not removed during the oxidation process. Note that disordered carbon can refer to dangling bonds in graphitic carbon, and its peak position is also congruent with that of amorphous carbon (285 ev),[171] whilst defective carbon is attributed to lattice

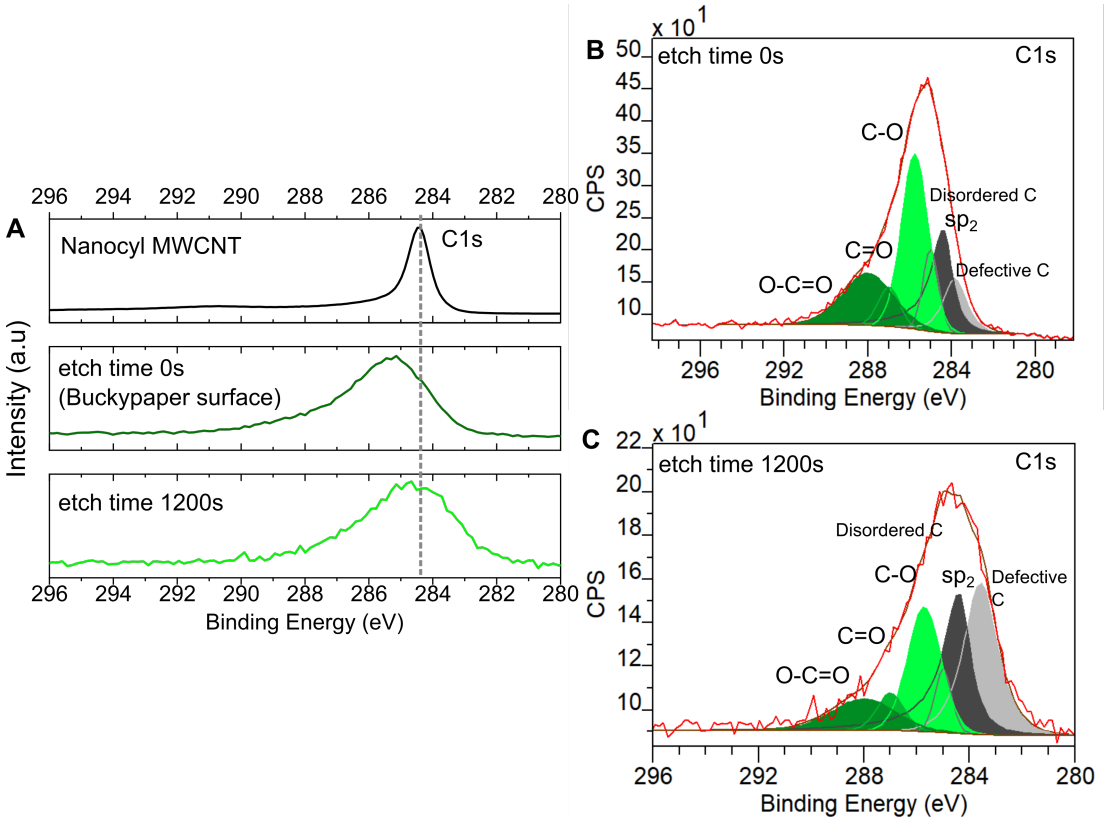


Figure 4.12: (A) A comparison of the normalised high resolution C1s XPS spectra of graphitic Nanocyl MWCNTs, BNNT buckypaper surface (etch time 0s) and BNNT buckypaper interior (etch time 1200s). Synthetic peaks are fitted to the C1s profile of the buckypaper surface (etch time 0s) in (B) and interior (etch time 1200s) in (C). Peak parameters are summarised in Table 4.2. Noticeably, the buckypaper surface C1s profile has more contributions from higher binding energies, corresponding to C-O type bonds.

Etch time 0s					
Bond Identity	**Binding Energy (eV)**	**FWHM**	**% Area**		**Sum %**
Defective C	283.8	1.25	9.5	Def/sp^2/Dis	44.07
sp^2	284.4	1	24.4		
Disordered C*	285	0.9	10.17		
C-O	285.8	1.5	33.61	C-O types	55.94
C=O	287	1.13	5.57		
O-C=O	288	2.5	16.76		
Etch time 1200s					
Bond Identity	**Binding Energy (eV)**	**FWHM**	**% Area**		**Sum %**
Defective C	283.6	1.25	26.34	Def/sp^2/Dis	65.31
sp^2	284.4	1	29.4		
Disordered C*	285	0.9	9.57		
C-O	285.8	1.5	20.41	C-O types	34.69
C=O	287	1.16	5.03		
O-C=O	288	2.5	9.25		

Table 4.2: Summarised description of synthetic peaks fitted to the high resolution XPS C1s spectra collected from the BNNT buckypaper surface and interior, shown in Figure 4.12. All peaks are fitted in CasaXPS with Gaussian-Lorentzian lineshapes, except for sp^2 carbon, fitted with an asymmetric Lorentzian LF lineshape (see also Figure 2.22 and Table 2.8 for comparison to deconvoluted C1s of graphitic Nanocyl MWCNT. *Hydrocarbons present in adventitious carbon can also be associated with C1s peaks in the binding energy range of 284.8-285.3 eV.

imperfections (e.g. vacancies)[314] in graphitic sp^2 carbon.[171,315] Whilst the fitted synthetic peak positions for these graphitic components correspond with those in the literature, it must be acknowledged here that there is an ambiguity associated with their accuracy in the context of the buckypapers studied here. The reason for this is that the hydrocarbon component of adventitious carbon (including e.g. aromatic and aliphatic polymers) exhibits C1s peaks ranging from ca. 284.8 to ca. 285.3 eV,[316] which overlaps with the peak range also associated with disordered C and sp^2 carbon. Consequently, it is possible, particularly for the spectrum collected on the buckypaper surface, that the peaks attributed to graphite-like chemical environments are instead due to hydrocarbons present in adventitious carbonaceous deposits.

However, polymeric hydrocarbons are not associated with C1s low binding energy contributions below 284.2 eV.[316] This is especially relevant to the interpretation of the buckypaper C1s spectrum collected after etch time 1200s, which has a

significant component at 283.6 eV (Figure 4.12C). Given that both oxidised carbon and hydrocarbons have no known influence at this binding energy, it is inferred here that this component is not due to adventitious carbon, but instead to defective carbon native to the buckypaper, i.e. defect-ridden graphitic carbon that is residual after the sacrificial templating process. Ion beam sputtering related damage to graphitic carbon can also be eliminated as the cause of the 283.6 eV feature, since Ar^+ ion beam damage has been shown to initiate broadening of the C1s peak in the direction of the higher binding energies.[317] Thus, this result points towards the presence of a few at.% of defective carbon in the oxidised BNNT buckypaper (<9 at.%). A repeated XPS depth profiling experiment on a separate area of BNNT buckypaper also corroborates this finding, as the C1s peaks undergo both a decrease in intensity (associated with declining at.%) as well as a downshift in peak position to lower binding energies (associated with more graphite-like carbon) as sputter time increases (see Appendix Figure C.6C)

4.3.2.2.2 B,N,O depth profiles As shown in Figure 4.11B, the composition of B was recorded to remain relatively steady with depth (ca. 40 at.%), whilst that of N decreased slightly and quickly plateaued to ca. 16 at.%. The most dramatic change was observed for O, which reached 35 at.% after 1200s etch time. These trends were similarly observed in Figure C.6.

The difference in atomic composition of B and N is attributed here to the partial oxidation of the BNNTs, which skews the B:N atomic ratio away from 1:1 towards higher B content (see also §3.3.3.2). Such partial oxidation is supported by the B1s and N1s spectra (Figure 4.11C & E respectively) that show peaks at high binding energies associated with B-O and N-O type bonds.

However, the noticeable rise in O content with increasing buckypaper etch depth cannot be solely ascribed to the partial oxidation of the BNNTs, given that the degree of oxidation is not anticipated to increase with depth. It is thus speculated here that the climb in O at.% is owed to the presence of oxygen containing impurities (e.g. Al_2O_3 and $Al_4B_2O_9$) within the buckypaper. The source of these

impurities is outlined in §A.3. This hypothesis regarding the high content of O within the BP could be later tested by measuring the Al at.% depth profile concomitantly with B,C,N and O.

4.3.2.3 Adventitious Carbon & CO_2 Adsorption by BNNTs

Until now, the argument presented here in favour of the presence of adventitious carbon on the buckypaper has addressed its characteristics but not addressed its source; but where could the adventitious carbon come from?

The earliest theories on the formation of adventitious carbon proposed that hydrocarbons present in the ambient or vacuum atmospheres adsorb onto the surface of exposed samples, and are subsequently reduced into carbonaceous materials at active surface sites that are pre-exisiting or introduced during processes such as XPS.[318] Later, Miller *et al.* highlighted inadequacies in this theory, primarily that the most abundant hydrocarbons in standard air (methane and ethane),[319] had very low partial pressures and low sticking coefficients, both unfavourable factors for reactivity with surfaces to form carbonaceous deposits.[313] As such, they advocated that CO_2, the most abundant carbon-containing gas in the atmosphere and also one of the main constituents in residual air in vacuum chambers (alongside CO, H_2O and H) is the key contributor to adventitious carbon formation. Indeed, they discovered that initially clean iron surfaces exposed to varying pressures (10-10^4 Pa) of CO_2 and CO quickly acquired carbonaceous surface deposits that were constituted of predominantly hydrocarbons followed by oxidised carbons. This thus provided evidence that adventitious carbon can originate from adsorbed CO_2, which subsequently undergo reduction at reactive sites to form a carbonaceous residue.

Interestingly, materials identified by Barr *et al.*[320] as having a 'propensity to adsorb unusually large amounts of adventitious carbon' that exhibit 'inordinately large amounts of oxidised carbon species' are also materials favoured for CO_2 capture, e.g. alumina, zeolites, silicates in the form of solid, porous sorbents.[321] This association thus begs the question of whether a buckypaper composed of BNNTs is effective at CO_2 capture. If so, it is hypothesised here that this CO_2

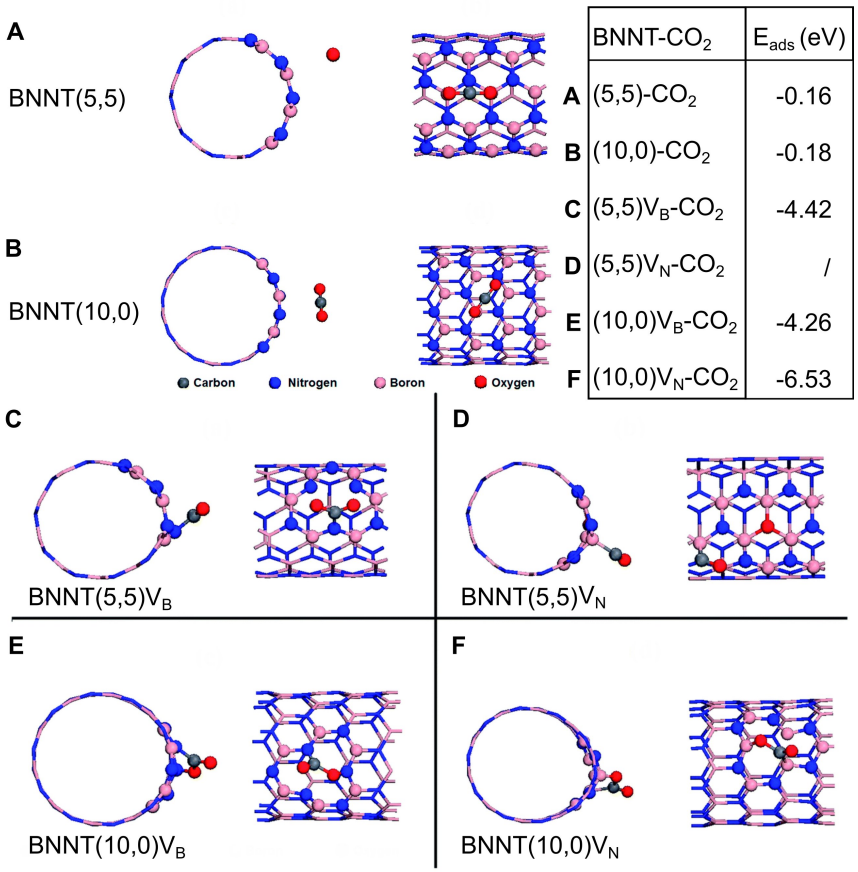
adsorption could be a source of adventitious carbon of the heavily oxidised nature on (and in) the porous BNNT buckypaper.

In fact, in recent years, boron nitride, particularly with a high surface area porous structure, has garnered research interest as a candidate CO_2 capture material; porous[‡] boron nitride nanosheets,[322,323] fibres,[324] flakes[325,326] and 3D assemblies of nanosheets in foams[327,328] and flower-like assemblies[329] have exhibited extremely promising CO_2 adsorption capacity, one of the main reasons being the intrinsically high surface area available.[330]

BNNTs also fulfill the large surface area criteria to be adsorbents for gases such as CO_2, but to our best knowledge, there has been no reported empirical investigations of a BNNT macroscopic assembly's CO_2 adsorption capacity to date. However, theoretical studies have demonstrated that the interactions between CO_2 and ideal, defect free BNNTs (and also 2D h-BN) are weak, whereby CO_2 is only physisorbed to the h-BN through van der Waals forces. However, defect sites in the BNNT, including B antisites[332] and B/N vacancies[331,333] have been predicted to be highly reactive sites for CO_2 chemisorption, which would facilitate enhanced CO_2 adsorption even at ambient conditions. For example, Paura *et al.* calculated via DFT the adsorption energies (E_{ads}) between CO_2 and B/N vacancy defect sites on single wall BNNTs of two different chiralities (zigzag and armchair), as demonstrated alongside illustrations of their equilibrium binding configurations in Figure 4.13. In comparison to the small E_{ads} values obtained for weak physisorption between defect free BNNTs and CO_2, E_{ads} values are much more significant for interactions of CO_2 at BNNT vacancy defect sites, which is characteristic of chemisorption.[331]

In the context of the BNNT buckypapers synthesised here, in which the BNNTs are known to be defective (as detailed in Chapter 3), the aforementioned theoretical models lend to the prediction that these BNNTs have a propensity to chemisorb CO_2 even at ambient conditions. The extrapolated implication of this is that these BNNT buckypapers are likely to have adventitious carbon deposits composed of oxidised carbon species that originate from CO_2 reactions with defective BNNT surface sites.

[‡]Porous boron nitride is composed of turbostratic and amorphous BN



	BNNT-CO_2	E_{ads} (eV)
A	(5,5)-CO_2	-0.16
B	(10,0)-CO_2	-0.18
C	(5,5)V_B-CO_2	-4.42
D	(5,5)V_N-CO_2	/
E	(10,0)V_B-CO_2	-4.26
F	(10,0)V_N-CO_2	-6.53

Figure 4.13: Density Functional Theory calculations conducted by Paura *et al.* of interactions between BNNTs (armchair (5,5) or zigzag(10,0)) and CO_2 molecule. Frontal and side view equilibrium configurations are shown for (A-B) CO_2 weak interaction with defect free BNNTs, (C-D) CO_2 strong interactions at B or N vacancy defect sites of armchair BNNT and (E-F) CO_2 strong interactions at B or N vacancy defect sites of zigzag BNNT. Calculated adsorption energies are shown in the accompanying table; large is associated with chemisorption. No E_{ads} value is given for BNNT(5,5)V_N-CO_2 because of the dissociation of CO_2 to O_2 and CO. Adapted with permission from Ref. [331]. (Copyright 2015, Royal Society of Chemistry)

4.3.3 Buckypaper surface platelet formation

In this section, the platelets observed on the surface of the oxidised BNNT buckypapers are investigated to determine their structure, composition and growth mechanism. Characterisation techniques implemented include SEM, TEM, FTIR and EDX. Monte Carlo electron trajectory simulations by CASINO v2.51 were also conducted to assist in interpretation of EDX data of the thin platelets.

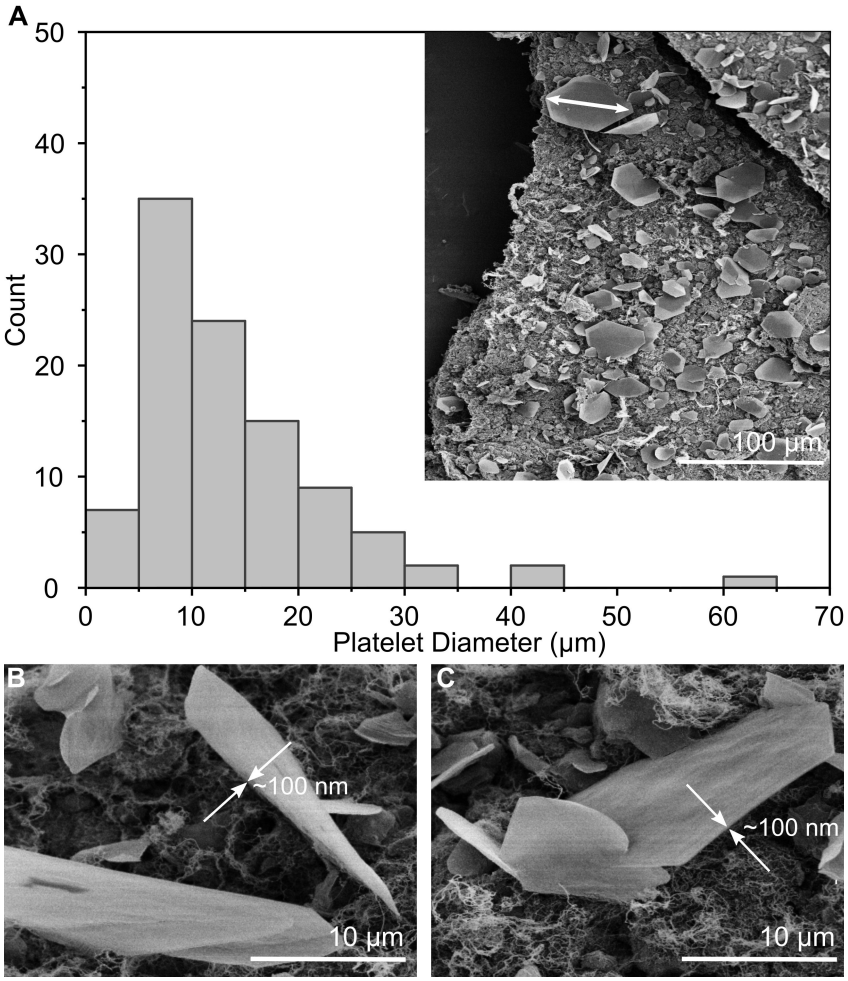


Figure 4.14: (A) Distribution of surface platelet diameters as measured from 100 platelets in SEM images (e.g. inset) collected across multiple buckypaper samples. (B-C) SEM images of typical platelet thickness, observed to be ca. 100 nm thin.

According to the measured sizes summarised in Figure 4.14A, the average platelet diameter was 14±9 μm with nanometre scale thickness.

Whilst the platelet formation was initially unexpected and seemingly anomalous, further exploration of the literature on similar material systems revealed two candidate explanations for their occurrence. These are presented here as two separate theories in §4.3.3.1 (nanotube unzipping and coalescence) and §4.3.3.2 (spontaneous boric acid crystallisation). Whilst the former theory has been previously proposed for platelet formation specifically on a BNNT assembly surface, the latter theory has not, and so the discussion here represents the first such interpretation.

Evidence is then presented in §4.3.3.3 and §4.3.3.4, on platelet structure and composition respectively, in support of the boric acid crystallisation theory.

4.3.3.1 Theory I: BNNT Oxidative Unzipping & Coalescence

To the best of the our knowledge, there is one report by Nautiyal *et al.*, 2016 on observed platelet-type formations on bundles of BNNTs after oxidation treatment at 750 °C and above.[237] These BNNTs were synthesised by the HTP method, sourced from BNNT, LLC.[61]

Subsequent to heat treatment in air at 750 °C, B_2O_3 was identified in the BNNT sample by XRD and FTIR. SEM images taken of the oxidised sample (Figure 4.15) revealed that polygonal platelets more than 10 μm wide had formed. Although not explicitly stated, it appeared that the original BNNT sample was prepared into a sheet type macroscopic assembly as SEM images showed that the platelets had formed on the surface of a mesh-like flat arrangement of BNNTs, i.e. BNNT buckypaper or similar.

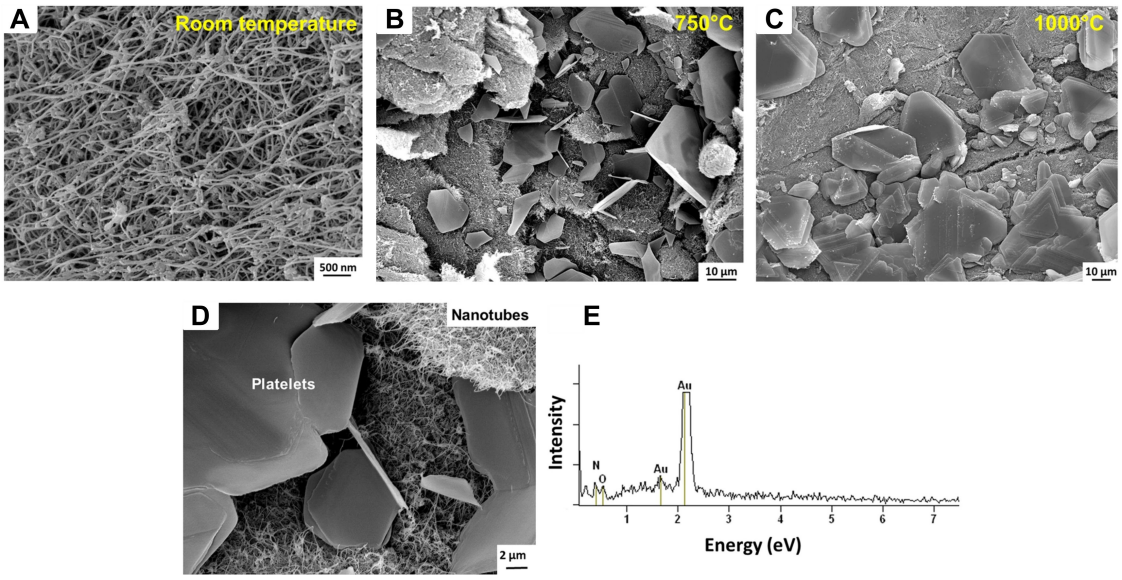


Figure 4.15: SEM images of BNNTs (BNNT, LLC grade) at (A) room temperature, and after oxidation in air at (B) 750 °C and (C) 1000 °C. Polygonal platelets were formed on the surface, as further magnified in (D). The "white graphene oxide" (oxidised h-BN) composition of the platelets is partly interpreted by Nautiyal *et al.*, from the EDX presented in (E). Reproduced with permission from Ref.[237] (Copyright 2016, Springer Nature)

Evidence of the composition of the platelets is not conclusive, as one EDX scan (Figure 4.15E) is provided without discussion on the atomic composition detected, along with a convenient dismissal of boron from the spectrum, stating that it 'cannot be detected' because of its low atomic number. Further discussion of the composition of the platelets is based on the results of bulk analysis techniques such as XRD and FTIR, which show the simultaneous occurrence of B−N and B−O type bonds in the post-oxidised BNNT sample. The conclusion thus drawn was that the platelets were boron nitride oxide (white graphene oxide), analogous in structure to graphene oxide. Given that XRD and FTIR are not surface analysis techniques, and the EDX results are not discussed with consideration of the depth of specimen analysis, it is impossible to interpret accurately the localised composition of the surface platelets solely from these presented results.

The study's proposed platelet growth mechanism involves (i) oxidative unzipping of the BNNTs at high temperature into unfolded nanoribbons, followed by (ii) coalescence of the nanoribbons into stacked platelets.

According to Nautiyal *et al.*, the oxidative unzipping occurs preferentially at Stone-Wales defect sites on the BNNTs, particularly at B−B homonuclear bonds. Chemisorbed O_2 at these defect sites are believed to result in cylic B_2O_2 ring structures that are broken upon thermal vibration to from strong B−O bonds. This exothermic cleaving of the B-B bond is said to induce strain on the BNNT such that it unzips into a nanoribbon. Another proposed pathway to BNNT unzipping is via the higher energy, endothermic process of direct oxygen attack of B−N 'pure' sites, thought to only occur above 1000 °C.

For stage (ii) of the proposed mechanism, the authors suggest that the unzipped BN nanoribbons coalesce directly into platelets, growing layer by layer and increasing in area as more BNNTs unzip and coalesce on the periphery and top of the previous platelet layer. The provided evidence for this is SEM images showing coexistence of some large fused areas with remaining BNNTs on the periphery or on the surface (Figure 4.16). Nevertheless, the provided images of BNNT partially fused into the large, flat areas appears distinctly different to the sharp polygonal platelet

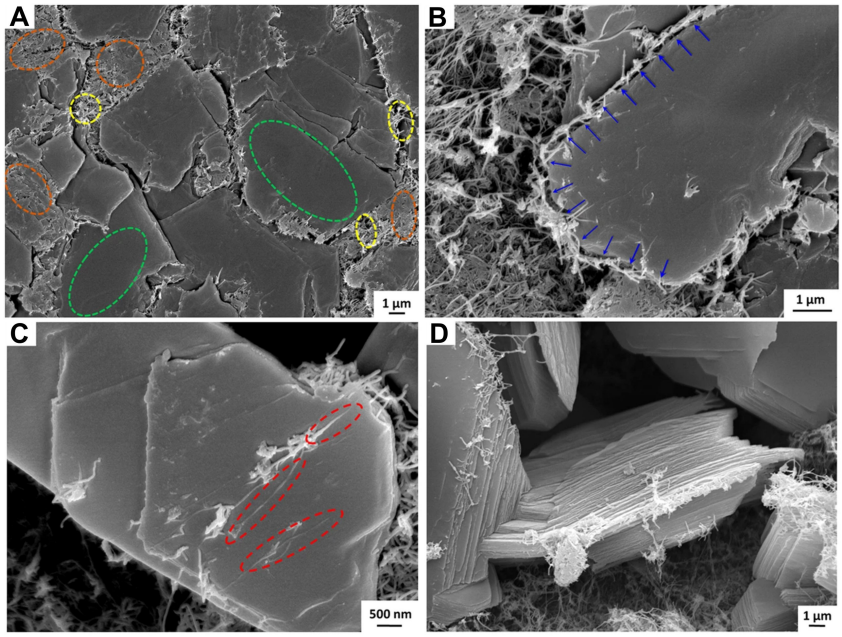


Figure 4.16: SEM images showing regions of post oxidised BNNTs that are used by Nautiyal et al., to support their theory on unzipping of BNNTs into BN nanoribbons and their subsequent coalescence into large stacks. However, these areas are noticeably different to the platelets presented in Figure 4.15. Reproduced with permission from Ref.[237] (Copyright 2016, Springer Nature)

morphologies shown in Figure 4.15. These fused areas are more irregular in shape and lie flat, i.e. parallel to the surrounding plane of BNNTs, whilst the platelets previously depicted are oriented in random directions. This exposes some ambiguity regarding the similarity of the platelet structures and the fused areas used to justify the hypothesis of nanoribbon coalescence, although the results are said to be obtained from BNNT subjected to the same oxidation temperature of 750 °C.

Furthermore, whilst the unzipping of BNNTs into BN nanoribbons has been previously demonstrated by plasma etching,[334] potassium-induced splitting[335,336] or *in situ* unzipping during BNNT synthesis,[337] there have been no other reports of coalescence of such BN nanoribbons into larger platelet structures.

In summary, an evaluation of this theory indicates that it is refutable, as the composition of the platelets and the proposed growth mechanism by nanoribbon coalescence are not conclusive. However, until this thesis, the report by Nautiyal *et al.*, remained the sole study to report on the occurrence of such platelets after BNNT oxidation and to propose their possible growth mechanism and chemical composition.

4.3.3.2 Theory II: Spontaneous Boric Acid Crystallisation

4.3.3.2.1 Literature review A literature search conducted to explore the occurrence of platelet-like morphologies in B,N or B,O material systems revealed some findings that are extrapolated here to develop a new theory on platelet formation on oxidised BNNT buckypaper surfaces.

To the our best knowledge, a study by Rand *et al.*, 1968 at Bell Laboratories, one of the earliest to report on CVD of h-BN thin films, was the first to observe the formation of polygonal crystallites on the h-BN thin film surface when stored at room ambient.[189] These crystals, shown in Figure 4.17A, were identified as boric acid (by electron diffraction) and unpleasantly referred to as the boric acid pox. Incredibly, there appears to be an unusual dormancy in the literature on this BN/water/boric acid system. A much later study by Quan *et al.*, 2017 also observed the boric acid pox phenomenon on h-BN thin films, grown by magnetron sputtering, which were also exposed to moist air (Figure 4.17B).[338]

In an entirely separate stream of research, Edemir *et al.*, 1990 discovered that a B_2O_3 thin film (2 μm thick), which had been deposited by use of a electron-beam-heated evaporator, spontaneously transformed into platelet-like crystallites upon exposure to the open air (Figure 4.18A).[339] The transparent B_2O_3 film was also reported to convert to an opaque, mother of pearl colour. The low friction character of the crystallites, oriented during frictional sliding, strongly indicated that the

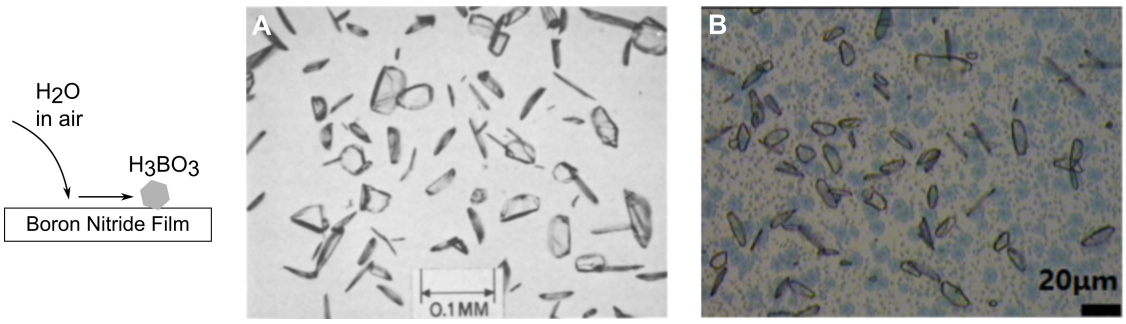


Figure 4.17: The exposure of h-BN thin films to ambient water vapour can result in the growth of boric acid H_3BO_3 crystals on the surface, as shown in the optical microscopy images (A) & (B), reproduced with permission from Ref.[189] (Copyright 1968, IOP Publishing Ltd.) and Ref.[338] (Copyright 2017, Elsevier Ltd.)

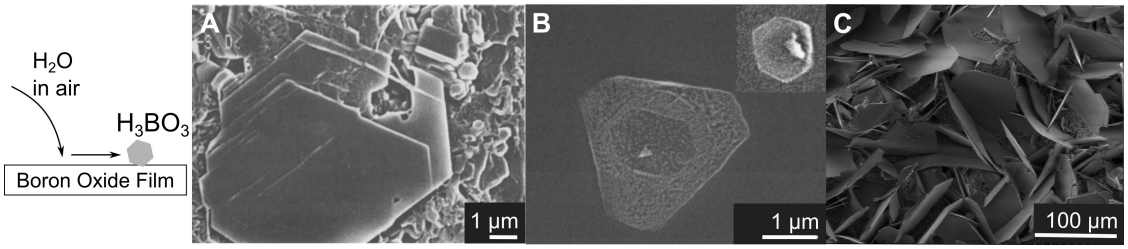


Figure 4.18: The exposure of boron oxide thin films to ambient water vapour can result in the growth of boric acid H_3BO_3 crystals on the surface, as shown in the SEM images (A-C), reproduced with permission from Ref.[339] (Copyright 1990, Elsevier Ltd.), Ref.[340] (Copyright 2007, Elsevier Ltd.) and Ref.[341] (Copyright 2017, Elsevier Ltd.)

platelet structure was lubricious. The Erdemir *et al.* explanation accounting for all these observations was that the B_2O_3 film had adsorbed moisture of the open air (relative humidity 60 ±5%) to form boric acid (H_3BO_3).

Reaction R 4.1 below, describing the conversion of B_2O_3 to H_3BO_3 in the presence of H_2O, occurs spontaneously as it has a negative standard heat of reaction $\triangle H_{298} = -45.1 kJ/mol$:[342]

$$\frac{1}{2}B_2O_3 + \frac{3}{2}H_2O \longrightarrow H_3BO_3 \qquad \text{(R 4.1)}$$

That Erdemir *et al.*, made no reference to the earlier example of H_3BO_3 formation on h-BN films by Rand *et al.*, possibly indicates a lack of convergence between the fields of B_2O_3 and h-BN thin film investigation at the time. However, it is apparent here that evidence of H_3BO_3 crystallisation on B_2O_3 films illustrates the likely mechanism of H_3BO_3 growth from h-BN, with B_2O_3 as the hygroscopic intermediate.

Since the Erdemir *et al.*, study, there have been additional examples of H_3BO_3 platelet crystallite formation on magnetron sputter deposited boron oxide films (BO_x, x $\geqslant$0.15)[340,343](Figure 4.18B) as well as on B_2O_3 films that condensed onto combusted elemental boron (Figure 4.18C).[344] The presence of surface H_3BO_3 has also been detected on ultra-thin boron films,[345] and on boron doped silicon carbide films[344] or pure boron carbide films, all exposed to air.[346] In these cases, the instability of boron to oxidation to form B_2O_3 is explained as the source for subsequent H_3BO_3 crystal growth.

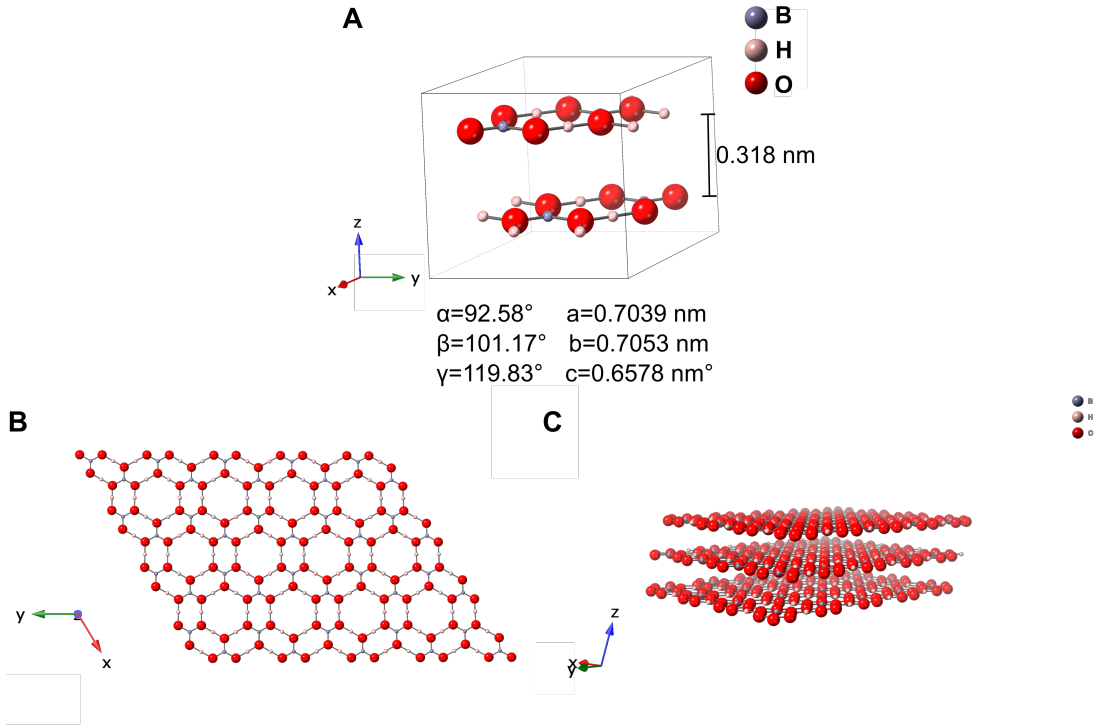


Figure 4.19: (A) Triclinic unit cell of H_3BO_3. (B) [001] orientation of a monolayer of H_3BO_3, showing hexagonal configuration of planar BO_3^{3-} groups. (C) Depiction of lamellar nature of an H_3BO_3 crystal. CIF file for modelling, based on H_3BO_3 crystal structure as determined by Zachariasen *et al.*,[347] was downloaded from the AMCS database.[350] Images were generated using CrystalMaker®.

Common to all the above mentioned studies is the polygonal, often hexagonal geometry of the observed H_3BO_3 crystallites. This H_3BO_3 form of boric acid is a lamellar crystal structure, more formally known as orthoboric acid. It is constituted of B,O and H lying in plane, according to a triclinic unit cell structure. According to the layer structure determined by Zachariasen *et al.*,[347–349] covalently bonded BO_3^{3-} groups are arranged in a hexagonal configuration and hydrogen bonds occur between these planar BO_3^{3-} groups. The lattice parameters and angles are responsible for the pseudo-hexagonal crystallites (hexagonal in shape without belonging to the hexagonal crystal system). The interlayer atomic distance is 3.18 Å and interlayer interaction occurs through van der Waals forces lending to the lubricious nature of H_3BO_3. Model depictions of H_3BO_3 structure are shown in Figure 4.19 A-C. Example bulk morphology of H_3BO_3 crystals are depicted in Figure 4.20.

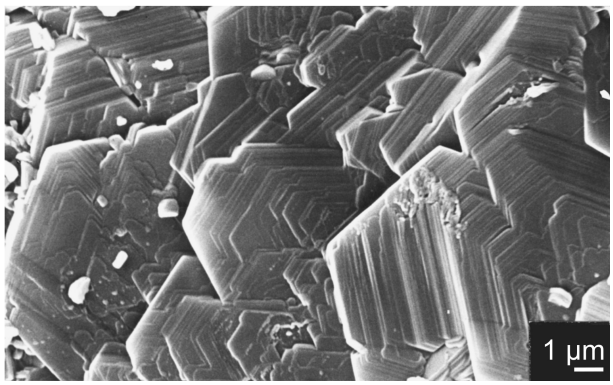


Figure 4.20: SEM image depicting the pseudo-hexagonal geometry and lamellae of bulk H_3BO_3 crystals. Alternate layers are shifted along the c-axis due to its inclination at 101° to the basal plane in the triclinic crystal structure. Reproduced with permission from Ref.[342] (Copyright 2001, CRC Press LLC.)

4.3.3.2.2 Extrapolating the theory to platelet formation on oxidised BNNT buckypapers Based on the evidence in the literature of spontaneous crystallisation of H_3BO_3 platelets on h-BN and B_2O_3 thin films exposed to ambient moisture, it is deduced here that this phenomenon could also occur on partially oxidised BNNT buckypaper surfaces.

As discerned in §4.3.2, the thermal oxidation process to sacrifice graphitic components in the CNT@BN buckypapers to leave BNNT buckypapers also results in the partial oxidation of the BNNTs at 700 °C. Thus, B_2O_3 is present in the as synthesised BNNT buckypapers. Secondly, the partial oxidation of the BNNTs reduces their crystallinity, making them less stable against room temperature oxidation, thus allowing for further generation of B_2O_3.

Consequently, the presence of B_2O_3 on the BNNT buckypaper surface is proposed here as the cause for the observed surface platelet formations according to the same $B_2O_3 \longrightarrow H_3BO_3$ conversion mechanism observed on B_2O_3 and h-BN thin films exposed to ambient moisture.

The evolution of the BNNT buckypaper surface toward H_3BO_3 platelet coverage is schematically depicted in Figure 4.21. Thermal oxidation occurring at the surface results in the formation of B_2O_3 nuclei as BNNTs are partially or fully oxidised. At the oxidation temperature of 700 °C, these nuclei begin to form liquid clusters of B_2O_3, which becomes liquid-like above 450 °C.[342] These mobile clusters grow and

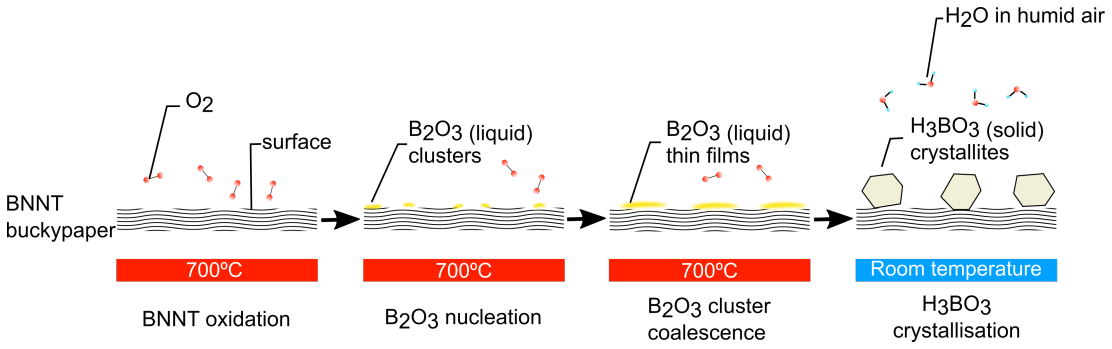


Figure 4.21: Schematic for the proposed mechanism of H_3BO_3 crystallite formation on partially oxidised BNNT buckypaper surfaces that have been exposed to ambient moisture.

coalesce into larger continuous thin films on the surface of the BNNT buckypaper. At 700 °C, these B_2O_3 films are unlikely to be hydrated into H_3BO_3, which can only occur below 170 °C.[342] Upon cooling of the buckypaper to room ambient, the thin films of B_2O_3 spontaneously react with water vapour in the air to form H_3BO_3 platelet crystallites that exhibit a characteristic polygonal and lamellar morphology.

Interestingly, electron microscopy of the oxidised BNNTs starting from loose powder CNT@BN did not reveal obvious platelet formations. However, very apparent polygonal platelets are seen on the surface of BNNT buckypapers synthesised by the same oxidation process of CNT@BN buckypapers. This suggests that the growth process of these platelets is dependent on the existence of a 'flat' surface topography, as imitated by the buckypaper surface. Indeed, all studies that have reported H_3BO_3 platelet crystallisation, as discussed in §4.3.3.2.1, provided flat surfaces as substrates. Perhaps the larger surface area provided by the BNNT buckypaper (as opposed to loose powder agglomerates) facilitates coalescence of B_2O_3 in larger clusters, increasing the likelihood that the critical nuclei size of H_3BO_3 is met for crystal growth to occur.[351,352]

4.3.3.3 Observed H_3BO_3 platelets

One distinct characteristic of H_3BO_3 is its crystal structure, as illustrated in Figure 4.19. It was thus anticipated that analysis of platelet structure by HRTEM would validate its crystalline nature and confirm its H_3BO_3 structural identity.

Briefly, to isolate the platelets from the buckypaper, a TEM copper grid was gently passed across the surface of the buckypaper. This was done for three separate buckypaper samples. The platelet number density that was successfully transferred to the grid proved to be quite low, as deduced by the time-intensive challenge in locating platelets for imaging. Fortunately, after extensive search, two platelets were found on two separate copper grids.

The structures were visually identified in TEM as being the platelets of interest based on their polygonal structure and straight edges previously seen by SEM. The two observed platelets are shown in Figure 4.22 A and B.

The distinctive lamellar attribute of crystalline H_3BO_3 was confirmed by HRTEM of platelet edge regions, which revealed the cross sectional view. For Platelet 1 (Area 1), seen in Figure 4.22C, the lattice spacing determined from the HRTEM and FFT matched the 0.318 nm interlayer (d_{002}) spacing of H_3BO_3.[348] This same spacing was observed for a thinner sheet extending off from Platelet 1 (Area 2) in Figure 4.22D. The H_3BO_3 platelet structure is again corroborated by the 0.318 nm lamellar spacing observed in Platelet 2 (Figure 4.22E).

This HRTEM analysis thus substantiates the theory proposed here that these platelets are indeed H_3BO_3 and not partially oxidised h-BN, as suggested by the Nuatiyal *et al.* theory.

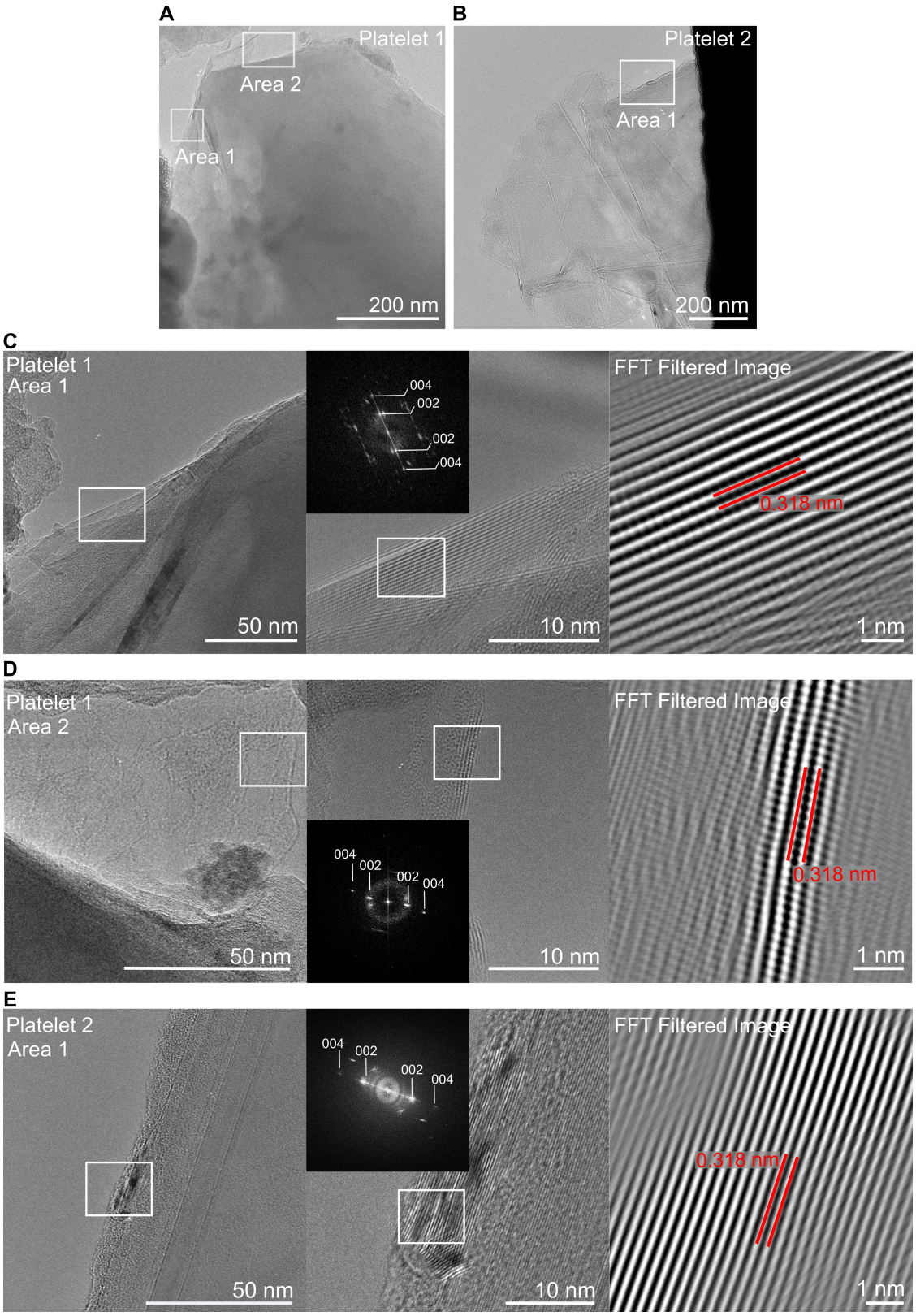


Figure 4.22: Two platelet structures shown in TEM images (A) & (B) were imaged by HRTEM (C-E), which revealed their 0.318 nm interlayer spacing matching the d_{002} spacing of H_3BO_3. White boxes highlight regions imaged at higher magnification and selected regions for FFT (inset) and FFT filtered images.

4.3.3.3.1 FTIR In support of the localised platelet H_3BO_3 characterisation by TEM above, FTIR spectra collected from BNNT buckypapers also indicate the presence of H_3BO_3.

Figure 4.23 shows a BNNT buckypaper FTIR spectrum. Absorption peaks that correspond to the characteristic profile of H_3BO_3 are present in this spectrum, as summarised in Table 4.3.

FTIR Frequencies (cm^{-1})				
BNNT buckypaper sample	**Boric Acid; H_3BO_3**			
Absorption bands	**Absorption bands**	**Description**	**Vibration**	**Refs.**
3200	**3200,3270**	very strong	O-H stretching	[353–355]
-	2674	very weak	-	[353]
-	2505,2506	weak	-	[353,354]
-	2370	weak	-	[353]
2259	**2257**	medium	-	[353]
-	2092	very weak	-	[353]
-	2028	very weak	-	[353]
1460	**1450**	very strong	B-O stretching	[353–356]
1373	*B-N stretching; h-BN*			
1225	**1224**	shoulder	B-O-H bending	[357]
1197	**1180,1190,1195,1197**	strong,sharp	B-O-H bending	[353–357]
1021	-	-	-	
884	**882,885**	weak,sharp	symmetric B-O stretching	[353–355]
-	824	medium,broad	O-H twisting	[353–355]
726	*B-N-B bending; h-BN*			
642	**640,648,650**	weak	BO_3 bending	[353–356]

Table 4.3: List of absorption peaks recorded from the BNNT buckypaper FTIR spectrum in Figure 4.23, alongside the reference FTIR peak profile of boric acid (H_3BO_3). Emboldened frequencies highlight correlations between the specimen and H_3BO_3 references; notably these are mainly strong/medium absorption bands that have been assigned to specific infrared-active vibrations of H_3BO_3. Frequencies associated with h-BN were also detected *(italicised)*. Note that the peak at 2361 cm^{-1} is excluded from the table; this is a result of atmospheric and/or adsorbed CO_2.

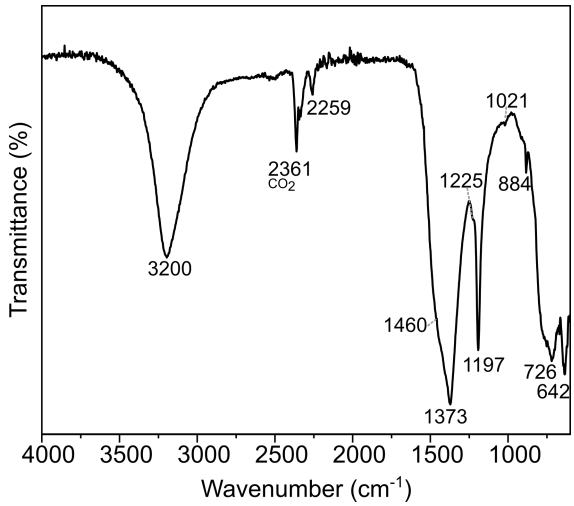


Figure 4.23: FTIR spectrum of BNNT buckypaper exposed to ambient air.

4.3.3.4 Platelet Composition by EDX analysis

Notably, platelets observed on oxidised BNNT buckypapers by Nautiyal *et al.*[237] were cursorily characterised by EDX spectroscopy (See Figure 4.15e) to draw an inadequately substantiated conclusion that they were partially oxidised 2D h-BN.

Here, the challenges associated with EDX analysis of nanomaterials, in this case 2D platelets located on the surface of bulk buckypaper, are addressed in relation to the the platelets synthesised in this chapter.

As shown in Figure 4.24, platelets of this work were analysed by EDX *in situ*, i.e. on the buckypaper surface where they were originally formed. Based on the collected EDX spectra (Figure 4.24B) and elemental maps (Figure 4.24C), there are two matters to address.

Firstly, the platelets are not aluminium derived, as there is no noticeable intensity of Al outlining the platelet shape on the EDX maps, and only a weak signal of Al on the collected spectra, the source of which will be discussed below. This eliminates the possibility that these platelets were alumina or aluminium borate impurities exposed to the surface subsequent to oxidation treatment of the buckypaper.

Secondly, EDX spectra acquired within platelet areas show signals from B, C, N, O, Al and Pt. The Pt signal is known to originate from the conductive Pt coating added to prevent the insulator sample from charging during electron

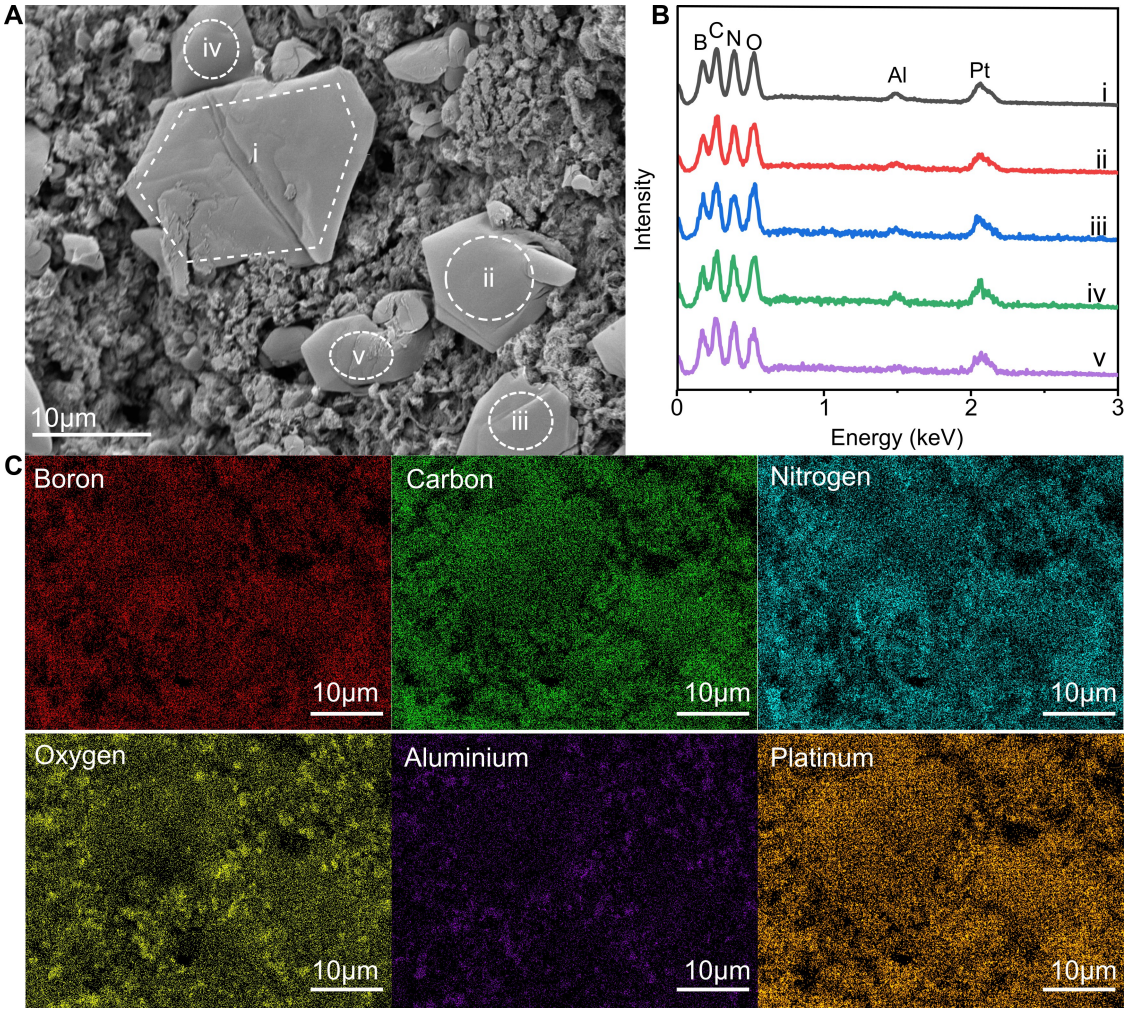


Figure 4.24: (A) SEM of 2D polygonal platelets on surface of oxidised BNNT buckypaper. (B) EDX spectra for platelets highlighted (i)-(v) in the SEM image. (C) EDX elemental maps of the corresponding SEM area show no apparent distinction between buckypaper and platelet composition, likely due to X-ray generation depth being greater than platelet thickness. The EDX acquisition details (Acceleration Voltage: 3 kV, Pixel Size: 0.04951 μm, Energy per channel: 5 eV, Dwell time: 160 μs, Stage Tilt: 0 °, Detector Elevation: 30 °)

microscopy. EDX maps show no distinct difference in elemental distribution between the platelets and the supporting buckypaper. Thus, this appears to gives no conclusive corroboration of the H_3BO_3 composition of the platelets. However, a more thorough interpretation of these EDX results is required, with particular attention to the depth resolution of these spectra and maps, i.e. do they represent the surface platelets features alone?

4.3.3.4.1 X-ray Generation Depth X-rays detected for EDX analysis originate from certain depths within the imaged specimen, depending on factors such as the specimen composition as well as the incident electron beam acceleration voltage (beam energy). An estimation of X-ray generation depth for the imaged platelet areas is necessary, especially as the thin 2D platelets (ca. 100 nm thickness) lie on top of a buckypaper that can contribute its own X-rays upon electron excitation.

In practice, a low acceleration voltage results in a lower electron penetration range within the specimen, which is desired in this scenario where ideally only the surface platelets undergo excitation. Here, a 3 kV acceleration voltage was implemented, which still satisfies the minimum $\times 2$ overvoltage ratio requirement for the light elements (ratio of acceleration energy to critical ionisation energy of an atomic shell). A low acceleration voltage is also suitable here to reduce the charging of the insulator specimen, thus preventing the occurrence of specimen drifting, blurring and low contrast imaging.

Whilst the selected 3 kV low acceleration voltage is favourable for more shallow specimen excitation, it is not immediately guaranteed that the excitation depth is contained within the platelets. To obtain an estimate of electron range and thus X-ray generation depth, Monte-Carlo electron trajectory simulations were conducted using CASINO v2.51 software, for a model specimen under the same experimental microscope settings. Further details of the pertinence of Monte-Carlo simulations to assist EDX spectra interpretation are included in Appendix C, along with microscope settings and physical theories for calculations.

Briefly, a platelet is modelled as a 100 nm thin film layer of H_3BO_3 on top of a B,C,N,O containing substrate bulk layer. Pt is also included as a surface layer to mirror experimental conditions whereby Pt is present as conductive coating. See Appendix §C.4.1.2 for a full description of the modelled specimen.

The output of the simulation includes complete electron trajectories for 500 electrons (Appendix Figure C.7A) and an energy by position map which shows the spatial distribution of electron energy absorption within the specimen (Appendix Figure C.7B). A combination of these electron histories facilitates extraction of

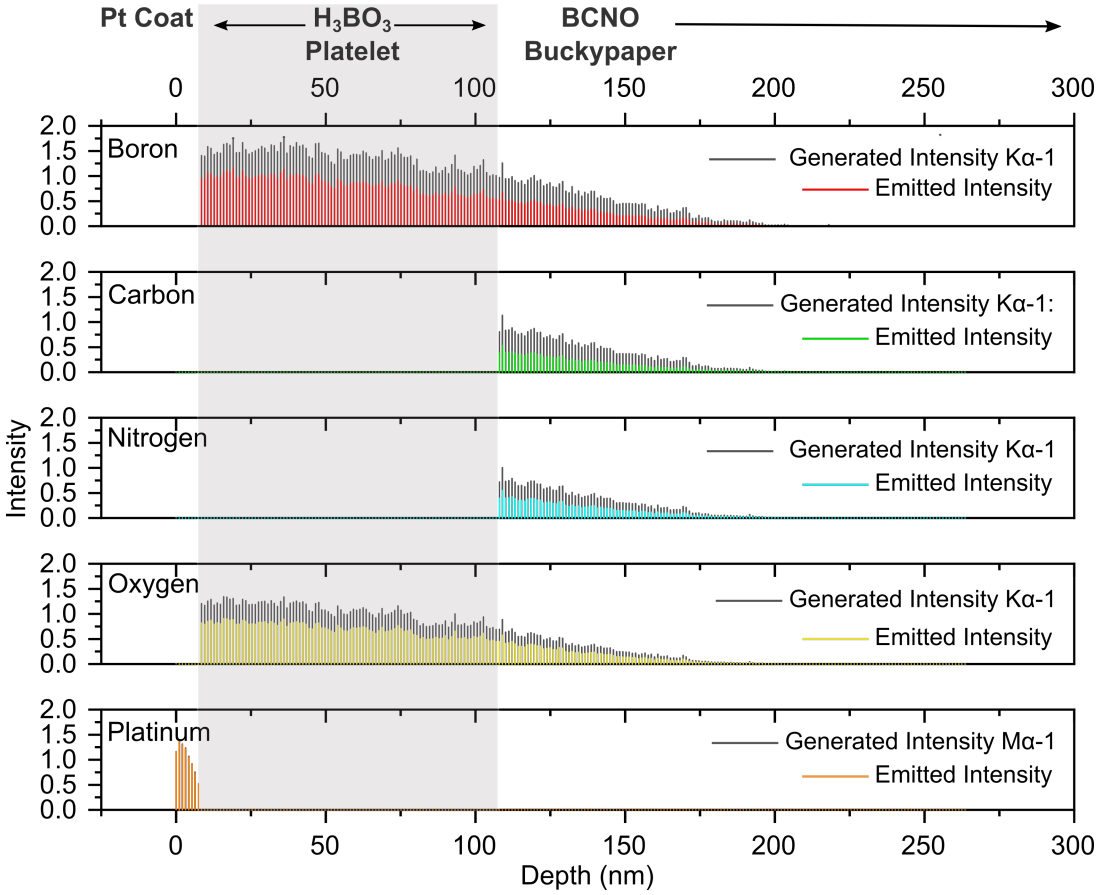


Figure 4.25: ($\phi(\rho z)$) distributions for elements B,C, N, O and Pt from the multilayer specimen of top to bottom: 8 nm Pt coat, 100 nm H_3BO_3 thin film and B,C,N,O containing substrate, described in Appendix Table C.1. Emitted intensity refers to the X-rays that can escape the specimen without being absorbed (a portion of the generated X-rays). For a 3 keV beam, the X-ray generation depth extends outside of the H_3BO_3 feature of interest; detected signals are mixed with those from the buckypaper substrate.

a distribution of X-ray generation as a function of specimen depth (termed ϕ (ρ z) for each element in the specimen.

The simulated X-ray depth generation ($\phi(\rho)z$) curves in Figure 4.25 demonstrate that even for a low energy 3 keV electron beam, stimulated X-rays originate from beyond the 100 nm thick H_3BO_3 feature. This suggests that B,C,N and O signals from a substrate buckypaper could compound the B, O signals from the nanoscale thin H_3BO_3 platelet.

Thus, the EDX spectra collected in Figure 4.24B neither disprove the theorised (and TEM corroborated) H_3BO_3 composition of the platelets, nor are they accurate for qualitative and quantitative assessment of platelet composition.

For these platelets, especially because of their 2D nature (nanoscale depth dimension), accurate EDX analysis is not a straight-forward task. As demonstrated with other nanomaterials positioned on a substrate bulk material (e.g. $AuIn_2$ nanowires on InSb substrate[358]), SEM EDX spectra have a high probability of containing substrate signals, thus complicating chemical quantification of the surface-based nanomaterial itself.

There are three possible solutions to the issues precluding accurate EDX analysis of the platelets demonstrated above. Ideally, EDX spectra should be obtained of the platelets without the presence of a substrate material. Otherwise, to contain the electron penetration range and thus X-ray generation depth within the platelet, microscope settings could be optimised with the planning input from Monte-Carlo simulations or alternatively, the depth dimension of the platelet itself should be increased. Whilst the ideal scenario has yet to be achieved, thick platelets were indeed observed, as discussed below.

4.3.3.4.2 EDX analysis of thicker platelets Thicker platelets, with similar polygonal geometry and lamellar structure as their thinner counterparts, were observed on oxidised buckypapers that had been stored for >6 months prior to characterisation, as imaged in Figure 4.26.

The growth of these thicker platelets after an extended time of specimen exposure to ambient moisture appears to corroborate the active role of humidity in platelet formation. Ambient moisture spontaneously reacts with B_2O_3 films on the buckypaper surface to form H_3BO_3 platelets. Furthermore, ambient moisture can also de-stabalise BNNTs, particularly those that are low in crystallinity,[188,195] to form more B_2O_3. This would supplement the availability of B_2O_3 for H_3BO_3 conversion and thus would facilitate thicker platelet growth after longer timescales of ambient moisture exposure.

The thicker platelets (on the scale of micrometer thickness) are more favourable for EDX analysis for reasons explained above in §4.3.3.4.1.

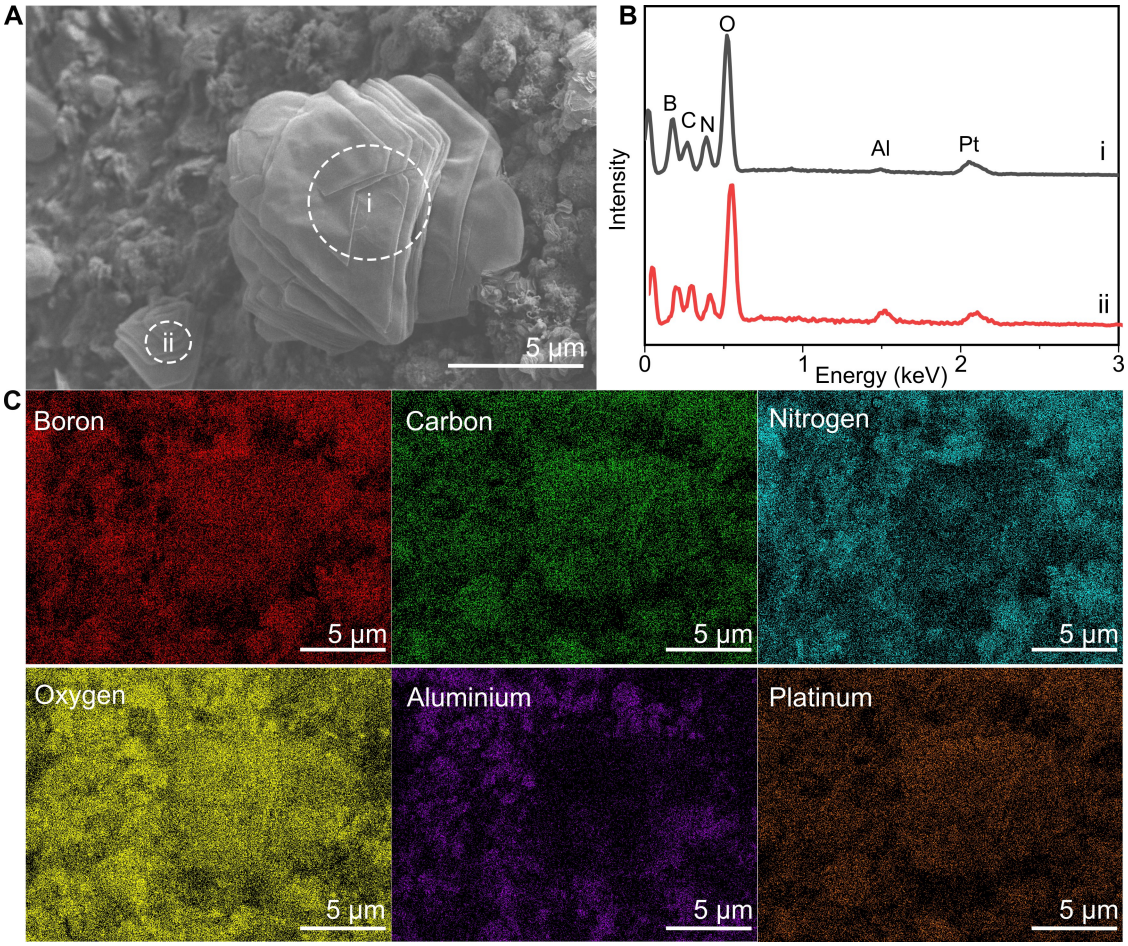


Figure 4.26: (A) SEM of polygonal multi-layer thick platelet structures observed on the surface of an oxidised BNNT buckypaper. (B) EDX spectra of regions (i) and (ii) highlighted in the SEM image over a large and small platelet exhibit the same composition dominated by oxygen. (C) EDX elemental maps of the SEM imaged area show a clear superposition of B and O in the large platelet and a deficiency of nitrogen compared to the surrounding buckypaper. Pt from the conductive coating and C have unusually similar elemental maps. EDX acquisition details (Acceleration Voltage: 3.13 kV, Pixel Size: 0.02084 μm, Energy per channel: 10 eV, Dwell time: 923 μs, Stage Tilt: -4 °, Detector Elevation: 30 °)

The high intensity oxygen signal detected from the thicker platelets as shown in Figure 4.26B and the corresponding oxygen elemental map in Figure 4.26C confirm their predominant oxygen composition (40 at.%). Boron makes the next highest contribution to atomic composition (30 at.%), and the elemental map indicates its co-location with oxygen at the site of the platelet. Noticeably, nitrogen is still detected, albeit at a low atomic composition (14 at.%) and its elemental map does not show strong intensities outlining the silhouette of the platelet. One

posited explanation for the detected nitrogen is the presence of BNNTs trapped between H_3BO_3 layers, as observed in the cross section of another platelet, shown in Appendix Figure C.8. As for the aluminium, this evidently arises from the surrounding buckypaper impurity and is disregarded here. Interestingly, the carbon and platinum elemental maps were found to be almost identical for coloured pixel position, i.e. outline of features in the maps are matching. Like the platinum, the carbon was also detected evenly everywhere on the surface. This suggests possible hydrocarbon contamination during the Pt sputter coating process, as supported by additional EDX evidence below.

In Figure 4.27, another thick platelet is imaged by SEM and EDX at higher magnification. It is very obvious here that carbon and platinum have strikingly similar EDX maps, thus supporting the speculation that there was hydrocarbon contamination introduced during the sputter coating process, potentially from the faulty backstreaming of pump oil into the vacuum chamber (and also from adventitious carbon deposition). In order to extract a more accurate quantification of the platelet composition, the carbon is thus removed from analysis as a deconvolution element.[§] The consequent estimation of platelet composition from the EDX spectrum gives 42 at.% B, 5 at.% N and 53 at.% O. The calculated B:O atomic ratio is thus 1:1.3. Similarly, for the thick platelet pictured in Appendix Figure C.8, the B:O atomic ratio is 1:1.5. These results emphasise the principal B,O composition of the platelets.

In fact, the calculated B:O atomic ratios correspond closely to that of B_2O_3. Coupled with the observed platelet deformation during imaging into an increasingly crumpled appearance,[¶]it is possible that the thick H_3BO_3 platelets underwent dehydration in the ultra high vacuum (ca. 10^{-7} mbar) of the Zeiss Merlin SEM sample chamber into amorphous B_2O_3. Similarly, Li *et al.*, (2003) demonstrated the dehydration of crystalline H_3BO_3 nanotubes and nanorods into amorphous

[§]Note that a super atmospheric thin window (SATW) was used in front of the XMaxN-150 X-ray detector. SATW is polymer based with a high carbon content, so contributes to a carbon signal. However, this artefact is intentionally corrected for in the AZtec® software and is done for all EDX analysis presented here.[359]

[¶]Electron beam heating may also contribute to H_3BO_3 dehydration and platelet deformation.[340]

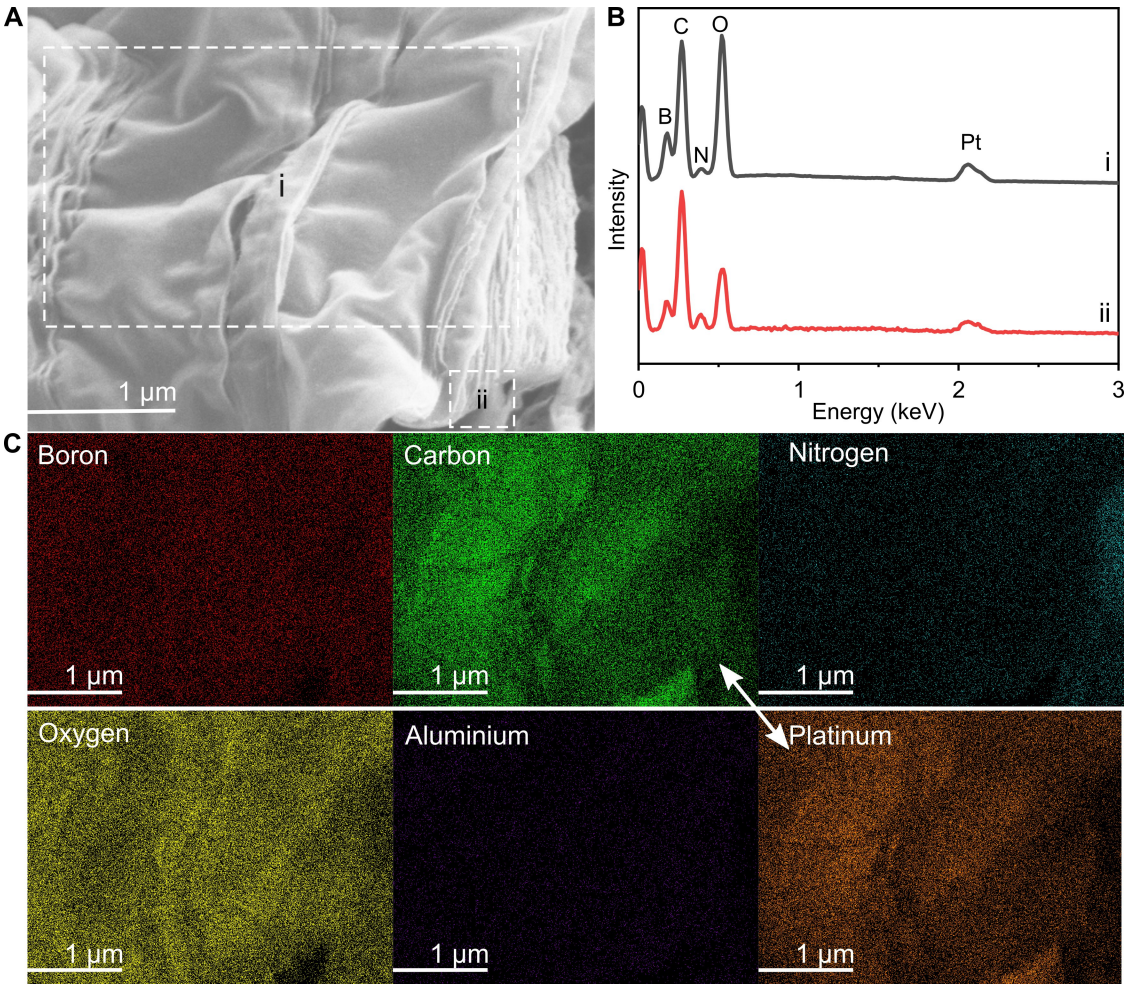


Figure 4.27: (A) High magnification SEM image of multi-layer ca. μm thick platelet found on the surface of oxidised BNNT buckypaper.(B) EDX spectra collected from the regions (i) and (ii) highlighted in the SEM image. (C) EDX elemental maps of the EDX elemental maps of the SEM imaged area. Pt and C again show evidently similar maps; see the triangle at the bottom right of the C and Pt maps corresponding to area (ii), suggesting hydrocarbon contamination. Otherwise the platelet shows strong B and O signals and low N. EDX acquisition details (Acceleration Voltage: 3.13 kV, Pixel Size: 0.00376 μm, Energy per channel: 10 eV, Dwell time: 500 μs, Stage Tilt: -4 °, Detector Elevation: 30 °)

B_2O_3 under vacuum, whereby the drop of H_2O partial pressure below that of the dissociation reaction equilibrium acts as the driving force of dehydration.[351] At higher vacuum levels, i.e. lower air pressure, the Li *et al.*, H_3BO_3 nanostructures were found to dehydrate at a faster rate. This could potentially explain why the platelets observed by TEM retained their crystalline H_3BO_3 structure but those imaged in the Zeiss Merlin by SEM/EDX exhibited a B_2O_3 composition; the JEOL

3000F TEM has a vacuum level of ca.$10^{-5} - 10^{-6}$ mbar, which is 1-2 orders of magnitude lower than that in the Zeiss Merlin SEM, and is thus speculated here to result in a slower rate of H_3BO_3 dehydration.

4.4 Conclusion

In this chapter, a method for the fabrication of BNNT buckypaper by combining the methods described in Chapter 2 and 3 on the macroscopic scale has been demonstrated. Here, instead of first synthesising the BNNTs in powder form and then assembling the powder, i.e.the traditional route adopted in the literature, pre-fabricated buckypaper templates of MWCNT@BN heteronanotubes were converted directly into a free-standing BNNT buckypaper. The achieved BNNT buckypapers have low density (0.17-0.2 g/cm^3), with BNNTs randomly entangled in a mesoporous-macroporous network assembly.

The first step in fabricating the BNNT buckypapers involved fabricating the MWCNT@BN heteronanotube buckypaper templates. Two methods were explored for template fabrication that involved the same steps but differed in the sequence in which these steps were implemented. Specifically, according to a first sequence, MWCNTs were coated with h-BN by CVD, and MWCNT@BN powder was then assembled into a buckypaper after sonication and vacuum filtration (Grade A). In contrast, the second sequence involved assemblage of pristine MWCNTs into a buckypaper, which was then coated with h-BN by CVD (Grade B). It was discovered that the sequence of steps influenced the structure of the BNNT buckypaper, i.e. the product of thermal oxidation of the MWCNT@BN buckypapers. Whilst BNNT buckypapers resulting from oxidation of Grade B MWCNT@BN buckypaper templates exhibited curled edges and thin cross-sections (30-40 μm), those resulting from Grade A exhibited a preserved geometry of the original template and a greater cross-sectional thickness (80-90 μm). Analysis of the h-BN content and electrical resistivity of the two grades of MWCNT@BN template buckypapers revealed that Grade A MWCNT@BN buckypaper had both a higher h-BN content (50%) and a five-fold higher electrical resistivity relative to Grade B MWCNT@BN

buckypaper. From this evidence, it is inferred that first coating h-BN onto MWCNTs and then fashioning the MWCNT@BN into a buckypaper template (according to Grade A) is the more efficient route for making MWCNT@BN buckypaper templates with a high, uniformly distributed h-BN content that is more favourable for BNNT buckypaper fabrication.

The composition of the BNNT buckypapers was also characterised to assess their h-BN purity. With regard to carbon impurities, EDX analysis revealed carbon content up to 19 at.%, whilst 26 at.% was detected by XPS. Whilst these values confirm the presence of carbon, they themselves do not provide a detailed description of the distribution or chemical nature of the carbon. Furthermore, these values are not directly comparable because of the fundamental differences in probing depths achieved by these two characterisation techniques. To address the outstanding questions regarding carbon impurity, XPS depth profiling was conducted with high resolution XPS scans taken at each depth interval. The C1s spectra reveal the carbon content is composed of heavily oxidised carbon species. In view of this C1s signature, alongside the higher carbon content on the buckypaper surface (26 at.%) relative to within its depths (9 at%), it is hypothesised that a significant contributor to the carbon impurity is from deposition of adventitious carbon. This hypothesis is supported by theoretical studies that modelled the propensity of h-BN, particularly defective h-BN as synthesised in this work, to chemisorb CO_2. The large surface area of the buckypaper is also likely to promote the CO_2 absorption capacity of the BNNT buckypaper. However, the possibility that heavily oxidised carbon species originate from the buckypaper itself, i.e. from oxidation of the graphitic components, cannot be eliminated. In comparison to free powder, the density of the nanotube network in buckypaper assembly could be a factor that limits the rate at which oxidised carbon is purged from the buckypaper by airflow. Similarly, the buckypaper could inherently have a slower rate of oxidation of the graphitic components at its core relative to its surfaces. This might explain the difference in the C1s spectra of the buckypaper surface and in its depths, the latter exhibiting peak contributions at binding energies associated with defective sp^2 carbon.

Oxygen impurities were also detected by EDX and XPS in all BNNT buckypapers. Based on evidence in preceeding Chapters 2 and 3, oxygen content can be attributed to the $Al_4B_2O_9$ impurities as well as to partial oxidation of the BNNTs themselves, resulting in B-O bonds incorporated into the nanotube lattice as well as the B_2O_3 oxidation by-product. Indeed, the partial oxidation of the BNNTs is prominently addressed in this chapter with focus on impurity structures detected on the surface of the buckypapers.

Particularly, polygonal platelets were discovered on the surface of all BNNT buckypapers fabricated here. Reference to the literature revealed the reporting of similar structures on assemblies of commercially available BNNTs that had undergone thermal oxidation to 750°C. Whilst that literature report proposed that these platelets were composed of partially oxidised h-BN resulting from unzipping of BNNTs, this hypothesis is refuted here. Instead, based on FTIR, TEM and EDX analysis (including Monte-Carlo modelling to predict X-ray Generation Depth) of the BNNT buckypapers and the surface platelets, it is presented here that these platelets are composed of H_3BO_3. A mechanism of H_3BO_3 crystallite formation is outlined, which involves partial oxidation of the BNNTs during thermal treatment to remove MWCNT, such that B_2O_3 clusters are formed. The large surface area provided by the buckypaper surface is postulated to promote coalescence of the B_2O_3 clusters, which upon exposure to ambient moisture spontaneously form the H_3BO_3 platelets. The role of ambient moisture in the H_3BO_3 growth mechanism is further evidenced by the thicker H_3BO_3 platelets observed and the increased oxygen content detected in the buckypapers after extending the period of BNNT buckypaper storage. More generally, the identification of these H_3BO_3 platelets and their growth mechanism is important to understanding BNNT macroscopic assembly behaviour at high temperature, which is an extreme environment in which they are anticipated to be increasingly applied, as outlined in Chapter 1.

Overall, in comparison to the few BNNT buckypapers reported in the literature, those synthesised here have comparable density to *in-situ* grown buckypapers and are less dense that those made by the traditional filtration route which use significantly

greater quantities of commercially available BNNTs to make buckypapers. However, unlike buckypaper made from highly crystalline commercially available BNNT, those made here are composed of more oxygen impurity in view of the partially oxidised BNNTs and the H_3BO_3 surface crystallites. These BNNT buckypapers also appear to contain non-negligible quantities of heavily oxidised carbon contaminant species. The influence of these impurities on the properties of the BNNT buckypaper remains to be tested. It is also proposed that some of these issues could be addressed in the future by improving the crystallinity of the deposited h-BN, thereby improving BNNT oxidative and hydrolytic stability and reducing the number of defects sites that can chemisorb CO_2. Otherwise, these BNNT buckypapers present a high selectivity to nanotube morphologies, i.e. no other h-BN polymorphs as are common in the commercial BNNT assemblies, and provide a route to forming buckypapers with a diversity in BNNT dimensions. Further, as it is proven here that the BNNT buckypaper can retain the geometry of its MWCNT template, it is envisaged that this method can be adopted for BNNT buckypaper fabrication using any MWCNT template buckypaper shape/form.

Chapter 5
Outlook

Contents

5.1 Summary 180
5.2 Future Work 181

5.1 Summary

This work has demonstrated the viability of a new synthesis pathway for the fabrication of BNNTs and their macroscopic, sheet-like assemblies. It is a step towards scalable BNNT production that is versatile, economically feasible and non-hazardous.

The first stage of the proposed synthesis pathway is the deposition of h-BN onto the surface of MWCNTs under atmospheric pressure CVD conditions and using ammonia borane as the precursor. In depth characterisation of the heteronanotube revealed the advantage of this method over others in the literature for synthesising a high purity of h-BN that is selectively deposited as coaxial layers, and has minimal covalent interactions with the core MWCNT.

It was then proven that these heteronanotubes can act as intermediate products that, when subjected to thermal oxidation at appropriate temperatures to

purposefully remove the MWCNT cores, leave the coaxial h-BN shells as residual BNNTs. The potential for this method to facilitate diameter tunablity of the BNNT shells was evidenced by use of MWCNTs of varying outer diameter.

It was also demonstrated here that the above described two-stage process can be implemented in conjunction with vacuum filtration to fabricate sheet-like (buckypaper) macroscopic assemblies of BNNTs with variable yields, thicknesses and geometries.

Finally, platelet structures were discovered on the surface of the BNNT buckypapers, which were identified as boric acid crystallites. This finding has substantiated the hygroscopic nature of BNNTs, particularly those of lower crystallinity, and contributes to a new understanding of their oxidation behaviour.

5.2 Future Work

There are several recommended paths of research following on from this work.

5.2.0.1 BNNT Structure

As the crystallinity of the BNNTs fabricated here was demonstrated to be low, a near-term objective would be to improve this. There are two proposed paths to achieve this, the first being the introduction of a high temperature grapitisation step for the CNTs prior to their use as templates for h-BN deposition. This is based on the findings that CNT template surface crystallinity influences the crystallinity of h-BN deposited onto it. Alternatively, subsequent to BNNT fabrication by sacrificial templating, the BNNTs could be treated to an additional annealing step, during which they are heated to high temperatures. The design of this crystallisation procedure could be informed by previous investigations on the conversion of turbostratic BN into h-BN.[170] In conjunction with the BNNT synthesis route in this work, these additional crystallisation steps could facilitate the fabrication of BNNTs of the same diameter but with varying degrees of crystallinity. This would be especially beneficial for isolating and subsequently investigating the effect of crystallinity on BNNT properties.

Future work could also improve upon the purity of the BNNT product by selecting CNT templates with fewer impurities themselves, i.e. fewer catalyst particles and catalyst-substrate particles. A lower residual catalyst content would also reduce the occurrence of unintentional growth of BNNTs by catalytic CVD amongst the template-assisted BNNTs.

Beyond improvements in the quality of BNNTs fabricated, there is also potential for parametric investigation of the CVD variables in order to control the thickness of deposited h-BN (and the consequent wall thickness of BNNTs). Variables in relation to the ammonia borane precursor, such as its heating temperature and the flow rate at which its vapour-phase constituents are introduced into the CVD reactor furnace are suggested starting points for such future studies.

5.2.0.2 BNNT Buckypaper Architectures

At the macroscopic scale, only buckypapers with randomly oriented BNNTs were fabricated in this work. However, buckypapers with aligned nanotubes would be predictably more effective at exhibiting anisotropic properties, e.g. greater in-plane thermal conductivity for in-plane aligned nanotubes. To this end, trials were made here to fabricate MWCNT buckypapers with in-plane alignment by adapting a method found in the literature for spontaneous alignment of SWCNTs.[360] SEM characterisation suggested that global uni-directional alignment was not achieved. Nevertheless, these MWCNT buckypaper appeared to have a more densely packed architecture with perceptibly better in-plane (x,y) alignment than those detailed in Chapter 4 (See Figure 5.1). A preliminary attempt to fabricate a BNNT buckypaper from this MWCNT template buckypaper resulted in a similarly more densely packed architecture than previously achieved; interestingly, this had a translucent and diaphanous appearance. This early result is a promising indicator that the sacrificial templating method could be used to fabricate BNNT buckypapers of a variety of architectures, with alignment being one target of future research.

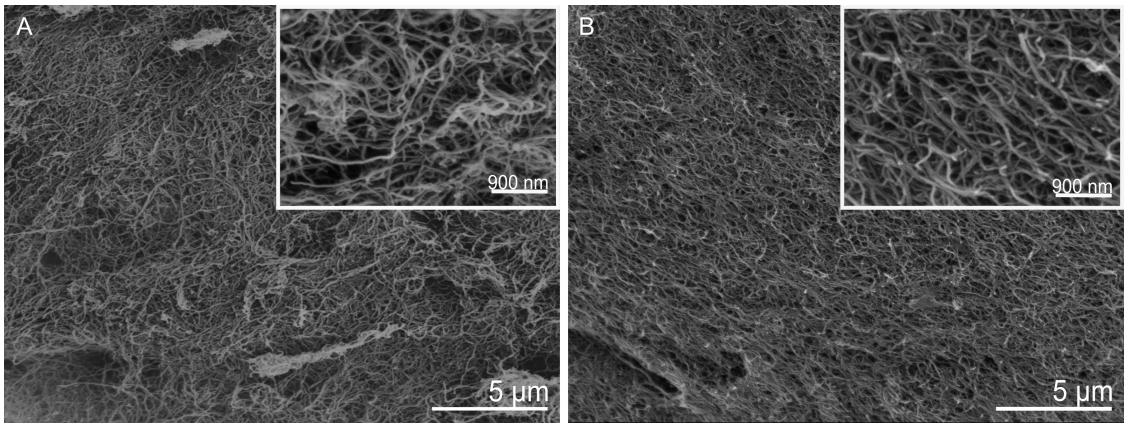


Figure 5.1: Examples of buckypapers with (A) randomly entangled MWCNTs compared to (B) more densely packed MWCNTs with better in plane (x,y) alignment.

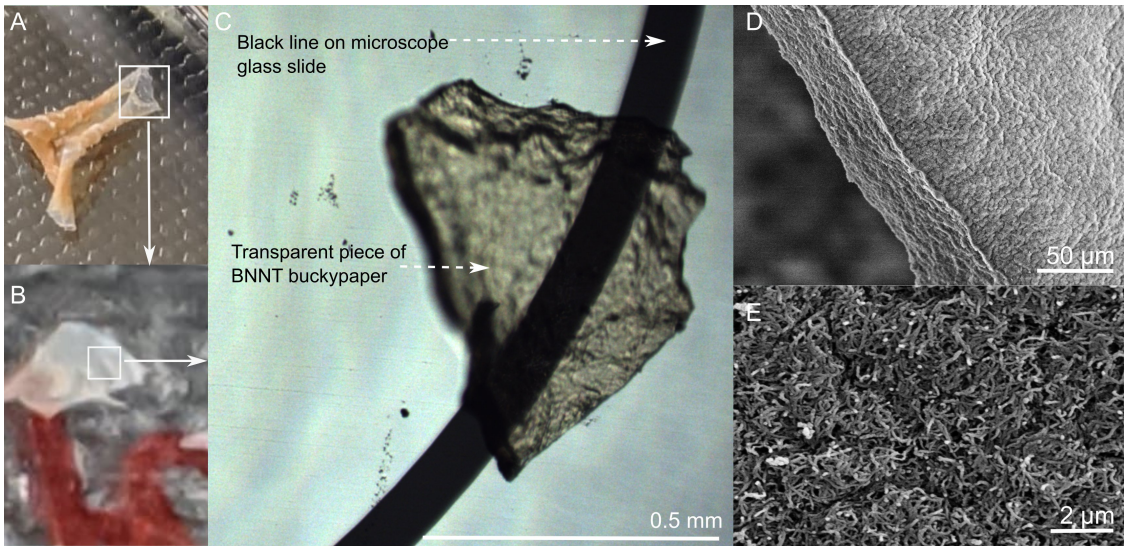


Figure 5.2: BNNT buckypaper assembly with transparent, diaphanous appearance, as fabricated by the sacrificial templating of a more densely packed MWCNT buckypaper assembly shown in Figure 5.1B. (A-B) Camera Images (C) Optical Microscope image (D-E) SEM images of cross section and surface respectively.

5.2.0.3 Hierarchical Structure Assemblies

Beyond macroscopic sheet assemblies solely composed of nanotubes, it is also envisaged here that such assemblies could incorporate hiearchicial nanostructures, such as with nanotubes hybridised with nanosheets.

Indeed, the earliest examples of hybridisation of 1D and 2D nanomaterials involves carbon nanomaterials systems. For instance, CNTs have been synthesised with graphene flakes covalently attached as 'foliates'.[361–366] These hybrid CNT-

graphene structures present increased surface area and a high edge density, which is beneficial for increased surface charge density for supercapacitor applications.[364] Moreover, these hierarchical nanostructures have also been deemed advantageous for replacing pristine CNTs as reinforcing fillers in composites, since the protruding foliates present more surface area for matrix-filler interaction and better frictional resistance.[361,365]

Only recently, in our group, has this concept of 1D-2D hybridisation been demonstrated for h-BN foliates decorated around MWCNTs. Meysami *et al.*, (*in preparation)*, implemented CVD at 1300 °C with the precursors Boron powder, MgO, Fe_2O_3 in the molar ratio of 2:1:1 under an NH_3 (100 sccm in 50 sccm N_2) flow to foliate h-BN nanoflakes onto MWCNTs already assembled into vertically aligned carpets.

Preliminary experiments were conducted here to investigate whether the method described by Meysami *et al.*, was also feasible for the introduction of h-BN nanosheets (BNNS) onto the surface of BNNTs. Note that the BNNTs were already assembled into buckypapers as achieved in Chapter 4. The results are depicted in Figure 5.3, which show that the BNNT buckypaper remained intact following the additional CVD treatment (Figure 5.3A) and that h-BN nanosheet foliage had fully covered the BNNTs (Figure 5.3B-C). As shown in Figure 5.3D-E, the h-BN flakes were only few-layers thin. This described route of hierarchical BNNT-BNNS structures fabrication is thus promising and remains to be further explored to refine control of structural parameters such as h-BN nanosheet dimensions and homogeneity of coverage (along the nanotubes and throughout the buckypaper assembly).

Whilst there are a few works in the literature that demonstrated fabrication of BNNT-BNNS hybrids,[367–369] to the best of our knowledge, these involve synthesis of BNNT and BNNS during the same reaction procedure, thereby presenting limitations to the independent control of BNNT and BNNS structural parameters. Instead, separation of these synthesis steps, as proposed here, alongside leveraging of the versatile sacrificial templating method for BNNT synthesis, could potentially facilitate the fabrication of a dimensional spectrum of BNNT-BNNS hierarchical

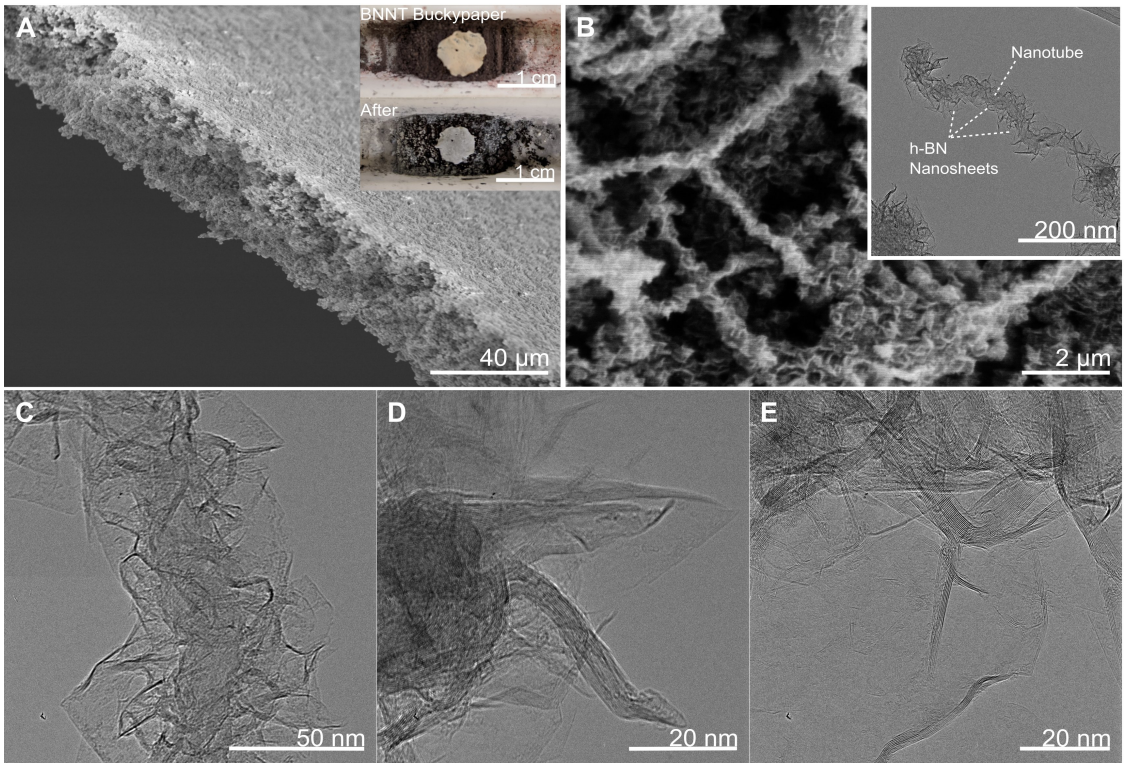


Figure 5.3: (A) SEM cross section of BNNT buckypaper after undergoing CVD process to introduce nanosheet (BNNS) foliates. (Inset: Before and after images of BNNT buckypaper resting on unreacted and reacted precursor powders respectively). (B) SEM image showing hierarchical structure BNNT-BNNS within the buckypaper. (Inset: TEM image of inidividual BNNT foliated with BNNS.) (C-E) HRTEM images showing the nano-dimensional foliates that are ultra-thin (electron beam transparent). The nanosheet d_{002} spacing is 0.33 nm, as expected of h-BN.

structures. Interestingly, the BNNS foliation demonstrated in Figure 5.3 was achieved within a relatively short CVD duration of 30 minutes, as opposed to a multi-hour treatment process. It is hypothesised that the defects present in the as-synthesised BNNTs promoted BNNS nucleation and further investigation is necessary to understand their growth mechanism.

Furthermore, the assembly of BNNT-BNNS hierarachical structures into macroscopic sheets or other architectures as proposed here, has yet to be reported elsewhere. These assemblies could potentially be used to form three-dimensional thermal networks within polymer composites to improve thermal conductivity more effectively than if only BNNTs or BNNS were added as fillers. Indeed, the synergetic effect of BNNTs and BNNS has been demonstrated to enhance

thermal conductivity when mixed together as fillers in an epoxy nanocomposite.[370] In comparison, BNNT-BNNS hierchical structure buckypapers are predicted to facilitate higher filler loading into the polymer nanocomposite and consequently greater enhancement of thermal conductivity.

5.2.0.4 Buckypaper Composites and Properties

One of the next steps towards application of these BNNT buckypapers is the fabrication of BNNT buckypaper composites. Of particular interest are BNNT polymer composites, for which the buckypaper assembly provides a route to the inclusion of a high weight % of BNNTs into the polymer matrix, i.e. by polymer infiltration of the buckypaper. There remains significant work to be done in optimising such composite fabrication.

The potential scope of this CNT template-assisted method in developing a spectrum of BNNT crystallinities, diameters and wall thicknesses, as well as buckypaper densities and alignments, will conceivably facilitate a better understanding of the influence of these characteristics on the overall buckypaper and/or composite performance. The present literature is deficient in this envisaged diversity of BNNT structures and assemblies.

The properties (e.g. thermal conductivity, mechanical strength *etc.)* of these as-fabricated BNNT buckypapers as well as their future composites remains to be tested to realise their potential applications as described in Chapter 1.

5.2.0.5 Heteronanotube Assemblies and Properties

Whilst much of this outlook discussion has focused on BNNTs, it must be acknowledged that the intermediate product of the templating process, i.e. the heteronanotubes of CNT coated with coaxial h-BN, are themselves garnering research interest for a range of applications including high temperature composites, nano-mechanical components , nano-electronics, field emitters and thermal management materials.[138] The synthesis method presented here could be implemented to make a range of heteronanotube morphologies (e.g. bamboo, herringbone, cylindrical) CNTs coated with h-BN. As such true van der Waals type heteronanotubes are

under-represented in the literature and are often not clearly distinguished from partially covalent heteronanotubes, there is still significant progress to be made in the understanding and characterisation of their properties. Furthermore, there is limited investigation into such heteornanotube macroscopic assemblies relative to their pristine CNT or BNNT counterparts.

Appendices

Appendix A

Chapter 2 Appendix

Contents

A.1 EELS Quantitative Analysis Parameters 189
A.2 Synthesis of MWCNT@BN by $B_2O_3 + NH_3$ precursors 193
A.2.1 Materials and Methods 193
A.2.2 Results 194
A.3 Nanocyl NC7000™ Impurities 197
A.3.1 Effects of Ammonia Borane CVD on Al_2O_3 198

A.1 EELS Quantitative Analysis Parameters

The EELS composition quantification parameters used to analyse spectra included in Figures 2.8, 2.9, 2.10, 2.11B-E are included in the Tables below.

Spectral Image: Figure 2.8

Probe Size (nm^2)	**Exposure Time (s)**	**Integration Time (s)**	**Spectral Image Acquisition Time**	**Resolution (eV)**	**Dispersion (eV/pixel)**	**t/λ**
1	0.09996	0.1999	2 min 37 s	2.8	0.25	0.15
Elements	**C**					
Background Removal Parameters						
Fitting Range (eV) (Power Law)	251.5 - 280.3					
Signal Quantification Parameters						
Signal Counts	4.62e+007 ± 7789					
Integration Range (eV)	282.0 - 312.0					
Cross section (barns) (Hartree-Slater)	2325 ± 232					
Absolute Quantification						
Areal density (atoms/nm^2)	1.99e+014 ± 2.0e+013 / I_o					

Table A.1: EELS Experimental conditions and quantification parameters for spectral image in Figure 2.8

Spectral Image : Figure 2.9

Probe Size (nm^2)	**Exposure Time (s)**	**Integration Time (s)**	**Spectral Image Acquisition Time**	**Resolution (eV)**	**Dispersion (eV/pixel)**	**t/λ**
1	0.0999	0.0999	11 mins	1.3	0.25	0.08
Elements	**B**	**C**	**N**	**O**		
Background Removal Parameters						
Fitting Range (eV) (Power Law)	167.8 - 187.3	250.8 - 279.3	355.3 - 394.5	475.5 - 529.0		
Signal Quantification Parameters						
Signal Counts	1.78e+008 ± 22555	2.02e+008 ± 19767	3.03e+007 ± 13649	5.76e+006 ± 9393		
Integration Range (eV)	188.0 - 218.3	280.3 - 310.8	395.5 - 426.0	530.5 - 560.8		
Cross section (barns) (Hartree-Slater)	5991 ± 599	2383 ± 238	1101 ± 110	683 ± 68		
Absolute Quantification						
Areal density (atoms/nm^2)	2.98e+014 ± 3.0e+013 /I_o	8.49e+014 ± 8.5e+013 / I_o	2.75e+014 ± 2.7e+013 / I_o	8.43e+013 ± 8.4e+012 / I_o		

Table A.2: EELS Experimental conditions and quantification parameters for spectral image in Figure 2.9

Spectral Image : Figure 2.10

Probe Size (nm^2)	**Exposure Time (s)**	**Integration Time (s)**	**Spectral Image Acquisition Time**	**Resolution (eV)**	**Dispersion (eV/pixel)**	**t/λ**
1	0.0999	0.0999	5 min 12 seconds	1.3	0.25	0.08
Elements	**B**	**C**	**N**	**O**		
Background Removal Parameters						
Fitting Range (eV) (Power Law)	170.5 - 188.8	252.8 - 280.8	358.8 - 398.0	476.8 - 530.3		
Signal Quantification Parameters						
Signal Counts	9.85e+007 ± 15884	8.87e+007 ± 13444	1.70e+007 ± 9327	3.40e+006 ± 6450		
Integration Range (eV)	189.5 - 219.5	281.8 - 312.0	399.0 - 429.0	532.0 - 561.8		
Cross section (barns) (Hartree-Slater)	6190 ± 619	2480 ± 248	1220 ± 122	705 ± 70		
Absolute Quantification						
Areal density (atoms/nm^2)	1.59e+014 ± 1.6e+013 /I_o	3.58e+014 ± 3.6e+013 /I_o	1.39e+014 ± 1.4e+013 /I_o	4.83e+013 ± 4.8e+012 /I_o		

Table A.3: EELS Experimental conditions and quantification parameters for spectral image in Figure 2.10

Spectral Image : Figure 2.11B-C

Probe Size (nm^2)	**Exposure Time (s)**	**Integration Time (s)**	**Spectral Image Acquisition Time**	**Resolution (eV)**	**Dispersion (eV/pixel)**	**t/λ**
1	0.1999	0.1999	9 mins 14 s	1.3	0.25	0.03
Elements	**B**	**C**	**N**	**O**		
Background Removal Parameters						
Fitting Range (eV) (Power Law)	170.3 - 188.3	252.0 - 280.0	357.0 - 396.3	477.0 - 530.0		
Signal Quantification Parameters						
Signal Counts	6.00e+007 ± 12429	6.15e+007 ± 10598	1.04e+007 ± 6935	1.70e+006 ± 4387		
Integration Range (eV)	189.0 - 219.0	281.0 - 311.0	397.3 - 427.3	531.0 - 560.8		
Cross section (barns) (Hartree-Slater)	6111 ± 611	2403 ± 240	1151 ± 115	683 ± 68		
Absolute Quantification						
Areal density (atoms/nm^2)	9.82e+013 ± 9.8e+012 /I_o	2.56e+014 ± 2.6e+013 / I_o	9.06e+013 ± 9.1e+012 /I_o	2.50e+013 ± 2.5e+012 /I_o		

Table A.4: EELS Experimental conditions and quantification parameters for spectral image in Figure 2.11

Line Scan : Figure 2.11D

Probe Size (nm^2)	**Exposure Time (s)**	**Integration Time (s)**	**Spectral Image Acquisition Time**	**Resolution (eV)**	**Dispersion (eV/pixel)**	**t/λ**
1	0.1999	0.1999	1 min 40 s	1.3	0.25	0.05
Elements	**B**	**C**	**N**	**O**		
Background Removal Parameters						
Fitting Range (eV) (Power Law)	168.5 - 187.5	252.0 - 280.3	355.0 - 394.8	475.3 - 529.0		
Signal Quantification Parameters						
Signal Counts	1.41e+007 ± 6228	1.81e+007 ± 5573	2.36e+006 ± 3572	4.22e+005 ± 2273		
Integration Range (eV)	188.0 - 218.0	281.0 - 311.3	395.8 - 426.0	530.5 - 561.0		
Cross section (barns) (Hartree-Slater)	5951 ± 595	2422 ± 242	1101 ± 110	688 ± 69		
Absolute Quantification						
Areal density ($atoms/nm^2$)	2.37e+013 ± 2.4e+012 /I_o	7.49e+013 ± 7.5e+012 / I_o	2.14e+013 ± 2.1e+012 /I_o	6.12e+012 ± 6.1e+011 / I_o		

Table A.5: EELS Experimental conditions and quantification parameters for linescan 1 in Figure 2.11D

Line Scan : Figure 2.11E

Probe Size (nm^2)	**Exposure Time (s)**	**Integration Time (s)**	**Spectral Image Acquisition Time**	**Resolution (eV)**	**Dispersion (eV/pixel)**	**t/λ**
1	0.1999	0.1999	2 min 4 s	1.3	0.25	0.04
Elements	**B**	**C**	**N**	**O**		
Background Removal Parameters						
Fitting Range (eV) (Power Law)	169.0 - 187.3	252.5 - 280.5	355.3 - 394.8	476.8 - 530.5		
Signal Quantification Parameters						
Signal Counts	1.62e+007 ± 6395	1.72e+007 ± 5543	2.77e+006 ± 3628	3.39e+005 ± 2294		
Integration Range (eV)	189.0 - 218.5	281.5 - 311.8	395.8 - 426.3	532.0 - 562.8		
Cross section (barns) (Hartree-Slater)	6031 ± 603	2461 ± 246	1111 ± 111	727 ± 73		
Absolute Quantification						
Areal density ($atoms/nm^2$)	2.69e+013 ± 2.7e+012 / I_o	6.97e+013 ± 7.0e+012 / I_o	2.49e+013 ± 2.5e+012 /I_o	4.66e+012 ± 4.7e+011 / I_o		

Table A.6: EELS Experimental conditions and quantification parameters for linescan 2 in Figure 2.11E

A.2 Synthesis of MWCNT@BN by $B_2O_3 + NH_3$ precursors

This method of coating h-BN onto MWCNTs was adapted from Chang *et al.*, (2015).[119] It was conducted in this work for the purpose of comparing the degree of covalent bonding between the h-BN coating and underlying MWCNT when implementing CVD with the $B_2O_3 + NH_3$ versus H_3NBH_3 precursor pathways. See Chapter 2.

A.2.1 Materials and Methods

Name	Purity	Supplier
Reactants		
Solids		
MWCNT Nanocyl NC7000™	90 %	Nanocyl SA
Boric anhydride	99.98 %	Sigma-Aldrich
Gases		
Argon	99.998%	Air Products
Ammonia	99.98%	BOC
Solvents		
Deionized Water		-
Acetone		Sigma Aldrich
Methanol		Sigma Aldrich
Isopropanol		Sigma Aldrich

Table A.7: Summary of reactants implemented for synthesis of MWCNT@BN by the $B_2O_3 + NH_3$ CVD pathway. Solvents used for rinsing the product or cleaning of substrates, sample holders are also listed.

The Nanocyl MWCNTs (12 mg) were mixed with boric anhydride powder (B_2O_3) (69 mg) in a glass bottle. This solid mixture was transferred to an alumina boat which had been previously cleaned by a solvent wash with Acetone, Methanol, Isopropanol and UV/Ozone treated.

The alumina boat was placed into an alumina tube reactor, which was sealed and purged with Ar at the flow rate of 300 sccm for 20 mins. Subsequently, furnace heating was initiated, and at the target temperature of 1200°C, the gas flow was switched from 300 sccm Ar to 300 sccm Ar/NH_3 (1:4) mixture for 1 hour.

After cooling the reactor, the product was collected and dispersed in boiling water for 1 hour to dissolve any residual B_2O_3. After centrifugation, the precipitate was dried under 70°C for 2 hours, and the final powder was collected into a glass vial.

A.2.2 Results

The results highlighted here confirm that the Chang *et al.* method was successfully repeated to introduce an h-BN coating onto MWCNTs. As shown in the example HRTEM images in Figure A.1, the nanotubes maintained a coaxial structure with no protrusions or structural collapse, whilst an increase in their diameter was observed that corresponds to a 2-3 nm h-BN thick coating.

EDX spectra of the MWCNT@BN validate the presence of B and N , as shown in Figure A.2D, spectrum 1. The estimated atomic ratio of B:N is 0.9:1, close to the 1:1 ratio of h-BN.

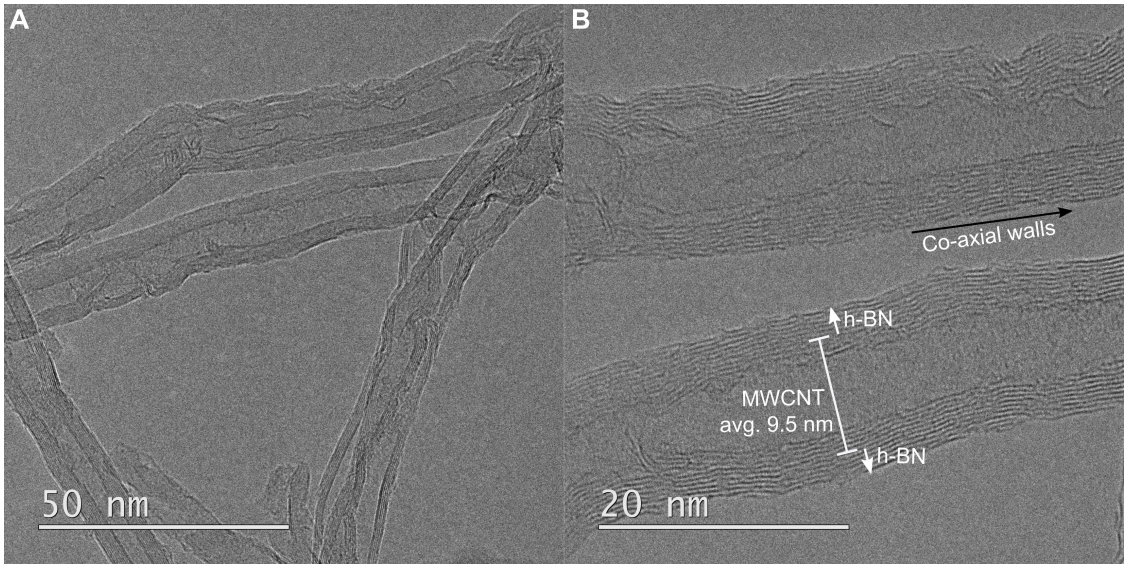


Figure A.1: HRTEM images of Nanocyl NC7000 MWCNTs after undergoing APCVD with B_2O_3+ NH_3 precursors ($MWCNT@BN_{B_2O_3+NH_3}$, according to the method published by Chang *et al.*, 2015. [119] A $\sim$ 4 nm increase in outer diameter was observed, corresponding to the deposited h-BN coaxial layers.

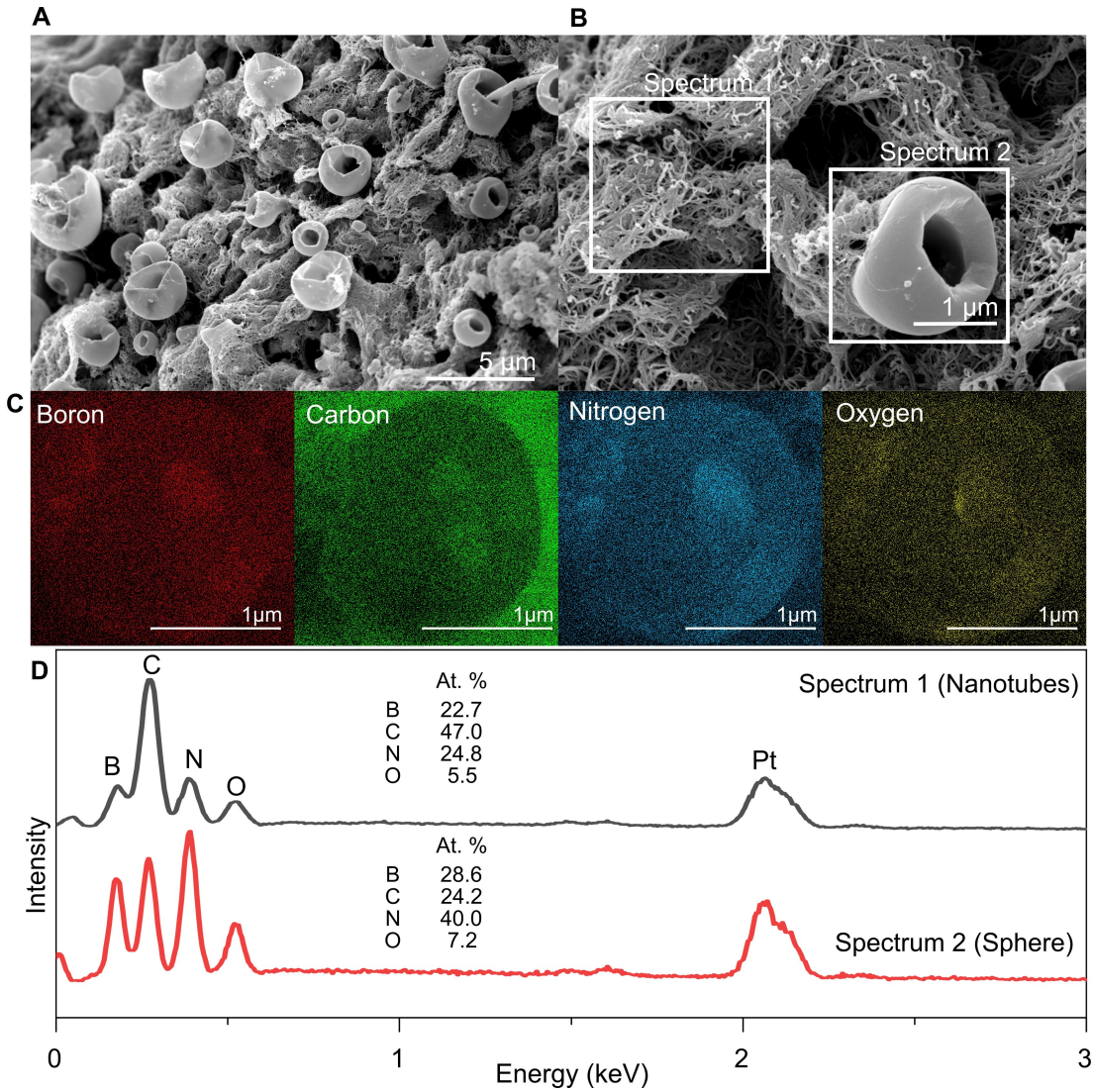


Figure A.2: (A-B) SEM images of MWCNT@BN as produced by APCVD and B_2O_3+NH_3 precursors, and the impurity spheres grown on the surface of the nanotube agglomerates.(C) EDX elemental maps of a highlighted sphere in (B). The associated EDX spectrum for the sphere is shown in (D), alongside an EDX spectrum of the nanotubes. The Pt signal is due to a Pt coating used to reduce sample charging during electron microscopy. EDX acquisition details (Acceleration Voltage: 5 kV, Pixel Size: 0.00159 μm, Energy per channel: 5 eV, Dwell time: 50 μs, Stage Tilt: 0 °, Detector Elevation: 30 °)

Also observable on the SEM images in Figures A.2A-B, are spherical micro-structures which appear to by deflated/collapsed. EDX maps and spectra of the spheres, exemplified in Figure A.2C and D (spectrum 2) appear to suggest a B,C,N,O composition. However, as discussed in §4.3.3.4 and Appendix C, EDX of structures on the surface of an underlying material is prone to mixing of signals from both surface + substrate. Hence, the carbon component in the imaged sphere (spectrum

2) could potentially be from the MWCNT@BN. However, it is evident that the sphere itself contains BN (see maps in Figure A.2C).

The implications of the spheres are addressed in §2.3.3.

Further analysis of the MWCNT@BN, particularly by XPS to address the nature of bonding between the h-BN and MWCNT as well as the nature of the detected oxygen, is included in §2.3.2.2.

A.3 Nanocyl NC7000™ Impurities

The Nanocyl NC7000™ MWCNTs is an economical 'industrial grade' of CNT that is commercially available for bulk acquisition. This facilitates its prospective use in up-scaled synthesis techniques involving CNT material.

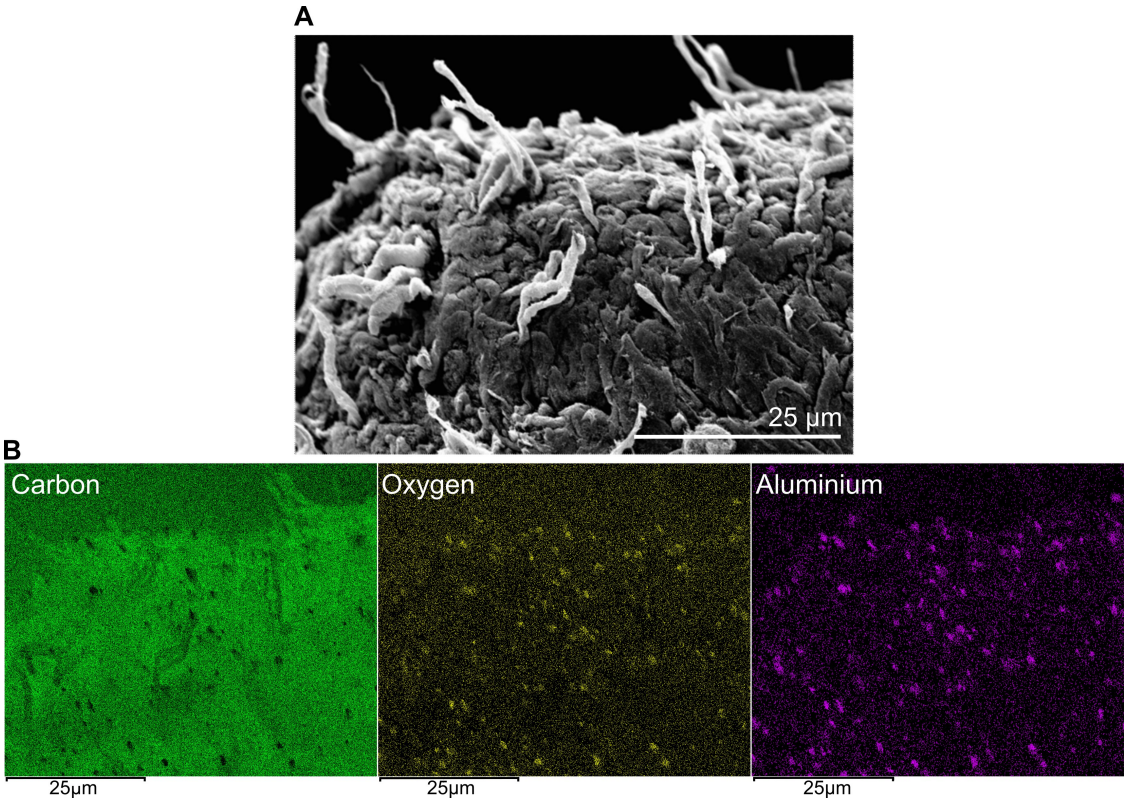


Figure A.3: (A) Low Magnification SEM of agglomerated Nanocyl NC7000™ MWCNTs along with (B) corresponding EDX elemental maps depicting dispersed oxygen and aluminium containing impurity amongst the MWCNTs. EDX acquisition details (Acceleration Voltage: 5 kV, Pixel Size: 0.06584 μm, Energy per channel: 10 eV, Dwell time: 120 μs, Stage Tilt: 0 °, Detector Elevation: 30 °)

Characterisation of the Nanocyl NC7000™ MWCNTs was required to examine the purity composition of the as-received batch. As shown in the EDX elemental maps of Figure A.3, there are distinctive micrometer scale particles distributed amongst the CNTs that are composed of oxygen and aluminium. To determine the wt.% contribution of these impurities to the CNT sample and to isolate them for further composition analysis, TGA was conducted. Subsequent to the oxidation and vaporisation of graphitic carbon in air at high temperatures, there is a residual weight

of $\sim 10\%$ (Figure A.4A). Analysis of this residual reveals that it is composed of the micrometer scale flat-surfaced particles (Figure A.4B) that have an aluminium and oxygen ratio closely corresponding to Al_2O_3, as concluded from the EDX spectrum in Figure A.4. Other trace impurities detected include iron, cobalt and sodium. These results closely correspond to the expected impurity composition of the NC7000™grade of MWCNTs; the Al_2O_3 act as supports for the transition metal oxide catalysts (Fe,Co) used for CVD synthesis of these MWCNTs. Trace Na, also previously detected in NC7000 grade[145], is not a catalyst material and its origin is unspecified, but is likely introduced at some stage of the Nanocyl proprietary synthesis process.

A.3.1 Effects of Ammonia Borane CVD on Al_2O_3

It was discovered that the CVD method implemented here to coat h-BN onto the MWCNTs also resulted in a change of composition of the Al_2O_3 impurity intrinsic to NC7000™. As shown in the SEM image in Figure A.5A, clusters of nanorod-like structures were found in the MWCNT@BN sample. A literature search for similar structures revealed that they resembled aluminium borate nanorods produced via pyrolysis of polyaminoborane ($[NH_2{-}BH_2]_n$) over Al_2O_3 powder at 1000°C under N_2 flow.[371] Indeed, XRD analysis of the MWCNT@BN indicated that newly observed peaks can be indexed to $Al_4B_2O_9$. Interestingly, the original Al_2O_3 is not detected by XRD in the raw MWCNT sample or MWCNT@BN sample.

TEM of a nanorod, as seen in Figure A.5B revealed a 0.51 nm lattice spacing, corresponding to the (220) plane of $Al_4B_2O_9$, as identified from JCPDS 00-029-0010.[372–374] Nanorods observed here have an average diameter of 42 ± 13 nm based on measurements of 40 nanorods imaged via SEM.

It is theorised here that vapour phase decomposition of the molecular precursor H_3BNH_3 over the Al_2O_3 platelets in the Nanocyl NC7000™ MWCNT sample led to their conversion into $Al_4B_2O_9$. This is the first reported instance of this path to $Al_4B_2O_9$ nanorod synthesis, and is likely most similar to the polyaminoborane polymer precursor route[371] and unlike other chemical routes.[372,375–377]

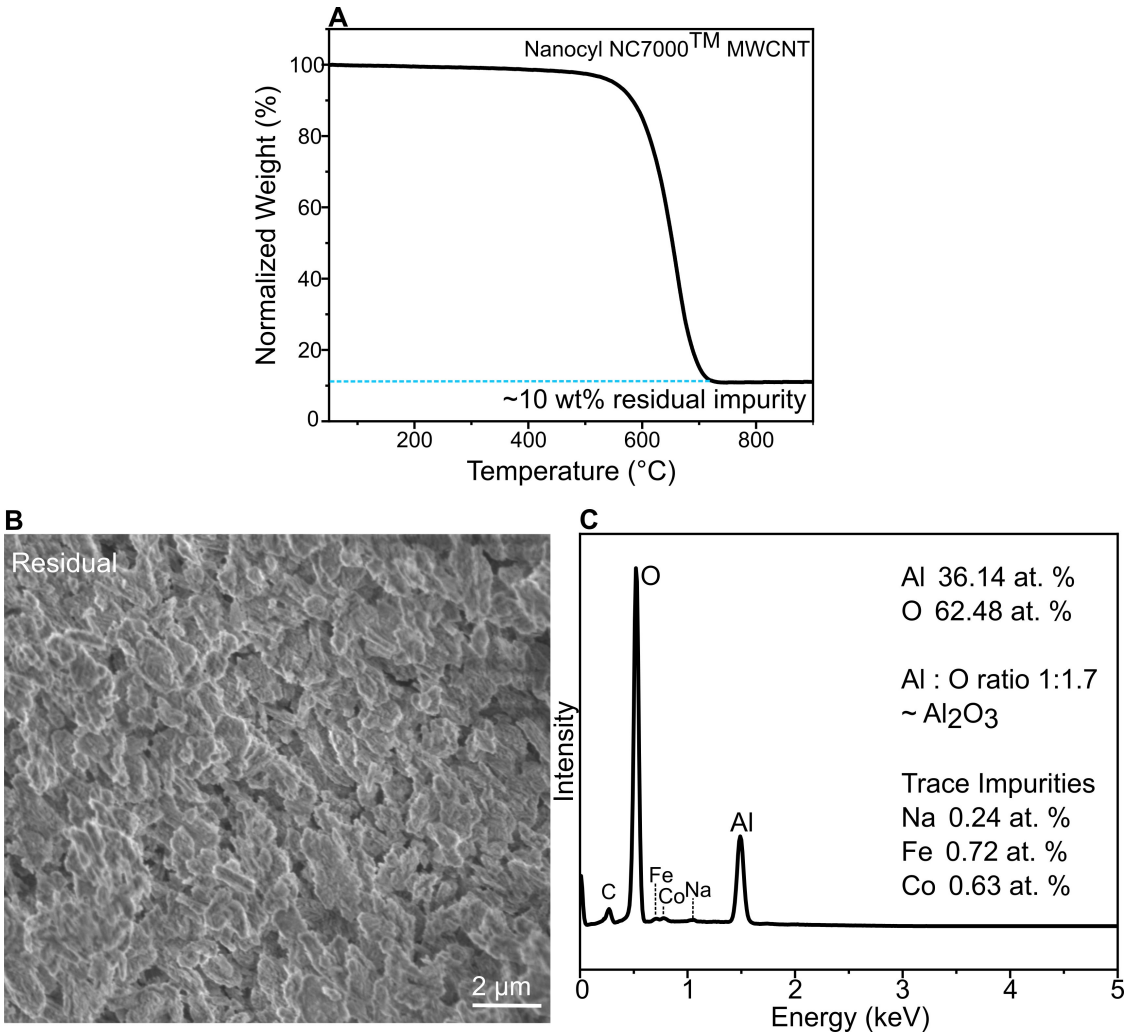


Figure A.4: (A) Thermogravimetric analysis of Nanocyl NC7000™ to detect weight % contribution of non-carbon impurities. (B) SEM image of residual collected after TGA shows plate-like particles. (C) EDX spectrum of residual concludes that main impurity is Al_2O_3. EDX acquisition details (Acceleration Voltage: 3 kV, Pixel Size: 0.01459 μm, Energy per channel: 10 eV, Dwell time: 150 μs, Stage Tilt: 0 °, Detector Elevation: 30 °)

As proposed by Du *et al.*, the decomposition of the polyaminoborane precursor (or the molecular ammonia borane precursor in the case here) facilitates the diffusion of boron into the Al_2O_3, whilst nitrogen is released at the surface.[371] The preferential growth of $Al_4B_2O_9$ in the nanorod morphology emerging from Al_2O_3 is a 'means to relieve residual stress that arises due to thermal expansion mismatch between the aluminum borate and alumina phases.'[375]

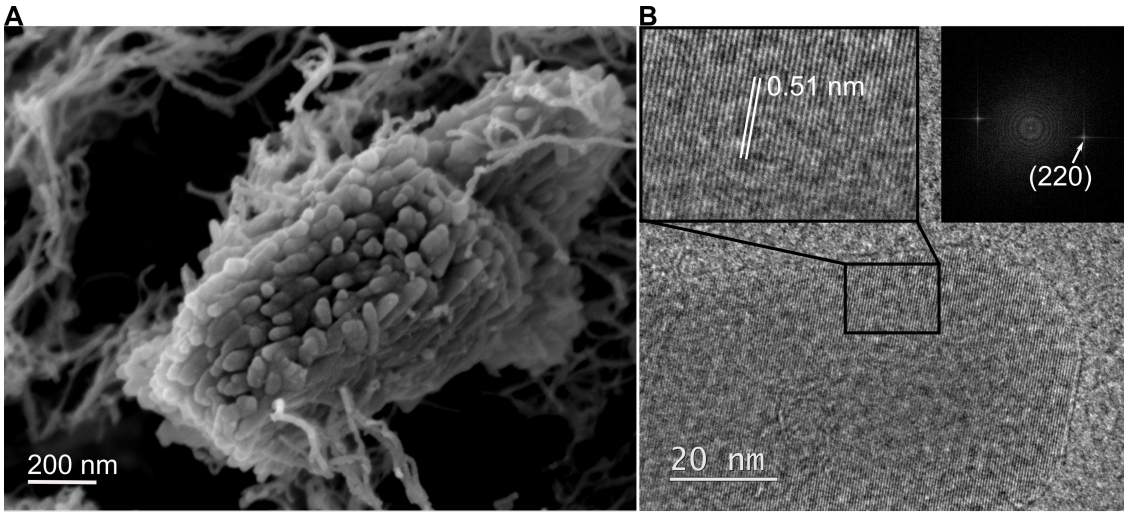


Figure A.5: (A) SEM image of clustered nanorod structures observed in MWCNT@BN sample. (B) HRTEM image of single nanorod. 0.51 nm spacing is indexed to the (220) plane of $Al_4B_2O_9$. Inset is a magnified view of the interlayer spacing and corresponding FFT

Appendix B

Chapter 3 Appendix

Contents

B.1 Oxidation Rate Calculations 201
B.2 Additional BNNT Characterisation 202
B.2.1 EELS quantitative analysis parameters 202
B.2.2 BNNTs after 900°C 204
B.2.3 Catalysed BNNT growth 205
B.3 AACVD MWCNTs characterisation 206

B.1 Oxidation Rate Calculations

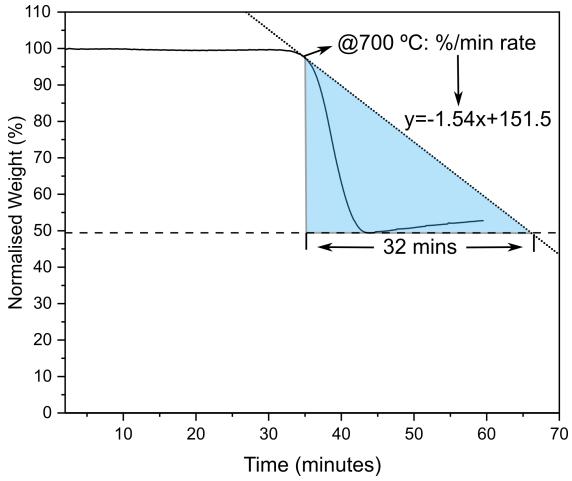


Figure B.1: TGA graph of Normalised Weight % vs. Time for MWCNT@BN heteronanotube oxidised in air. Tangential rate of oxidation is calculated at 700 °C as 1.54%/min.

B.2 Additional BNNT Characterisation

B.2.1 EELS quantitative analysis parameters

The Table below includes the EELS experimental conditions and quantification parameters for the spectral image in Figure 3.14.

Spectral Image : BNNT						
Probe Size (nm^2)	**Exposure Time (s)**	**Integration Time (s)**	**Spectral Image Acquisition Time**	**Resolution (eV)**	**Dispersion (eV/pixel)**	**t/λ**
1	0.1999	0.1999	2 min 32 seconds	3.3	0.25	0.03
Elements	**B**	**C**	**N**	**O**		
Background Removal Parameters						
Fitting Range (eV) (Power Law)	169.8-188.5	252.3 - 280.3	359.3-398.3	478.0531.3		
Signal Quantification Parameters						
Signal Counts	2.34e+007 ± 6888	6.81e+006 ± 4735	4.27e+006 ± 3459	6.37e+005 ± 2228		
Integration Range (eV)	189.0-219.0	281.0-312.0	399-429.0	532.0-561.0		
Cross section (barns) (Hartree-Slater)	6111 ± 611	2480 ± 248	1220 ± 122	688 ± 69		
Absolute Quantification						
Areal density (atoms/nm^2)	3.83e+013 ± 3.8e+012	2.75e+013 ± 2.7e+012	3.50e+013 ± 3.5e+012	9.26e+012 ± 9.3e+011		

Table B.1: EELS Experimental conditions and quantification parameters for spectral image in Figure 3.14

B.2.2 BNNTs after 900°C

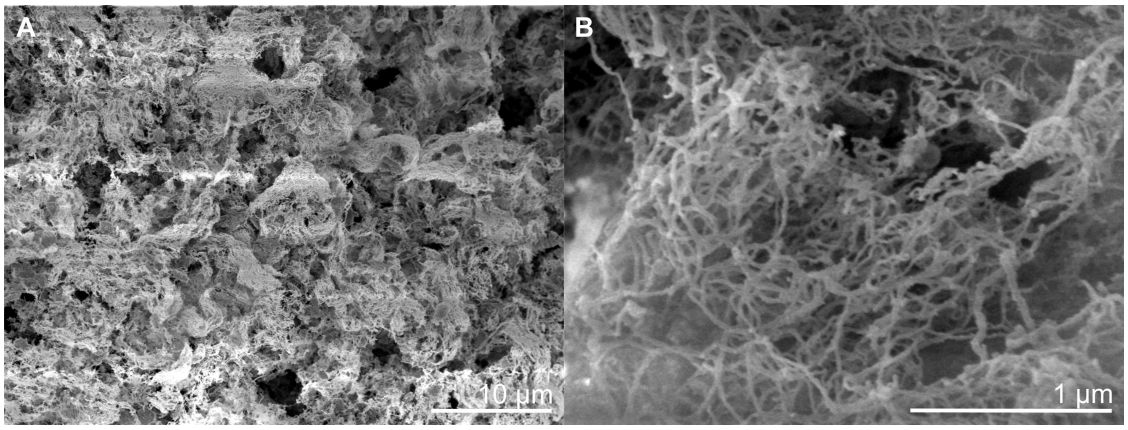


Figure B.2: SEM images of BNNTs collected after exposure to 900°C in air. The nanotube morphology still appears to be maintained.

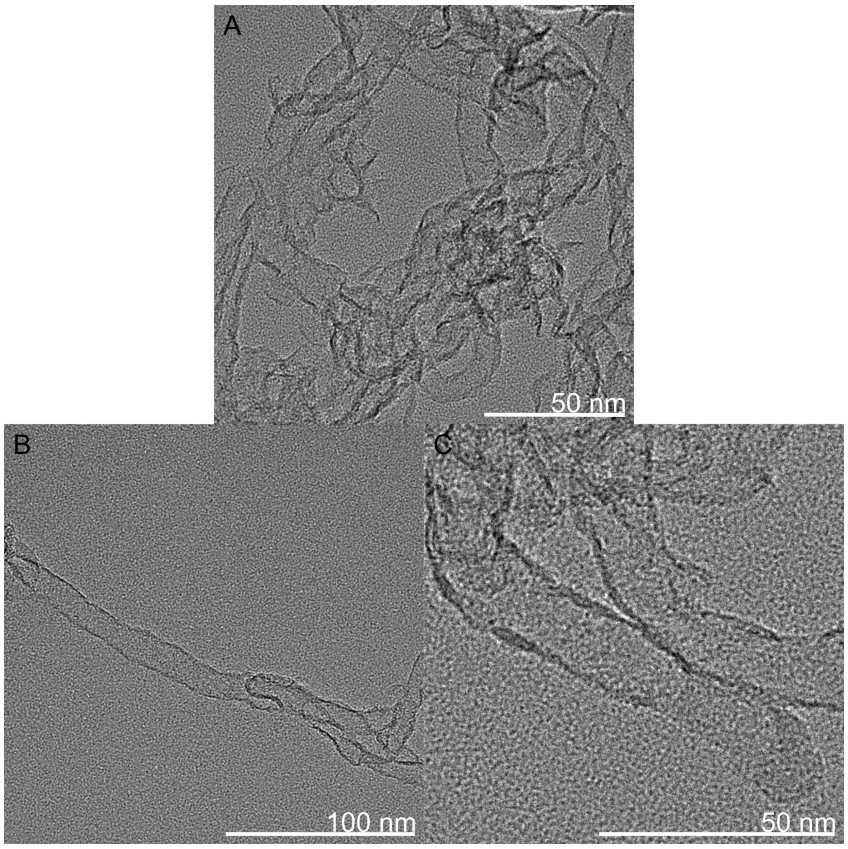


Figure B.3: TEM images of BNNTs after exposure to 900°C in air.

B.2.3 Catalysed BNNT growth

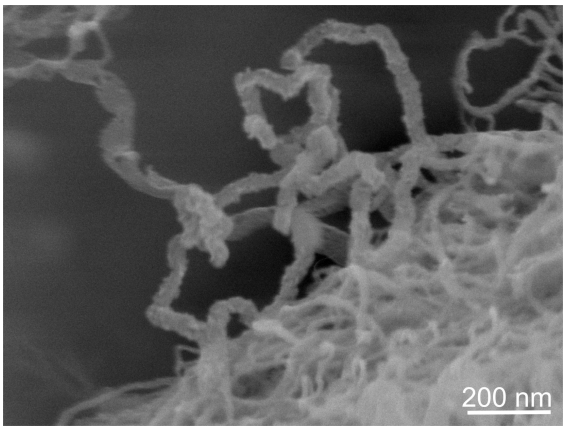


Figure B.4: SEM image of large diameter nanotube structures observed amongst BNNTs synthesised by sacrificial templating of Nanocyl MWCNTs. These nanotubes are believed to be BNNTs that nucleate and grow from residual metal oxide catalyst particles that become saturated with B/N containing vapours during ammonia borane CVD.

B.3 AACVD MWCNTs characterisation

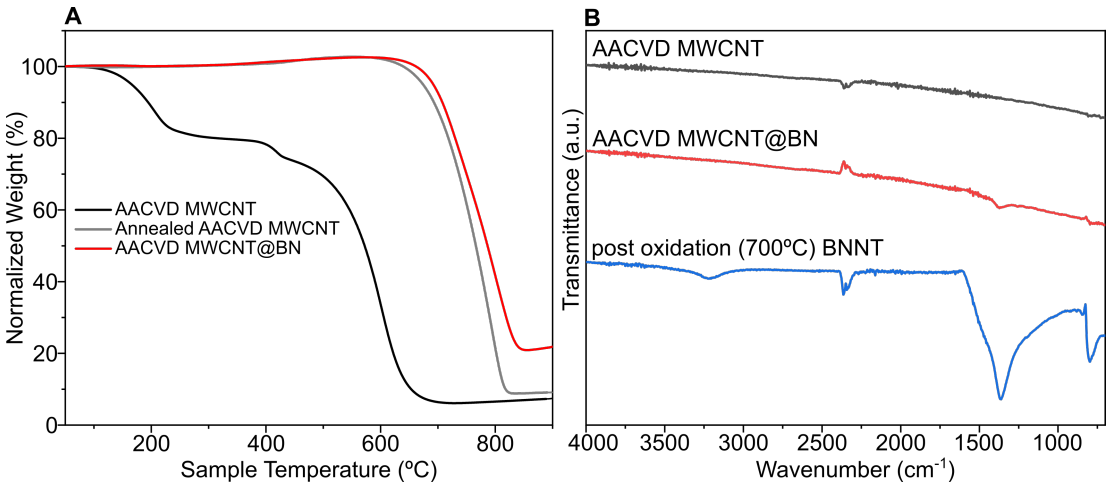


Figure B.5: (A) TGA curves of AACVD synthesised MWCNTs, along with their annealed and h-BN coated variants. The improvement in oxidation resistance from pristine MWCNTs to annealed and finally to MWCNT@BN follows the same trend observed when Nanocyl NC7000™ MWCNTs were similarly treated. See Chapter 3, Figure 3.5 for comparison. (B) FTIR transmission spectra as-collected from AACVD MWCNTs, successor MWCNT@BNs and their post-oxidised product BNNTs. Adsorption peaks related to h-BN at 1363 cm^{-1} and 798 cm^{-1} are observed as prominent features in the post-oxidised BNNTs spectrum and as weak features in the MWCNT@BN spectrum. A broad peak at 3220 cm^{-1} on the BNNT spectrum is associated to adsorbed moisture and/or bonded hydroxyl groups.

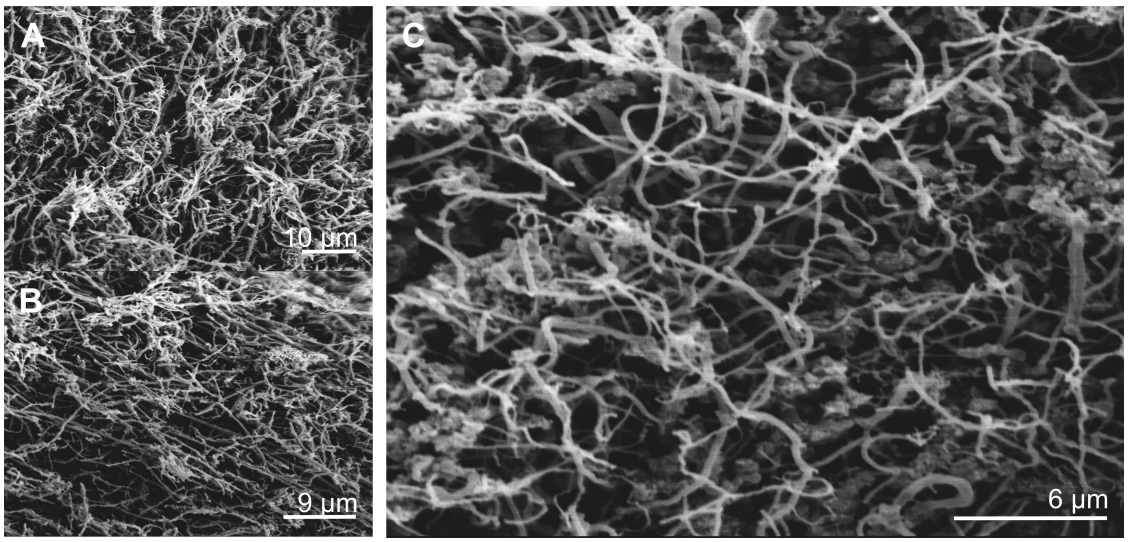


Figure B.6: SEM images of (A) AACVD synthesised MWCNTs (B) AACVD MWCNTs after h-BN coating (i.e. MWCNT@BN) and (C) BNNTs after 700°C oxidation treatment of AACVD MWCNT@BN.

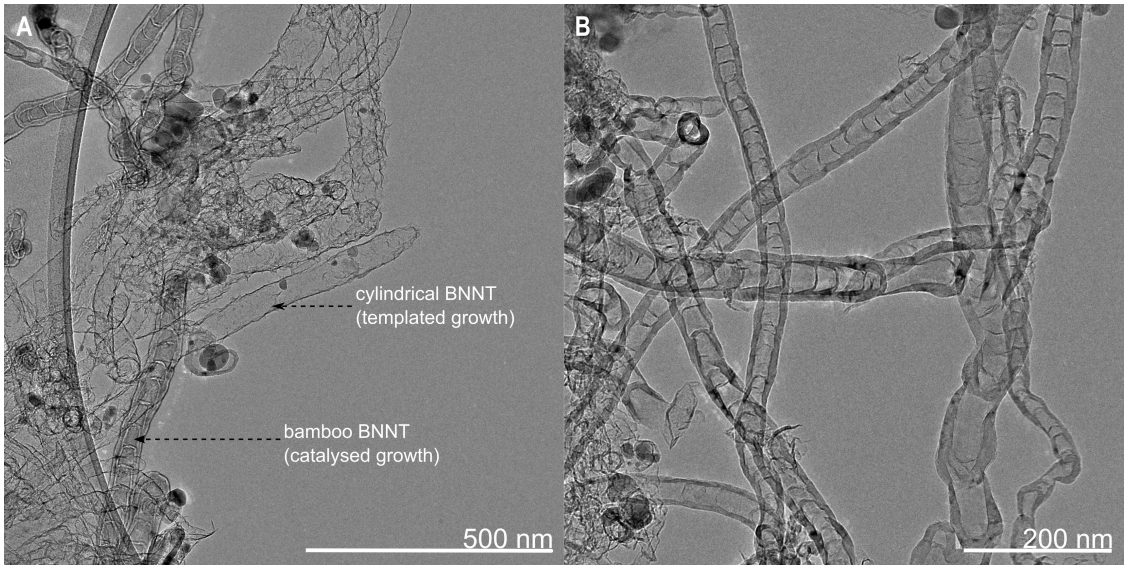


Figure B.7: TEM images of (A) cylindrical and bamboo morphology BNNT nanotubes observed after oxidation of AACVD MWCNT@BN at 700°C. The cylindrical nanotubes with large inner diameters and thin walls are a result of the sacrificial templating process, whilst the bamboo nanotubes, highlighted in (B), originate from catalyst-assisted growth, likely involving Fe-based residual catalyst that become saturated with ammonia borane precursor vapour.

Appendix C

Chapter 4 Appendix

Contents

C.1 Sonication and Vacuum Filtration of BNNT powder . 208
C.1.1 Materials and Methods 209
C.1.2 Results 209
C.2 Measurement of hybrid Buckypaper Electrical Resistivity 212
C.3 Additional BNNT Buckypaper Characterisation 214
C.3.1 SEM & EDX 214
C.3.2 XPS 216
C.4 Predicting X-ray Generation Depth for EDX analysis 217
C.4.1 monte CArlo SImulations of electroN trajectory in sOlids: CASINO v2.51 217
C.5 Additional Platelet SEM and EDX 223

C.1 Sonication and Vacuum Filtration of BNNT powder

This section reviews the attempt to fabricate BNNT buckypaper by the traditional vacuum filtration route using BNNT powder as synthesised by sacrificial templating.

Although the fabrication of BNNT buckypapers by dispersing and filtering BNNT powders has already been presented in the literature, albeit to a limited

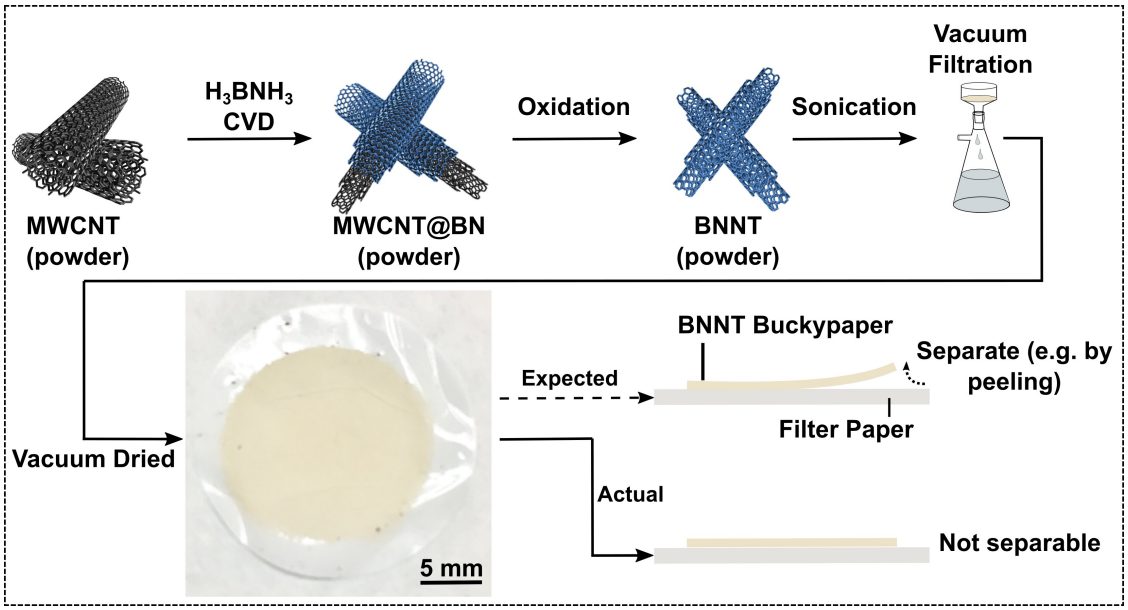


Figure C.1: Schematic of method trialled for BNNT buckypaper fabrication by sonication and vacuum filtration of BNNTs as synthesised in Chapter 3.

extent as reviewed in Chapter 4, this route has yet to be demonstrated using BNNT powders as synthesised according to the method presented in this work.

C.1.1 Materials and Methods

BNNT powder, as synthesised according to the method outlined in Chapter 3, was dispersed in ethanol solution in a glass vial and sonicated in an ultrasonic bath at room temperature for 4 hours at a frequency of 20 kHz. Following sonication, dispersions were vacuum filtered onto Whatman's Cyclopore track etched, polycarbonate filter paper with 0.4μ pore size. Two different concentrations of BNNT in ethanol were tested: (i) 4 mg/20 ml and (ii) 5 mg/20 ml.

C.1.2 Results

Trials according to this route did not result in free-standing BNNT buckypapers. Instead powdery films were formed on the polycarbonate filter paper, as shown in Figure C.1. These films could not be peeled off from the underlying filter paper and neither could the films be collected intact by dissolution of the polycarbonate filter paper.

It was extrapolated from these results that, unlike the demonstrated facile fabrication of MWCNT buckypapers by this similar method, extensive future work is necessary to optimise this route for successful fabrication of BNNT buckypapers. Potential parameters for future exploration include those in the sonication regime (e.g. BNNT solvent, BNNT concentration, duration and strength of the sonication) and filtration regime (e.g. filter membrane material and pore size, and filtration speed). It is also anticipated that the success of this method is dependent on the quality of the BNNTs prior to sonication, wherein there is a predictable inverse relationship between BNNT crystallinity and BNNT susceptibility to sonication induced damage. Low crystallinity BNNTs as synthesised in Chapter 3 may therefore be more vulnerable during sonication treatment, becoming damaged and shortened in the process and consequently less effective at forming an entangled nanotube network of a buckypaper.

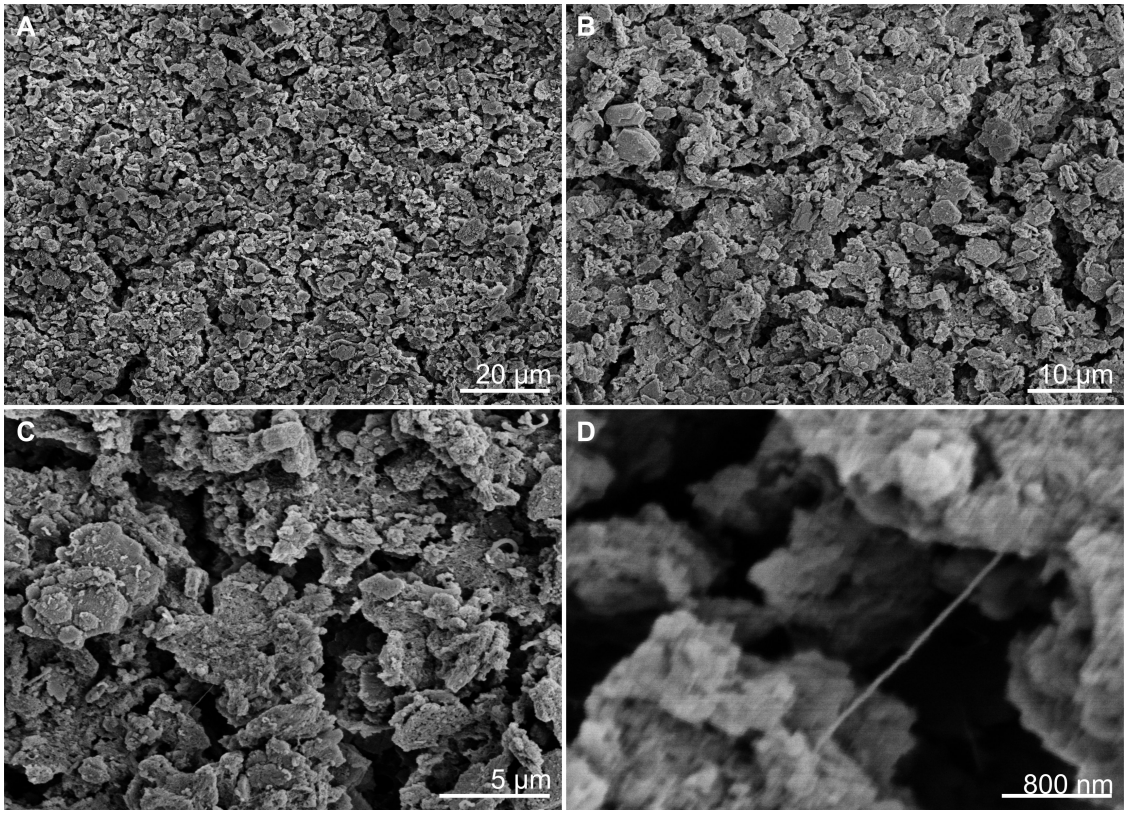


Figure C.2: SEM images of BNNT film deposited on filter paper after sonication and vacuum filtration of BNNT powders as synthesised in Chapter 3.

Typical SEM images of the films obtained are shown in Figure C.2. These were taken with the film still intact atop the insulating filter paper. Even after a 15 nm Pt coating was introduced, there was significant charging of the films under the electron beam, which was a challenge for imaging at high resolution and magnification to better resolve the entangled nanotubes. However, as shown in Figure C.2D, nanotubes are still present in the film subsequent to the sonication process. The BNNT nanotubes appear to be entangled into large agglomerates (e.g. Figure C.2D) rather than forming a uniformly entangled network.

Potential routes to optimisation of this technique for fabrication of self-supporting, more uniformly entangled BNNT buckypaper structure include investigation of the sonication and filtration regimes, including increasing the quantity of BNNT powder used. In view of the limited yield of BNNT obtained per experiment from the lab-accessible CVD reactor in this work, it was deduced that further optimisation would not be possible within an efficient time-frame in the context of this thesis. Thus, exploration of this method of buckypaper fabrication would benefit from upscaling of BNNT powder yield, which is an anticipated future phase of this work. However, the results here also highlight the advantage of the alternative method of BNNT buckypaper fabrication developed in Chapter 4, wherein a free-standing BNNT buckypaper macroscopic assembly was achieved even with small quantities of BNNTs, e.g <5 mg.

C.2 Measurement of hybrid Buckypaper Electrical Resistivity

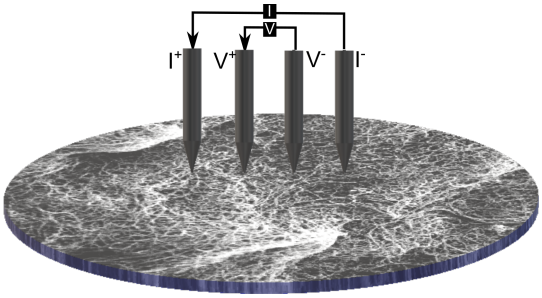


Figure C.3: Illustration of Four Point Probe setup

A four point probe was used to measure the resistivity of the MWCNT and MWCNT/h-BN hybrid buckypapers reported in §4.3.1.2.

The four point probe has two inner probes that measure voltage (V) and two outer probes that supply current (I), as shown in schematic in Figure C.3. A 1 μA current was applied. Output voltage (V) readings were taken for 10 positions on each buckypaper, including on both sides and after rotations of the buckypaper. The calibration of the voltage readings was checked with ITO glass. The buckypaper resistivity(ρ_o), was calculated according to the equation below for resistivity of thin film samples which have a thickness much less than the distance between the probes (i.e. t$\ll$S):

$$\rho_o = \frac{\pi}{ln2}\left(\frac{V}{t}\right)I \tag{C.1}$$

C.2.0.0.1 Error on Resistivity Standard deviations were calculated for measured values of V (i.e. ΔV) and t (i.e. Δt). The error on resistivity $\Delta\rho_o$ was propagated as follows:

$$constant(c) = \frac{\pi}{ln2}I \tag{C.2}$$

$$\therefore \rho_o = c \cdot \left(\frac{V}{t}\right) \tag{C.3}$$

$$\Delta\rho_o = c \cdot \left(\frac{V}{t}\right)\sqrt{\left(\frac{\Delta V}{V}\right)^2 + \left(\frac{\Delta t}{t}\right)^2} \tag{C.4}$$

C.3 Additional BNNT Buckypaper Characterisation

C.3.1 SEM & EDX

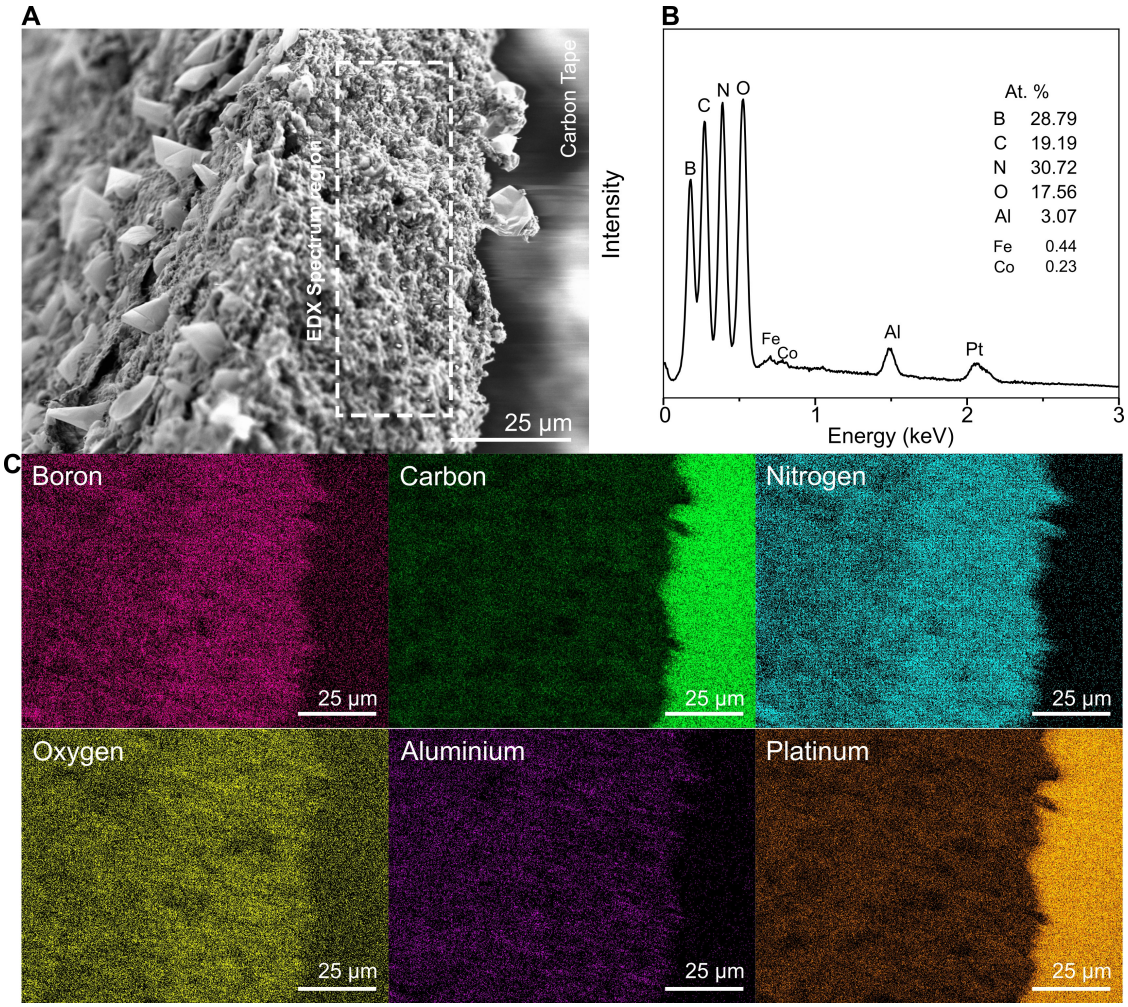


Figure C.4: (A) SEM of a BNNT buckypaper, with EDX analysis conducted on the cross section region. The accompanying EDX spectrum is shown in (B) and elemental maps in (C). B and N are the principle components, but C and O are the main impurities detected, along with trace Fe and Co. EDX acquisition details (Acceleration Voltage: 3 kV, Pixel Size: 0.116 μm, Energy per channel: 5 eV, Dwell time: 96 μs, Stage Tilt: 0 °, Detector Elevation: 30 °)

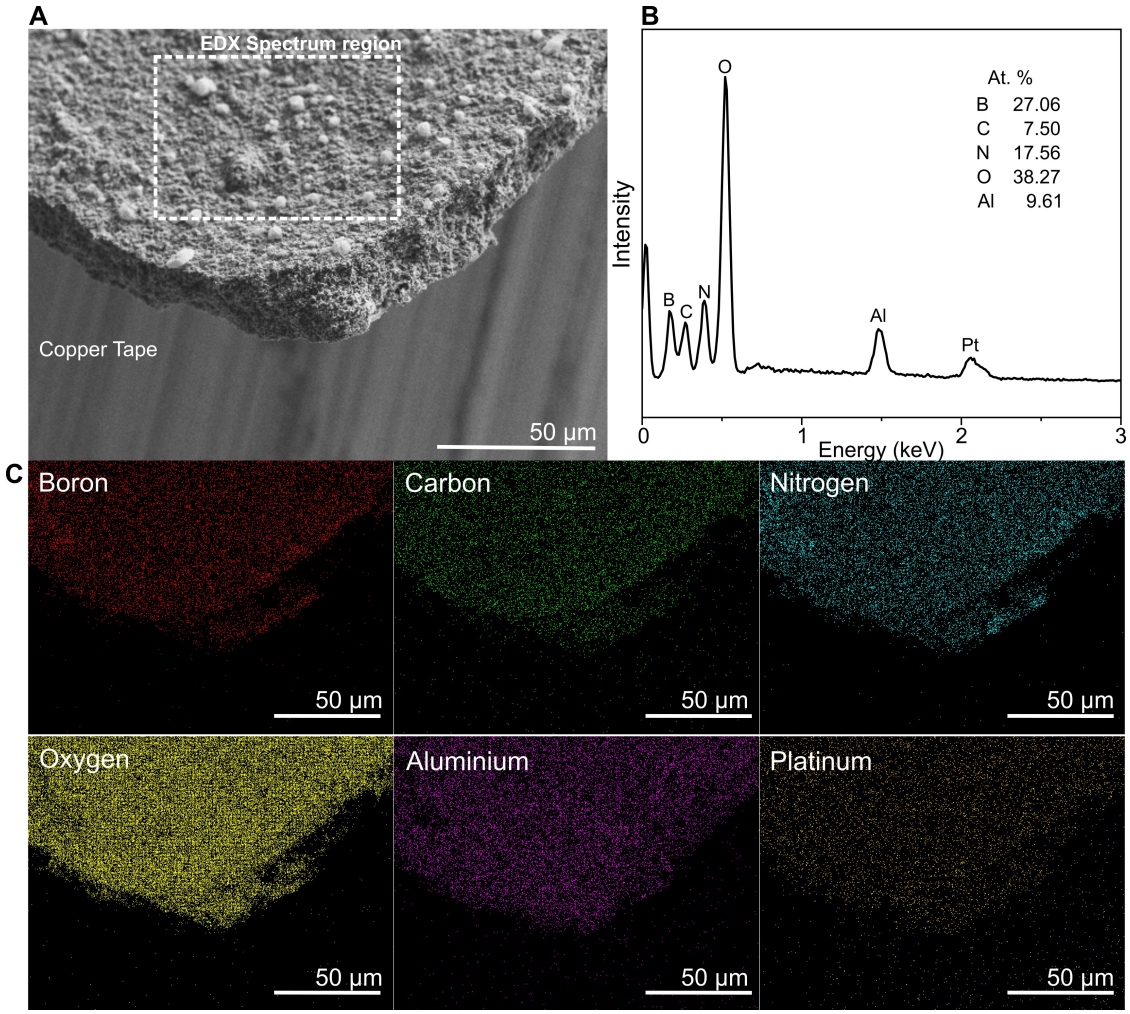


Figure C.5: (A) SEM of another BNNT buckypaper subjected to the same oxidation treatment as the buckypapers analysed in Figure C.4 above and Figure 4.10. Accompanying EDX spectrum and maps are shown in (B) and (C). However, this sample was tested after a longer duration in storage (several months). Notably, the O content is increased up to 38 at.%, which is near the contribution of the principle B and N components (collectively $\sim$ 45 at.%) Carbon content is low at 7.5 at.%. EDX acquisition details (Acceleration Voltage: 3.13 kV, Pixel Size: 0.169 μm, Energy per channel: 10 eV, Dwell time: 200 μs, Stage Tilt: -1.85 °, Detector Elevation: 30 °)

C.3.2 XPS

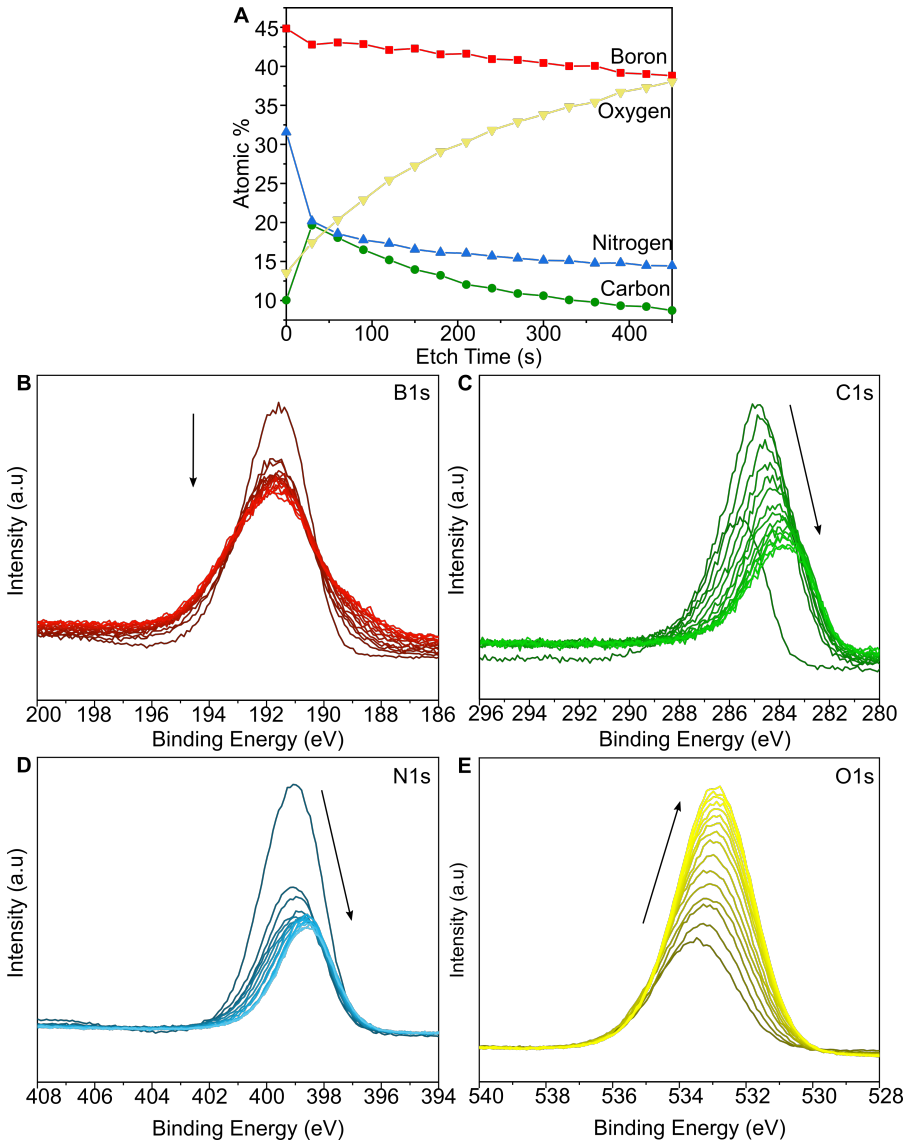


Figure C.6: (A) BNNT buckypaper XPS depth profile composition results for B,C,N and O at 15 probed depth levels and 450s total etch time. (B-E) High resolution XPS of B1s, C1s, N1s and O1s at increasing depth, corresponding to each etch time data point in (A).

C.4 Predicting X-ray Generation Depth for EDX analysis

In Chapter 4, platelet features were observed to evolve on oxidised BNNT buckypapers. A new theory on platelet chemical composition was put forward in §4.3.3.2, and analysis by TEM and FTIR revealed evidence to support their proposed H_3BO_3 identity.

Chemical composition analysis by EDX spectroscopy of these platelets *in-situ*, i.e. in their original position on the buckypaper surface, revealed spectra containing peaks associated with B,C,N and O characteristic X-ray emissions. Due to the 2D nature of the platelets (thickness $\sim$ 100 nm), it is crucial to interpret these EDX results with concomitant consideration of the depth of origination of detected X-rays. Examination of the X-ray generation depth can reveal whether the collected EDX spectra are representative of solely the platelet feature of interest, or both the platelet and underlying buckypaper.

C.4.1 monte CArlo SImulations of electroN trajectory in sOlids: CASINO v2.51

C.4.1.1 Brief Introduction to principles of CASINO

Monte-Carlo modelling of electron interaction with a solid specimen is a useful tool to simulate the electron trajectories and energy histories in a sample of known composition.

In these simulations, a specified large number of electrons are targeted at the specimen surface. Each individual electron then undergoes interaction events including scattering and energy loss. In the CASINO program implemented here,[378–381] as in most Monte-Carlo programs, the scattering events that deviate the direction of the electrons is based on large-angle scattering (elastic), and scattering angles are informed by a random number generator[382] paired with a scattering angle probability distribution function (elastic cross-section) that is dependent on specimen composition. As each electron undergoes its own individual sequence of scattering deviations, the simulation results in a zig-zag depiction of all electron trajectories.

The interval between consecutive scattering events is depicted by a straight line, along which there is a modelled rate of energy loss according to inelastic scattering and ionisation processes. This rate of energy loss function is known as the stopping power (dE/dS), and depends both on specimen composition (e.g atomic number and weight, density, mean ionisation potential) and electron energy (in eV).[383]

In CASINO, the simulation steps are iterated until all simulated electrons reach instantaneous energy of 50 eV, or are backscattered. The combination of scattering and energy loss simulations generates a 3D electron penetration volume of defined size and shape, alongside electron energy distributions in both radial and depth dimensions. Generally, such Monte-Carlo simulations can accurately predict that higher electron acceleration voltages result in greater electron range within the specimen, and that specimens of higher atomic number tend to have wider excitation volumes due to a greater number of large angle scattering events.

Given electron excitation volume and spatial resolution of electron energy, it is then possible to extract an ionisation distribution function for both the depth and radial distribution of X-ray emission. The probability of inner shell ionisation (ionisation cross section), and hence X-ray generation, is inversely associated with the electron energy. Consequently, with the depth resolution of simulated electron energies, it is possible to calculate the distribution of X-ray generation as a function of specimen depth (termed ϕ (ρ z) curves).[384]

C.4.1.2 Specimen Model and Microscope Settings

Here, a platelet of H_3BO_3 was modelled as a thin film of 100 nm thickness. This was layered onto the buckypaper, modelled as a homogeneous substrate containing B, C, N and O (in atomic ratios matching those measured by XPS in §4.3.2). All sample modelling settings are included in Table C.1. An 8 nm platinum top layer was also included in the specimen model to mirror the empirical Pt conductive coating implemented to prevent sample charging in the SEM. Microscope and X-ray detector settings (Table C.1) important to the simulation, e.g. electron beam energy (3 keV), were chosen to reflect real settings used in the EDX measurements of platelets in Figure 4.24.

Multilayer Sample Settings				
	Name	**Thickness (nm)**	**Density (g/cm^3)**	**Atomic Fraction**
Layer 1	Pt	8	21.4	Pt:1.0
Layer 2	H_3BO_3	100	0.86	H:0.43 B:0.14 O:0.43
Layer 3	BCNO	Substrate	1.67	B:0.40 C:0.10 N:0.15 O:0.35
Microscope Simulation Settings				
Electron Beam Energy (keV)	3	**Beam radius (nm)**	40	
Number of electrons simulated	500	**Tilt of Specimen (deg)**	0	
Physical Models				
Total Cross Section	Mott by Interpolation	**Random Number Generator**	Press *et al.* (1986)	
Partial Cross Section	Mott by Interpolation	**Directing Cosin**	Drouin (1996)	
Effective Section Ionisation	Casnati	**dE/dS Calculation**	Joy and Luo	
Ionisation Potential	Joy and Luo (1989)			
X-ray Detector Position Relative to Sample				
Elevation (deg)	30	**Azimuth (deg)**	0	

Table C.1: Summary of multilayer specimen parameters, microscope settings, physical models and X-ray detector position applied in the CASINO Monte Carlo simulations.

C.4.1.3 Results of Simulation

The complete trajectories of 500 electrons through the depth (XZ plane) of the modelled specimen is depicted in Figure C.7A.

Figure C.7B portrays an energy by position map on the XZ plane, which shows the spatial distribution of electron energy absorption within the specimen. Grey scale shading is utilised to depict relative energy absorption density, i.e. darker shading equates to higher absorption density. Contour lines, graded with colour and percentage, delineate the percent of collective electron energy which is present outside of the contoured region.

This simulation data visualised in Figure C.7 is used to compute the X-ray generation depth curves for each element in the specimen, shown in Chapter 4, Figure 4.25. The maximum electron range is sliced into 500 divisions each of ΔZ thickness and X-ray intensities for each of these slices is computed. As X-rays can also be absorbed by the specimen, absorption correction is applied by the program to the X-ray intensities; the corrected intensities are those predicted to be emitted from the specimen and detected.[378,379]

The implications of the generated ϕ (ρ z) curves towards interpretation of platelet EDX spectra are discussed in Chapter 4.

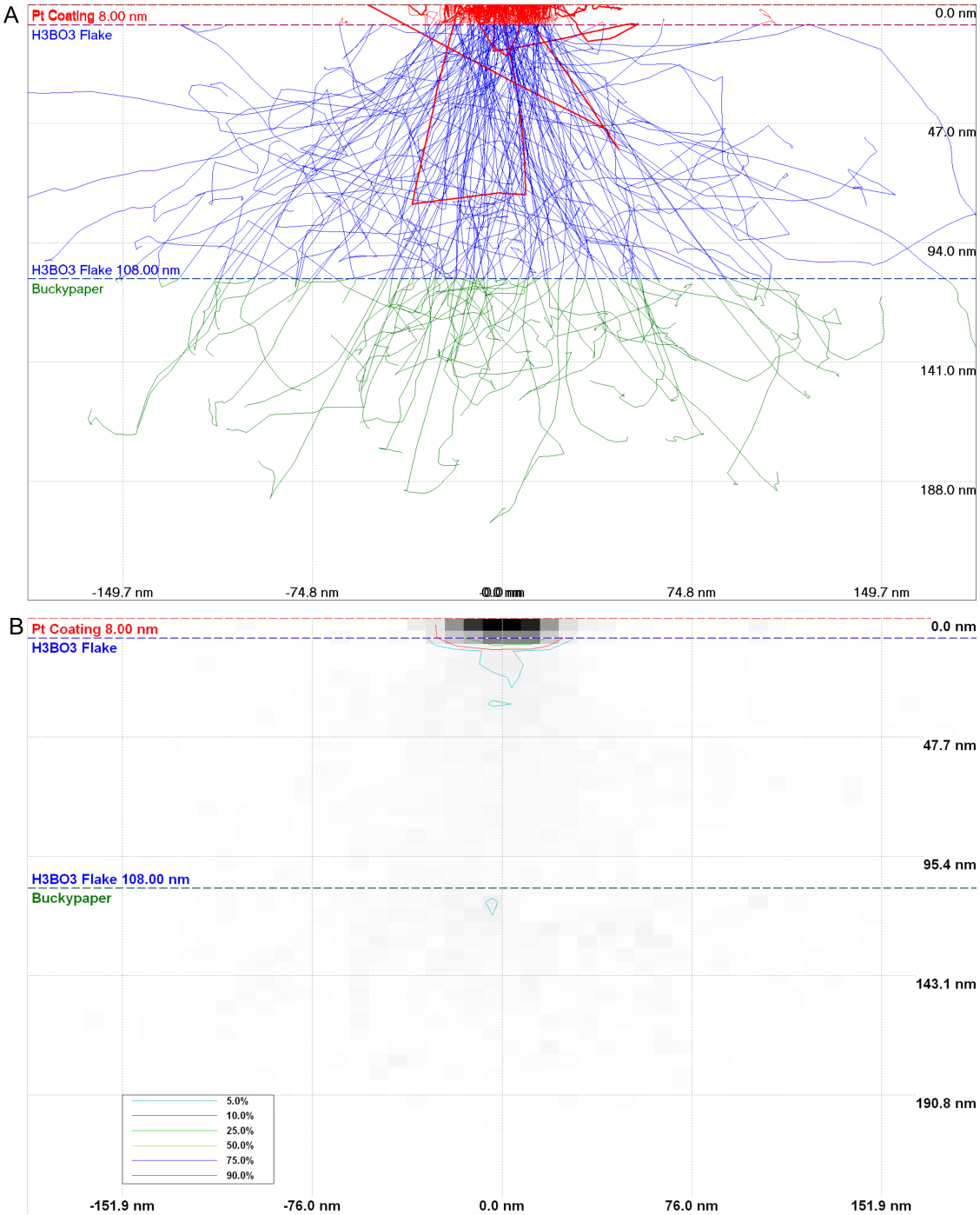


Figure C.7: (A) CASINO v2.51 simulated electron trajectories (XZ plane) for 500 electrons (3 keV incident beam energy) through a multilayer specimen of Pt (8nm) , H_3BO_3(100 nm) and BCNO (substrate). Trajectory coloration is done according to layer composition. (B) Energy by position map of XZ plane spatial distribution of electron energy absorption within the specimen. Energy absorption density is highest in the darker coloured regions. Percentages associated to contour lines highlight remaining % of energy outside of region.

C.5 Additional Platelet SEM and EDX

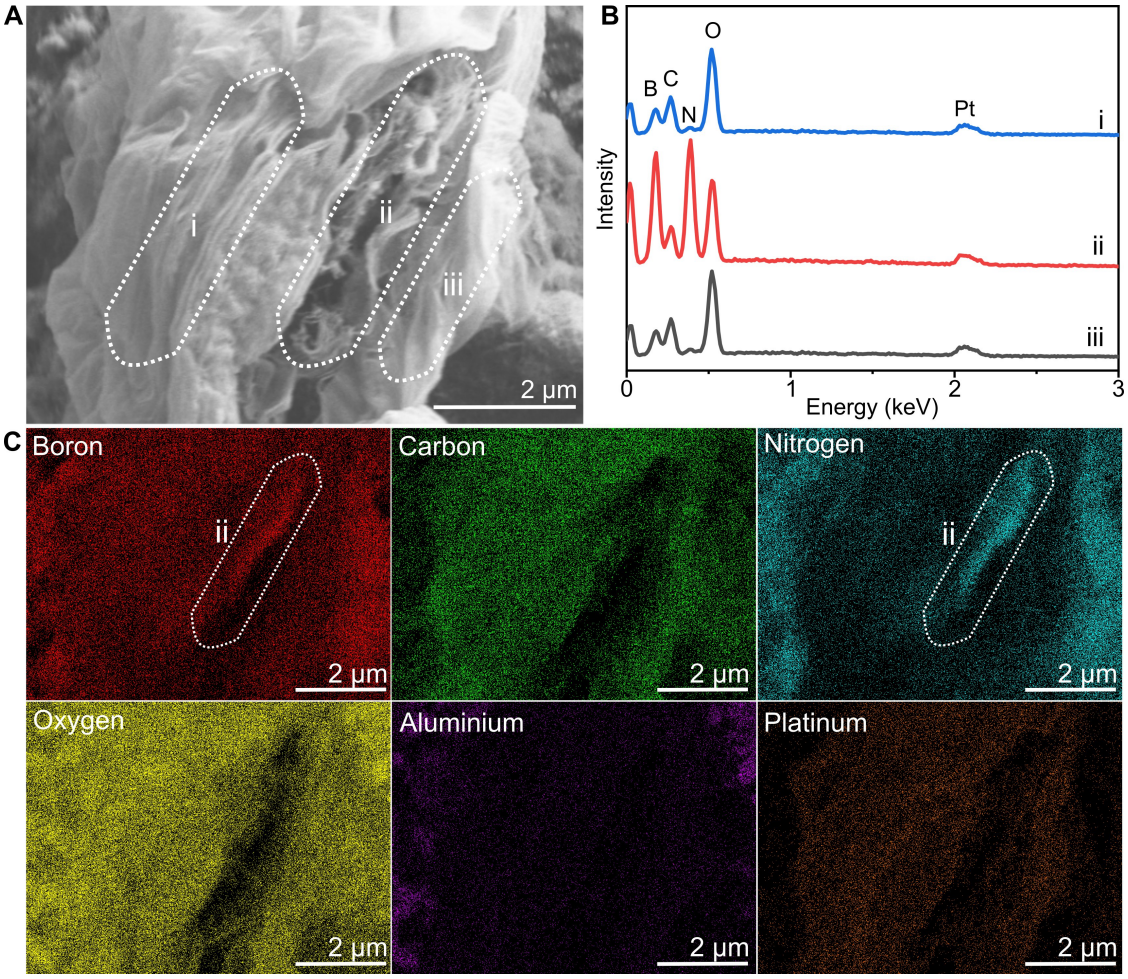


Figure C.8: (A) High magnification SEM image of the cross section of a platelet, showing its multiple layers which are undergoing deformation by crumpling during the imaging. From the (B) EDX spectra of regions (i)-(iii) and the (C) EDX elemental maps, it appears that there is a BN rich zone at site (ii) sandwiched between B,O rich platelet layers in (i) and (iii). The sandwiched BN rich region appears to be composed of entangled nanotubules. EDX acquisition details (Acceleration Voltage: 3.13 kV, Pixel Size: 0.00778 μm, Energy per channel: 10 eV, Dwell time: 600 μs, Stage Tilt: -4 °, Detector Elevation: 30 °)

An additional SEM/EDX analysis for a multi-layer thick platelet is presented in Figure C.8 below. This example is referred to in §4.3.3.4.2 as evidence supporting the presence of BNNTs sandwiched between platelet layers. This platelet also underwent a crinkling deformation, which is ascribed to dehydration of the crystalline H_3BO_3, in the ultra-high vacuum and under electron beam heating, into amorphous B_2O_3. After treating the C and Pt as deconvolution elements

(unintentional hydrocarbon contamination and intentional Pt conductive sputter coating), the atomic composition of the shown platelet is calculated as B (38.81 at.%), N (4.73 at.%), O (56.44 at.%) (from spectrum i in Figure C.8B). This gives a B:O ratio of 1:1.5.

References

1. Pauling, L. The Structure and Properties of Graphite and Boron Nitride. *Proceedings of the National Academy of Sciences* **56,** 1646–1652 (1966).
2. Carter, C. & Norton, M. *Ceramic Materials: Science and Engineering* (Springer New York, 2007).
3. Cohen, M. L. & Zettl, A. The physics of boron nitride nanotubes. *Phys. Today* **63,** 34–38 (2010).
4. Pease, R. S. An X-ray study of boron nitride. *Acta Crystallographica* **5,** 356–361 (1952).
5. Rubio, A., Corkill, J. L. & Cohen, M. L. Theory of graphitic boron nitride nanotubes. *Phys. Rev. B* **49,** 5081–5084 (1994).
6. Low-dimensional boron nitride nanomaterials. *Materials Today* **15,** 256–265 (2012).
7. Golberg, D. *et al.* Boron nitride nanotubes and nanosheets. *ACS Nano* **4,** 2979–2993 (2010).
8. Wilder, J. W., Venema, L. C., Rinzler, A. G., Smalley, R. E. & Dekker, C. Electronic structure of atomically resolved carbon nanotubes. *Nature* **391,** 59–62 (1998).
9. Iijima, S. Helical microtubules of graphitic carbon. *Nature* **354,** 56–58 (1991).
10. Chopra, N. G. *et al.* Boron Nitride Nanotubes. *Science* **269,** 966–967 (1995).
11. Saito, R., Fujita, M., Dresselhaus, G. & Dresselhaus, M. S. Electronic structure of chiral graphene tubules. *Applied Physics Letters* **60,** 2204–2206 (1992).
12. Blase, X., Rubio, A., Louie, S. G. & Cohen, M. L. Stability and Band Gap Constancy of Boron Nitride Nanotubes. *Europhysics Letters (EPL)* **28,** 335–340 (1994).
13. Chopra, N. G. & Zettl, A. Measurement of the elastic modulus of a multi-wall boron nitride nanotube. *Solid State Communications* **105,** 297–300 (1998).
14. Hernández, E., Goze, C., Bernier, P. & Rubio, A. Elastic Properties of C and $B_xC_yN_z$ Composite Nanotubes. *Phys. Rev. Lett.* **80,** 4502–4505 (1998).
15. Chang, C. W. *et al.* Isotope Effect on the Thermal Conductivity of Boron Nitride Nanotubes. *Phys. Rev. Lett.* **97,** 085901 (2006).
16. Chen, X., Dmuchowski, C. M., Park, C., Fay, C. C. & Ke, C. Quantitative characterization of structural and mechanical properties of boron nitride nanotubes in high temperature environments. *Scientific Reports* **7,** 1–9 (2017).

17. Golberg, D., Bando, Y., Kurashima, K. & Sato, T. Synthesis and characterization of ropes made of BN multiwalled nanotubes. *Scripta Materialia* **44,** 1561–1565 (2001).

18. Chen, Y., Zou, J., Campbell, S. J. & Le Caer, G. Boron nitride nanotubes: Pronounced resistance to oxidation. *Applied Physics Letters* **84,** 2430–2432 (2004).

19. Yang, K., Gu, M., Han, H. & Mu, G. Influence of chemical processing on the morphology, crystalline content and thermal stability of multi-walled carbon nanotubes. *Materials Chemistry and Physics* **112,** 387–392 (2008).

20. Kim, K. S. *et al.* Scalable manufacturing of boron nitride nanotubes and their assemblies: a review. *Semiconductor Science and Technology* **32,** 013003 (2016).

21. Nakhmanson, S. M., Calzolari, A., Meunier, V., Bernholc, J. & Buongiorno Nardelli, M. Spontaneous polarization and piezoelectricity in boron nitride nanotubes. *Phys. Rev. B* **67,** 235406 (2003).

22. Bai, X. *et al.* Deformation-Driven Electrical Transport of Individual Boron Nitride Nanotubes. *Nano Letters* **7,** 632–637 (2007).

23. Thibeault, S. A. *et al. Radiation Shielding Materials Containing Hydrogen, Boron, and Nitrogen: Systematic Computational and Experimental Study. Phase I* (NIAC Final Report, 2012).

24. Shi, D., Guo, Z. & Bedford, N. in *Nanomaterials and Devices* (eds Shi, D., Guo, Z. & Bedford, N.) 49–82 (William Andrew Publishing, Oxford, 2015).

25. Kim, P., Shi, L., Majumdar, A. & McEuen, P. L. Thermal Transport Measurements of Individual Multiwalled Nanotubes. *Phys. Rev. Lett.* **87,** 215502 (2001).

26. Xiao, Y. *et al.* Specific heat and quantized thermal conductance of single-walled boron nitride nanotubes. *Phys. Rev. B* **69,** 205415 (2004).

27. Kim, K. S. *et al.* Polymer nanocomposites from free-standing, macroscopic boron nitride nanotube assemblies. *RSC Advances* **5,** 41186–41192 (2015).

28. Thibeault, S. A. *et al.* Nanomaterials for radiation shielding. *MRS Bulletin* **40,** 836–841 (2015).

29. Wang, J., Lee, C. H. & Yap, Y. K. Recent advancements in boron nitride nanotubes. *Nanoscale* **2,** 2028–2034 (2010).

30. Zhi, C., Bando, Y., Tang, C. & Golberg, D. Boron nitride nanotubes. *Materials Science and Engineering: R: Reports* **70,** 92–111 (2010).

31. Kim, J. H., Pham, T. V., Hwang, J. H., Kim, C. S. & Kim, M. J. Boron nitride nanotubes: synthesis and applications. *Nano convergence* **5,** 1–13 (2018).

32. Jakubinek, M. B. *et al.* in *Nanotube Superfiber Materials* 91–111 (Elsevier, 2019).

33. Moore, A. L. & Shi, L. Emerging challenges and materials for thermal management of electronics. *Materials Today* **17,** 163–174 (2014).

34. Frear, D. in *Springer Handbook of Electronic and Photonic Materials* (eds Kasap, S. & Capper, P.) 1–1 (Springer International Publishing, Cham, 2017).

35. Zhi, C. *et al.* Towards thermoconductive, electrically insulating polymeric composites with boron nitride nanotubes as fillers. *Advanced Functional Materials* **19,** 1857–1862 (2009).

36. Meng, W., Huang, Y., Fu, Y., Wang, Z. & Zhi, C. Polymer composites of boron nitride nanotubes and nanosheets. *J. Mater. Chem. C* **2,** 10049–10061 (2014).

37. Jakubinek, M. B. *et al.* Thermal conductivity of bulk boron nitride nanotube sheets and their epoxy-impregnated composites. *physica status solidi (a)* **213,** 2237–2242 (2016).

38. Zhi, C. *et al.* Boron nitride nanotubes/polystyrene composites. *Journal of Materials Research* **21,** 2794–2800 (2006).

39. Bansal, N. P., Hurst, J. B. & Choi, S. R. Boron Nitride Nanotubes-Reinforced Glass Composites. *Journal of the American Ceramic Society* **89,** 388–390 (2006).

40. BNNT Technology Ltd. *Transparent Armour* `https://www.bnnt-technology.com/about-bnnt/transparent-armour/f` (2021).

41. Yamaguchi, M., Meng, F., Firestein, K., Tsuchiya, K. & Golberg, D. Powder metallurgy routes toward aluminum boron nitride nanotube composites, their morphologies, structures and mechanical properties. *Materials Science and Engineering: A* **604,** 9–17 (2014).

42. Bhuiyan, M. M. H. *et al.* Boron nitride nanotube reinforced titanium metal matrix composites with excellent high-temperature performance. *Journal of Materials Research* **32,** 3744–3752 (2017).

43. Wang, W.-L. *et al.* Fabrication of alumina ceramic reinforced with boron nitride nanotubes with improved mechanical properties. *Journal of the American Ceramic Society* **94,** 3636–3640 (2011).

44. Xu, J.-J. *et al.* Toughening and reinforcing zirconia ceramics by introducing boron nitride nanotubes. *Materials Science and Engineering: A* **546,** 301–306 (2012).

45. Li, T. *et al.* Fabrication and mechanical properties of boron nitride nanotube reinforced silicon nitride ceramics. *Ceramics International* **44,** 6456–6460 (2018).

46. BNNT, LLC. *Proposed Applications* `https://www.bnnt.com/resources/applications` (2021).

47. BNNT Technology Ltd. *Stronger Ceramics* `https://www.bnnt-technology.com/about-bnnt/stronger-ceramics/#` (2021).

48. Lim, H. *et al.* High-performance, recyclable ultrafiltration membranes from P4VP-assisted dispersion of flame-resistive boron nitride nanotubes. *Journal of Membrane Science* **551,** 172–179 (2018).

49. Kang, J. H. *et al.* Multifunctional electroactive nanocomposites based on piezoelectric boron nitride nanotubes. *ACS Nano* **9,** 11942–11950 (2015).

50. BNNT Technology Ltd. *High Performance Batteries* `https://www.bnnt-technology.com/about-bnnt/batteries/` (2021).

51. Augustine, J. *et al.* Assessing size-dependent cytotoxicity of boron nitride nanotubes using a novel cardiomyocyte AFM assay. *Nanoscale Adv.* **1,** 1914–1923 (2019).

52. Merlo, A., Mokkapati, V. R. S. S., Pandit, S. & Mijakovic, I. Boron nitride nanomaterials: biocompatibility and bio-applications. *Biomater. Sci.* **6,** 2298–2311 (2018).

53. Narita, I. & Oku, T. Synthesis of boron nitride nanotubes by using YB_6 powder. *Solid State Communications* **122,** 465–468 (2002).

54. Loiseau, A., Willaime, F., Demoncy, N., Hug, G. & Pascard, H. Boron Nitride Nanotubes with Reduced Numbers of Layers Synthesized by Arc Discharge. *Phys. Rev. Lett.* **76,** 4737–4740 (1996).

55. Cumings, J. & Zettl, A. Mass-production of boron nitride double-wall nanotubes and nanococoons. *Chemical Physics Letters* **316,** 211–216 (2000).

56. Kuno, M., Oku, T. & Suganuma, K. Synthesis of boron nitride nanotubes and nanocapsules with LaB6. *Diamond and Related Materials* **10.** 11th European Conference on Diamond, Diamond-like Materials, Carbon Nanotubes, Nitrides and Silicon Carbide, 1231–1234 (2001).

57. Terrones, M. *et al.* Metal particle catalysed production of nanoscale BN structures. *Chemical Physics Letters* **259,** 568–573 (1996).

58. Golberg, D. *et al.* Nanotubes in boron nitride laser heated at high pressure. *Applied Physics Letters* **69,** 2045–2047 (1996).

59. Lee, R. S. *et al.* Catalyst-free synthesis of boron nitride single-wall nanotubes with a preferred zig-zag configuration. *Phys. Rev. B* **64,** 121405 (2001).

60. Arenal, R., Stephan, O., Cochon, J.-L. & Loiseau, A. Root-Growth Mechanism for Single-Walled Boron Nitride Nanotubes in Laser Vaporization Technique. *Journal of the American Chemical Society* **129,** 16183–16189 (2007).

61. Smith, M. W. *et al.* Very long single- and few-walled boron nitride nanotubes via the pressurized vapor/condenser method. *Nanotechnology* **20,** 505604 (2009).

62. Shimizu, Y., Moriyoshi, Y., Tanaka, H. & Komatsu, S. Boron nitride nanotubes, webs, and coexisting amorphous phase formed by the plasma jet method. *Applied Physics Letters* **75,** 929–931 (1999).

63. Kim, K. S. *et al.* Hydrogen-catalyzed, pilot-scale production of small-diameter boron nitride nanotubes and their macroscopic assemblies. *ACS Nano* **8,** 6211–6220 (2014).

64. Kim, K. S. *et al.* Role of Hydrogen in High-Yield Growth of Boron Nitride Nanotubes at Atmospheric Pressure by Induction Thermal Plasma. *ACS Nano* **12,** 884–893 (2018).

65. Fathalizadeh, A., Pham, T., Mickelson, W. & Zettl, A. Scaled Synthesis of Boron Nitride Nanotubes, Nanoribbons, and Nanococoons Using Direct Feedstock Injection into an Extended-Pressure, Inductively-Coupled Thermal Plasma. *Nano Letters* **14,** 4881–4886 (2014).

66. Chen, Y., Fitz Gerald, J., Williams, J. & Bulcock, S. Synthesis of boron nitride nanotubes at low temperatures using reactive ball milling. *Chemical Physics Letters* **299,** 260–264 (1999).

67. Chen, Y., Conway, M., Williams, J. S. & Zou, J. Large-quantity production of high-yield boron nitride nanotubes. *Journal of Materials Research* **17,** 1896–1899 (2002).

68. Kim, J. *et al.* Synthesis and growth of boron nitride nanotubes by a ball milling–annealing process. *Acta Materialia* **59,** 2807–2813 (2011).

69. Yu, J., Chen, Y., Wuhrer, R., Liu, Z. & Ringer, S. P. In Situ Formation of BN Nanotubes during Nitriding Reactions. *Chemistry of Materials* **17,** 5172–5176 (2005).

70. Li, L. *et al.* Mechanically activated catalyst mixing for high-yield boron nitride nanotube growth. *Nanoscale research letters* **7,** 417 (2012).

71. Tang, C., Bando, Y., Sato, T. & Kurashima, K. A novel precursor for synthesis of pure boron nitride nanotubes. *Chem. Commun.* 1290–1291 (2002).

72. Zhi, C., Bando, Y., Tan, C. & Golberg, D. Effective precursor for high yield synthesis of pure BN nanotubes. *Solid State Communications* **135,** 67–70 (2005).

73. Huang, Y. *et al.* Bulk synthesis, growth mechanism and properties of highly pure ultrafine boron nitride nanotubes with diameters of sub-10 nm. *Nanotechnology* **22,** 145602 (2011).

74. Lee, C. H., Wang, J., Kayatsha, V. K., Huang, J. Y. & Yap, Y. K. Effective growth of boron nitride nanotubes by thermal chemical vapor deposition. *Nanotechnology* **19,** 455605 (2008).

75. Lee, C. H., Xie, M., Kayastha, V., Wang, J. & Yap, Y. K. Patterned Growth of Boron Nitride Nanotubes by Catalytic Chemical Vapor Deposition. *Chemistry of Materials* **22,** 1782–1787 (2010).

76. Wang, L. *et al.* Bimetallic catalytic growth of boron nitride nanotubes. *Nanoscale* **9,** 1816–1819 (2017).

77. Pakdel, A., Zhi, C., Bando, Y., Nakayama, T. & Golberg, D. A comprehensive analysis of the CVD growth of boron nitride nanotubes. *Nanotechnology* **23,** 215601 (2012).

78. Lourie, O. R. *et al.* CVD growth of boron nitride nanotubes. *Chemistry of Materials* **12,** 1808–1810 (2000).

79. Kim, M. J. *et al.* Double-Walled Boron Nitride Nanotubes Grown by Floating Catalyst Chemical Vapor Deposition. *Nano Letters* **8,** 3298–3302 (2008).

80. Chatterjee, S. *et al.* Syntheses of Boron Nitride Nanotubes from Borazine and Decaborane Molecular Precursors by Catalytic Chemical Vapor Deposition with a Floating Nickel Catalyst. *Chemistry of Materials* **24,** 2872–2879 (2012).

81. Adnan, M. *et al.* Extraction of Boron Nitride Nanotubes and Fabrication of Macroscopic Articles Using Chlorosulfonic Acid. *Nano Letters* **18,** 1615–1619 (2018).

82. Marincel, D. M. *et al.* Scalable Purification of Boron Nitride Nanotubes via Wet Thermal Etching. *Chemistry of Materials* **31,** 1520–1527 (2019).

83. Tibbetts, G. G. Why are carbon filaments tubular? *Journal of Crystal Growth* **66,** 632–638 (1984).

84. Wagner, a. R. & Ellis, s. W. Vapor-liquid-solid mechanism of single crystal growth. *Applied Physics Letters* **4,** 89–90 (1964).

85. Givargizov, E. in *Vapour Growth and Epitaxy* 20–30 (Elsevier, 1975).

86. Deck, C. P. & Vecchio, K. Prediction of carbon nanotube growth success by the analysis of carbon–catalyst binary phase diagrams. *Carbon* **44,** 267–275 (2006).

87. Hurst, J. *Aligned Boron Nitride Nanotube Forests for Thermal Management* `https://nari.arc.nasa.gov/sites/default/files/SeedlingHURST.pdf` (2017).

88. Han, W., Bando, Y., Kurashima, K. & Sato, T. Synthesis of boron nitride nanotubes from carbon nanotubes by a substitution reaction. *Applied Physics Letters* **73,** 3085–3087 (1998).

89. Han, W., Bando, Y., Kurashima, K. & Sato, T. Formation of Boron Nitride (BN) Fullerene-Like Nanoparticles and (BN)xCy Nanotubes Using Carbon Nanotubes as Templates. *Japanese Journal of Applied Physics* **38,** L755–L757 (1999).

90. Nakanishi, R. *et al.* Thin single-wall BN-nanotubes formed inside carbon nanotubes. *Scientific Reports* **3,** 1385 (2013).

91. Li, L. H., Chen, Y. & Glushenkov, A. M. Boron nitride nanotube films grown from boron ink painting. *J. Mater. Chem.* **20,** 9679–9683 (2010).

92. Li, L. H., Chen, Y. & Glushenkov, A. M. Synthesis of boron nitride nanotubes by boron ink annealing. *Nanotechnology* **21,** 105601 (2010).

93. Lashmore, D. S. & Bennett, T. US 2015/0033937 A1 (2015).

94. Song, Y. *et al.* Ultralight boron nitride aerogels via template-assisted chemical vapor deposition. *Scientific Reports* **5,** 10337 (2015).

95. Xue, Y. *et al.* Multifunctional Superelastic Foam-Like Boron Nitride Nanotubular Cellular-Network Architectures. *ACS Nano* **11,** 558–568 (2017).

96. Tay, R. Y. *et al.* Facile Synthesis of Millimeter-Scale Vertically Aligned Boron Nitride Nanotube Forests by Template-Assisted Chemical Vapor Deposition. *Chemistry of Materials* **27,** 7156–7163 (2015).

97. Liu, J. *et al.* Fullerene Pipes. *Science* **280,** 1253–1256 (1998).

98. Endo, M. *et al.* 'Buckypaper' from coaxial nanotubes. *Nature* **433,** 476–476 (2005).

99. Xia, Q., Zhang, Z., Liu, Y. & Leng, J. Buckypaper and its composites for aeronautic applications. *Composites Part B: Engineering* **199,** 108231 (2020).

100. Ribeiro, B., Botelho, E. C., Costa, M. L. & Bandeira, C. F. Carbon nanotube buckypaper reinforced polymer composites: a review. *Polımeros* **27,** 247–255 (2017).

101. Shore, S. G. & Parry, R. W. The crystalline compound Ammonia-Borane,1 H3NBH3. *Journal of the American Chemical Society* **77,** 6084–6085 (1955).

102. Klooster, W. T., Koetzle, T. F., Siegbahn, P. E. M., Richardson, T. B. & Crabtree, R. H. Study of the NH $\cdots$ HB Dihydrogen Bond Including the Crystal Structure of BH_3NH_3 by Neutron Diffraction. *Journal of the American Chemical Society* **121,** 6337–6343 (1999).

103. Staubitz, A., Robertson, A. P. M. & Manners, I. Ammonia-Borane and Related Compounds as Dihydrogen Sources. *Chemical Reviews* **110,** 4079–4124 (2010).

104. Frueh, S. *et al.* Pyrolytic Decomposition of Ammonia Borane to Boron Nitride. *Inorganic Chemistry* **50,** 783–792 (2011).

105. Whittell, G. R. & Manners, I. Advances with Ammonia-Borane: Improved Recycling and Use as a Precursor to Atomically Thin BN Films. *Angewandte Chemie International Edition* **50,** 10288–10289 (2011).

106. Bernard, S. & Miele, P. Nanostructured and architectured boron nitride from boron, nitrogen and hydrogen-containing molecular and polymeric precursors. *Materials Today* **17,** 443–450 (2014).

107. Koepke, J. C. *et al.* Role of Pressure in the Growth of Hexagonal Boron Nitride Thin Films from Ammonia-Borane. *Chemistry of Materials* **28,** 4169–4179 (2016).

108. Kim, G. *et al.* Growth of High-Crystalline, Single-Layer Hexagonal Boron Nitride on Recyclable Platinum Foil. *Nano Letters* **13,** 1834–1839 (2013).

109. Mayer, E. Symmetrical cleavage of diborane by ammonia in solution. *Inorganic Chemistry* **11,** 866–869 (1972).

110. Hu, M., Van Paasschen, J. & Geanangel, R. New synthetic approaches to ammonia-borane and its deuterated derivatives. *Journal of Inorganic and Nuclear Chemistry* **39,** 2147–2150 (1977).

111. Alton, E. R., Brown, R. D., Carter, J. C. & Taylor, R. C. Vapor Pressures of the Methylamine-Boranes and Ammonia-Triborane1. *Journal of the American Chemical Society* **81,** 3550–3551 (1959).

112. Sams, R. L., Xantheas, S. S. & Blake, T. A. Vapor Phase Infrared Spectroscopy and Ab Initio Fundamental Anharmonic Frequencies of Ammonia Borane. *The Journal of Physical Chemistry A* **116,** 3124–3136 (2012).

113. Babenko, V. *et al.* Time dependent decomposition of ammonia borane for the controlled production of 2D hexagonal boron nitride. *Scientific Reports* **7,** 1–12 (2017).

114. Song, L. *et al.* Large Scale Growth and Characterization of Atomic Hexagonal Boron Nitride Layers. *Nano Letters* **10,** 3209–3215 (2010).

115. Liu, Z. *et al.* Direct Growth of Graphene/Hexagonal Boron Nitride Stacked Layers. *Nano Letters* **11,** 2032–2037 (2011).

116. Mickelson, W., Aloni, S., Han, W.-Q., Cumings, J. & Zettl, A. Packing C60 in boron nitride nanotubes. *Science* **300,** 467–469 (2003).

117. Walker, K. E. *et al.* Growth of Carbon Nanotubes inside Boron Nitride Nanotubes by Coalescence of Fullerenes: Toward the World's Smallest Coaxial Cable. *Small Methods* **1,** 1700184 (2017).

118. Arenal, R. & Lopez-Bezanilla, A. In situ formation of carbon nanotubes encapsulated within boron nitride nanotubes via electron irradiation. *ACS Nano* **8,** 8419–8425 (2014).

119. Chang, H.-C., Tsai, H.-J., Lin, W.-Y., Chu, Y.-C. & Hsu, W.-K. Hexagonal Boron Nitride Coated Carbon Nanotubes: Interlayer Polarization Improved Field Emission. *ACS Applied Materials & Interfaces* **7,** 14456–14462 (2015).

120. Chiang, W.-H. *et al.* C/BCN core/shell nanotube films with improved thermoelectric properties. *Carbon* **109,** 49–56 (2016).

121. Chen, L., Ye, H. & Gogotsi, Y. Synthesis of boron nitride coating on carbon nanotubes. *Journal of the American Ceramic Society* **87,** 147–151 (2004).

122. Mohai, I. *et al.* Formation of thin boron nitride coating on multiwall carbon nanotube surfaces. *Diamond and Related Materials* **20,** 227–231 (2011).

123. Jing, L. *et al.* Coaxial carbon@boron nitride nanotube arrays with enhanced thermal stability and compressive mechanical properties. *Nanoscale* **8,** 11114–11122 (2016).

124. Jing, L. *et al.* Thermal Conductivity Enhancement of Coaxial Carbon@Boron Nitride Nanotube Arrays. *ACS Applied Materials & Interfaces* **9,** 14555–14560 (2017).

125. Joo Jeong, Y. & Islam, M. F. Compressible elastomeric aerogels of hexagonal boron nitride and single-walled carbon nanotubes. *Nanoscale* **7,** 12888–12894 (2015).

126. Gomathi, A., Harika, M. R. & Rao, C. Urea route to coat inorganic nanowires, carbon fibers and nanotubes by boron nitride. *Materials Science and Engineering: A* **476,** 29–33 (2008).

127. Yan, W. *et al.* Polyimide nanocomposites with boron nitride-coated multi-walled carbon nanotubes for enhanced thermal conductivity and electrical insulation. *J. Mater. Chem. A* **2,** 20958–20965 (2014).

128. Li, X., Li, Q. & Chen, G.-X. Alkali metal surfactant-facilitated formation of thick boron nitride layers on carbon nanotubes by dip-coating. *Materials Letters* **134,** 38–41 (2014).

129. Yang, X. *et al.* Enhanced Field Emission from a Carbon Nanotube Array Coated with a Hexagonal Boron Nitride Thin Film. *Small* **11,** 3710–3716 (2015).

130. Zou, Q. M. *et al.* Refractory Vertically Aligned Carbon Nanotube–Boron Nitride Nanocomposites for Scalable Electrical Anisotropic Interconnects. *ACS Applied Nano Materials* **2,** 100–108 (2019).

131. Xiang, R. *et al.* One-dimensional van der Waals heterostructures. *Science* **367,** 537–542 (2020).

132. Wang, P. *et al.* Enhanced In-Plane Thermal Conductance of Thin Films Composed of Coaxially Combined Single-Walled Carbon Nanotubes and Boron Nitride Nanotubes. *ACS Nano* **14,** 4298–4305 (2020).

133. Wang, W.-L. *et al.* Facile synthesis of boron nitride coating on carbon nanotubes. *Materials Chemistry and Physics* **122,** 129–132 (2010).

134. Morihisa, Y. *et al.* Improved field emission characteristics of individual carbon nanotube coated with boron nitride nanofilm. *Journal of Vacuum Science & Technology B: Microelectronics and Nanometer Structures Processing, Measurement, and Phenomena* **26,** 872–875 (2008).

135. Su, C., Juang, Z., Chen, Y., Leou, K. & Tsai, C. The field emission characteristics of carbon nanotubes coated by boron nitride film. *Diamond and Related Materials* **16,** 1393–1397 (2007).

136. Arenal, R., Stephan, O., Cochon, J.-L. & Loiseau, A. Root-growth mechanism for single-walled boron nitride nanotubes in laser vaporization technique. *Journal of the American Chemical Society* **129,** 16183–16189 (2007).

137. Lipp, A., Schwetz, K. & Hunold, K. Hexagonal boron nitride: Fabrication, properties and applications. *Journal of the European Ceramic Society* **5,** 3–9 (1989).

138. Jones, R. S., Maciejewska, B. & Grobert, N. Synthesis, characterisation and applications of core–shell carbon–hexagonal boron nitride nanotubes. *Nanoscale Adv.* **2,** 4996–5014 (2020).

139. Emission characteristics of boron nitride coated carbon nanotubes. *Physica B: Condensed Matter* **323,** 180–181 (2002).

140. Mohai, M. *et al.* Surface characterisation of boron nitride layers on multiwalled carbon nanotubes. *Surface and Interface Analysis* **42,** 1148–1151 (2010).

141. Li, Y. *et al.* Synthesis, structure and antioxidant performance of boron nitride (hexagonal) layers coating on carbon nanotubes (multi-walled). *Applied Surface Science* **450,** 284–291 (2018).

142. Hesjedal, T. Continuous roll-to-roll growth of graphene films by chemical vapor deposition. *Applied Physics Letters* **98,** 133106 (2011).

143. Zhong, G. *et al.* Growth of continuous graphene by open roll-to-roll chemical vapor deposition. *Applied Physics Letters* **109,** 193103 (2016).

144. Khan, M. H. *et al.* Carbon- and crack-free growth of hexagonal boron nitride nanosheets and their uncommon stacking order. *Nanoscale* **8,** 15926–15933 (2016).

145. White, C. M., Banks, R., Hamerton, I. & Watts, J. F. Characterisation of commercially CVD grown multi-walled carbon nanotubes for paint applications. *Progress in Organic Coatings* **90,** 44–53 (2016).

146. Yang, X. *et al.* Wet-Chemistry-Assisted Nanotube-Substitution Reaction for High-Efficiency and Bulk-Quantity Synthesis of Boron- and Nitrogen-Codoped Single-Walled Carbon Nanotubes. *Journal of the American Chemical Society* **133,** 13216–13219 (2011).

147. Schmid, Herbert K. Phase Identification in Carbon and BN Systems by EELS. *Microsc. Microanal. Microstruct.* **6,** 99–111 (1995).

148. Smith, B. W. & Luzzi, D. E. Electron irradiation effects in single wall carbon nanotubes. *Journal of Applied Physics* **90,** 3509–3515 (2001).

149. Yuzvinsky, T. D. *et al.* Shrinking a Carbon Nanotube. *Nano Letters* **6,** 2718–2722 (2006).

150. Banhart, F. Irradiation effects in carbon nanostructures. *Reports on Progress in Physics* **62,** 1181–1221 (1999).

151. Zobelli, A., Gloter, A., Ewels, C. P. & Colliex, C. Shaping single walled nanotubes with an electron beam. *Phys. Rev. B* **77,** 045410 (2008).

152. Crespi, V. H., Chopra, N. G., Cohen, M. L., Zettl, A. & Louie, S. G. Anisotropic electron-beam damage and the collapse of carbon nanotubes. *Phys. Rev. B* **54,** 5927–5931 (1996).

153. Chopra, N. G., Ross, F. & Zettl, A. Collapsing carbon nanotubes with an electron beam. *Chemical Physics Letters* **256,** 241–245 (1996).

154. Wei, X., Tang, D.-M., Chen, Q., Bando, Y. & Golberg, D. Local Coulomb Explosion of Boron Nitride Nanotubes under Electron Beam Irradiation. *ACS Nano* **7,** 3491–3497 (2013).

155. Yang, N. *et al.* Preparation and properties of thermally conductive polyimide/boron nitride composites. *RSC Adv.* **6,** 18279–18287 (2016).

156. Dresselhaus, M., Dresselhaus, G., Saito, R. & Jorio, A. Raman spectroscopy of carbon nanotubes. *Physics Reports* **409,** 47–99 (2005).

157. DiLeo, R. A., Landi, B. J. & Raffaelle, R. P. Purity assessment of multiwalled carbon nanotubes by Raman spectroscopy. *Journal of Applied Physics* **101,** 064307 (2007).

158. Pimenta, M. *et al.* Studying disorder in graphite-based systems by Raman spectroscopy. *Physical chemistry chemical physics* **9,** 1276–1290 (2007).

159. Ferrari, A. C. Raman spectroscopy of graphene and graphite: Disorder, electron–phonon coupling, doping and nonadiabatic effects. *Solid State Communications* **143,** 47–57 (2007).

160. Iyyamperumal, E., Wang, S. & Dai, L. Vertically aligned BCN nanotubes with high capacitance. *ACS Nano* **6,** 5259–5265 (2012).

161. Koós, A. A., Dillon, F., Obraztsova, E. A., Crossley, A. & Grobert, N. Comparison of structural changes in nitrogen and boron-doped multi-walled carbon nanotubes. *Carbon* **48,** 3033–3041 (2010).

162. Geick, R., Perry, C. & Rupprecht, G. Normal modes in hexagonal boron nitride. *Physical Review* **146,** 543 (1966).

163. Nemanich, R., Solin, S. & Martin, R. M. Light scattering study of boron nitride microcrystals. *Physical Review B* **23,** 6348 (1981).

164. Flygare, M. & Svensson, K. Quantifying crystallinity in carbon nanotubes and its influence on mechanical behaviour. *Materials Today Communications* **18,** 39–45 (2019).

165. Cançado, L. G. *et al.* General equation for the determination of the crystallite size La of nanographite by Raman spectroscopy. *Applied Physics Letters* **88,** 163106 (2006).

166. Warren, B. E. X-Ray Diffraction in Random Layer Lattices. *Phys. Rev.* **59,** 693–698 (1941).

167. Warren, B. E. *X-ray diffraction* eng (Dover, New York, 1990).

168. Saito, Y., Yoshikawa, T., Bandow, S., Tomita, M. & Hayashi, T. Interlayer spacings in carbon nanotubes. *Phys. Rev. B* **48,** 1907–1909 (1993).

169. Kiang, C.-H., Endo, M., Ajayan, P. M., Dresselhaus, G. & Dresselhaus, M. S. Size Effects in Carbon Nanotubes. *Phys. Rev. Lett.* **81,** 1869–1872 (1998).

170. Thomas, J., Weston, N. E. & O'Connor, T. E. Turbostratic1 Boron Nitride, Thermal Transformation to Ordered-layer-lattice Boron Nitride. *Journal of the American Chemical Society* **84,** 4619–4622 (1962).

171. Blume, R. *et al.* Characterizing Graphitic Carbon with X-ray Photoelectron Spectroscopy: A Step-by-Step Approach. *ChemCatChem* **7,** 2871–2881 (2015).

172. Zielke, U., Hüttinger, K. & Hoffman, W. Surface-oxidized carbon fibers: I. Surface structure and chemistry. *Carbon* **34,** 983–998 (1996).

173. Zhou, J. *et al.* Vertically-aligned BCN nanotube arrays with superior performance in electrochemical capacitors. *Scientific Reports* **4,** 6083 (2014).

174. Kim, S. Y. *et al.* X-ray photoelectron spectroscopy and first principles calculation of BCN nanotubes. *Journal of the American Chemical Society* **129,** 1705–1716 (2007).

175. Ci, L. *et al.* Atomic layers of hybridized boron nitride and graphene domains. *Nature Materials* **9,** 430–435 (2010).

176. Chandni, U., Watanabe, K., Taniguchi, T. & Eisenstein, J. P. Signatures of Phonon and Defect-Assisted Tunneling in Planar Metal–Hexagonal Boron Nitride–Graphene Junctions. *Nano Letters* **16,** 7982–7987 (2016).

177. Jakubinek, M. B. *et al.* Assessment of boron nitride nanotube materials using X-ray photoelectron spectroscopy. *Canadian Journal of Chemistry* **97,** 457–464 (2019).

178. Sediri, H. *et al.* Atomically Sharp Interface in an h-BN-epitaxial graphene van der Waals Heterostructure. *Scientific Reports* **5,** 1–10 (2015).

179. Liu, Q. *et al.* Porous Hexagonal Boron Nitride Sheets: Effect of Hydroxyl and Secondary Amino Groups on Photocatalytic Hydrogen Evolution. *ACS Applied Nano Materials* **1,** 4566–4575 (2018).

180. Raidongia, K. *et al.* Synthesis, structure and properties of homogeneous BC 4 N nanotubes. *Journal of Materials Chemistry* **18,** 83–90 (2008).

181. Li, H. *et al.* Composition-controlled synthesis and tunable optical properties of ternary boron carbonitride nanotubes. *RSC Adv.* **7,** 12511–12517 (2017).

182. Arenal, R., Blase, X. & Loiseau, A. Boron-nitride and boron-carbonitride nanotubes: synthesis, characterization and theory. *Advances in Physics* **59,** 101–179 (2010).

183. Han, W.-Q., Cumings, J., Huang, X., Bradley, K. & Zettl, A. Synthesis of aligned BxCyNz nanotubes by a substitution-reaction route. *Chemical Physics Letters* **346,** 368–372 (2001).

184. Deepak, F., Vinod, C., Mukhopadhyay, K., Govindaraj, A. & Rao, C. Boron nitride nanotubes and nanowires. *Chemical Physics Letters* **353,** 345–352 (2002).

185. Reckinger, N., Felten, A., Santos, C. N., Hackens, B. & Colomer, J.-F. The influence of residual oxidizing impurities on the synthesis of graphene by atmospheric pressure chemical vapor deposition. *Carbon* **63,** 84–91 (2013).

186. Choubak, S., Biron, M., Levesque, P. L., Martel, R. & Desjardins, P. No Graphene Etching in Purified Hydrogen. *The Journal of Physical Chemistry Letters* **4,** 1100–1103 (2013).

187. Lee, Y.-H. *et al.* Growth selectivity of hexagonal-boron nitride layers on Ni with various crystal orientations. *RSC Adv.* **2,** 111–115 (1 2012).

188. Matsuda, T. Stability to moisture for chemically vapour-deposited boron nitride. *Journal of Materials Science* **24,** 2353–2357 (1989).

189. Rand, M. J. & Roberts, J. F. Preparation and properties of thin film boron nitride. *Journal of the Electrochemical Society* **115,** 423 (1968).

190. Cao, F., Liu, K., Fang, Z. & Wang, S. Hydrolysis Mechanism of Borazine-derived Boron Nitride Pyrolysized below 1200 °C. *Journal of Materials Science & Technology* **28,** 956–960 (2012).

191. Chemical vapour deposition of thin films of BN onto fused silica and sapphire. *Thin Solid Films* **83,** 247–251 (1981).

192. Motojima, S., Tamura, Y. & Sugiyama, K. Low temperature deposition of hexagonal BN films by chemical vapour deposition. *Thin Solid Films* **88,** 269–274 (1982).

193. Anutgan, T. A., Anutgan, M., Atilgan, I. & Katircioglu, B. Stability and degradation of plasma deposited boron nitride thin films in ambient atmosphere. *Thin Solid Films* **518,** 419–425 (2009).

194. Cholet, V., Vandenbulcke, L., Rouan, J., Baillif, P. & Erre, R. Characterization of boron nitride films deposited from BCl_3-NH_3-H_2 mixtures in chemical vapour infiltration conditions. *Journal of Materials Science* **29,** 1417–1435 (1994).

195. Cofer, C. G. & Economy, J. Oxidative and hydrolytic stability of boron nitride — A new approach to improving the oxidation resistance of carbonaceous structures. *Carbon* **33,** 389–395 (1995).

196. Zhong, B. *et al.* Boron nitride hollow nanospheres: Synthesis, formation mechanism and dielectric property. *Materials Research Bulletin* **64,** 61–67 (2015).

197. Wang, Y., Yamamoto, Y., Kiyono, H. & Shimada, S. Effect of Ambient Gas and Temperature on Crystallization of Boron Nitride Spheres Prepared by Vapor Phase Pyrolysis of Ammonia Borane. *Journal of the American Ceramic Society* **92,** 787–792 (2009).

198. Kovalskii, A. M. *et al.* Growth of spherical boron oxynitride nanoparticles with smooth and petalled surfaces during a chemical vapour deposition process. *CrystEngComm* **18,** 6689–6699 (2016).

199. Pruss, E. A., Wood, G. L., Kroenke, W. J. & Paine, R. T. Aerosol Assisted Vapor Synthesis of Spherical Boron Nitride Powders. *Chemistry of Materials* **12,** 19–21 (2000).

200. Casa Software Ltd. *CasaXPS Manual* (2013).

201. Gatan. *EELS.info* `https://eels.info/how` (2020).

202. Belin, T. & Epron, F. Characterization methods of carbon nanotubes: a review. *Materials Science and Engineering: B* **119,** 105–118 (2005).

203. Ma, R. & Bando, Y. Pyrolytic-grown B–C–N and BN nanotubes. *Science and Technology of Advanced Materials* **4,** 403–407 (2003).

204. Zhong, B. *et al.* Large-scale fabrication of boron nitride nanotubes via a facile chemical vapor reaction route and their cathodoluminescence properties. *Nanoscale Res Lett* **6,** 36 (2011).

205. Wang, Y., Yamamoto, Y., Kiyono, H. & Shimada, S. Highly ordered boron nitride nanotube arrays with controllable texture from ammonia borane by template-aided vapor-phase pyrolysis. *Journal of Nanomaterials* **2008** (2008).

206. Tang, C., Bando, Y. & Sato, T. Catalytic growth of boron nitride nanotubes. *Chemical Physics Letters* **362,** 185–189 (2002).

207. Su, C.-Y. *et al.* Selective Growth of Boron Nitride Nanotubes by the Plasma-Assisted and Iron-Catalytic CVD Methods. *The Journal of Physical Chemistry C* **113,** 14681–14688 (2009).

208. Pawlow, P. The dependency of the melting point on the surface energy of a solid body. *Z. Phys. Chem* **65,** 545–548 (1909).

209. Goldstein, A., Echer, C. & Alivisatos, A. Melting in semiconductor nanocrystals. *Science* **256,** 1425–1427 (1992).

210. Buffat, P. & Borel, J.-P. Size effect on the melting temperature of gold particles. *Phys. Rev. A* **13,** 2287–2298 (1976).

211. Guo, L. & Singh, R. N. Selective growth of boron nitride nanotubes by plasma-enhanced chemical vapor deposition at low substrate temperature. *Nanotechnology* **19,** 065601 (2008).

212. Hansen, T. W., DeLaRiva, A. T., Challa, S. R. & Datye, A. K. Sintering of catalytic nanoparticles: particle migration or Ostwald ripening? *Accounts of chemical research* **46,** 1720–1730 (2013).

213. Moulijn, J. A., Van Diepen, A. & Kapteijn, F. Catalyst deactivation: is it predictable?: What to do? *Applied Catalysis A: General* **212,** 3–16 (2001).

214. Helveg, S. *et al.* Atomic-scale imaging of carbon nanofibre growth. *Nature* **427,** 426–429 (2004).

215. Meysami, S. S., Dillon, F., Koós, A. A., Aslam, Z. & Grobert, N. Aerosol-assisted chemical vapour deposition synthesis of multi-wall carbon nanotubes: I. Mapping the reactor. *Carbon* **58,** 151–158 (2013).

216. Meysami, S. S., Koós, A. A., Dillon, F. & Grobert, N. Aerosol-assisted chemical vapour deposition synthesis of multi-wall carbon nanotubes: II. An analytical study. *Carbon* **58,** 159–169 (2013).

217. Meysami, S. S., Koós, A. A., Dillon, F., Dutta, M. & Grobert, N. Aerosol-assisted chemical vapour deposition synthesis of multi-wall carbon nanotubes: III. Towards upscaling. *Carbon* **88,** 148–156 (2015).

218. El-Barbary, A. A., Telling, R. H., Ewels, C. P., Heggie, M. I. & Briddon, P. R. Structure and energetics of the vacancy in graphite. *Phys. Rev. B* **68,** 144107 (2003).

219. Liu, Z. *et al.* Ultrathin high-temperature oxidation-resistant coatings of hexagonal boron nitride. *Nature Communications* **4,** 1–8 (2013).

220. Lehman, J. H., Terrones, M., Mansfield, E., Hurst, K. E. & Meunier, V. Evaluating the characteristics of multiwall carbon nanotubes. *Carbon* **49,** 2581–2602 (2011).

221. Huang, W., Wang, Y., Luo, G. & Wei, F. 99.9% purity multi-walled carbon nanotubes by vacuum high-temperature annealing. *Carbon* **41,** 2585–2590 (2003).

222. Kowalska, E. *et al.* Influence of high vacuum annealing treatment on some properties of carbon nanotubes. *Journal of thermal analysis and calorimetry* **86,** 115–119 (2006).

223. Osswald, S., Havel, M. & Gogotsi, Y. Monitoring oxidation of multiwalled carbon nanotubes by Raman spectroscopy. *Journal of Raman Spectroscopy: An International Journal for Original Work in all Aspects of Raman Spectroscopy, Including Higher Order Processes, and also Brillouin and Rayleigh Scattering* **38,** 728–736 (2007).

224. Zhou, W. *et al.* Structural characterization and diameter-dependent oxidative stability of single wall carbon nanotubes synthesized by the catalytic decomposition of CO. *Chemical Physics Letters* **350,** 6–14 (2001).

225. Trigueiro, J. P. C. *et al.* Purity evaluation of carbon nanotube materials by thermogravimetric, TEM, and SEM methods. *Journal of Nanoscience and Nanotechnology* **7,** 3477–3486 (2007).

226. Lima, A. M., Musumeci, A. W., Liu, H.-W., Waclawik, E. R. & Silva, G. G. Purity evaluation and influence of carbon nanotube on carbon nanotube/graphite thermal stability. *Journal of thermal analysis and calorimetry* **97,** 257 (2009).

227. McKee, G. S., Deck, C. P. & Vecchio, K. S. Dimensional control of multi-walled carbon nanotubes in floating-catalyst CVD synthesis. *Carbon* **47,** 2085–2094 (2009).

228. Arepalli, S. *et al.* Protocol for the characterization of single-wall carbon nanotube material quality. *Carbon* **42,** 1783–1791 (2004).

229. White, D., Walsh, P. N., Goldstein, H. W. & Dever, D. F. Rare Earths.II. A Mass Spectrometric Determination of the Heats of Sublimation (or vaporization) of neodymium, praseodymium, gadolinium, terbium, dysprosium, holmium, erbium and lutetium1. *The Journal of Physical Chemistry* **65,** 1404–1409 (1961).

230. Shieh, M. & Lee, C. A more general structural model which includes the induction time for gas-solid reactions-II. The kinetics of alpha-boron nitride oxidation. *Chemical Engineering Science* **48,** 1851–1857 (1993).

231. Oda, K. & Yoshio, T. Oxidation kinetics of hexagonal boron nitride powder. *Journal of Materials Science* **28,** 6562–6566 (1993).

232. Pang, L. S. K., Saxby, J. D. & Chatfield, S. P. Thermogravimetric analysis of carbon nanotubes and nanoparticles. *The Journal of Physical Chemistry* **97,** 6941–6942 (1993).

233. Scheibe, B., Borowiak-Palen, E. & Kalenczuk, R. J. Oxidation and reduction of multiwalled carbon nanotubes — preparation and characterization. *Materials Characterization* **61,** 185–191 (2010).

234. Landi, B. J., Cress, C. D., Evans, C. M. & Raffaelle, R. P. Thermal Oxidation Profiling of Single-Walled Carbon Nanotubes. *Chemistry of Materials* **17,** 6819–6834 (2005).

235. Shi, Z. *et al.* Large scale synthesis of single-wall carbon nanotubes by arc-discharge method. *Journal of Physics and Chemistry of Solids* **61,** 1031–1036 (2000).

236. Liao, Y. *et al.* Oxidative etching of hexagonal boron nitride toward nanosheets with defined edges and holes. *Scientific Reports* **5,** 14510 (2015).

237. Nautiyal, P. *et al.* Oxidative unzipping and transformation of high aspect ratio boron nitride nanotubes into "white graphene oxide" platelets. *Scientific Reports* **6,** 1–8 (2016).

238. Li, J.-S., Zhang, C.-R. & Li, B. Preparation and characterization of boron nitride coatings on carbon fibers from borazine by chemical vapor deposition. *Applied Surface Science* **257,** 7752–7757 (2011).

239. El Mendili, Y. *et al.* Raman Open Database: first interconnected Raman–X-ray diffraction open-access resource for material identification. *Journal of Applied Crystallography* **52,** 618–625 (June 2019).

240. Zhong, B. *et al.* Fabrication and Raman scattering behavior of novel turbostratic BN thin films. *Materials Letters* **151,** 130–133 (2015).

241. Si, P. Z. *et al.* Amorphous boron nanoparticles and BN encapsulating boron nano-peanuts prepared by arc-decomposing diborane and nitriding. *Journal of Materials Science* **38,** 689–692 (2003).

242. Lei, Y., Wang, Y. & Song, Y. Atmosphere influence in the pyrolysis of poly[(alkylamino)borazine] for the production of BN fibers. *Ceramics International* **39,** 6847–6851 (2013).

243. Tuschel, D. & Adar, F. Selecting an excitation wavelength for Raman spectroscopy. *Spectroscopy* **31,** 14–23 (3 2016).

244. Ferraro, J. R., Nakamoto, K. & Brown, C. W. *Introductory Raman Spectroscopy. [electronic resource]* 2nd ed. eng (Burlington, 2003).

245. Dong, Z. & Song, Y. Transformations of cold-compressed multiwalled boron nitride nanotubes probed by infrared spectroscopy. *The Journal of Physical Chemistry C* **114,** 1782–1788 (2010).

246. Wei, D., Chen, S. & Liu, Q. Review of Fluorescence Suppression Techniques in Raman Spectroscopy. *Applied Spectroscopy Reviews* **50,** 387–406 (2015).

247. Zhi, C. *et al.* Phonon characteristics and cathodolumininescence of boron nitride nanotubes. *Applied Physics Letters* **86,** 213110 (2005).

248. Chen, Z.-G. *et al.* Long wavelength emissions of periodic yard-glass shaped boron nitride nanotubes. *Applied Physics Letters* **94,** 023105 (2009).

249. Wu, J. *et al.* Raman Spectroscopy and Time-Resolved Photoluminescence of BN and BxCyNz Nanotubes. *Nano Letters* **4,** 647–650 (2004).

250. Yong Bae, S. *et al.* Boron nitride nanotubes synthesized in the temperature range 1000–1200 °C. *Chemical Physics Letters* **374,** 534–541 (2003).

251. Xu, S. *et al.* Phonon characteristics and photoluminescence of bamboo structured silicon-doped boron nitride multiwall nanotubes. *Applied Physics Letters* **90,** 013115 (2007).

252. Exarhos, G. J. & Schaaf, J. W. Raman scattering from boron nitride coatings at high temperatures. *Journal of Applied Physics* **69,** 2543–2548 (1991).

253. Tang, C. *et al.* Thermal conductivity of nanostructured boron nitride materials. *The Journal of Physical Chemistry B* **110,** 10354–10357 (2006).

254. Lu, J. *et al.* Temperature-dependent Raman spectra of bamboo-like boron nitride nanotubes. *Applied Physics Express* **7,** 022401 (2014).

255. Arenal, R. *et al.* Raman Spectroscopy of Single-Wall Boron Nitride Nanotubes. *Nano Letters* **6,** 1812–1816 (2006).

256. Arutyunyan, N. R. *et al.* Thermal effects in Raman spectra of hexagonal boron nitride and nanotube-containing boron nitride soot. *physica status solidi (b)* **243,** 3316–3319 (2006).

257. Cuscó, R., Gil, B., Cassabois, G. & Artús, L. Temperature dependence of Raman-active phonons and anharmonic interactions in layered hexagonal BN. *Phys. Rev. B* **94,** 155435 (2016).

258. Mackenzie, J. D. & Claussen, W. F. Crystallization and Phase Relations of Boron Trioxide at High Pressures. *Journal of the American Ceramic Society* **44,** 79–81 (1961).

259. Gurr, G. E., Montgomery, P. W., Knutson, C. D. & Gorres, B. T. The crystal structure of trigonal diboron trioxide. *Acta Crystallographica Section B* **26,** 906–915 (1970).

260. Aziz, M. J., Nygren, E., Hays, J. F. & Turnbull, D. Crystal growth kinetics of boron oxide under pressure. *Journal of Applied Physics* **57,** 2233–2242 (1985).

261. Egerton, R. F. *Electron energy-loss spectroscopy in the electron microscope [electronic resource]* 3rd ed. eng (Springer, New York, 2011).

262. Silva, L. A., Guerini, S. C., Lemos, V., *et al.* Electronic and structural properties of oxygen-doped BN nanotubes. *IEEE transactions on nanotechnology* **5,** 517–522 (2006).

263. Guimon, C. *et al.* XPS study of BN thin films deposited by CVD on SiC plane substrates. *Surface and Interface Analysis* **16,** 440–445 (1990).

264. Bresnehan, M. S. *et al.* Prospects of direct growth boron nitride films as substrates for graphene electronics. *Journal of Materials Research* **29,** 459–471 (2014).

265. Wagner, C., Riggs, W., Davis, L., Moulder, J. & Muilenberg, G. Handbook of X-ray photoelectron spectroscopy, Perkin-Elmer Corp. *Eden Prairie, MN* **38** (1979).

266. Sutter, P., Lahiri, J., Zahl, P., Wang, B. & Sutter, E. Scalable synthesis of uniform few-layer hexagonal boron nitride dielectric films. *Nano Letters* **13,** 276–281 (2013).

267. Zhang, G., Zang, S. & Wang, X. Layered Co(OH)2 Deposited Polymeric Carbon Nitrides for Photocatalytic Water Oxidation. *ACS Catalysis* **5,** 941–947 (2015).

268. Zaleska, A., Sobczak, J. W., Grabowska, E. & Hupka, J. Preparation and photocatalytic activity of boron-modified TiO2 under UV and visible light. *Applied Catalysis B: Environmental* **78,** 92–100 (2008).

269. Chen, D., Yang, D., Wang, Q. & Jiang, Z. Effects of Boron Doping on Photocatalytic Activity and Microstructure of Titanium Dioxide Nanoparticles. *Industrial & Engineering Chemistry Research* **45,** 4110–4116 (2006).

270. Da Silva, W. M. *et al.* Efficient sensitive polymer-grafted boron nitride nanotubes by microwave-assisted process. *Nano-Structures & Nano-Objects* **15,** 186–196 (2018).

271. Burghaus, U. Surface chemistry of CO_2 – Adsorption of carbon dioxide on clean surfaces at ultrahigh vacuum. *Progress in Surface Science* **89,** 161–217 (2014).

272. Rance, G. A., Marsh, D. H., Nicholas, R. J. & Khlobystov, A. N. UV–vis absorption spectroscopy of carbon nanotubes: Relationship between the -electron plasmon and nanotube diameter. *Chemical Physics Letters* **493,** 19–23 (2010).

273. Cheung, W. *et al.* π-Plasmon absorption of carbon nanotubes for the selective and sensitive detection of Fe^{3+} ions. *Chem. Sci.* **7,** 5192–5199 (2016).

274. Ferreira, F., Chaves, A., Peres, N. & Ribeiro, R. Excitons in hexagonal boron nitride single-layer: a new platform for polaritonics in the ultraviolet. *JOSA B* **36,** 674–683 (2019).

275. Wirtz, L., Marini, A. & Rubio, A. Excitons in Boron Nitride Nanotubes: Dimensionality Effects. *Phys. Rev. Lett.* **96,** 126104 (2006).

276. Tauc, J., Grigorovici, R. & Vancu, A. Optical Properties and Electronic Structure of Amorphous Germanium. *physica status solidi (b)* **15,** 627–637 (1966).

277. Mott, N. F. & Davis, E. A. *Electronic processes in non-crystalline materials* Second edition. eng (Oxford, 2012).

278. Davis, E. A. & Mott, N. F. Conduction in non-crystalline systems V. Conductivity, optical absorption and photoconductivity in amorphous semiconductors. *The Philosophical Magazine: A Journal of Theoretical Experimental and Applied Physics* **22,** 0903–0922 (1970).

279. Mergen, Ö. B. & Arda, E. Determination of Optical Band Gap Energies of CS/MWCNT Bio-nanocomposites by Tauc and ASF Methods. *Synthetic Metals* **269,** 116539 (2020).

280. AL-ANI, S. K. J. Determination of the optical gap of amorphous materials. *International Journal of Electronics* **75,** 1153–1163 (1993).

281. Gauglitz, G. & Moore, D. S. *Handbook of spectroscopy.* Second, enlarged edition / edited by Günter Gauglitz and David S. Moore. eng (Weinheim, Germany, 2014).

282. Bernath, P. F. *Spectra of atoms and molecules* eng (Oxford University Press, New York ; Oxford, 1995).

283. Watanabe, K., Taniguchi, T. & Kanda, H. Direct-bandgap properties and evidence for ultraviolet lasing of hexagonal boron nitride single crystal. *Nature Materials* **3,** 404–409 (2004).

284. Arenal, R. *et al.* Electron Energy Loss Spectroscopy Measurement of the Optical Gaps on Individual Boron Nitride Single-Walled and Multiwalled Nanotubes. *Phys. Rev. Lett.* **95,** 127601 (2005).

285. Hoffman, D. M., Doll, G. L. & Eklund, P. C. Optical properties of pyrolytic boron nitride in the energy range 0.05—10 eV. *Phys. Rev. B* **30,** 6051–6056 (1984).

286. Ban, C., Jiang, X., Li, L. & Liu, X. The piezoelectric and dielectric properties of flexible, nanoporous, self-assembled boron nitride nanotube thin films. *Journal of Materials Science,* 1–11.

287. Nautiyal, P., Zhang, C., Loganathan, A., Boesl, B. & Agarwal, A. High Temperature Mechanics of Boron Nanotube "Buckypaper" for Engineering Advanced Structural Materials. *ACS Applied Nano Materials* (2019).

288. Han, W.-Q., Mickelson, W., Cumings, J. & Zettl, A. Transformation of BxCyNz nanotubes to pure BN nanotubes. *Applied Physics Letters* **81,** 1110–1112 (2002).

289. Chang, C.-W., Han, W.-Q. & Zettl, A. Thermal conductivity of BCN and BN nanotubes. *Journal of Vacuum Science & Technology B: Microelectronics and Nanometer Structures Processing, Measurement, and Phenomena* **23,** 1883–1886 (2005).

290. Yuan, S. *et al.* Synthesis of BN nanobamboos and nanotubes from barium metaborate. *Journal of Crystal Growth* **256,** 67–72 (2003).

291. Tang, C., Bando, Y., Ding, X., Qi, S. & Golberg, D. Catalyzed collapse and enhanced hydrogen storage of BN nanotubes. *Journal of the American Chemical Society* **124,** 14550–14551 (2002).

292. Hong, X., Wang, D. & Chung, D. Boron nitride nanotube mat as a low-k dielectric material with relative dielectric constant ranging from 1.0 to 1.1. *Journal of Electronic Materials* **45,** 453–461 (2016).

293. Hong, X., Wang, D. & Chung, D. Strong viscous behavior discovered in nanotube mats, as observed in boron nitride nanotube mats. *Composites Part B: Engineering* **91,** 56–64 (2016).

294. Chen, H., Chen, Y., Yu, J. & Williams, J. S. Purification of boron nitride nanotubes. *Chemical Physics Letters* **425,** 315–319 (2006).

295. Liao, Y. *et al.* Chemical sharpening, shortening, and unzipping of boron nitride nanotubes. *Advanced Functional Materials* **24,** 4497–4506 (2014).

296. Lee, C. H., Zhang, D. & Yap, Y. K. Functionalization, dispersion, and cutting of boron nitride nanotubes in water. *The Journal of Physical Chemistry C* **116,** 1798–1804 (2011).

297. Kleinerman, O. *et al.* Dissolution and Characterization of Boron Nitride Nanotubes in Superacid. *Langmuir* **33,** 14340–14346 (2017).

298. McWilliams, A. D. S. *et al.* Surfactant-assisted individualization and dispersion of boron nitride nanotubes. *Nanoscale Adv.* **1,** 1096–1103 (2019).

299. Dumée, L. F. *et al.* Characterization and evaluation of carbon nanotube Bucky-Paper membranes for direct contact membrane distillation. *Journal of Membrane Science* **351,** 36–43 (2010).

300. Her, S.-C. & Hsu, W.-C. Strain and Temperature Sensitivities Along with Mechanical Properties of CNT Buckypaper Sensors. *Sensors* **20** (2020).

301. Nirmalraj, P. N., Lyons, P. E., De, S., Coleman, J. N. & Boland, J. J. Electrical connectivity in single-walled carbon nanotube networks. *Nano Letters* **9,** 3890–3895 (2009).

302. Allaoui, A., Hoa, S. V., Evesque, P. & Bai, J. Electronic transport in carbon nanotube tangles under compression: the role of contact resistance. *Scripta Materialia* **61,** 628–631 (2009).

303. Zhang, L., Zhang, G., Liu, C. & Fan, S. High-Density Carbon Nanotube Buckypapers with Superior Transport and Mechanical Properties. *Nano Letters* **12,** 4848–4852 (2012).

304. Rouquerol, J. *et al.* Recommendations for the characterization of porous solids (Technical Report). *Pure and Applied Chemistry* **66,** 1739–1758 (1994).

305. Sears, K. *et al.* Recent developments in carbon nanotube membranes for water purification and gas separation. *Materials* **3,** 127–149 (2010).

306. Smajda, R., Kukovecz, Á., Kónya, Z. & Kiricsi, I. Structure and gas permeability of multi-wall carbon nanotube buckypapers. *Carbon* **45,** 1176–1184 (2007).

307. Zhang, J. & Jiang, D. Influence of geometries of multi-walled carbon nanotubes on the pore structures of Buckypaper. *Composites Part A: Applied Science and Manufacturing* **43,** 469–474 (2012).

308. Kukovecz, Á., Smajda, R., Kónya, Z. & Kiricsi, I. Controlling the pore diameter distribution of multi-wall carbon nanotube buckypapers. *Carbon* **45,** 1696–1698 (2007).

309. Whitby, R. L., Fukuda, T., Maekawa, T., James, S. L. & Mikhalovsky, S. V. Geometric control and tuneable pore size distribution of buckypaper and buckydiscs. *Carbon* **46,** 949–956 (2008).

310. Špitalský, Z. *et al.* The effect of oxidation treatment on the properties of multi-walled carbon nanotube thin films. *Materials Science and Engineering: B* **165.** 5th International Workshop on Nanosciences and Nanotechnologies, 135–138 (2009).

311. Barr, T. L. & Seal, S. Nature of the use of adventitious carbon as a binding energy standard. *Journal of Vacuum Science & Technology A* **13,** 1239–1246 (1995).

312. Siegbahn, K. ESCA: atomic, molecular and solid state structure studies by means of electron spectroscopy; pres. to the Royal Society of Sciences of Uppsala, Dec. 3rd, 1965. *Nova Acta Regiae Societatis Scientiarum Upsaliensis* (1967).

313. Miller, D. J., Biesinger, M. C. & McIntyre, N. S. Interactions of CO_2 and CO at fractional atmosphere pressures with iron and iron oxide surfaces: one possible mechanism for surface contamination? *Surface and Interface Analysis* **33,** 299–305 (2002).

314. Barinov, A., Gregoratti, L., Dudin, P., La Rosa, S. & Kiskinova, M. Imaging and Spectroscopy of Multiwalled Carbon Nanotubes during Oxidation: Defects and Oxygen Bonding. *Advanced Materials* **21,** 1916–1920 (2009).

315. Lizzit, S. *et al.* C 1*s* photoemission spectrum in graphite(0001). *Phys. Rev. B* **76,** 153408 (2007).

316. Barth, G., Linder, R. & Bryson, C. Advances in charge neutralization for XPS measurements of nonconducting materials. *Surface and Interface Analysis* **11,** 307–311 (1988).

317. Khanaki, A. *et al.* Effect of high carbon incorporation in Co substrates on the epitaxy of hexagonal boron nitride/graphene heterostructures. *Nanotechnology* **29,** 035602 (2017).

318. Brandt, E., Untereker, D., Reilley, C. & Murray, R. W. A comparison of carbon contaminant buildup on conductors and insulators in X-ray photoelectron spectroscopy. *Journal of Electron Spectroscopy and Related Phenomena* **14,** 113–120 (1978).

319. Houghton, E. *Climate change 1995: The science of climate change: contribution of working group I to the second assessment report of the Intergovernmental Panel on Climate Change* (Cambridge University Press, 1996).

320. Barr, T. L. *Modern ESCA : The Principles and Practice of X-ray Photoelectron Spectroscopy* eng (CRC Press, Boca Raton ; London, 1994).

321. Singh, G. *et al.* Emerging trends in porous materials for CO_2 capture and conversion. *Chem. Soc. Rev.* **49,** 4360–4404 (2020).

322. Xiao, F. *et al.* Controllable synthesis of few-layered and hierarchically porous boron nitride nanosheets. *Chem. Commun.* **52,** 3911–3914 (2016).

323. Li, S. *et al.* Porous hexagonal boron nitride nanosheets from g-C3N4 templates with a high specific surface area for CO_2 adsorption. *Ceramics International* **46,** 27627–27633 (2020).

324. Liang, J. *et al.* Pore structure regulation and carbon dioxide adsorption capacity improvement on porous BN fibers: Effects of high-temperature treatments in gaseous ambient. *Chemical Engineering Journal* **373,** 616–623 (2019).

325. Marchesini, S., McGilvery, C. M., Bailey, J. & Petit, C. Template-Free Synthesis of Highly Porous Boron Nitride: Insights into Pore Network Design and Impact on Gas Sorption. *ACS Nano* **11,** 10003–10011 (2017).

326. Shankar, R. *et al.* Porous boron nitride for combined CO_2 capture and photoreduction. *J. Mater. Chem. A* **7,** 23931–23940 (2019).

327. Owuor, P. S. *et al.* Lightweight hexagonal boron nitride foam for CO_2 absorption. *ACS Nano* **11,** 8944–8952 (2017).

328. Jiang, H. *et al.* Three-dimensional porous boron nitride foam for effective CO_2 adsorption. *Solid State Communications* **294,** 1–5 (2019).

329. Yang, C. *et al.* One-step template-free synthesis of 3D functionalized flower-like boron nitride nanosheets for NH_3 and CO_2 adsorption. *Nanoscale* **10,** 10979–10985 (2018).

330. Xiong, J., Di, J., Zhu, W. & Li, H. Hexagonal boron nitride adsorbent: Synthesis, performance tailoring and applications. *Journal of Energy Chemistry* **40,** 99–111 (2020).

331. Costa Paura, E. N. *et al.* CO_2 adsorption on single-walled boron nitride nanotubes containing vacancy defects. *RSC Adv.* **5,** 27412–27420 (2015).

332. Choi, H., Park, Y. C., Kim, Y.-H. & Lee, Y. S. Ambient Carbon Dioxide Capture by Boron-Rich Boron Nitride Nanotube. *Journal of the American Chemical Society* **133,** 2084–2087 (2011).

333. Jiao, Y. *et al.* A density functional theory study on CO_2 capture and activation by graphene-like boron nitride with boron vacancy. *Catalysis Today* **175.** The 6th International Conference on Environmental Catalysis (6th ICEC) Beijing, China, September 12-15, 2010, 271–275 (2011).

334. Zeng, H. *et al.* "White Graphenes": Boron Nitride Nanoribbons via Boron Nitride Nanotube Unwrapping. *Nano Letters* **10,** 5049–5055 (2010).

335. Erickson, K. J. *et al.* Longitudinal Splitting of Boron Nitride Nanotubes for the Facile Synthesis of High Quality Boron Nitride Nanoribbons. *Nano Letters* **11,** 3221–3226 (2011).

336. Sinitskii, A. *et al.* High-Yield Synthesis of Boron Nitride Nanoribbons via Longitudinal Splitting of Boron Nitride Nanotubes by Potassium Vapor. *ACS Nano* **8,** 9867–9873 (2014).

337. Li, L. *et al.* High-quality boron nitride nanoribbons: unzipping during nanotube synthesis. *Angewandte Chemie* **125,** 4306–4310 (2013).

338. Quan, H. *et al.* Stability to moisture of hexagonal boron nitride films deposited on silicon by RF magnetron sputtering. *Thin Solid Films* **642,** 90–95 (2017).

339. Erdemir, A., Fenske, G. & Erck, R. A study of the formation and self-lubrication mechanisms of boric acid films on boric oxide coatings. *Surface and Coatings Technology* **43-44,** 588–596 (1990).

340. Buc, D. *et al.* Analysis of magnetron sputtered boron oxide films. *Thin Solid Films* **515.** First International Symposium on Transparent Conducting Oxides, 8723–8727 (2007).

341. Liang, D., Liu, J., Zhou, Y., Zhou, J. & Cen, K. Ignition and combustion characteristics of molded amorphous boron under different oxygen pressures. *Acta Astronautica* **138,** 118–128 (2017).

342. Erdemir, A. in *Modern Tribology Handbook* chap. 22 (CRC Press LLC, 2000).

343. Music, D. *et al.* Synthesis and mechanical properties of boron suboxide thin films. *Journal of Vacuum Science & Technology A* **20,** 335–337 (2002).

344. Vassen, R. & Stöver, D. Growth of Boric Acid Crystallites on the Surface of Boron-Doped Silicon Carbide Samples. *Journal of the American Ceramic Society* **79,** 1699–1702 (1996).

345. Bayu Aji, L. *et al.* Degradation of ultra-thin boron films in air. *Applied Surface Science* **448,** 498–501 (2018).

346. Erdemir, A., Bindal, C. & Fenske, G. R. Formation of ultralow friction surface films on boron carbide. *Applied Physics Letters* **68,** 1637–1639 (1996).

347. Zachariasen, W. H. The Crystal Lattice of Boric Acid, BO_3H_3. *Zeitschrift für Kristallographie - Crystalline Materials* **88,** 150–161 (1934).

348. Zachariasen, W. H. The precise structure of orthoboric acid. *Acta Crystallographica* **7,** 305–310 (1954).

349. Cowley, J. M. Structure analysis of single crystals by electron diffraction. II. Disordered boric acid structure. *Acta Crystallographica* **6,** 522–529 (1953).

350. Downs, R. T. & Hall-Wallace, M. The American Mineralogist crystal structure database. *American Mineralogist* **88,** 247–250 (2003).

351. Li, Y., Ruoff, R. S. & Chang, R. P. H. Boric Acid Nanotubes, Nanotips, Nanorods, Microtubes, and Microtips. *Chemistry of Materials* **15,** 3276–3285 (2003).

352. Ohring, M. *Materials Science of Thin Films* 2nd ed. (Burlington, 2001).

353. Parsons, J. L. & Milberg, M. E. Vibrational Spectra of Vitreous $B_2O_3.xH_2O$. *Journal of the American Ceramic Society* **43,** 326–330 (1960).

354. Bethell, D. E. & Sheppard, N. The infra-red spectrum and structure of boric acid. *Trans. Faraday Soc.* **51,** 9–15 (1955).

355. Miller, F. A. & Wilkins, C. H. Infrared Spectra and Characteristic Frequencies of Inorganic Ions. *Analytical Chemistry* **24,** 1253–1294 (1952).

356. Gouin, X., Grange, P., Bois, L., L'Haridon, P. & Laurent, Y. Characterization of the nitridation process of boric acid. *Journal of Alloys and Compounds* **224,** 22–28 (1995).

357. Davis, H. B. & Mott, C. J. B. Interaction of boric acid and borates with carbohydrates and related substances. *J. Chem. Soc., Faraday Trans. 1* **76,** 1991–2002 (1980).

358. Jany, B. R., Janas, A. & Krok, F. Retrieving the Quantitative Chemical Information at Nanoscale from Scanning Electron Microscope Energy Dispersive X-ray Measurements by Machine Learning. *Nano Letters* **17,** 6520–6525 (2017).

359. Green, G. *AZtecOne User Guide* version 1. Oxford Instruments NanoAnalysis (2018).

360. He, X. *et al.* Wafer-scale monodomain films of spontaneously aligned single-walled carbon nanotubes. *Nature Nanotechnology* **11,** 633–638 (2016).

361. Trasobares, S. *et al.* Carbon nanotubes with graphitic wings. *Advanced Materials* **16,** 610–613 (2004).

362. Zeng, L. *et al.* Preparation of carbon nanosheets deposited on carbon nanotubes by microwave plasma-enhanced chemical vapor deposition method. *Applied Surface Science* **254,** 1700–1704 (2008).

363. Yu, K., Lu, G., Bo, Z., Mao, S. & Chen, J. Carbon Nanotube with Chemically Bonded Graphene Leaves for Electronic and Optoelectronic Applications. *The Journal of Physical Chemistry Letters* **2,** 1556–1562 (2011).

364. Stoner, B. R., Raut, A. S., Brown, B., Parker, C. B. & Glass, J. T. Graphenated carbon nanotubes for enhanced electrochemical double layer capacitor performance. *Applied Physics Letters* **99,** 183104 (2011).

365. Parker, C. B., Raut, A. S., Brown, B., Stoner, B. R. & Glass, J. T. Three-dimensional arrays of graphenated carbon nanotubes. *Journal of Materials Research* **27,** 1046–1053 (2012).

366. Ubnoske, S. M. *et al.* Perspectives on the Growth of High Edge Density Carbon Nanostructures: Transitions from Vertically Oriented Graphene Nanosheets to Graphenated Carbon Nanotubes. *The Journal of Physical Chemistry C* **118,** 16126–16132 (2014).

367. Wang, H. *et al.* Defect-induced formation mechanism for boron nitride nanosheets-nanotubes hybrid structures. *Scripta Materialia* **171,** 16–20 (2019).

368. Wang, J. *et al.* Effective Preparation of One-Dimensional Boron-Nitride-Nanotube-Supported Nanosheet Hierarchical Structures and Their Optical/Adsorption Properties. *ChemistrySelect* **3,** 10832–10836 (2018).

369. Pan, A., Chen, Y. & Li, J. An effective route for the synthesis of boron nitride micro-nano structures and the growth mechanism. *CrystEngComm* **17,** 1098–1105 (2015).

370. Su, J., Xiao, Y. & Ren, M. Enhanced thermal conductivity in epoxy nanocomposites with hybrid boron nitride nanotubes and nanosheets. *physica status solidi (a)* **210,** 2699–2705 (2013).

371. Du, V. A., Whittell, G. R., Manners, I., *et al.* Aluminum borate nanowires from the pyrolysis of polyaminoborane precursors. *Dalton Transactions* **45,** 1055–1062 (2016).

372. Zhou, J., Su, D., Luo, J. & Zhong, M. Synthesis of aluminum borate nanorods by a low-heating-temperature solid-state precursor method. *Materials Research Bulletin* **44,** 224–226 (2009).

373. Maia, L. J. Q., Faria Filho, F. M., Jerez, V., Moura, A. L. & de Araújo, C. B. Structural and luminescence properties of Nd^{3+}/Yb^{3+} codoped $Al_4B_2O_9$ nanocrystalline powders. *J. Mater. Chem. C* **3,** 11689–11696 (2015).

374. Yu, Z. *et al.* Low-temperature synthesis of aluminum borate nanowhiskers on the surface of aluminum powder promoted by ball-milling pretreatment. *Powder Technology* **212,** 310–315 (2011).

375. Gonzalez-Martinez, I. *et al.* Defect assisted thermal synthesis of crystalline aluminum borate nanowires. *Journal of Applied Physics* **112,** 024308 (2012).

376. Liu, Y., Li, Q. & Fan, S. Self-catalytic growth of aluminum borate nanowires. *Chemical Physics Letters* **375,** 632–635 (2003).

377. Elssfah, E. *et al.* Low-temperature performance of $Al_4B_2O_9$ nanowires. *Materials Research Bulletin* **42,** 482–486 (2007).

378. Drouin, D. *et al.* CASINO V2.42—A Fast and Easy-to-use Modeling Tool for Scanning Electron Microscopy and Microanalysis Users. *Scanning* **29,** 92–101 (2007).

379. Hovington, P., Drouin, D. & Gauvin, R. CASINO: A new monte carlo code in C language for electron beam interaction —part I: Description of the program. *Scanning* **19,** 1–14 (1997).

380. Drouin, D., Hovington, P. & Gauvin, R. CASINO: A new monte carlo code in C language for electron beam interactions—part II: Tabulated values of the mott cross section. *Scanning* **19,** 20–28 (1997).

381. Hovington, P., Drouin, D., Gauvin, R., Joy, D. C. & Evans, N. CASINO: A new monte Carlo code in C language for electron beam interactions—part III: Stopping power at low energies. *Scanning* **19,** 29–35 (1997).

382. Press, W. H. & Teukolsky, S. A. Portable Random Number Generators. *Computers in Physics* **6,** 522–524 (1992).

383. Joy, D. C. & Luo, S. An empirical stopping power relationship for low-energy electrons. *Scanning* **11,** 176–180 (1989).

384. Russ, J. C. *Fundamentals of energy dispersive x-ray analysis* eng (Butterworths, London ; Boston, 1984).